

Physics Division Activity Report

January 1–December 31, 2004

Managing Editors: Josef Bachmeier, Jean Butterworth, and Grace Hollen

Science Writers-Editors: Desiree Archuleta, Josef Bachmeier, Todd Heinrichs, and Grace Hollen

Design Direction: Jean Butterworth

Composition: Jean Butterworth

Illustration and Design: Jean Butterworth, Vicente Garcia, and Donald Montoya

Technical Review: Joysree Aubrey, Cris Barnes, Martin Cooper, Stephen Glick, Doug Fulton, Jon Kapustinsky, Carter Munson, Brent Park, James Ray, Robert Scarlett, Jeffrey Schinkel, Jack Shlachter, David Scudder, John Tapia, Scott Wilburn, Charles Wood

Physics Division managers and the editors would like to acknowledge the valuable contributions of all subject-matter experts throughout the Division and from other Laboratory organizations who provided technical information and guidance.

CD Integration Design and Production: Jean Butterworth

Printing Coordination: IM-9 Imaging Services

Physics Division Activity Report

Abstract

This issue of the Physics Division Activity Report describes some of our activities and achievements in applied and basic science during the calendar year 2004. The report covers activities of the five Physics Division groups, which represent the main areas in which we serve Los Alamos National Laboratory and the nation: Biological and Quantum Physics, Hydrodynamics and X-ray Physics, Neutron Science and Technology, Plasma Physics, and Subatomic Physics. This report includes a message from the acting Physics Division Leader, Jack Shlachter; general information about the mission and organization of the Division; our staffing and funding data for the fiscal year; descriptions of the activities of each of our groups; highlights of major research efforts throughout the Division; and a list of our publications and conference presentations.

Contents

Group Descriptions	1
Material Studies	19
Optical Pyrometry on the Armando Subcritical Experiment	21
Armando: The Final Subcritical Experiment in the Stallion Series	25
Material Strength under Shock and Shock-Free Loading Conditions	28
Plasma Physics	31
Understanding Mix in Inertial-Confinement Fusion	33
Beryllium Ablator Microstructure and Stability Experiments	37
Ultra-High-Intensity Laser Physics at the LANL Trident Laser Facility	41
Inertial-Electrostatic-Confinement Fusion Device	45
Plasma-Enhanced Combustion of Propane using a Silent Discharge	49
Angular Momentum Transport and Dynamo Studies in the Flowing Magnetized Plasma Experiment	53
Instrumentation	57
Design Feasibility and Cost Estimate for a Single-Axis, Multipulse Proton Radiography Facility	59
Cygnus—A New Radiographic Diagnostic for Subcritical Experiments	63
Nuclear Physics and Astrophysics	67
Detection of Dark Matter and Low-Energy Solar Neutrinos with Liquid Neon	69
Research and Development Progress toward a New Search for the Electric Dipole Moment	73
The Highest Energy Emission from Gamma-Ray Bursts	77
Muon Production with the PHENIX Muon Spectrometers and Color Glass Condensate	81
J/ψ and Charm Quark Production Measurements with the PHENIX Detector at RHIC	85
The NPDGamma Experiment	89
Biophysics	93
Experimental Studies and Computer Models of the Retina for Visual Prostheses	95
Ultra-Low-Field Nuclear Magnetic Resonance and Magnetic Resonance Imaging	99
Stochastic Closure for Multiscale Simulations	103
Atomic Physics	107
Quantum Simulations of Condensed Matter Systems using Trapped Ions	109
Novel Broadband Light Sources—Guiding Light through Glass and Holes	113
Time Variation of Alpha	117
Appendices	121
Acronyms	123
Publications	126

Division Leader's Introduction

The exciting research captured in this Physics (P) Division Activity Report for calendar year 2004 stands as a tribute to the outstanding professionalism of the technical staff within this organization. To say that 2004 was a tumultuous year for the Division and the Laboratory would be an understatement. The year began with change; on January 26, 2004, Susan Seestrom left her position as P-Division Leader to assume acting responsibilities as Associate Director (AD) for Weapons Physics. Later in the year Susan was selected and approved by the Regents of the University of California as the permanent AD. The domino effect brought me to the acting Division Leader position. I immediately asked Jeff Schinkel from P-23 to join the Division Office (P-DO) team in the acting Deputy Division Leader role; this recognized my appreciation of the need for a stronger emphasis on quality operations in P Division. Not long afterwards, I asked John Tapia to serve the Division Office as our acting Chief of Staff, replacing Pam French who joined Susan in the Directorate Office. With this many actors, there was some talk of forming a thespian society in P-DO.

Our annual Physics Division Review Committee (PDRC) meeting was conducted in February, and this year's focus was our contributions to the nuclear-weapons program, principally in radiography, experimental boost/thermonuclear physics, and experimental material studies. The nuclear-weapons program remains a core activity for P Division. We were pleased to receive PDRC confirmation of the high quality of our radiography research, and we are trying hard to keep this effort healthy despite the financial pressures associated with the DARHT II (Dual-Axis Radiographic Hydrodynamic Test facility) project. The exciting advances in proton radiography, resulting in spectacular images, and the outstanding science performed with this technique, are indeed a source of pride for us.

As expressed at our review, P Division has elevated the experimental boost/thermonuclear physics efforts to a high degree of visibility. In association with this emphasis, we reported on a novel, Laboratory-Directed Research and Development-funded effort on the short-pulse Trident laser. Great importance is placed on our engagement at the National Ignition Facility, and P Division has reported on our past year's progress in this area.

Perhaps the most dramatic event of the year was an unprecedented shut down of the Laboratory in the summer, which affected everyone in the Division. The shut down was called after two computer disks believed to contain classified information were reported missing and an intern sustained an eye injury from a laser. In an effort that spanned several months,

many within P Division and several outside contributed to a review of our operations using a formal procedure referred to as a Management Self-Assessment (MSA). The MSA involved the review of documentation, detailed interviews with selected staff, and intense walkdowns of representative simulated activities. The results of the MSA have been incorporated into a set of local corrective-action plans, and we anticipate implementing these plans consistent with resources available.

At this time, the uncertainty that surrounds the Department of Energy (DOE) contract with the University of California (UC) continues to affect employees at both a personal and professional level. Despite these uncertainties and distractions, our staff continues to be honored with important awards and fellowships; for example, the Division received two American Physical Society fellowships in 2004.

This report, like P Division as a whole, is largely organized by physics disciplines, and we continue to lead experiments in areas of importance both for national security and basic science. Under the rubric of materials studies, one of the major strategic goals for the Laboratory, P-Division researchers continued their tradition of capturing complex, dynamic data in harsh environments on plutonium in subcritical tests. Two of our research highlights pertain to the Armando experiment conducted at the Nevada Test Site last year. An additional research highlight reports on experimental and theoretical studies of material strength using a technique developed by colleagues at the All-Russian Research Institute of Experimental Physics (VNIIEF).

Plasma physics remains a core capability of the Division with applications to nuclear-weapons performance, energy production, and astrophysics. This report addresses both inertial and magnetic fusion studies conducted within P Division at facilities both at Los Alamos and elsewhere. More fundamental plasma physics is covered in a paper on the flowing magnetized plasma experiment at Technical Area 35 while another highlight describes our efforts at enhancing combustion using a knowledge of plasma physics.

Our own in-house laser facility, the Trident laser, provides a diverse set of pulse-shape, energy, and wavelength options in a heavily diagnosed environment, available to both local and outside users, and Trident occupies an important place in P Division's portfolio. One of our research highlights describes exciting recent work on accelerating ions using ultra-high-intensity laser pulses.



Jack S. Shlachter, Physics Division Leader

Radiography is one of the key technology drivers at the Laboratory and in P Division as well. Protons have been demonstrated to be the radiography tool of choice for applications involving multipulse “movies,” and a paper study of the cost and feasibility of a single-axis proton radiography facility captures our planning for the future. The Armando subcritical experiment mentioned above was successful because of the development of a downhole x-ray radiographic capability known as Cygnus, and one highlight reports on this multiyear technology effort.

The strong neutrino effort at Los Alamos continues with plans about future experiments capable of detecting dark matter and low-energy solar neutrinos in the Cryogenic Low-Energy Astrophysics with Neon detector. Progress towards measurement of the neutron electric dipole moment, neutrino oscillations in accelerator experiments, and parity-violating gamma-ray asymmetry in the NPDGamma experiment are each described separately in highlight articles. Our work on PHENIX (Pioneering High-Energy Nuclear Interaction Experiment) continues at the Relativistic Heavy Ion Collider and is described in articles on muon, I/ψ , and charm quark production. Astrophysical data have resulted in an improved understanding of energy emission from gamma-ray bursts, the most extreme astrophysical energy sources known.

One of the applications of our information-processing studies in the biophysics arena is the development of models of the retina which can be applied to visual prostheses. For several years, we have been improving and applying the most sensitive magnetic sensors yet known, superconducting quantum interference devices, to the noninvasive study of the electrical activity in the brain. This work is now coupled with ultra-low-field nuclear magnetic resonance and could represent a major breakthrough for our biophysics team. How to handle subgrid phenomena in large-scale computer codes is a widespread problem, and one of our research highlights discusses stochastic closure techniques for multiscale simulations.

The atomic physics section of this activity report includes three papers covering a broad range of topics. One highlights the use of trapped ions as a testbed for quantum simulations of condensed-matter systems. Another article provides an overview of our work with photonic crystal fibers, one of the success stories of modern photonics. Finally, a fundamental-physics study with profound implications involves our efforts to measure a time variation to the fine structure “constant” known as alpha.

I believe these research highlights speak for themselves about the quality of research in P Division. Overall, 2004 was an enormously eventful year at Los Alamos National Laboratory, yet we remain optimistic that the Laboratory will continue to prove that UC management is sound and accountable so that our research can continue at the high level expected by our leadership, our scientists, and the nation.

A handwritten signature in dark ink, appearing to read "Jack Shlachter". The signature is fluid and cursive, with a long horizontal stroke extending to the right.

Mission and Goals

The mission of Physics (P) Division is to further our understanding of the physical world, to generate new or improved technology in experimental physics, and to establish a physics foundation for current and future LANL programs.

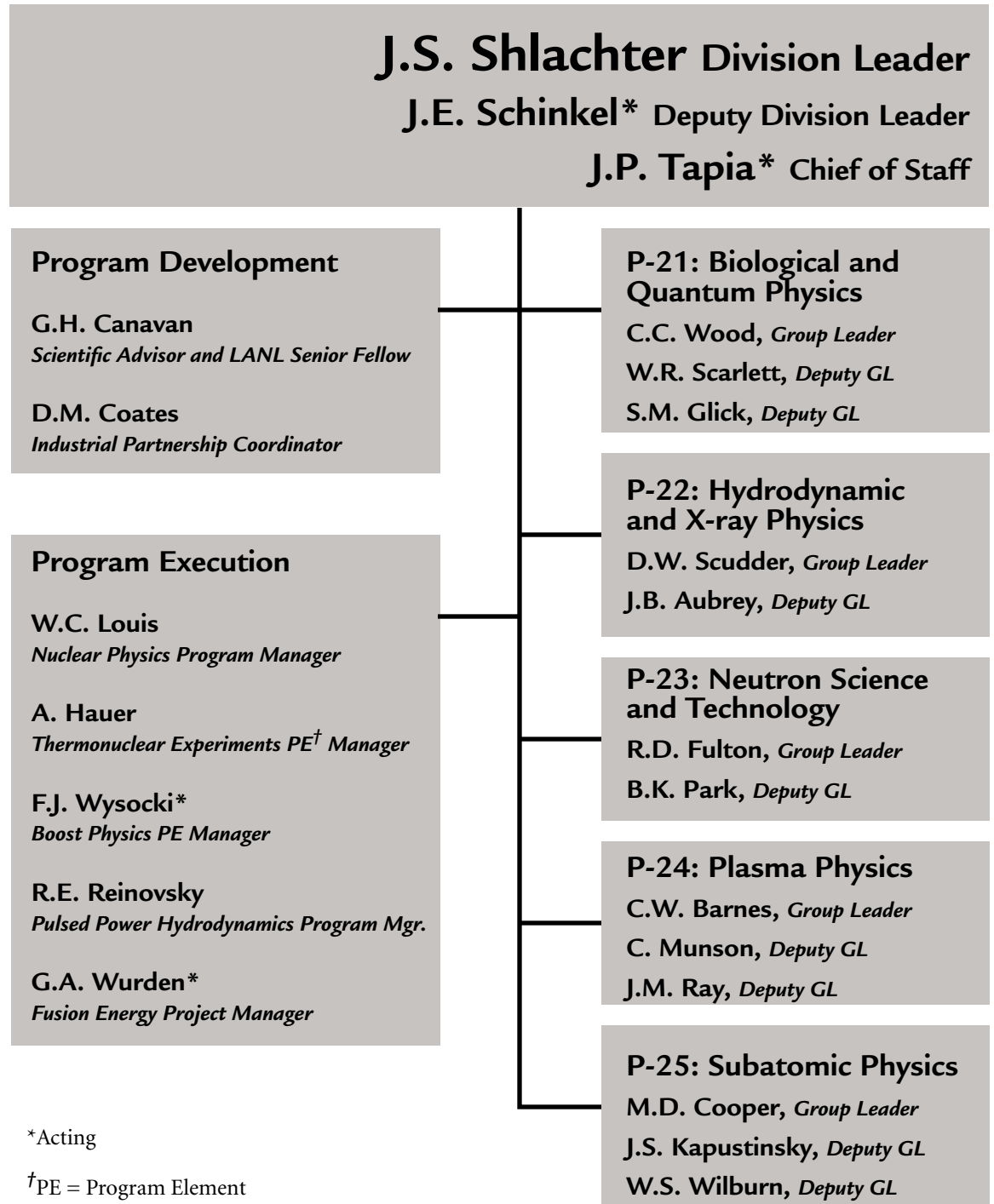
The goals of P Division are to

- provide the fundamental physics understanding supporting LANL programs;
- investigate the basic properties of nuclear interactions, high-energy-density and hydrodynamic systems, and biological systems with a view toward identifying technologies applicable to new LANL directions;
- identify and pursue new areas of physics research, especially those to which the unique capabilities of LANL may be applied;
- explore interdisciplinary areas of scientific endeavor to which physical principles and the methods of experimental physics can make an important contribution; and
- maintain strength in those disciplines that support LANL's mission.

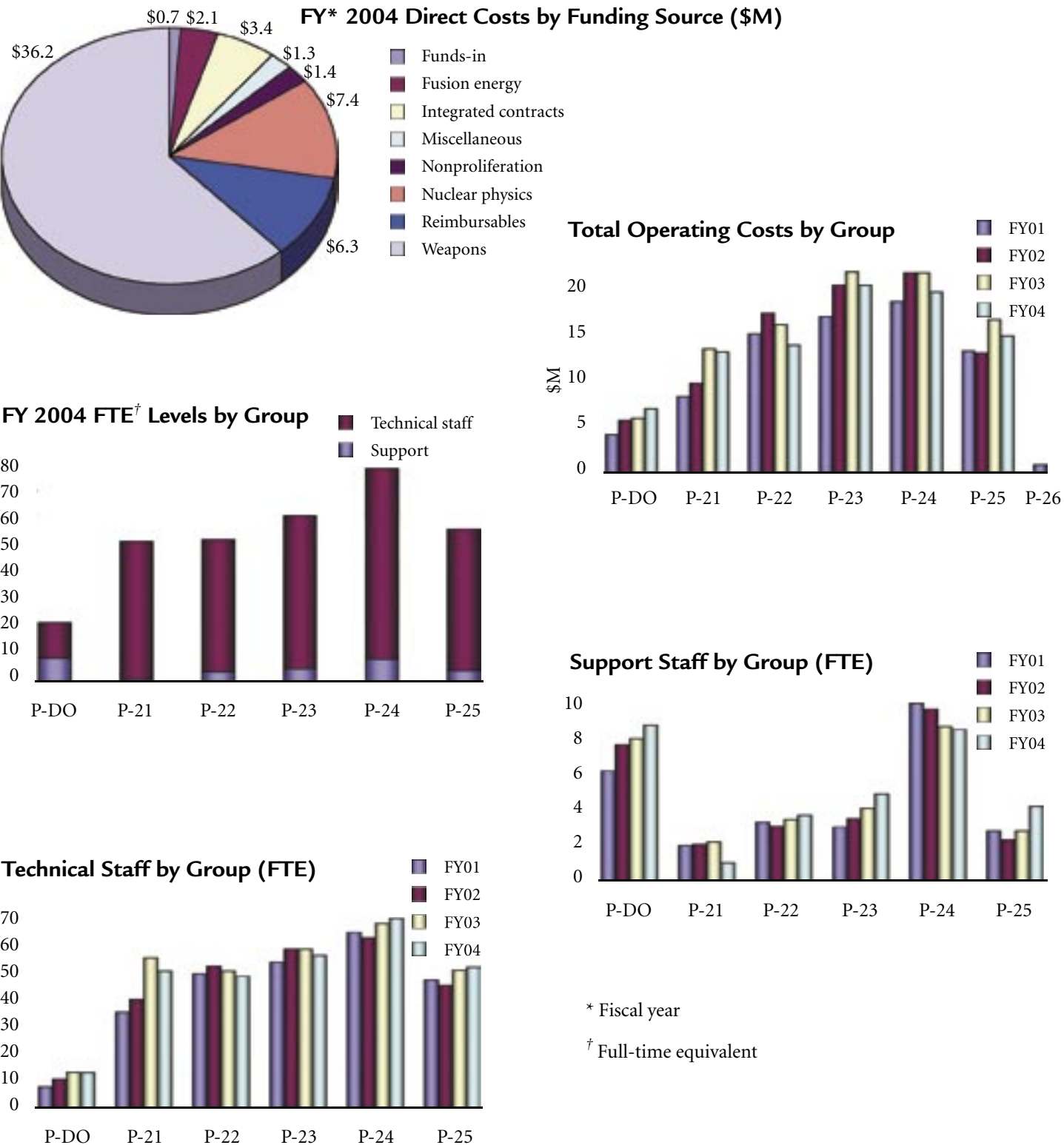
P Division pursues its goals by

- establishing and maintaining a scientific environment that promotes creativity, innovation, and technical excellence;
- undertaking research at the forefront of physics with emphasis on long-term goals, high risks, and multidisciplinary approaches;
- fostering dialogue within the Division and the scientific community to realize the synergistic benefits of our diverse research interests;
- encouraging the professional development of each member within the Division; and
- conducting all of its activities in a manner that maintains a safe and healthful workplace and protects the public and the natural environment.

Organization



Financial and Staffing Data



P-21: Biological and Quantum Physics Group

Charles Wood, Group Leader

Robert Scarlett and Stephen Glick, Deputy Group Leaders

The Biophysics Group (P-21) was founded in 1988 with the goal of applying the scientific and technical resources of Physics (P) Division to the biosciences. In October 2002, P-21 broadened its scope to become the Biological and Quantum Physics Group with the addition of the Quantum Information Team from P-23. This organizational change was initiated by P-Division leadership for two reasons. First, P-21 has longstanding experience in supporting entrepreneurial projects for non-DOE government agencies such as the National Institutes of Health, the Department of Defense, and the intelligence community, many of which are key sponsors for work in quantum-information research. Second, the Quantum Information Team and the Biophysics Group share common interests in the physics of information at all levels, from quantum information processing, computing, and cryptography to biological information processing by the nervous system. This common focus on the basic science and applications of information processing has already led to numerous constructive interactions between the biological and quantum components of P-21.

A new research interest in P-21 is the science and application of aerosols. Activities include measuring the background levels of biological organisms in public areas, detecting battlefield use of biological weapons, and monitoring and characterizing beryllium particles in the workplace.

Biological Physics

P-21's historical mission has been to contribute to an understanding of biological phenomena by means of the scientific, technical, and conceptual resources of physics; to use biological systems to elucidate general physical principles underlying complex phenomena; and to apply, where appropriate, our scientific and technical capabilities to core LANL programs. Just as the 20th century is regarded as the century of the physical sciences, the 21st century will likely become the century of the biological sciences. P-21 and biophysics as a discipline are well positioned to contribute to this biological revolution in progress through our emphasis on understanding biological systems using the scientific, technical, and conceptual resources of physics. Recent advances in biophysical measurement and in molecular biology are beginning to allow detailed physical understanding of biological phenomena that were previously understood only in qualitative terms. P-21 is well placed by virtue of its capabilities and research interests to contribute significantly to this important trend in the biosciences. In addition to the goal of achieving a physical understanding of biological phenomena, the biophysical research in

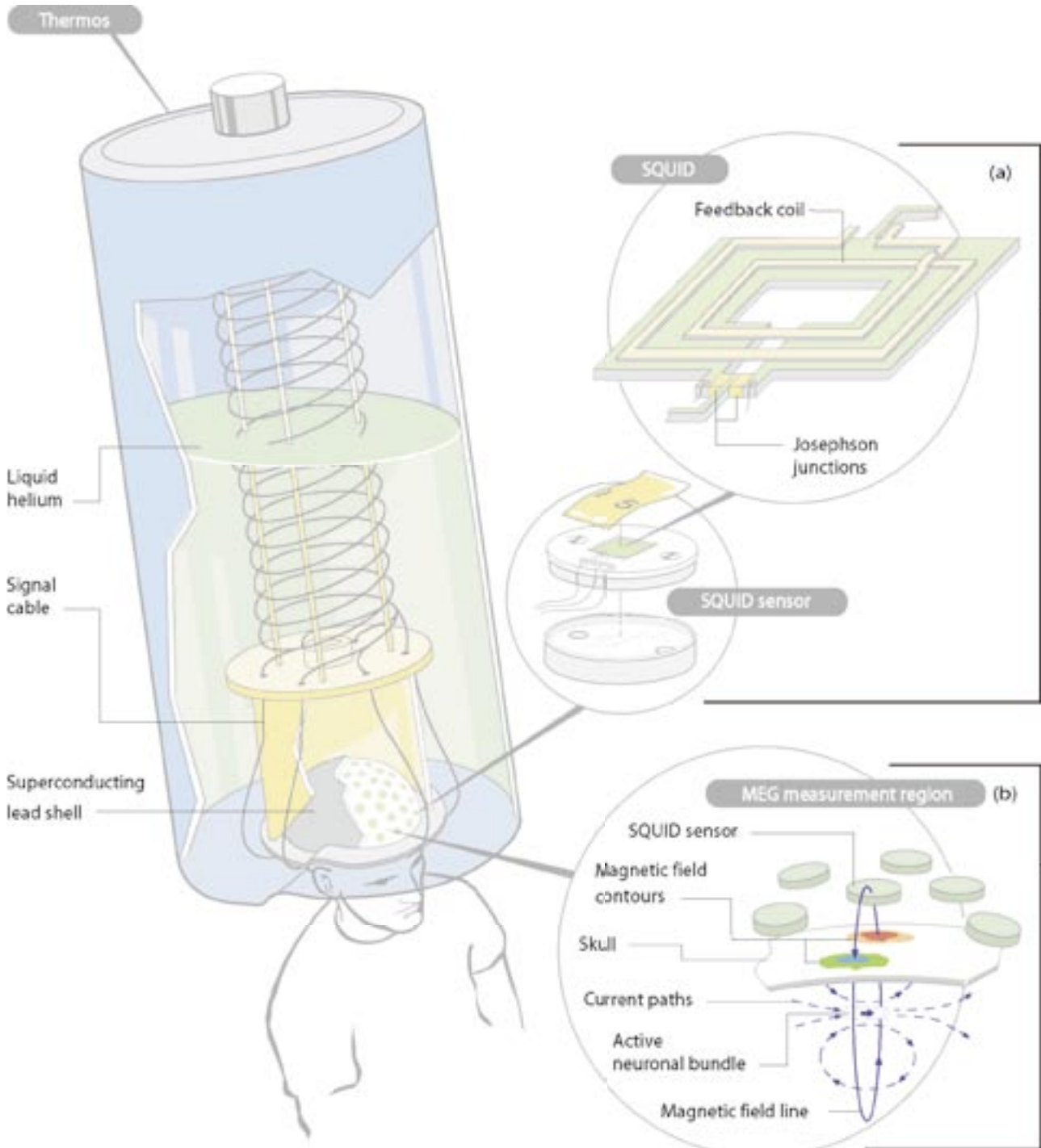
P-21 shares a number of other common characteristics. Specifically, we investigate the relationships between structure, dynamics, and function of biological phenomena over a wide range of scales (e.g., from biomolecules to the whole human brain). We also make extensive use of detection, imaging, and reconstruction techniques (e.g., x-ray crystallography, single-molecule electrophoresis, high-speed photon-counting optical imaging, magnetic resonance imaging [MRI], and magnetic-field measurements using technologies based on superconducting quantum interference devices [SQUIDS, Figure 1]). Finally, we attempt to achieve a detailed interplay between high-resolution physical measurements and large-scale computational modeling and analysis of complex systems.

We depend heavily on the tight connection and daily interactions between biologists and physical scientists within the group, the Division, and the Laboratory, and we apply the knowledge, techniques, and capabilities developed in our biological studies to national-security problems and those of specific interest to LANL when our ongoing efforts can offer unique solutions and significant mutual benefit. For example, P-21 has developed a new approach to the problem of "closure" in large-scale numerical models based on

RESEARCH HIGHLIGHT PHYSICS DIVISION

P-21 Group Description

Figure 1. The magnetoencephalography (MEG) helmet's array of SQUID sensors and the superconducting lead shell are cooled by immersion in liquid helium. Each SQUID sensor contains a coil of superconducting wire that receives the brain fields and is magnetically coupled to the SQUID, which produces a voltage proportional to the magnetic field received by the coil. A computer program converts the SQUID data into maps of the currents flowing throughout the brain as a function of time. (a) The magnetic field lines that pass through the square hole at the SQUID's center determine the phases of electron waves circulating in the SQUID's superconducting region (green): the waves' interference is proportional to the magnetic flux over the hole. Because superconductors have no electrical resistance, the interference can be measured only by interrupting the superconductor with small regions that have electrical resistance—the two Josephson junctions—so that voltage drops will develop across them. The voltage measured across the junctions is proportional to the magnetic flux over the SQUID's square hole. The feedback coil magnetically couples the SQUID to the pick-up coil in the SQUID sensor. A SQUID is typically 10 to 100 μm on a side. (b) The colored contours show how the magnetic field produced by neural brain currents (dashed arrows) changes in intensity and polarity over the skull's surface. In the red region, the field is most intense in a direction pointing out of the skull. In the blue region, the field is most intense in a direction pointing into the skull.



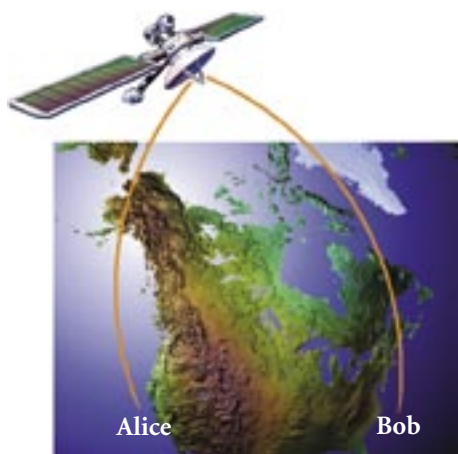


Figure 2. Illustration of the QKD communication between "Alice" and "Bob."

partial differential equations. This work is the focus of a Laboratory-Directed Research and Development-Director's Reserve funded project involving members of the ocean-, flow-, and weapons-modeling communities.

Quantum Information Science

A key discovery of 20th century science was the realization that information is physical. The representation of "bits" of information by classical physical quantities, such as the voltage levels in a microprocessor, is familiar to everyone and is the basis of the "information explosion" of the latter half of the 20th century. More recently, the field of quantum information science has made great progress in understanding information in terms of the laws of quantum mechanics. For example, a unit of quantum information, known as a "qubit," can be represented by single-photon polarization states. Remarkable new capabilities in the world of information security have been predicted that make use of quantum-mechanical superpositions of information, a concept that has no counterpart in conventional information science. For example, quantum cryptography allows two parties to communicate securely even in the presence of hostile monitoring by a third party (as described below). P-21's Quantum Information Team has experimental projects under way in quantum cryptography, quantum computation, quantum optics with trapped strontium ions, and atom interferometry with Bose-Einstein condensates.

Quantum cryptography. One of the main goals of cryptography is for two parties ("Alice" and "Bob," Figure 2) to render their binary communications unintelligible to a third party ("Eve"). This can be accomplished if Alice and Bob both possess a secret random-bit sequence, known as a cryptographic key. For example, in "one-time-pad" encryption, Alice adds the key to the original message, known as plaintext, and communicates the sum (ciphertext) to Bob. He is able to recover the plaintext by subtracting his key from the ciphertext, but Eve, who is assumed to have monitored the transmitted ciphertext, is unable to discern the underlying plaintext through the randomization introduced with Alice's key. So, although key material conveys no useful information in itself, it is a very valuable commodity, and methods for Alice and Bob to generate key material securely are correspondingly important. Using quantum key distribution (QKD), Alice and Bob can create shared cryptographic key material whose security is ensured by the laws of quantum mechanics.

QKD offers many security and ease-of-use advantages over existing key-distribution methods. Traditional key distribution using trusted couriers requires cumbersome security procedures for preparing, transporting, and handling the key before any communications can take place and may even be impractical (e.g., rekeying a satellite). In contrast, quantum keys do not exist before the QKD transmissions are made, and a key can be generated at message-transmission time. Public-key cryptography also avoids many of the difficulties of key distribution by courier but provides only the conditional security of intractable mathematical problems, such as integer factorization. Accurate assessment of an adversary's computing power over the useful lifetime

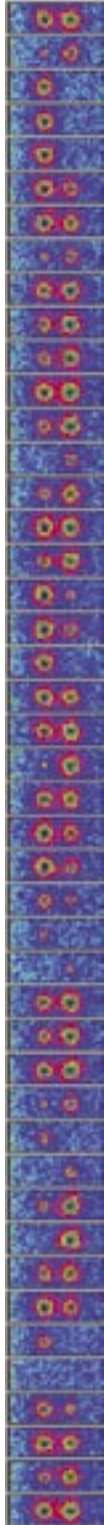
of encrypted information, which may be measured in years or even decades, is notoriously difficult—unanticipated advances in fields such as quantum computation could render public-key methods not just insecure in the future but also retroactively vulnerable. QKD could be used for real-time key generation in cryptographic applications where this long-term risk is unacceptable. Recent progress in QKD was described in a research highlight in last year's Physics Division Activity Report.

P-21's QKD Team leads the world in many aspects of quantum cryptography. We have demonstrated all aspects of quantum key exchange over 48 km of fiber at LANL and are leading a demonstration of these capabilities over an existing fiber network for the U.S. government. Free-space quantum cryptography was invented by our team, and we have now fully demonstrated the practicality of this approach for a variety of applications over a 10-km range. The QKD Team and six other institutions in the Information Society Technologies (IST) QuComm collaboration were named co-winners of the European Union's 1M-Euro Descartes Prize for Research. The IST-QuComm collaboration is made up of research groups in Sweden, Germany, France, Switzerland, Austria, and the United Kingdom, in addition to the Los Alamos team.

Quantum computation. With two or more qubits, it becomes possible to consider quantum logical-"gate" operations in which a controlled interaction between qubits produces a (coherent) change in the state of one qubit that is contingent upon the state of another. These gate operations are the building blocks of a quantum computer, which in principle is a much more powerful device than any classical computer because the superposition principle allows an extraordinarily large number of computations to be performed simultaneously. In 1994, it was shown that this "quantum parallelism" could be used to efficiently find the prime factors of composite integers. Integer

P-21 Group Description

Figure 3. A time series of two ions simultaneously undergoing quantum jumps.



factorization and related problems that are computationally intractable with conventional computers are the basis for the security of modern public-key cryptosystems. However, a quantum computer running at desktop-PC speeds could break the keys of these cryptosystems in only seconds (as opposed to the months or years required with conventional computers). This single result has turned quantum computation from a strictly academic exercise into a subject whose practical feasibility must be urgently determined. The architecture of a quantum computer is conceptually very similar to a conventional computer—multiqubit, or “multibit,” registers are used to input data. The contents of the registers undergo logical-gate operations to effect the desired computation under the control of an algorithm, and a result must be read out as the contents of a register.

Many fundamental issues key to quantum-science applications remain insufficiently investigated. Members of the P-21 Quantum Information Team are actively engaged in several of these areas. For example, we are using trapped ions to measure the randomness of atomic transitions (Figure 3), which constitute a key test of the predictions of quantum mechanics. Other studies involve ultracold

atoms collapsed into a Bose-Einstein condensate. These experiments, more fully described in last year's report, contribute to the worldwide goal of a complete understanding of this forefront of physical science.

Another important direction is quantum simulation, using one quantum system to simulate another. For example, the particle level modeling of a many-body quantum system is intractable for a realistic case, but may be simulated by a configuration of trapped ions. Measurements of such systems could increase understanding of condensed matter systems such as high- T_C superconductors. In a related effort, members of P-21 have initiated an “ion trap foundry” initiative to combine industrial-scale microfabrication techniques with trapped-ion quantum simulation and quantum computing. This work is an outgrowth of collaborations at Los Alamos involving P, Theoretical, and Chemistry Divisions and involves a developing collaboration between quantum scientists at Los Alamos and microfabrication experts at Sandia National Laboratories. Such an “ion trap foundry” would significantly accelerate progress toward trapped-ion quantum computation, an important national-security goal.



The World's Greatest Science Protecting America

Los Alamos National Laboratory, an affirmative action/equal opportunity employer, is operated by the University of California for the U.S. Department of Energy under contract W-7405-ENG-36.



P-22: Hydrodynamics and X-ray Physics Group

David Scudder, Group Leader
Joysree Aubrey, Deputy Group Leader

The activities of the Hydrodynamics and X-ray Physics Group (P-22) help support LANL's mission of ensuring the safety and reliability of the nation's nuclear stockpile. Group members are also involved in research that addresses fundamental issues related to hydrodynamic phenomena at extreme pressures, high-energy-density plasmas, fusion physics, and exploration of the dynamic properties of materials. Other endeavors have led to innovations with commercial potential.

The tremendous challenge of certifying the stockpile in the absence of testing requires that we marshal all the capabilities and resources at our disposal. As the materials in nuclear weapons age, they become further and further removed from the states under which they were tested. Defects in devices and engineering modifications have introduced uncertainties in performance and reliability. To address these issues, we must have a fundamental understanding of the physical processes involved in the performances of nuclear weapons and the limits of models developed and benchmarked during the testing era. P-22 contributes to this challenge in a number of ways through the re-analysis and re-evaluation of archival Nevada Test Site (NTS) data in support of stockpile stewardship activities and validation of weapons design codes, diagnostic development and training to enhance the test-readiness posture of the nation, and the execution of above-ground experiments with the aim of understanding and resolving weapons-physics issues. The group has the resources

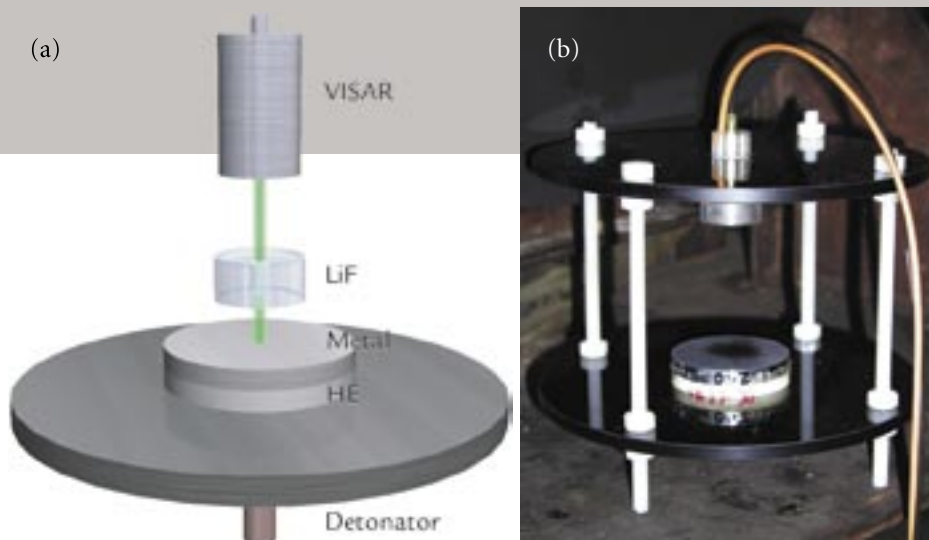


Figure 1. (a) Schematic of the experimental configuration used to study the behavior of shocked metals. VISAR and Asay windows were employed to measure surface velocities. (b) The same set-up was used (without the Asay window) for experiments diagnosed with proton radiography (pRad) and VISAR.

to assemble multidisciplinary teams to address these challenges. Our involvement with various experimental programs has required efforts in diverse areas such as optics, hydrodynamics, plasma physics, radiation transport, pulsed-power science, weapons physics, x-ray spectroscopy and imaging, microwaves, electromagnetics, and nuclear and atomic physics.

Dynamic Properties of Materials

Researchers in P-22 have used a variety of diagnostic tools to investigate damage and melting in materials which are subjected to explosively driven shocks.

The suite of diagnostics include VISAR (velocity interferometry for surfaces of any reflectivity), Asay windows, optical pyrometry, photon Doppler velocimetry, and radiography using x-rays and protons.

In a series of experiments designed to study mixed-mode damage in materials, disks of various metals, two inches in diameter and of different thicknesses were attached to cylinders of high explosives (HE: PBX-9501, two inches in diameter and one-half inch thick). A lithium fluoride (LiF) window was placed a few millimeters above the samples. This is known as an Asay window. The

RESEARCH HIGHLIGHT PHYSICS DIVISION

P-22 Group Description

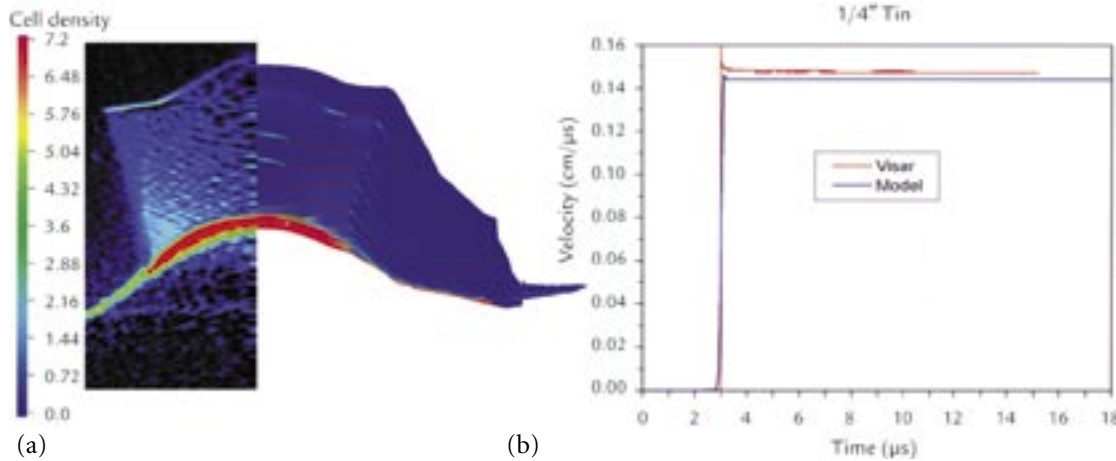


Figure 2. The time-dependent evolution of shock-melted tin was observed using pRad and VISAR. (a) A comparison of the areal densities in a pRad image with a calculation done by Michael Prime (ESA-WR) is shown. (b) The VISAR trace of the time-dependent surface velocity is compared to the results from the simulation.

experimental set-up is shown in Figure 1(a). The explosives were point-detonated and the time-dependent behavior of the metal coupons was tracked using VISAR. The VISAR was used to detect both the free-surface velocities and the times of arrival of the spalled layers at the Asay window. The ability to record the details of velocity structure during

an experiment is very important for understanding the physics of dynamic processes. Similar experiments were diagnosed using multiframe proton radiography (pRad) but without the Asay window [Figure 1(b)]. The combination of multiple radiographic images and spatially distributed VISAR data from the same experiment provided theorists with high-quality data for benchmarking materials models. Detailed continuous velocity measurements between images contributed to the overall understanding of dynamic processes.

Well-characterized samples of copper, aluminum, tin, and tantalum were used. Figure 2 shows a comparison of a pRad image of shock-melted tin with a simulation generated by one of our collaborators in Engineering Sciences and Applications (ESA) Division. The comparison of the calculation with VISAR data is also shown.

In support of the Dynamic Materials Campaign, we have conducted research in collaboration with the Materials Dynamics Group (DX-2) and the Neutron Science and Technology Group (P-23) on the production of ejecta from the surfaces of shocked materials and subsequent transport of the particles into gas.

These experiments were performed on tin targets at the LANL gas-gun facilities. Detailed information about the densities and velocities of particle clouds generated from shocked surfaces is necessary for the development of models of the phenomenon. Another series of experiments is being conducted (in partnership with DX-2) to investigate the behavior of shocked materials off the principal Hugoniot curve.

The resulting data provide information about the target material's equation of state (EOS) under pressure and temperature conditions that are not easily accessible by other means. In collaboration with P-23, DX-2, and the Polymers and Coatings Group (MST-7), P-22 staff used optical pyrometry to measure the temperature of shocked materials to elicit information about solid-solid and solid-liquid phase transitions. Such information has been very valuable in testing EOS models of materials

Pulsed-Power Hydrodynamics

Members of the group have done pioneering work in developing and applying pulsed-power facilities to explore

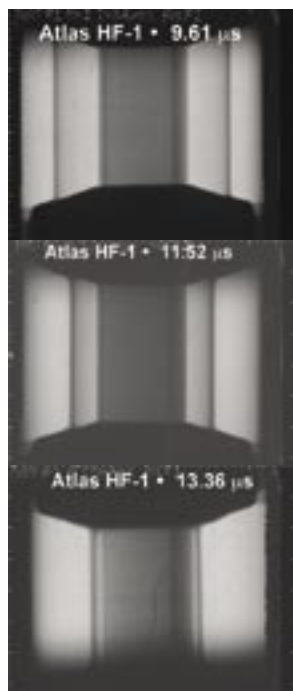


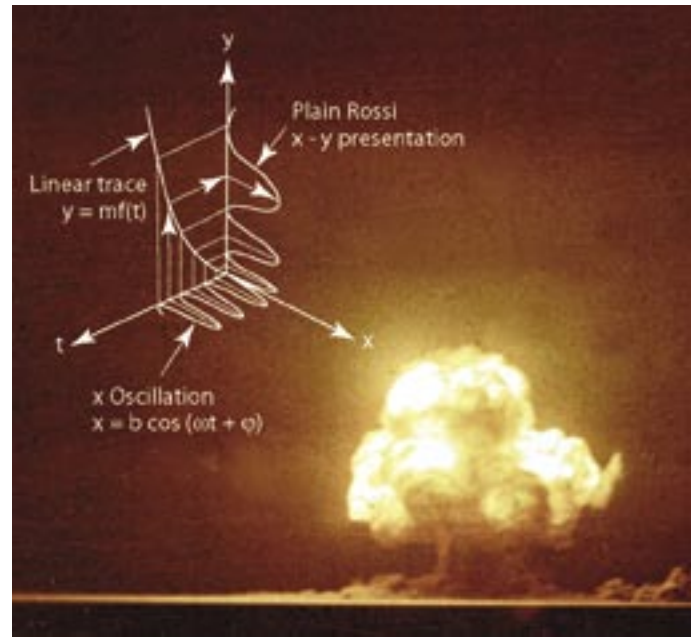
Figure 3. Liner implosion experiments on Atlas verified fundamental dynamics and demonstrated reproducibility.

Figure 4. Leonard Tabaka (P-22) examines a Faraday fiber before conducting an experimental shot carried out in Sarov, Russia. Scientists from LANL and VNIIEF performed a series of experiments aimed at determining the dynamic yield strength of copper. These "Russian High Strain-Rate" experiments are important to refine and validate computational models of dynamic material strength under high-strain and strain-rate conditions.



hydrodynamic phenomena at extreme pressures and convergent geometries. Under the Pulsed-Power Hydrodynamics (PPH) program, experiments were conducted to address issues related to LANL's main mission of supporting the nuclear stockpile in the absence of testing. The 4.6 MJ Pegasus II and the 23 MJ Atlas facilities were used to study dynamic material properties under extreme conditions. Energy stored in capacitor banks was delivered to a central cylindrical liner. The axial currents flowing through the liner gave rise to $\mathbf{J} \times \mathbf{B}$ forces, which drove the liner radially inwards at speeds of kilometers per second towards the central axis. High-precision radiography yielded information about the time-dependent behavior of the liner (Figure 3) and demonstrated reproducibility of the implosion. Experiments included studies of convergent material flow in asymmetric geometries. The data were used to validate models in modern weapons design codes. Other experiments looked at the growth of preformed perturbations during implosions, strength at high strain-rates, frictional forces between materials with differential velocities, and spall in materials driven by 50 kbar convergent shocks. The future of the LANL PPH program is full of challenges and exciting new opportunities. The Atlas facility has been moved to the NTS and was recommissioned during the summer of 2004. In addition to conducting experiments on the pulsed-power facilities at LANL, P-22 group members have had a long collaboration with scientists at the All-Russian Scientific Research Institute of Experimental Physics at Arzamas-16 (VNIIEF) (Figure 4). The Russians have developed large-scale explosive pulsed-power facilities capable of generating fields of thousands of Tesla. Joint experiments have explored instability growth in convergent geometries, magnetized target fusion, the design and development of a megajoule x-ray source, and the properties of materials in high fields and at cryogenic temperatures.

Figure 5. Archival photo of the Trinity event (July 16, 1945). The inset is a schematic representation of the Rossi technique.



Strongly Coupled Plasmas and Radiation Hydrodynamics

The understanding of the properties of strongly coupled plasmas and the interaction of these plasmas with radiation is important for fusion and weapons-physics applications. We are involved in various research projects in these areas using both local facilities and those elsewhere, such as the Z machine at Sandia National Laboratories (SNL) and the Omega laser at the University of Rochester. We are conducting investigating fundamental processes that are relevant to fusion and strongly coupled, multimaterial plasmas. The work is being done locally under a Laboratory-Directed Research and Development project and involves two experiments aimed at measuring the ion-ion diffusion coefficient and the temperature equilibration rate between ions and electrons in a dense plasma. We have also studied the propagation of radiation in materials using the x-ray source generated by SNL's Z machine, which generates currents of 20 MA and a peak electrical power of about 40 TW. This source has been used to study the physics of radiation-matter interactions.

NTS Data and Weapons Physics

The first alpha (neutron multiplication rate) measurement was performed by Bruno Rossi on the Trinity event (Figure 5). This diagnostic became a standard tool for assessing the nuclear and thermonuclear performances of devices fielded at the NTS and elsewhere.

Neutrons in a supercritical assembly increase exponentially according to the formula $N(t) = N_0 e^{\alpha t}$. If α is not a constant, then the equation is modified to $N(t) = N_0 e^{\int \alpha(t) dt}$. The time-dependent neutron population is proportional to the resulting leakage of gamma radiation from the surface of the device. The exponentially increasing gamma flux is converted to an electrical current by a series of detectors that span the dynamic range of the signal. The electrical signal in turn is recorded on oscilloscopes driven by oscillators at appropriate frequencies. The Rossi technique consists of the superposition of the exponentially increasing signal on a sinusoidal trace (inset in Figure 5). The time-dependent behavior of the gamma radiation can be extracted by using the known frequency of the sine wave.

P-22 Group Description

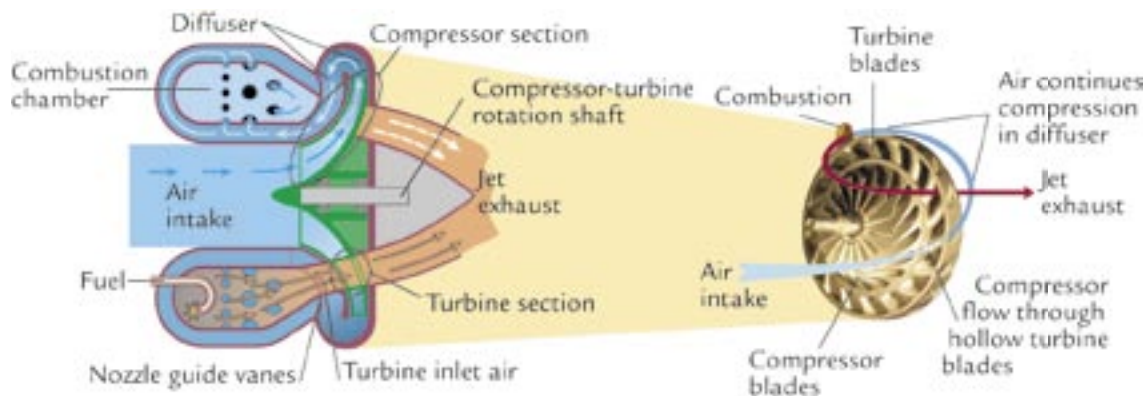


Figure 6. Composite drawing of the ASRT schematic and photo, showing how the ASRT operates. Air from the compressor section of the ASRT is channeled through the outer hollow turbine blades on the same rotor. The air, on its way to the combustion chamber, cools the turbine section allowing the engine to operate at higher temperatures. The fuel efficiency is increased in this case.

P-22 is the custodian of archival data from the NTS and is in the process of developing modern methods of analysis and applying them to nuclear events. We have completed work on software that automates the extraction of time and amplitude information from the film, eliminating the tedium (and possible errors) of manually obtaining the data points. New programs to generate gamma-flux and alpha (logarithmic derivative of the flux) curves from the data are under development. These codes will augment the existing software. In collaboration with our colleagues from Statistical Sciences (D-1), Weapons Response (ESA-WR), and Complex Systems (T-13), we are developing rigorous methods of error analysis for the data in order to deliver higher-fidelity information to the nuclear-weapons design and code development community. The re-analysis effort has given us new insights into the physics of individual devices and weapons systems. Diagnostic physicists who were responsible for designing and fielding the experiments on nuclear tests are also involved in the analysis, documentation, and mentoring activities within the group.

New Initiatives

A new type of engine developed by a group member, the Advanced, Single-Rotor Turbine (ASRT, Figure 6), was recently nominated for an R&D100 Award. The compressor and turbine are combined into a single piece, increasing reliability while reducing engine complexity and size, as well as fabrication and maintenance cost. Envisioned applications for this technology include portable power units and residential distributed power supplies, as well as small jet engines and turbo-shaft engines for turboprop aircraft, helicopters, and tanks. Centrifugal turbines could also be implemented in turbochargers for piston engines and turbopumps for liquid-fueled rockets, refrigeration, and applications in the chemical-processing industry.

A portable gamma-ray and neutron detector developed by another staff member in P-22 was also nominated for an R&D100 award. The detector, called GN-5, can be used to detect nuclear materials and explosives quickly and efficiently. The tool can be deployed at critical locations

such as border crossings, airports, sports arenas, and power plants. The heart of the instrument is a high-purity germanium (HPGe) gamma-ray detector and a bismuth germanate (BGO) scintillator. There is also a pair of helium-3-filled neutron detectors, one of which is shielded with cadmium. Because the HPGe crystal operates at very low temperatures (80 to 110 K), it is placed in a vacuum cryostat that is attached to a miniature mechanical refrigerator. A small, commercial Stirling-cycle cooler (1 kilogram, 3.5 watts) can be used. The weight of the unit is 8 kilograms and the battery lifetime is around 12 hours. The GN-5 has a large library of gamma-ray spectral information for over 200 isotopes which enables it to identify complex spectra.



The World's Greatest Science Protecting America

Los Alamos National Laboratory, an affirmative action/equal opportunity employer, is operated by the University of California for the U.S. Department of Energy under contract W-7405-ENG-36.



P-23: Neutron Science and Technology Group

*Doug Fulton, Group Leader
Brent Park, Deputy Group Leader*

The Neutron Science and Technology Group (P-23) executes a wide range of projects—spanning weapons physics and nuclear physics through fundamental and applied research. The core capabilities of the group are in the application of state-of-the-art techniques in particle and light detection and in the imaging and recording of transient events. Our efforts in weapons physics contribute to the national-security mission of LANL through the stockpile stewardship program by participating in the design and fielding of subcritical experiments (SCEs), small-scale dynamic experiments, and the reanalysis and archiving of data from past nuclear weapons tests. Our fundamental research contributes to science in support of LANL programs through studies on nuclear and weak-interaction physics and on state-of-the-art measurements of astrophysical phenomena such as solar neutrinos and ultra-high-energy gamma rays. Applied research includes the application of imaging and neutron technologies to problems relevant to national defense, homeland security, and industry. A number of the projects and programs described below are also featured in this report.

Weapons Physics

Members of P-23, working in collaboration with P-22 and various groups in Dynamic Experimentation (DX), Engineering Sciences and Applications (ESA), Applied Physics (X), Nuclear Materials Technology (NMT), and Materials Science and Technology (MST) Divisions, designed and executed the Stallion series (Vito, Mario, Rocco, and Armando) of SCEs.



Figure 1. Armando subcritical experiment at the Nevada Test Site.

The purpose of Vito was to examine ejecta formation in a particular region of a weapon, and it successfully demonstrated the LANL “racklet” approach that facilitates rapid and cost-effective turnaround between SCEs. The racklet method was subsequently employed for Mario and Rocco. The goal of Mario and Rocco was to compare the properties of cast versus wrought plutonium. Armando, the last of the SCEs in the Stallion series, was successfully fielded in May of 2004 to verify the behavior of the target surface observed in Rocco and Mario shots.

The specific properties investigated in SCEs include ejecta formation, spall

features, and surface temperature. Holography, used to measure ejecta-particle-size distributions, provide information about ejecta-particle transport in a gas environment. Another technique, soft x-ray imaging, was developed to measure ejecta-density distributions from shock-loaded metals. In a complementary experiment, proton radiography (pRad) was used for the first time to study material failure in depleted uranium and other samples. Surface temperature is measured with a high-speed, time-resolved, multiwavelength near-infrared surface pyrometer. All these methods provide data that contribute to our understanding of the strength,

RESEARCH HIGHLIGHT

PHYSICS DIVISION

P-23 Group Description

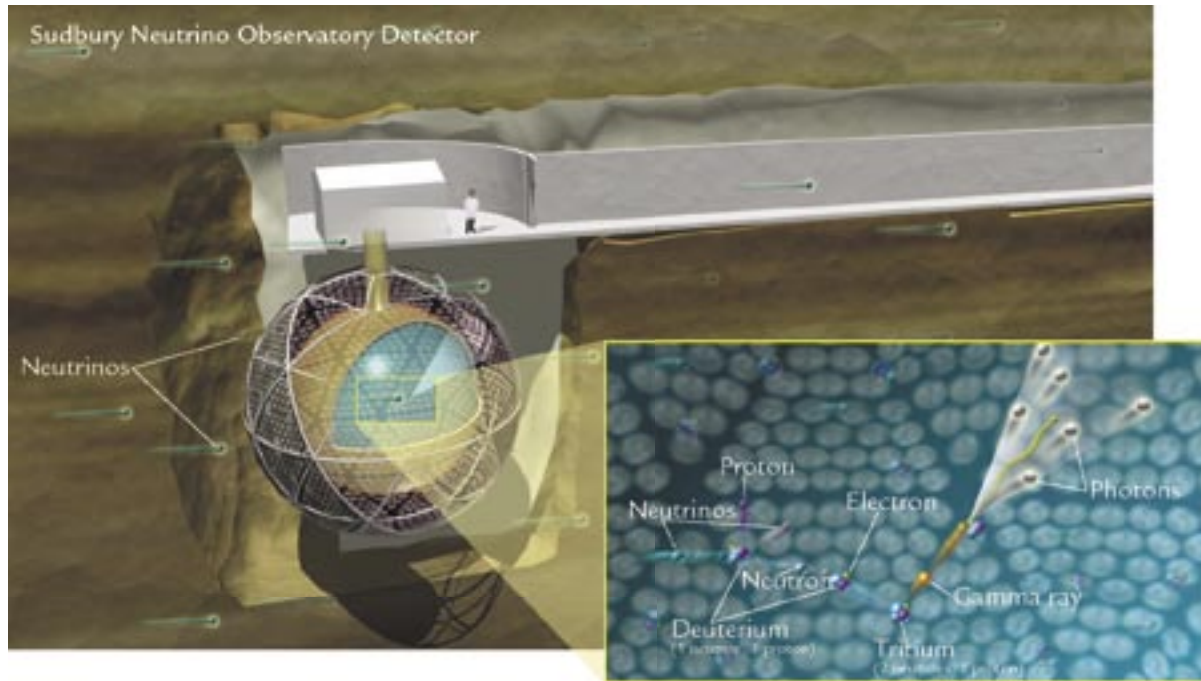


Figure 2. Three-dimensional rendering of SNO. In one of three neutrino reactions (in the inset) detected by SNO, a neutrino entering the detector interacts with a deuterium nucleus. The reaction produces a proton, neutrino, and neutron. The neutron is captured by another deuterium nucleus, producing a tritium atom in the process. The tritium atom decays and in that process releases a gamma ray, which then collides with an electron. Cerenkov light is emitted and detected by photomultiplier tubes that line inside of the SNO vessel.

failure properties, and equation of state (EOS) of materials important to the weapons program. Another EOS constraint can be obtained from volume temperatures. Neutron resonance spectroscopy (NRS) is used to determine volume temperatures by using Doppler-broadened neutron resonances to measure internal temperatures in dynamically loaded samples. Although still a nascent technique, our researchers plan on using NRS to measure the temperatures attained in shocked metals, at frictional interfaces, and in the “dead zones” of detonated chemical explosives.

P-23 also supports pRad and other experimental efforts and facilities such as DARHT (Dual-Axis Radiographic Hydrodynamic Test) facility by developing and fielding imaging systems and advanced detector systems. Historically, P-23 has been the locus for advanced imaging technologies developed to meet the demands of the weapons program.

Our imaging expertise is currently being applied to inertial-confinement-fusion (ICF) experiments via neutron pinhole imaging and to pRad. This simple yet powerful technique allows us to capture neutron images of capsules used in ICF experiments and thus contributes to improvements in capsule design. However, the application to ICF requires pinhole dimensions that push the limits for fabrication and fielding. In 2003, new milestones in pinhole fabrication were met, resulting in the highest-resolution images recorded to date, as well as the first “double-aperture” image. We continue to investigate different fast-imaging technologies especially hybrid/CMOS (complementary metal oxide semiconductor) that will provide needed infrared cameras and pixilated detector technology for pRad, hydrodynamic experiments, and SCEs. For example, P-23 has a new 3 MHz camera development work with Rockwell Scientific and University of California.

We also continue to preserve, analyze, and document the Nevada Test Site (NTS) and Pacific Proving Grounds weapons-test data to gain an understanding of physics and performance parameters of nuclear-weapons systems. P-23 analyzes imaging data from the pinhole neutron experiments (PINEX) and neutron-emission measurements from neutron experiments (NUEX) and threshold experiments (THREX) as well as continuous reflectometry for radius versus time experiments CORRTEX. The physicists and engineers who performed the original measurements are correlating and reanalyzing the data from different events, using new methodologies and improved computer and analytical techniques. Our aim is to develop better physics models and provide certified NTS data that will allow validation of the Advanced Simulation and Computing (ASC) program—an important goal of the stockpile stewardship program.

Nuclear Physics and Particle Astrophysics

The neutrino research effort in P-23 has focused on our continuing role in the Sudbury Neutrino Observatory (SNO) in Ontario, Canada (Figure 2). SNO is a 1000 metric ton, heavy-water Cerenkov detector operating deep underground in the Creighton mine in Sudbury, Ontario, Canada and can measure and separate all active flavors of neutrinos via charged-current, neutral-current, and elastic-scattering interactions on D_2O . Previous results employing a pure- D_2O detector provided direct evidence for resonant-enhanced solar-neutrino transformation and resolved the long-standing solar-neutrino problem. More recently, these results have been verified with unprecedented precision in the second phase of the SNO experiment. To accomplish this, NaCl was dissolved into the D_2O to enhance sensitivity to the neutral-current signal and separation from charged-current events. The SNO project has now entered its third and final phase wherein a discrete array of ultra-low-background helium-3 detectors have been deployed to separate all event classes on an event-by-event basis. This phase of the experiment promises to optimize the ultimate precision of the SNO experiment and offers a means to verify the solar-neutrino oscillations in a manner radically different than the previous two phases.

New efforts in P-23 are underway to elucidate further some of the most profound questions in modern physics following the seminal discoveries of neutrino mass and oscillations during the past few years. The Majorana project will attack the issue of absolute neutrino mass scale and character by exploiting a massive array of ultrapure germanium-76 in a search for the rare process of neutrinoless double decay. The Cryogenic Low-Energy Astrophysics with Neon project attempts to realize a liquid-neon-based target for low-energy solar neutrinos and cosmological dark matter.

A broad and ambitious set of neutron-research projects involves colleagues in P-25 and a host of collaborating universities and institutions. Two notable examples are $n + p \rightarrow d + \gamma$ (NPDGamma) and ultracold neutron (UCN) experiments. The NPDGamma experiment will help researchers better understand the nature of weak interactions between strongly interacting hadrons by measuring the parity-violating directional gamma-ray asymmetry to an accuracy of 5×10^{-9} , i.e., to within approximately 10% of its predicted value. This project has involved the design, construction, and commissioning of a pulsed, cold-neutron beam line along flight path 12 (FP12) at the Lujan Neutron Scattering Center at the Los Alamos Neutron Science Center (LANSCE). The NPDGamma collaboration successfully commissioned the beam line at FP12 during 2004.

FP12 will also be used, upon completion of the NPDGamma experiment, to measure the electric dipole moment (EDM) of the neutron. The goal of the EDM project is to achieve over two orders of magnitude improvement to the limit of the EDM by using UCNs (produced and stored in a bath of superfluid helium-4) and superconducting quantum interference devices to monitor helium-3 precession. FP12 may also be used to measure

pulsed cold neutron beta decay as a test of the standard model of electroweak interactions. This experiment incorporates an existing helium-3 spin-filter neutron polarizer and a new large-area spectrometer that are expected to reduce systematic errors to less than 0.1%. These fundamental and weapons-physics projects have driven improvements in detector capabilities, a hallmark of P-23.

P-23 is conducting an equally ambitious program of astrophysics research through its Milagro Observatory (Figure 3) located in the Jemez Mountains above Los Alamos, New Mexico, and by its participation in the High Resolution Fly's Eye (HiRes) experiment located in Utah. Milagro is the first detector of its kind—a large, water Cerenkov extensive-air-shower (EAS) detector—that can monitor the entire overhead sky in the TeV energy regime. Since its inception, Milagro has successfully detected the Crab Nebula with flux measurements that agree with values obtained using air Cerenkov telescopes. Building on this work, Milagro subsequently was used to produce a TeV gamma-ray map for the entire northern hemisphere.

The HiRes experiment looks for cosmic rays of energy greater than 10^{20} eV. HiRes detects the EASs that result from an



Figure 3. Milagro Observatory in the Jemez Mountains above Los Alamos.

P-23 Group Description

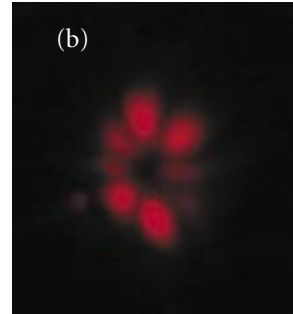
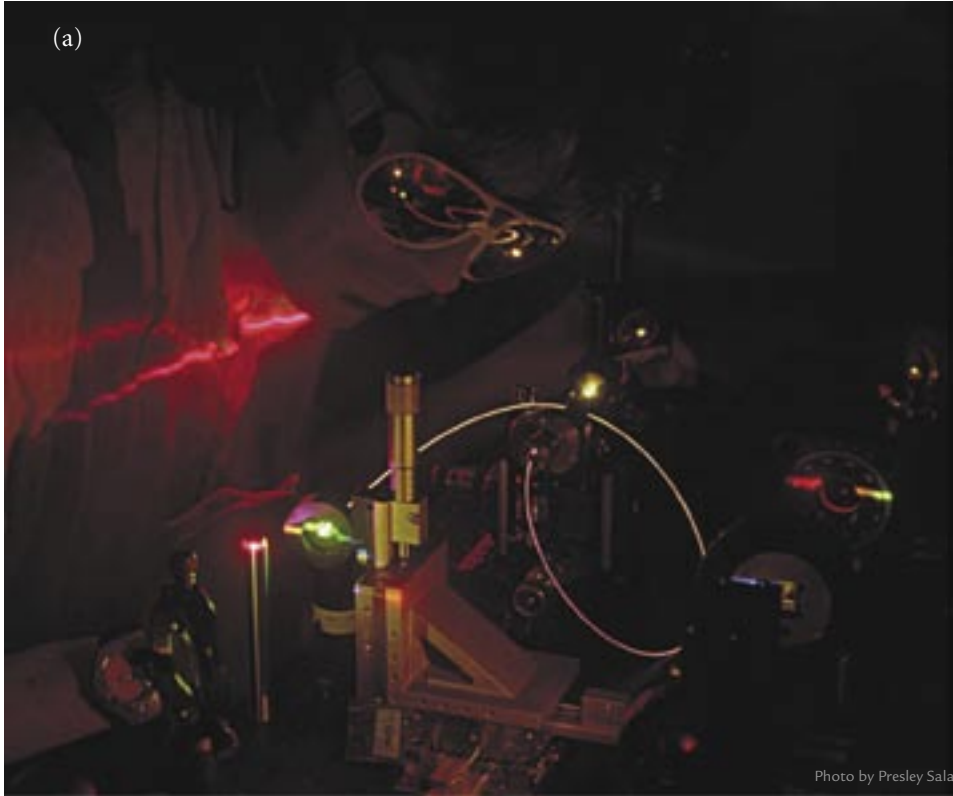


Figure 4. (a) Supercontinuum generation from a photonic crystal fiber obtained by propagation of 800 nm 100 fs pulses in it. (b) Far-field image of the output radiation obtained by converting Raman-shifted 1550 nm light in a photonic crystal fiber.

ultra-high-energy cosmic ray entering the atmosphere using two independent sites (12.6 km apart) to stereoscopically view the fluorescence caused by an event. A third experiment is the Wide-Angle Cerenkov Telescope (WACT) that employs an array of six atmospheric Cerenkov telescopes. WACT measures the lateral distribution of Cerenkov light created by EASs, allowing inference of the nuclear species of the primary cosmic ray. We have also re-examined archival data collected by the Burst and Transient Source Experiment and Energetic Gamma Ray Experiment Telescope satellites to discover a new high-energy component in one of the 24 gamma-ray burst emissions.

Finally, we have recently developed two experimental plans to search for a time variation of the fine-structure constant, α . The first plan involves comparison of three atomic optical frequency standards based on ion traps. The second plan involves a dysprosium-atomic-beam apparatus that will enable radio-frequency spectroscopy rather than optical-frequency metrology. P-23 also hosts an effort in nonlinear optics (Figure 4) which is focused on the next generation of fiber-based sources and detectors. The work performed on photonic crystals and photonic crystal fibers focuses on their application to frequency metrology, arbitrary signal generation, and spectrally broad ultrafast laser sources. The combination of nonlinear

optics and structured waveguides is also being investigated with an eye towards extremely sensitive biodetection schemes for homeland defense applications. Finally, ultrafast pulses and optical nonlinearity are being used to develop the next generation of advanced and highly secure communication protocols.

Our mission is to solve challenging experimental-physics problems relevant to our national security—aiming to reduce the threat of war by helping to ensure the reliability of our nuclear-weapons stockpile and by limiting the proliferation of weapons of mass destruction, and maintain first-rate fundamental physics research. We anticipate many exciting developments in the coming years, including experiments to measure the time variation of the fine-structure constant, new studies into the nonlinear interaction of ultrashort laser pulses with structured fibers, a series of new SCEs at NTS to be conducted in collaboration with the United Kingdom, and a proposed experiment (Majorana) to measure the fundamental character of the neutrino via double beta decay.



The World's Greatest Science Protecting America

Los Alamos National Laboratory, an affirmative action/equal opportunity employer, is operated by the University of California for the U.S. Department of Energy under contract W-7405-ENG-36.



P-24: Plasma Physics Group

Cris Barnes, Group Leader

Carter Munson and Mike Ray, Deputy Group Leaders

The Plasma Physics Group (P-24) at LANL has the mission “to nurture and use LANL’s core discipline of experimental plasma science in basic and applied research to benefit LANL and the nation.” The group applies an extensive knowledge of plasma physics, atomic physics, laser-matter-interaction physics, dynamic material properties, laser and pulsed-power technology, and plasma-diagnostic engineering and technology—all to study matter in the plasma state. P-24 addresses problems of national significance in inertial and magnetic fusion, laboratory plasma astrophysics, nuclear-weapons stewardship, conventional defense, environmental management, and plasma-based advanced manufacturing (<http://www-p24.lanl.gov>).

High-Energy Physics

The High-Energy-Density Physics and Fusion Team conducts target-physics experimental campaigns at our own Trident laser, as well as at the Omega laser at the Laboratory for Laser Energetics (University of Rochester) (Figure 1) and the Z pulsed-power facility at Sandia National Laboratories. Team members study physics issues relevant to achieving inertial fusion and relevant to weapons physics and basic high-energy-density physics, in particular, in the areas of laser-plasma instabilities, beryllium

materials characterization, and the other properties of dynamic materials, fusion-burn diagnosis and capsule implosions, hydrodynamics and mix, and radiation flow and radiation hydrodynamics. The team is developing a variety of diagnostics for the National Ignition Facility (NIF) and this past year performed the first hydrodynamic and hohlraum shots on NIF.

The Trident Team performs experiments relevant to inertial-confinement fusion

(ICF), weapons physics, and basic high-energy-density physics while operating the Trident laser facility (a three-beam, 500 J green laser with two separate target chambers and areas). Recent improvements to Trident have included a several-hundred-Joule few-microsecond capability for driving large flyer plates, and the facility now has a 20 J subpicosecond capability that is being enhanced to exceed 100 J and 200 TW (Figure 2). The team also works on advances in laser and optical science (Figure 3).

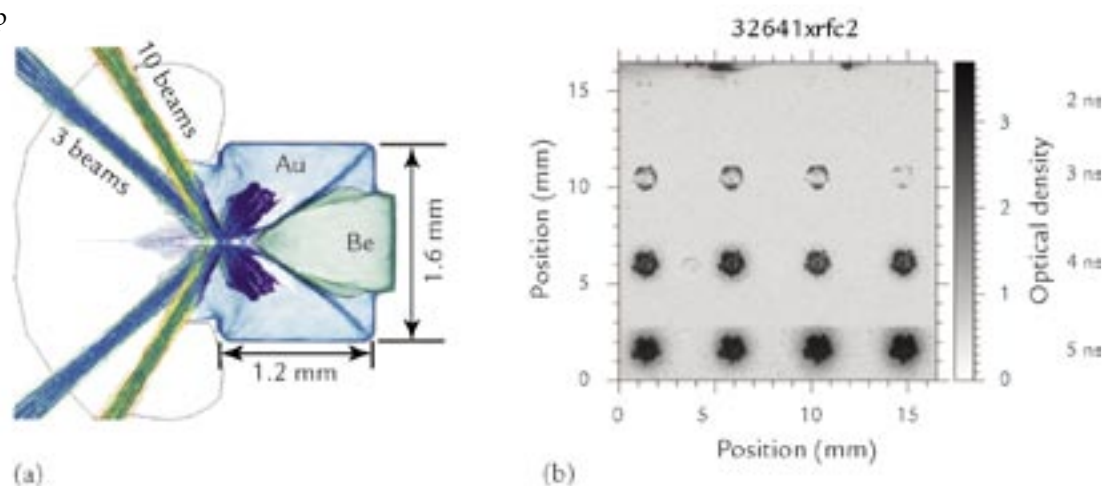


Figure 1. (a) Design of a gold vacuum hohlraum to be used at the Omega laser for beryllium microstructure stability studies. The laser beams enter from the left, and the 800 μm diam beryllium package is centered on the back wall to the right. (b) Gated x-ray framing camera images show the actual azimuthal filling of the hohlraum in time.

PLASMA PHYSICS



P-24 Group Description

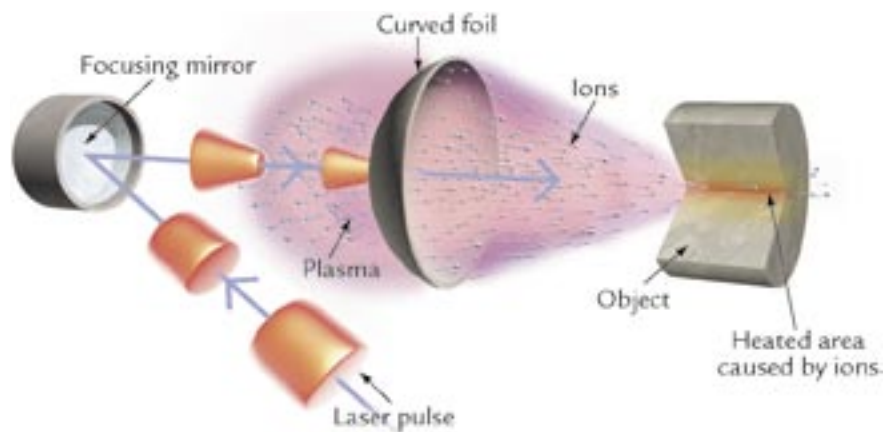


Figure 2. Ballistic focusing of a laser-accelerated ion beam into a secondary target. The secondary target will be heated isochorically to high temperatures while remaining at high density, recreating conditions found in the core of Jovian-like planets.

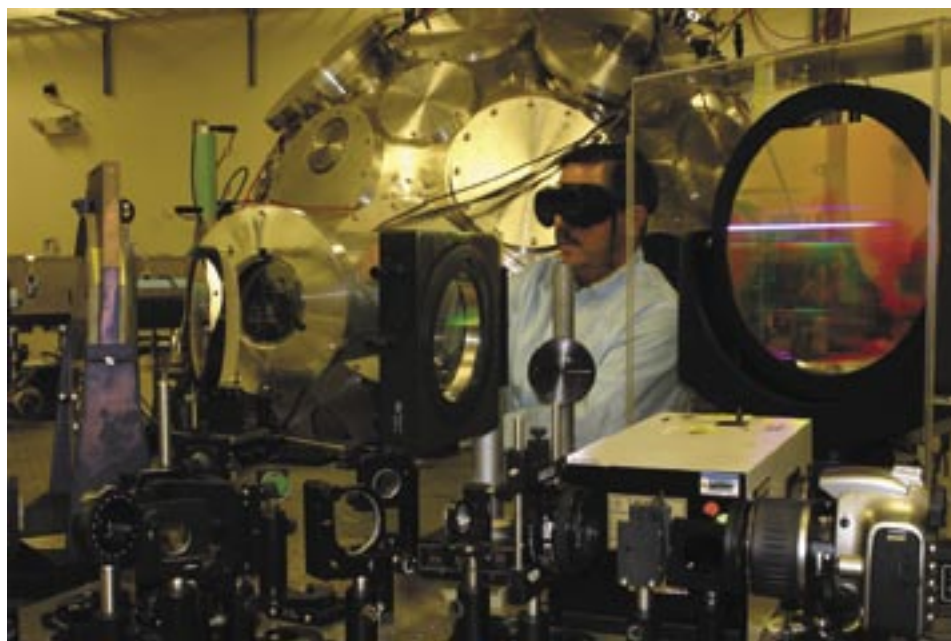


Figure 3. Tom Ortiz of P-24 adjusts the short-pulse compression optics (note the large gold grating to the right) on the north target chamber of Trident.

Plasma Physics

The Magnetic Fusion Team conducts experiments emphasizing innovative confinement concepts and diagnostics development. The primary focus is a field-reversed-configuration experiment aimed at investigating magnetized target fusion. Other projects include collaborations with scientists from the Massachusetts Institute of Technology, Princeton University, and the University of Washington. There is a growing focus on plasma science and laboratory plasma astrophysics, including a reconnection-scaling experiment and a new flowing-magnetized-plasma (FMP) experiment (Figure 4).

The Applied Plasma Technologies Team applies energetic nonequilibrium plasmas to environmentally conscious and industrially efficient processes with emphasis on basic physics, commercial applications, weapons-stockpile surety, and homeland defense. The work includes studies on nonthermal atmospheric-pressure plasmas and new applications such as plasma combustion and plasma aerodynamics (Figure 5).

Engineering and Administration

The Diagnostic, Engineering, and Operations Team provides engineering and technical support for many of the projects in the group. In addition to supporting experiments and diagnostics used at OMEGA, Trident, and soon NIF, the team designs, engineers, builds, and maintains diagnostic systems such as x-ray framing cameras (Figure 6), neutron imagers, gas Cerenkov burn-history diagnostics, streaked optical pyrometers, and target positioners. The team also operates a world-class research machine shop and provides photographic laboratory and digitization support.

The Administrative Team provides secretarial, operational, safety and security, computational and network, and general management support for the group.

P-24 Activities and Facilities

In the 2004 fiscal year, the group employed 92.3 full-time equivalent people on a nearly \$20 million budget. The group typically has over 100 people working during the summer months, including a student population of 26 during summer 2004. To attract and educate these students, challenge and inspire our staff, and provide connections to visiting scientists, we created a more formal Plasma Physics Summer School (http://wsx.lanl.gov/R SX/summer-school/Summer_school_homepage.htm) with 21 lectures and seminars. The group maintains a vital post-doctoral researcher program with ten postdocs at present, including a Reines Fellow and a Director's Funded postdoc; two postdocs were converted to staff in 2004. The postdoc program has contributed to a demographic staff profile that is nearly flat with age. Over twenty percent of the postdocs and staff are foreign nationals as the group maintains a commitment to hiring the best scientific talent to meet its mission. The group recognizes that its future scientific work will involve ever more complicated measurements on complicated experiments. We thus have a significant and growing engineering staff in the group and are actively recruiting and hiring a larger proportion of technicians for the group, mostly at the entry level to be trained over the next decade by our outstanding corps of senior technicians.

P-24 is located at Technical Area 35 in primarily six buildings covering a little over 53,000 sq ft. This area includes experimental laboratories for the Trident laser, the FRX-L magnetized-target-fusion experiment, the FMP experiment, the reconnection studies experiment, the Applied Plasma Technologies Laboratory, several laboratories for diagnostic development and checkout (i.e., x-ray sources, materials diagnostics, two laser laboratories, and an optical-diagnostic checkout facility), the machine shop and photo laboratories, and smaller

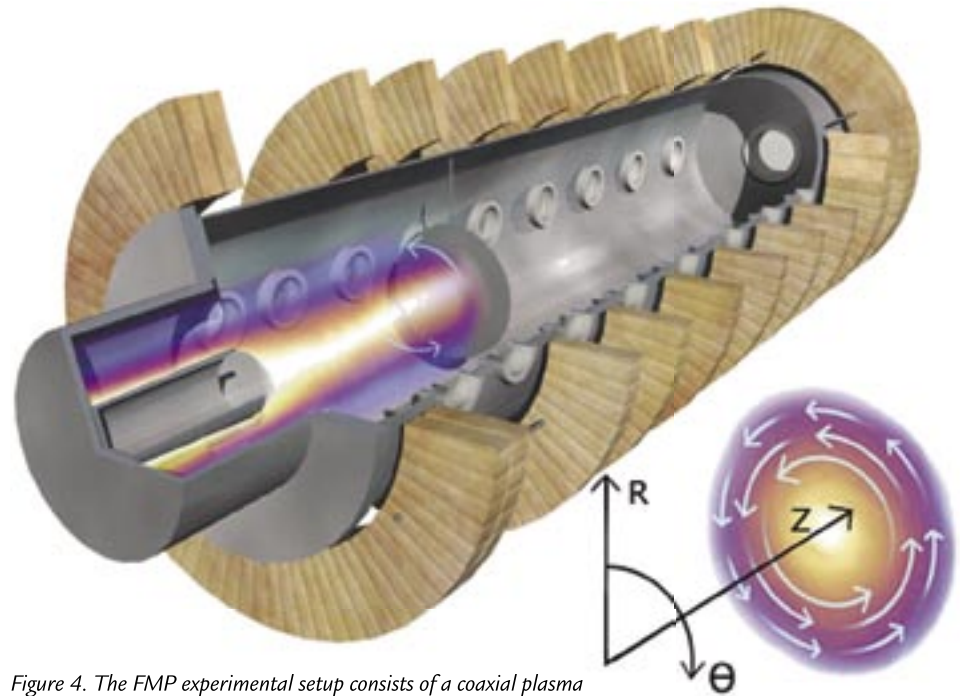


Figure 4. The FMP experimental setup consists of a coaxial plasma gun (front, left) mounted on one end of a large, cylindrical metal vacuum chamber surrounded by magnetic coils. The circular plate inside the chamber can be biased to different voltages, providing axial plasma confinement and some control over the potential profiles inside the plasma, which affects the azimuthal plasma rotation profile.

laboratories associated with many of the technicians. Because P-24 is located near the Materials Science Division Target Fabrication Facility and major collaborators for our high-energy-density physics and fusion work, the group is well situated for its laboratory infrastructure.

P-24 Strategic Objectives

P-24 has strategic objectives in high-energy-density physics with specific plans to grow LANL's involvement in NIF and in the science campaigns aimed at studying primaries (Campaign 1, or "Boost") and secondaries (Campaign 4). Strategic objectives also include high-intensity short-pulse (subpicosecond) laser-matter interactions, the properties of materials under dynamic conditions, innovative fusion-confinement concepts such as magnetized target fusion, development of laboratory plasma astrophysics, and new applications of nonthermal plasmas. All of these are exciting fields of physics

with strong growth potential that can contribute to achieving our vision "to be recognized as a world-leading organization for plasma physics and fusion science and technology, a home of trusted expertise, a place of choice for people to work and visit, and a partner of choice for sponsors and collaborators."



Figure 5. Effect of increasing the plasma power on plasma-assisted combustion. More power causes an increase in flame propagation speed, indicated by the movement of the flame from the top of the quartz tube (1) towards the electrodes [bottom, at location (2)].

P-24 Group Description

How we do business

- Emphasize personal growth and professional excellence—Cris Barnes, 505-665-5687, cbarnes@lanl.gov
- Implement improved operational efficiency and personal accountability—Carter Munson, 505-667-7509, cmunson@lanl.gov
- Continue to follow an academic alliance strategy—Cris Barnes
- Enhance our efforts to be recognized for technical excellence—Mike Ray, 505-665-6495, mray@lanl.gov
- Modernize the P-24 scientific and facility infrastructure—Cris Barnes

Main strategic accounts

- Maintain high-energy-density physics as a strategic account—Cris Barnes
- Grow our participation on NIF, leading LANL efforts on its scientific use and developing future diagnostics—Steve Batha, 505-665-5898, sbatha@lanl.gov
- Define a viable role for Los Alamos experimental work in ICF ignition, in particular, in implosion physics—George Kyrala, 505-667-7649, kyrala@lanl.gov
- Develop a robust program in Boost Physics—Carter Munson
- Achieve demonstration of magnetized target fusion—Tom Intrator, 505-665-2927, intrator@lanl.gov

Program development

- Become scientific leader in non-thermal plasma applications like plasma combustion—Lou Rosocha, 505-667-6493, rosocha@lanl.gov
- Define a strategy and grow our work in dynamic material properties—Damian Swift, 505-667-1279, dswift@lanl.gov
- Choose scientific thrusts in applications of short-pulse laser science and attract sponsors—Juan Fernández, 505-667-6575, juanc@lanl.gov
- Create a Lab-wide initiative in high-density magneto-inertial fusion in support of Office of Science strategic objectives—Glen Wurden, 505-667-5633, wurden@lanl.gov
- Create a supported focus research area in laboratory plasma physics in support of science-based prediction—Scott Hsu, 505-667-3386, scotthsu@lanl.gov
- Become funded as part of the U.S. International Thermonuclear Experimental Reactor program—Glen Wurden

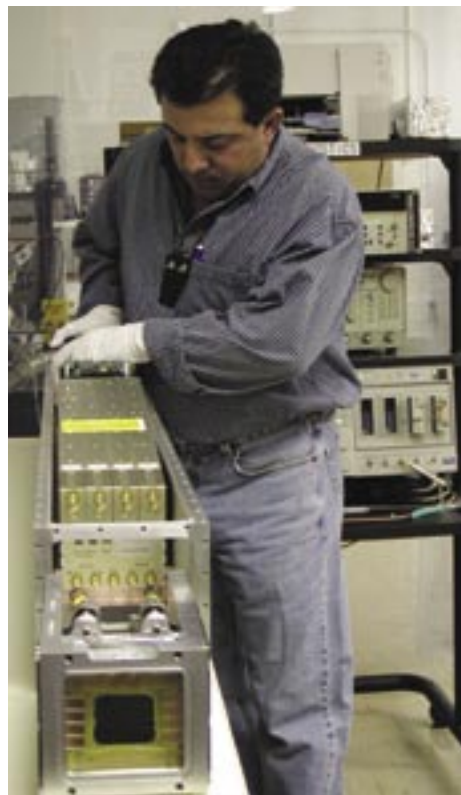


Figure 6. Tom Archuleta of P-24 carefully installs the components of the Gated X-ray Detector for NIF. The fully computer-controlled systems operate inside a cooled air box.



The World's Greatest Science Protecting America

Los Alamos National Laboratory, an affirmative action/equal opportunity employer, is operated by the University of California for the U.S. Department of Energy under contract W-7405-ENG-36.



P-25: Subatomic Physics Group

Martin Cooper, Group Leader

Jon Kapustinsky and Wesley Wilburn, Deputy Group Leaders

The Subatomic Physics Group (P-25) was created in 1994 as part of a reorganization of Physics (P) Division initiated by former P Division Leader Peter Barnes. The scientific staff of P-25 was formed from P-2 (Medium-Energy Physics) and the research groups MP-4 and MP-10 of the Medium-Energy Physics (MP) Division. The common thread uniting these groups was leadership in investigations of issues of subatomic physics that could be addressed in experiments at a number of accelerator facilities, including the Los Alamos Meson Physics Facility (LAMPF), currently known as the Los Alamos Neutron Science Center (LANSCE); the Fermi National Accelerator Laboratory (FNAL); the European Organization for Nuclear Research (CERN); and the Superconducting Super Collider. Because of the diverse physics being conducted in MP-4, MP-10, and P-2 and tight funding at the time, it was clear that the group would have to undergo a consolidation of its research priorities. John McClelland (now Deputy Director for Experimental Physics in the Weapons Physics Directorate at LANL) was the first group leader of P-25, and under his direction the research priorities were narrowed, and about half of the group redefined its area of focus.

New themes in P-25 became studies of fundamental issues of the standard model (the primary focus) and the search for a basis for stronger collaborations between fundamental physics and the weapons community. In carrying out its experimental investigations, P-25 staff members often participate in large-scale collaborations that involve physicists from universities and institutions from

around the world, and the group contributes to or leads experiments at a variety of facilities. The intellectual atmosphere in the group is enhanced by local workshops, by students who come to participate in the research, and by a small theory group that brings in numerous theory visitors involved in research areas of interest to the group. A few of the current programs and projects in P-25 are featured in the activities described below.

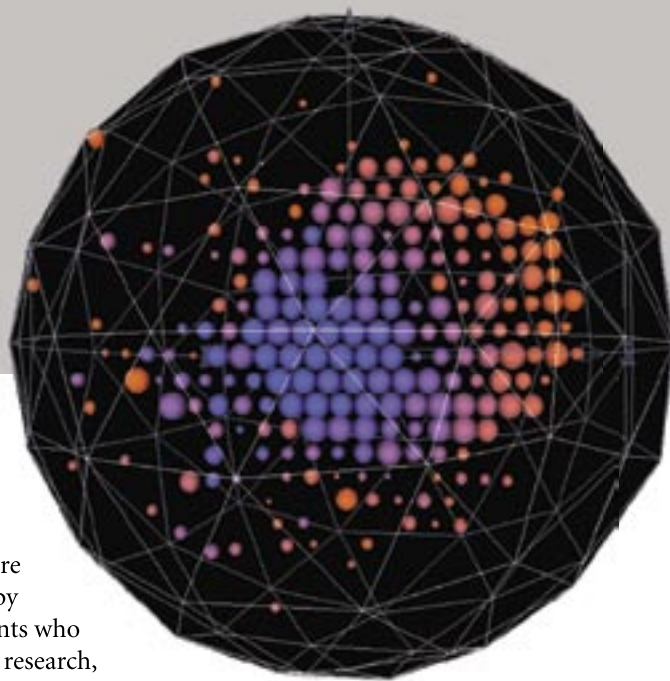
The group's current experimental activities evolved largely from the research priorities established during the consolidation of the mid 1990s. Neutrino physics, with an emphasis on searches for neutrino oscillations, now focuses on the MiniBooNE experiment at FNAL (Figure 1).

This experiment is the first phase of the larger Booster Neutrino Experiment (BooNE) that will definitively test results from the Liquid Scintillator Neutrino Detector (which took data from 1993–1998 at LAMPF) to confirm neutrino oscillations and will precisely measure the oscillation parameters. This experiment will also test *CP* (charge conjugation/parity transformation) and *CPT* (the combined operation of charge conjugation, parity

Figure 1. The colors in this typical MiniBooNE neutrino event relate to elapsed time—the blue represents early PMT hits and the orange represents later photomultiplier-tube hits. In this particular data event, there were fewer than six veto hits and over 200 tank hits.

inversion, and time reversal) violation in the lepton sector.

The Neutrino Physics Team also has interest in exploring new methods of detecting “double beta decay” of nuclei to further understand the nature of the neutrino. In addition to neutrino studies, P-25 is involved in the relativistic-heavy-ion investigations currently under way at the Relativistic Heavy-Ion Collider (RHIC) at Brookhaven National Laboratory. The goal of these investigations is to create and study the exotic properties of a primordial quark-gluon plasma in a laboratory. This activity was an outgrowth of the successful relativistic-heavy-ion program at CERN, which was under way in P Division at the time P-25 was formed, and the joint research program in P and MP Divisions



RESEARCH HIGHLIGHT

PHYSICS DIVISION

P-25 Group Description

to study Drell-Yan and charmonium physics at FNAL.

Members of P-25 are involved in the development of a silicon vertex detector upgrade for the PHENIX (Pioneering High-Energy Nuclear Interaction Experiment) detector at RHIC that enhances the capability for studying the gluon distributions in colliding nuclei and the early evolution of the formation of the quark-gluon plasma by directly detecting heavy-quark decays.

Detecting pairs of muons produced in deuteron-gold and gold-gold collisions at RHIC, members of P-25 are obtaining mass spectra of the J/ψ (a particle consisting of a charmed and an anticharm quark). Such spectra have been long awaited as a diagnostic of the quark-gluon plasma.

The High Resolution Fly's Eye (HiRes) experiment at the Dugway Proving Grounds in Utah is measuring ultra-high-energy cosmic rays (UHECRs) ($> 10^{18}$ eV) with detectors sensitive to the air fluorescence of showers caused by cosmic rays entering the atmosphere—HiRes is now helping researchers quantify mechanisms of production and propagation of UHECRs.

Another theme in P-25 involves neutron physics at LANSCE, which aims to study symmetry violation and search for physics beyond the standard model. Members of P-25 are currently planning a novel search for the electric dipole moment (EDM) of the neutron, an interest that grew out of their earlier work in fundamental symmetries.

In designing the experiment aimed at improving the limit on the EDM of the neutron, the team made the first measurement of the dielectric strength of helium-4 over a distance range of 1 to 7 cm with an area of 400 cm². The fact that voltages around 100 KeV/cm can be held is an important step forward in the feasibility of the experiment. The team also made its first sample of ultrapure helium-4 with the hope that it will have a purity of less than 10^{-12} atoms of helium-3. The team also



Figure 2. Members of P-25 performing calibration tasks before a pRad shot.

measured the cohesive force of Metglas at a temperature of 1.2 K and found it to have adequate magnetic shielding properties for the experiment.

P-25 is collaborating with P-23 to provide better sources of ultracold neutrons (UCNs)—neutrons that can be trapped by ordinary materials and then used for a variety of experiments that probe fundamental quantities with high precision. The team has recently commissioned tests of a full-scale UCN source based on their earlier pioneering development of the world's most intense source of UCN using solid deuterium.

Proton radiography (pRad)—a technology that images dynamic variations of macroscopic objects over small time intervals with millimeter spatial resolution—is a new activity that was inspired by P-25's familiarity with accelerator physics and its understanding of advanced detectors for imaging and handling high data rates (Figure 2).

Application of the same underlying principles is also contributing new ideas for homeland defense. P-25's pRad program has three goals: (1) to demonstrate that radiography with high-energy protons is a suitable technology for meeting the goals established for advanced radiographic imaging, (2) to advance the technology of charged-particle radiography, and (3) to apply radiography

with 800 MeV protons to the needs of the stockpile stewardship program. Members of the pRad Team recently commissioned a new radiography system that images dynamic events with an order of magnitude higher spatial resolution and another system that significantly improves sensitivity to thin objects. A prototype electron-radiography system, designed by P-25 and constructed at the Idaho Accelerator Center, was used to continue investigations in the use of electrons as direct probes for static and dynamic radiography of thin systems.

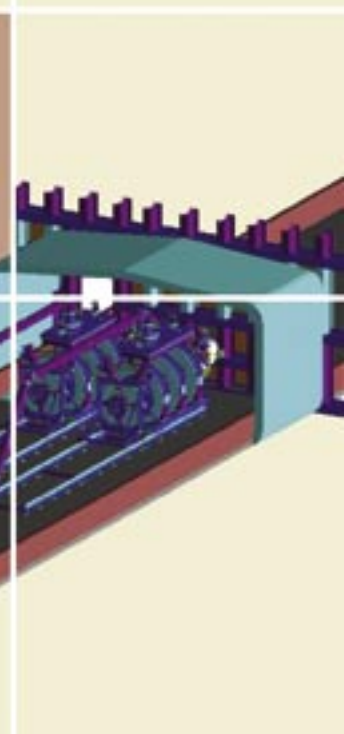
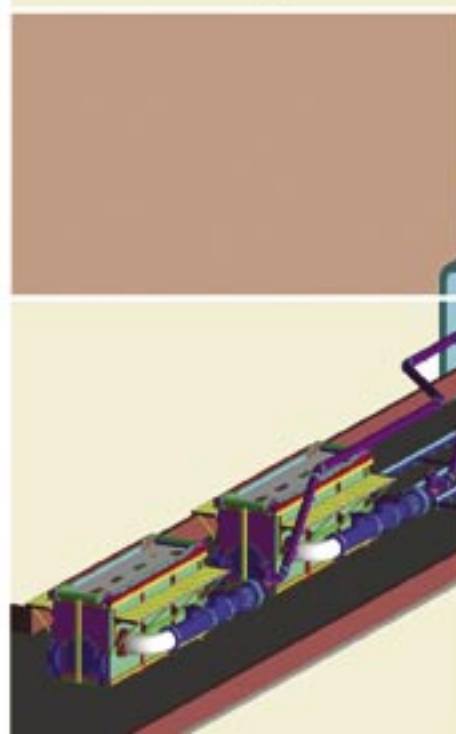
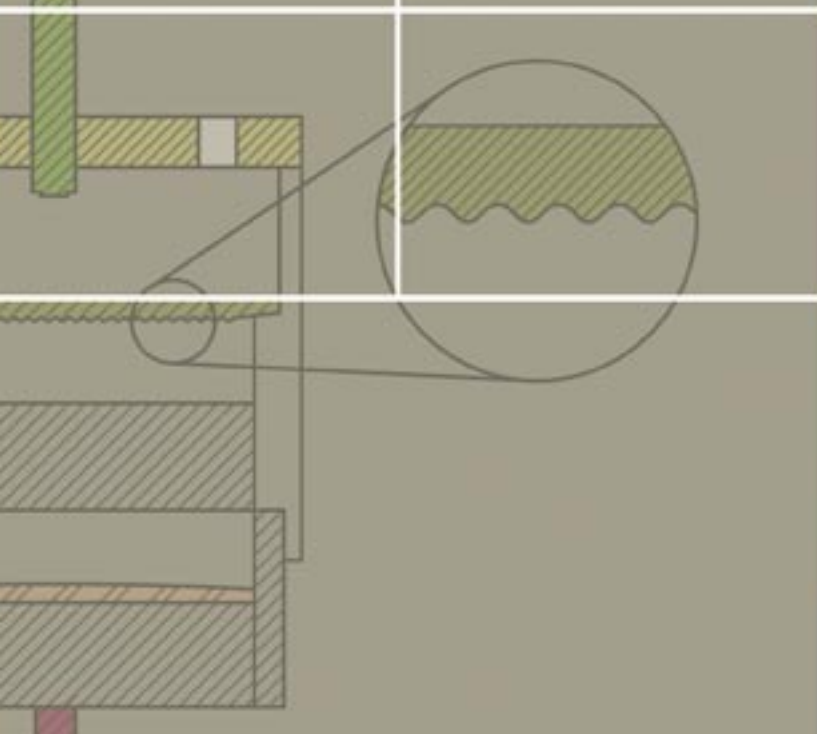
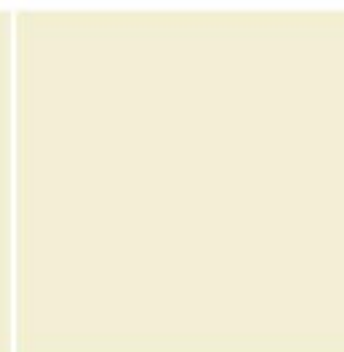
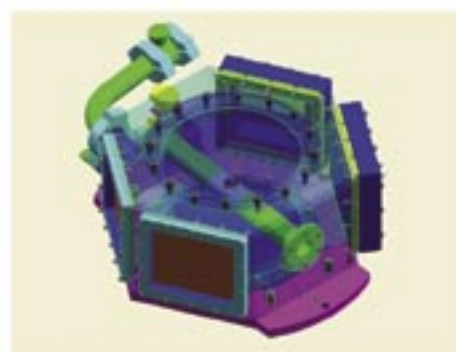
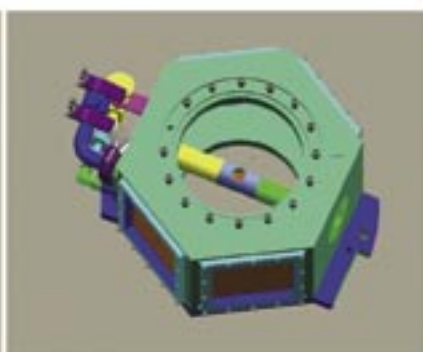
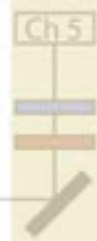
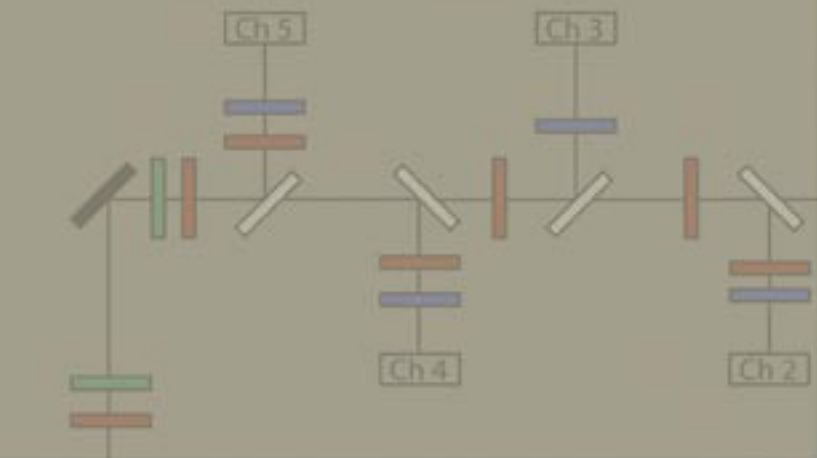
Recent theoretical activity in P-25 has focused on parity violation in chaotic nuclei, deep inelastic scattering, and Drell-Yan reactions as a means to explore quark propagation in nuclei, quantum chromodynamics at finite temperatures, and phase transitions in the early universe.

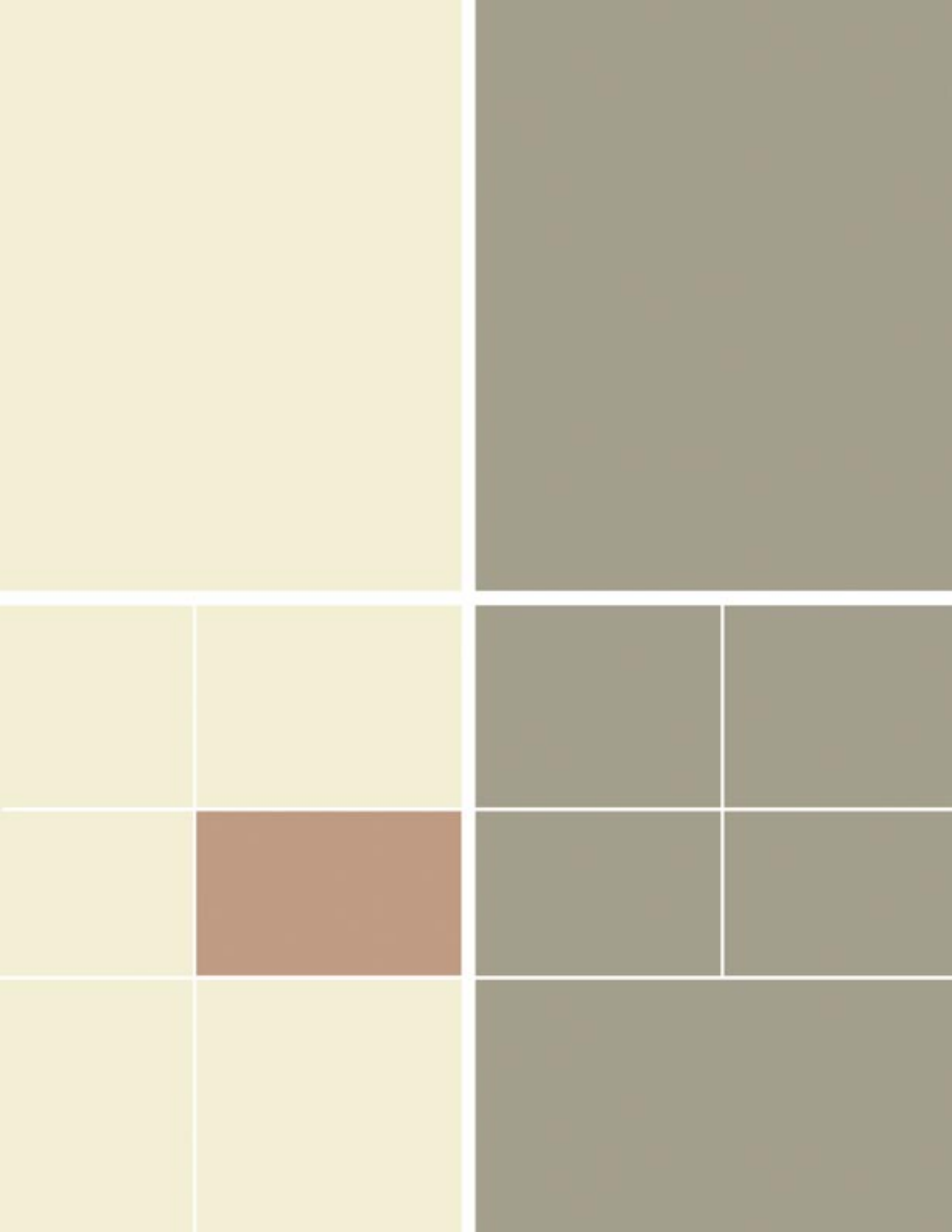
P-25 is making numerous contributions to homeland defense based on novel applications of nuclear-physics techniques. This includes muon radiography, which is a high-sensitivity detection technique relying on natural radiation that could aid in the surveillance for contraband special nuclear material, and Very Large Area Neutron Detector, which applies neutrino-detector technology to the identification of special nuclear materials.

P-25 group members continue to be active in education and outreach activities, both as participants in programs sponsored by LANL, whereby high school, undergraduate, and graduate students work on projects within the group, and as individual citizens who volunteer their time for various activities (visit <http://users.hubwest.com/hubert/mrscience/science1.html> for information about this activity).

The cutting-edge science described here not only advances fundamental knowledge and spawns creative ideas for new technology but also is a key ingredient of LANL's ability to attract and retain the high-caliber talent it needs to fulfill its national security mission.

Material Studies Research Highlights





Optical Pyrometry on the Armando Subcritical Experiment

C.M. Frankle, D.B. Holtkamp (P-22), S.D. Borrer, R.B. Corrow, J. Crystal, L. Woo (Bechtel Nevada)

The Armando subcritical experiment (SCE) was the final shot in the Stallion series of SCEs, also consisting of two previous shots, Mario and Rocco. The primary objective of the Stallion series was to investigate differences in material properties between cast and wrought plutonium driven by high explosives (HE). The Armando experiment contained two plutonium/HE packages, which were identical except one contained wrought plutonium while the other held cast plutonium. The two packages were also identical to those fired on Mario and Rocco. While Mario and Rocco were primarily diagnosed using point techniques, Armando was primarily diagnosed using an area technique (radiography). However, two diagnostics were common to all three shots—a single-point velocimetry measurement using the velocity interferometer system for any reflector (VISAR) and optical pyrometry.

The optical-pyrometry technique measures the surface temperature of the plutonium as it is heated by the passage of the HE's shock wave. Light is emitted from an ideal blackbody surface based on its temperature in accordance with Planck's law:

$$L_{\lambda} = \frac{2c^2 h}{\lambda^5 (e^{hc/\lambda kT} - 1)} \quad (1)$$

Here L_{λ} is the radiance in $\text{W/m}^2 \text{ sr m}$, c is the speed of light, h is Planck's constant, λ is the light's wavelength, k is Boltzmann's constant, and T is the temperature. In order to perform the measurement, a pyrometer is constructed using high-speed photomultiplier tubes (PMTs) filtered

to be responsive to certain wavelength bands. Due to the explosive nature of the experiment, the pyrometer is located remotely from the package. An optical probe collects the light emitted from the plutonium surface and is sent over $\sim 100 \text{ m}$ of 1 mm diameter optical fiber. High-speed digitizers then capture the signals from the PMTs.

Pyrometry data was successfully returned from Mario, Rocco, and Armando. The data is currently being analyzed.

Pyrometer Design

The pyrometer system was specifically designed to meet the needs of the Stallion SCE series. In other words, the expected range of temperatures and the operating conditions of the overall experiment dictated the selection and layout of components. Armando required two identical pyrometers, one for each plutonium piece. One of our primary considerations was measuring temperatures in the range of $\sim 300^\circ\text{C}$ to $\sim 1200^\circ\text{C}$, to operate with timing resolution of a few ns, and to coexist with large quantities (many Watts) of 532 nm light from the VISAR lasers. Figure 1 illustrates the experiment's schematics and design. The pyrometer utilizes five channels, three in the visible spectrum and

two in the near infrared. Each channel is a 2 in. diam PMT that has a $\sim 3 \text{ ns}$ rise time. The visible tubes are Hamamatsu R943-02 operating at room temperature, and the near-infrared tubes are Hamamatsu R5509-72 operating at -80°C . Optical bandpass filters are placed in front of each tube to select a particular wavelength band, which are listed in Table 1.

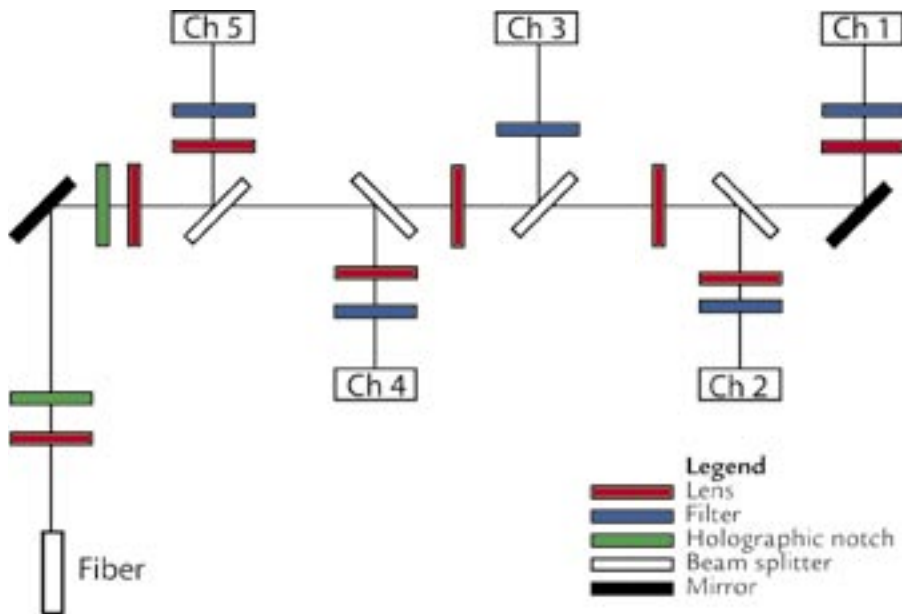
Referring to Figure 1, the operation of the pyrometer is as follows. First, light from the transporting optical fiber is brought into reasonable focus using a lens. The light then impinges on an OD6 holographic-notch filter which passes all light except those in a 10 nm wide band around 532 nm. The 532 nm light is reflected backward into a beam dump. The notation "OD6" indicates that the intensity of 532 nm light is reduced by a nominal factor of 10^6 in passing through the filter. After passing the first holographic-notch filter, the beam is bent 90° using a turning

Table 1. Wavelength coverage of Armando pyrometers

Channel	Spectral Range (nm)
1	1510–1670
2	1180–1300
3	800–900
4	690–750
5	496–517

RESEARCH HIGHLIGHT
PHYSICS DIVISION

Figure 1. Schematic diagram of the pyrometer.



mirror. It then passes through a second OD6 holographic-notch filter for a total reduction of 532 nm light of up to 12 orders of magnitude. The beam then passes through a lens to further adjust the focus before proceeding through a series of dichroic beam splitters. Each beam splitter reflects wavelengths shorter than a cutoff value into the PMT designated to measure a corresponding wavelength band. Each PMT also has a lens in front of it to focus the incident light for optimal geometric coverage of its photocathode. A passband filter is also used with each channel to define the wavelength coverage. The longest wavelengths are sent to channel 1 using a turning mirror instead of a beam splitter.

Armando Experiment Design

The Armando experimental package was designed to allow for simultaneous firing of two plutonium/HE subassemblies, identical except for the initial plutonium shaping technique. These two subassemblies were mounted on the top and bottom of a six-sided (HEX) package (Figure 2). Two radiographic lines of sight, spaced 60° apart, were aligned with four of the six package sides. A tube was mounted

through the remaining two sides of the package. At the center of the tube, a double-sided mirror was mounted at a 45° angle to the axis of the tube such that the upper plutonium surface could be viewed through one end of the tube and the lower plutonium surface could be viewed through the opposite end of the tube (Figure 3). The tube had to be made small, so that the two radiographic images could be obtained before the plutonium surface impacted the tube.

The central tube provided optical access for the pyrometry and VISAR diagnostics. Our colleagues at Bechtel Nevada (BN) did an outstanding job at designing an integrated optical probe, incorporating the needs of both the pyrometry and VISAR teams. The VISAR transmit fiber was mounted in a small hole drilled through the center of the two lenses which were mounted at the front of the probe. Return light for the VISAR was then focused on a receive fiber mounted behind the transmit fiber. The larger, 1 mm diameter, pyrometry fiber was mounted off-axis to the probe so that it received light from a spot on the plutonium surface approximately 1 cm away from the spot illuminated by the VISAR laser. This scheme is illustrated in Figure 4. A photograph of a completed probe is shown in Figure 5. One probe was inserted in each side of the hex package central tube.

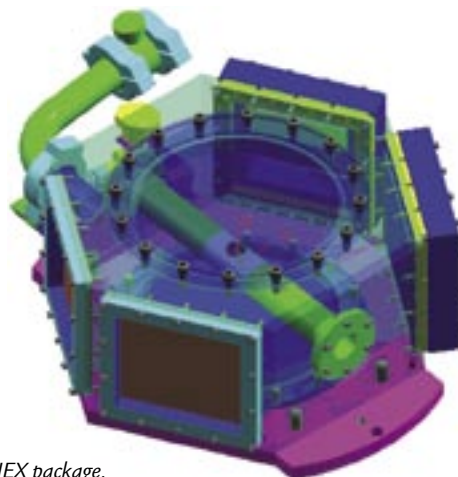


Figure 2. The Armando HEX package.

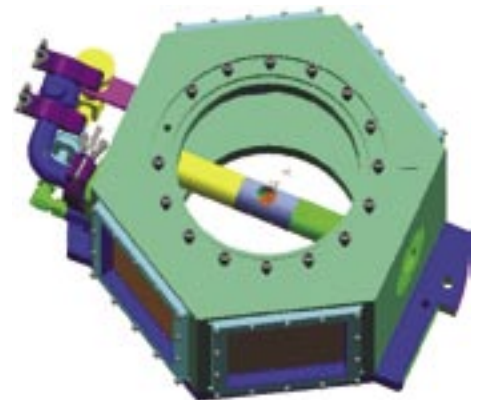
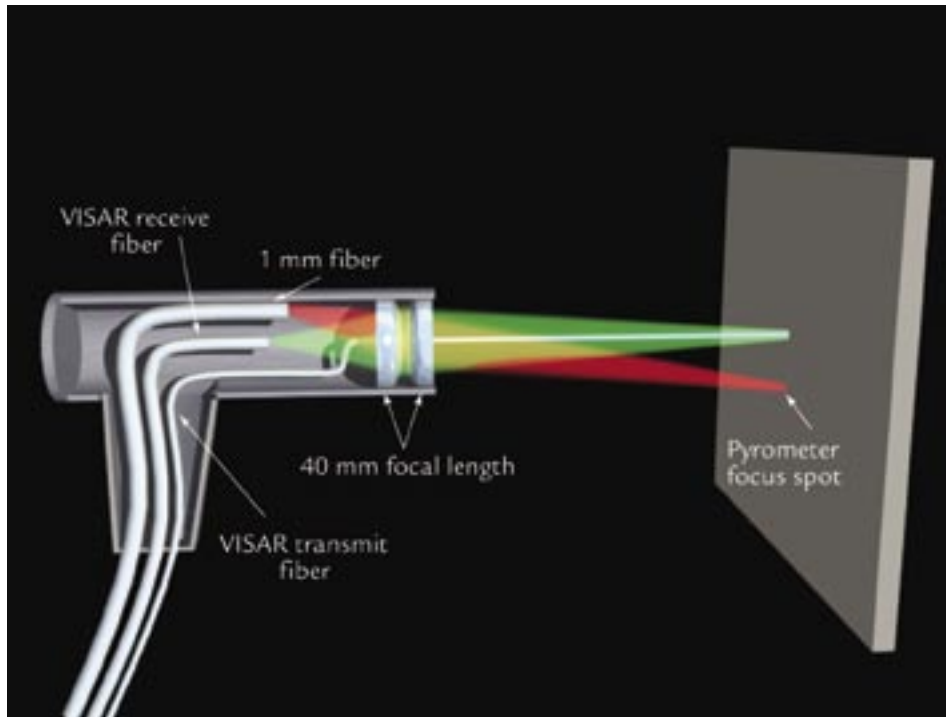


Figure 3. The Armando HEX package showing the location of the mirror in the center of the combined pyrometer/VISAR probe tube.

Figure 4. Schematic diagram of the combined pyrometry/VISAR probe.



Pyrometer Operation

Before the experiment, each pyrometer must first be calibrated with a blackbody source to obtain the relationship between measured output voltage on the PMTs and the incident radiance. The procedure is to set the blackbody at a specified temperature and measure the output voltage on each PMT. The radiance for each channel can then be calculated by

$$L_\lambda(\lambda, T) = \int_{\Delta\lambda} \epsilon_\lambda L_\lambda d\lambda \quad (2)$$

where L_λ is as before and ϵ_λ is the emissivity. For a blackbody, the emissivity is unity and the radiance is easily calculated using the known bandpass characteristics of each filter. An example of the resulting calibration data is shown in Figure 6. Note that the PMTs are linear from a few mV to a few tens of volts. We performed these calibrations using the complete optical system, including pyrometer, fiber, optical head, and hex package tube and mirror.

In the experiment, we measure a voltage, which has a corresponding radiance $L_i(\lambda, T)$, for each pyrometer channel. However, unlike in the calibration case, we do not know the emissivity of the plutonium surface. Hence, we have N measurements but $N+1$ unknowns, corresponding to the N unknown dynamic emissivities plus the temperature. In order to address this difficulty, we make two assumptions:

- (1) the radiances all correspond to a single temperature, even though the dynamic emissivities may be different (emissivity is in general wavelength dependent) and
- (2) that the dynamic emissivity can be bound using known properties of the material.

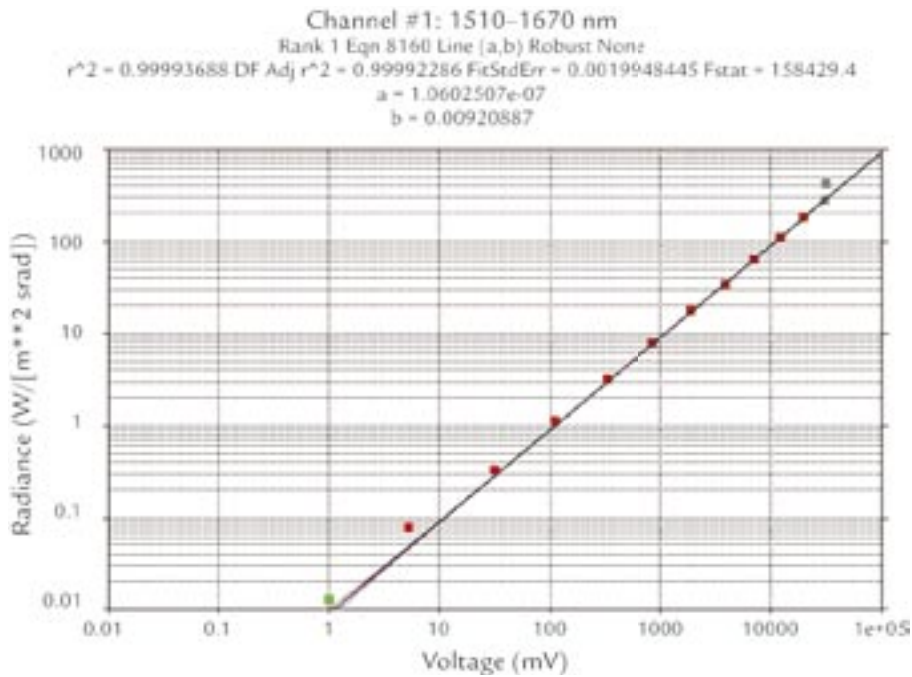
For example, the emissivity must have an upper bound of 1, corresponding to that of a blackbody. A reasonable lower bound might be the static emissivity of a freshly machined or polished surface. With these assumptions an additional $2N$ of constraints are introduced, allowing a temperature (and associated uncertainty) to be derived. Note that due to the shape of

Figure 5. Photograph of completed pyrometry/VISAR probe.



Material Studies Research Highlights

Figure 6. Example calibration data.



the radiance curve, the shorter wavelength channels most strongly constrain the temperature.

Armando was successfully fired on May 25, 2004. Pyrometry data was returned on all channels, and the analysis of the data is ongoing. However, our preliminary analysis clearly shows measurable differences in the radiance from the cast and wrought parts—in a manner similar to that observed between Mario and Rocco.

Acknowledgment

We gratefully acknowledge the contributions of the many individuals at LANL and BN who helped make this experiment possible. This work was funded by the U.S. DOE Office of Defense Programs.

For further information, contact Chris Frankle, 505-665-4138, cfrankle@lanl.gov.



The World's Greatest Science Protecting America

Los Alamos National Laboratory, an affirmative action/equal opportunity employer, is operated by the University of California for the U.S. Department of Energy under contract W-7405-ENG-36.



Armando: The Final Subcritical Experiment in the Stallion Series

R.D. Fulton

Armando was the final subcritical experiment (SCE) in the Stallion series. The Stallion series of experiments (Vito/Etna, Mario, Rocco, and Armando) were designed to evaluate high-explosive (HE) driven properties of cast and wrought plutonium; the cast and wrought materials being representative of the materials produced via the different manufacturing processes employed at Rocky Flats and LANL. Specific properties investigated were ejecta production, spall features, and surface temperatures. Ejecta is defined as the small particulate matter “ejected” from the surface of a solid when a strong shock wave interacts with the surface. Spall is a general term for bulk material failure near the surface of a solid created by a strong shock interacting with the surface. Both of these phenomena depend upon the material properties: material strength, grain size, impurities, etc., as well as the strength and temporal profile of the shock pressure. The surface temperature is an important constraint upon the final state of the shock-driven metal that will be important in a full understanding of the behavior of the material.

Vito/Etna was a joint experiment conducted with the Aldermaston Weapons Establishment (AWE) located in the United Kingdom that concentrated on ejecta. Rocco and Mario were separate cast and wrought experiments that examined the phenomena of interest with a suite of point diagnostics. These diagnostics provided either specific time arrival information at a single spatial point or a continuous time record of some material property at a single spatial point. Armando

was designed to complement and extend the measurements of Rocco and Mario by combining the two experiments into a single package and radiographing the behavior at two separate times along equivalent lines of sight. The paraphrased paradigm is: a picture is worth a thousand pins.

Diagnostics and Package Composition

HE diagnostics equivalent to those used on Rocco and Mario were implemented to verify identical HE performance. These consisted of a series of shorting switches combined with a microwave interferometer strip laid out symmetrically on the HE package to measure detonation times and velocities. Point VISARs (Velocity Interferometer System for Any Reflector) and optical pyrometers (that provide a measure of the surface temperature) were also implemented to verify equivalent behavior of the surface properties. The primary diagnostic for Armando was x-ray radiography along two equivalent axes separated by 60°. Physics packages identical to the Rocco and Mario packages were combined in a HEX package (6-sides or High-Energy X-ray) vertically separated with the free surfaces facing one another. This geometry allows for exactly equivalent radiographs to be taken of the two materials at the same time in

their evolution. The third axis of the HEX package is used for VISAR/pyrometry access.

The experimental package is contained within a 3 ft diam (inside diameter) containment vessel. This vessel and the camera box that houses the scintillator and camera system are placed within a “zero room” created by a large bulkhead completely sealing off the end of the U1a.05 drift. Thin radiographic windows in the bulkhead and vessel allow the x-rays to pass through the package and the containment vessel with minimal attenuation. Originally designed so as to expend the zero room, fielding the experiment within a containment vessel allows for the reuse of the zero room for multiple experiments and provides multiple redundant containment (Figure 1).

The Cygnus sources extend down the drift externally to the zero room. They are composed of a Marx bank system contained in large oil-filled tanks that pulse-charge adjacent pulse-forming lines (PFL). The output of the PFL is a short pulse (~ 60 ns), large-amplitude (~ 1 MV) electrical pulse that propagates down an 8 in. diam, water-filled, coaxial transmission line. This electrical pulse is coupled into the inductive voltage adder (IVA) cells that add the voltage

RESEARCH HIGHLIGHT

PHYSICS DIVISION



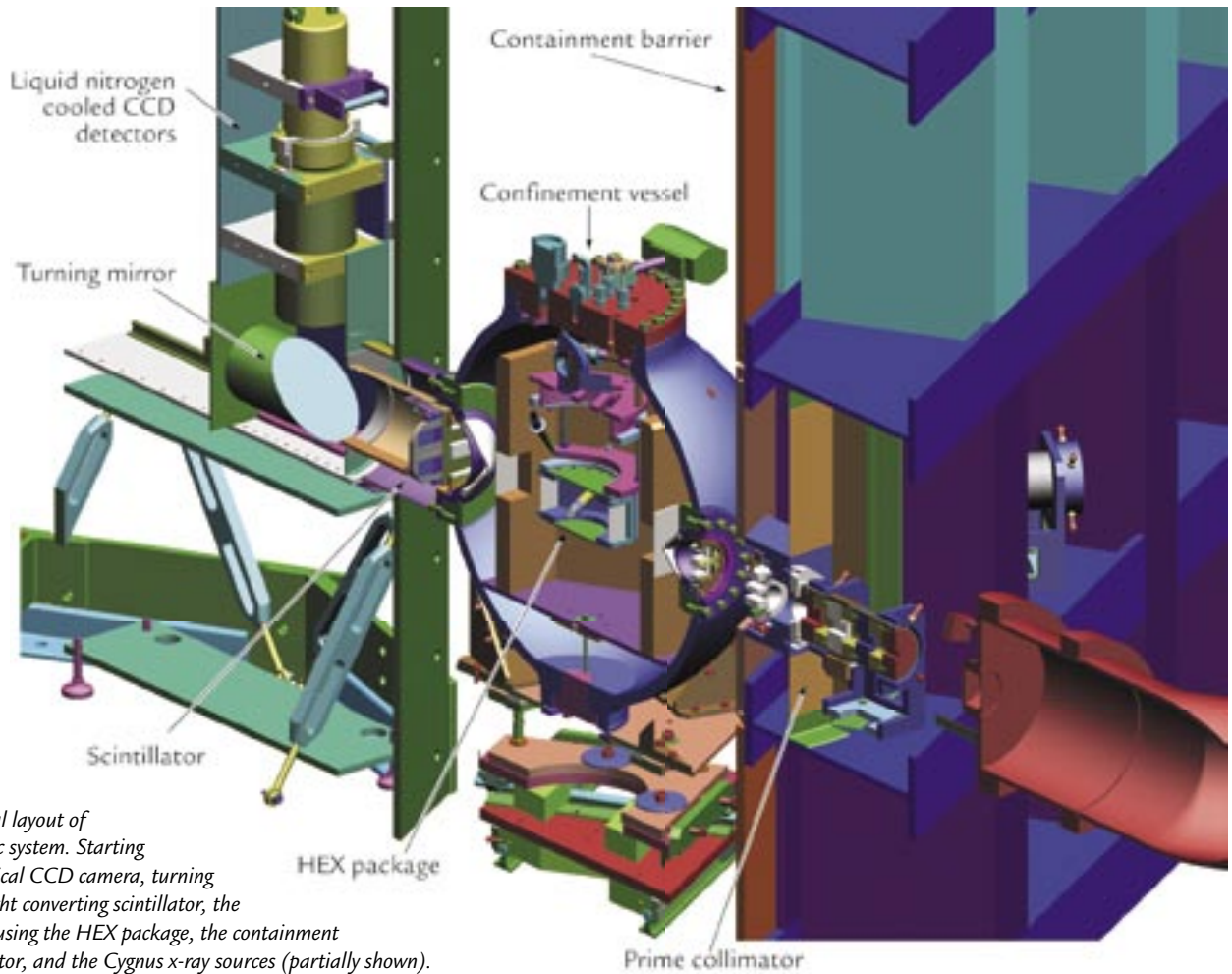


Figure 1. Experimental layout of Armando radiographic system. Starting from the left: the vertical CCD camera, turning mirror, the x-ray to light converting scintillator, the confinement vessel housing the HEX package, the containment barrier, prime collimator, and the Cygnus x-ray sources (partially shown).

in parallel to produce a 2.25 MV, low-impedance drive pulse for the rod-pinch diode. This last stage of voltage addition is accomplished in a high-vacuum suitable for diode operation. The expertise of Sandia National Laboratories (SNL) and Titan/Pulse Sciences Division (PSD) were instrumental in applying the technology developed at SNL to realize a robust and flexible pulse-powered driver capable of operating reliably underground.

Radiography and Detector Systems

The radiography employed on Armando represents a significant advance in the performance of medium-energy radiography. It has been the result of a multiyear, multi-Laboratory effort involving LANL, SNL, Bechtel Nevada

(BN), the Naval Research Laboratory (NRL), AWE, Titan/PSD, and Mission Research Corporation (MRC). Many innovations have been combined to lead to this advance in performance, but perhaps the most important has been the effective realization of the rod-pinch diode originally developed at NRL. The rod pinch has a similar geometry to standard x-ray diodes in use in industrial flash x-ray sources for several decades. However, researchers at NRL realized that when operated at low impedance (Z), the diode would transition from classic space charge limited (SCL) flow into magnetically limited (ML) flow whereby the electrons would be transported to the end of the central anode rod and then “pinch” producing a very bright, small diameter x-ray source (Figure 4). The Cygnus x-ray source was designed to provide a

low-impedance (high-current) source of voltage to effectively drive the diode into the ML regime. Measurements have demonstrated a 1 mm diam x-ray spot size producing 4 rad at 1 m in a reproducible manner.

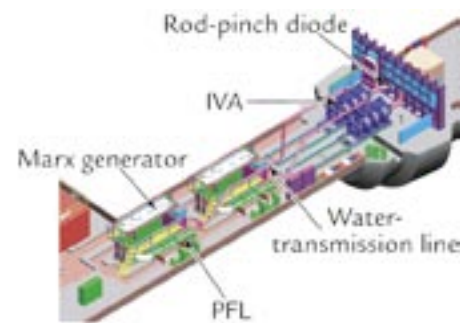


Figure 2. Layout of Cygnus x-ray sources in U1a.05 drift. Confinement vessel and camera box are not shown in this view.

The detector system is equally innovative. It combines technologies developed for Dual-Axis Radiographic Hydrodynamic Test (DARHT) and proton radiography to create a very high-resolution imaging system. It functions by converting the x-rays transmitted through the experimental package into visible light in a tiled LSO (lutetium oxyorthosilicate) scintillator. The light produced is transported by a low- $f/\#$ lens system to a LN_2 -cooled charged-coupled-device (CCD) chip that captures and records the image. In order to preserve maximum image resolution, the combined CCD camera system is not gated; all time resolution therefore derives from the flash nature of the illuminating x-ray pulse. While providing optimum resolution, this technique introduces a risk to the experiment, in that the scintillator-camera combination must be maintained in a light tight configuration throughout the HE detonation and long enough thereafter (~ 90 s) for the information to be read out of the CCD camera system to a remote data logging computer.

Results

The results of Armando have provided valuable data for stockpile stewardship. The HE diagnostics demonstrated identical performance of the HE detonation in all four packages: Rocco, Mario, and Armando cast and wrought. The VISAR measurement demonstrated that the measured surface velocity was reproduced within error bars. The radiography provided detailed subsurface data on the spalled material with a resolution and precision previously unobtainable. Radiographic data was obtained at two times allowing comparison with the VISAR data. The inferred velocity was in excellent agreement, further enhancing confidence in the accuracy of the results.



Figure 3. A view of the U1a.05 drift. The “zero room” bulkhead is seen with the two IVA structures fed by the water-filled coaxial transmission lines in the foreground.

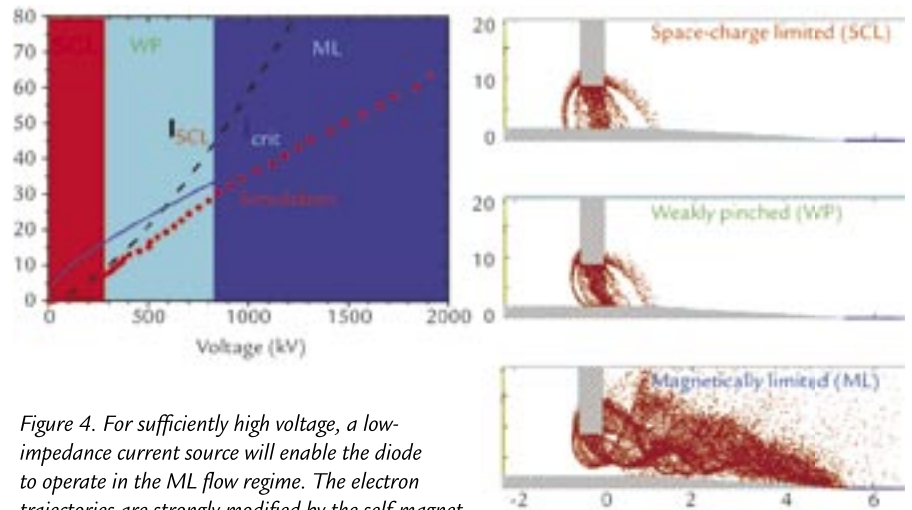


Figure 4. For sufficiently high voltage, a low-impedance current source will enable the diode to operate in the ML flow regime. The electron trajectories are strongly modified by the self-magnet field and propagate to the end of the anode producing an intense, small spot of x-rays. Dimensions are in millimeters. Figure courtesy of NRL.

Acknowledgment

A great many people in many divisions (Physics, Dynamic Experimentation, Engineering Sciences and Applications, Material Science and Technology, Applied Physics, Nuclear Materials Technology, Health, Safety, and Radiation Protection, and Earth and Environmental Sciences) at LANL worked in a very productive

partnership with SNL, Titan PSD, NRL, MRC, and BN to develop the technology and execute the Armando SCE. It is not possible to call out every individual in this format, but their efforts and dedication to this project are deeply appreciated.

For further information, contact Doug Fulton, 505-667-5005, fulton_robert_d@lanl.gov.

Material Strength under Shock and Shock-Free Loading Conditions

D.L. Preston, R.T. Olson (P-22), A. Kaul, R.J. Faehl (X-1)

Numerical simulations of explosively driven deformation and high-velocity impacts require rate-dependent models of material strength. The main challenge in constructing such models is the wide range of thermodynamic and mechanical conditions that occur in particular solid-flow processes: plastic strains to several hundred percent, plastic strain-rates up to 10^{11} s^{-1} , pressure to several megabars, and temperatures up to melt. Ideally, a material-strength model would be based on internal-state variables that provide a complete representation of the microstructural state and its evolution, but our limited knowledge of dislocation, grain-boundary dynamics, and phase-transformation kinetics currently precludes the construction of such a model. Nevertheless, steps towards developing such a material-strength model have been taken by Follansbee and Kocks who used the mechanical threshold stress (MTS, plastic-flow stress at 0 K) as a structure parameter.¹ Their MTS model only accounts for thermally activated dislocation motion, thus it cannot be reliably applied at strain rates much above 10^4 s^{-1} . This limitation was overcome by Preston, Tonks, and Wallace (PTW) who developed a model of material strength² applicable at strain rates from 10^{-3} s^{-1} to 10^{12} s^{-1} . The PTW model has been

implemented in several hydrodynamic codes at LANL and has been successfully used to simulate Taylor cylinder impacts, explosively driven systems, and high-velocity impact cratering.³ It should be mentioned that the 25-year-old rate-independent Steinberg-Guinan (SG) material-strength model is also still used in certain numerical simulations at LANL.⁴

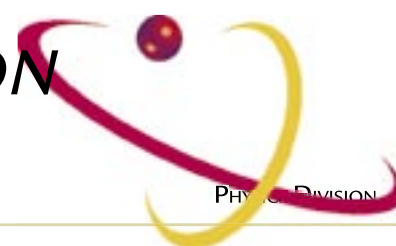
Adiabatic Shear-Band Formation and Time-Dependent Material Strength

The PTW, MTS, and SG models are all founded on the assumption that the plastic flow is spatially homogeneous, that is, the plastic deformation is not localized. However, recent experiments on copper by V.A. Raevsky *et al.* at the All-Russian Research Institute of Experimental Physics (VNIIEF) show that this assumption can break down under both shock and shock-free loading conditions.⁵ (These experiments were funded by LANL under the Gordon/Ryabev agreement.) The shock experiments are at strain rates above 10^9 s^{-1} , while the shock-free experiments are used to reduce strain rates to 10^{5-7} s^{-1} . The Raevsky experiments, which are described in more detail below, involve loading copper plates with surface perturbations by explosive detonation and then measuring the perturbation

amplitude as a function of time. In recent experiments at VNIIEF, some of the plates were recovered for subsequent metallographic analysis. Remarkably, shear bands, localized regions of large plastic deformation, were present in the recovered samples loaded to pressures above 27 GPa. The shear-band density increases in the direction of the compression wave's propagation into the sample, probably as a result of the increase in the strain rate as the compression wave steepens into a shock wave. Raevsky *et al.* have also carried out experiments in collaboration with Lawrence Livermore National Laboratory (LLNL) that show shear-band formation in 6061-T6 aluminum.⁶

We can deduce the implications of these findings for material strength by considering the formation and structure of a shear band. Approximately 90% of the work done during plastic deformation is converted into heat. If the strain rate in a region is sufficiently high, as is the case in a high-pressure shock front, then very little heat diffuses out of the region during its deformation, thus the heating is nearly adiabatic. If the decrease in strength due to the increase in temperature exceeds the increase in strength from work hardening, then the plastic deformation becomes unstable, resulting in the formation of an adiabatic shear band. The total plastic

RESEARCH HIGHLIGHT
PHYSICS DIVISION



PHYSICS DIVISION

strain in the shear band can be quite large: 500%–800%. The corresponding temperature rise is of order 10^3 K. The time scale for heat flow away from the hot shear band is $\tau_Q = w^2/\kappa$, where w is the width of the shear band and κ is the thermal diffusivity. As an example, for $w = 10 \mu\text{m}$ and $\kappa = 0.1 \text{ cm}^2 \text{ s}^{-1}$ (characteristic of steels) we find $\tau_Q = 10 \mu\text{s}$. The macroscopic (spatially averaged) strength (flow stress) will change during the time, τ_Q , required for temperature equilibration around the shear bands. Therefore, the heterogeneity causes the macroscopic material strength to be time dependent.

In view of these considerations, it is no surprise that none of our strength models agree with the Raevsky data on copper (Figure 1). The observed rate of perturbation growth is much greater than the predicted growth rate, which implies that the actual strength is less than that predicted by the models. This is consistent with the presence of hot shear bands in the copper. Unknowns in the Raevsky experiments such as the absolute pressure determination, experiment-to-experiment variability, and the unrealistically small error bars as determined from x-radiographs, raise questions about the overall accuracy of the Raevsky data. Even so, refinements in the Raevsky technique are not expected to bring the data into agreement with calculations based on current strength models.

Future Experiments Based on the Raevsky Technique

Efforts are currently underway in Physics (P) and Applied Physics Divisions to incorporate the effects of shear bands in the PTW model. Experimental data to validate the generalized model are absolutely essential. P Division is currently planning experiments that leverage upon the technique and data of Raevsky in order to create a validation database. These experiments will provide validation data precisely where the PTW model and other rate-dependent models (e.g., MTS and the LLNL Steinberg-Lund model) are least reliable, that is, at strain rates between 10^5 s^{-1} and 10^8 s^{-1} and strains up to several hundred percent, which are the conditions commonly achieved under explosive loading or high-velocity impact of metals. Furthermore, the development of this experimental capability will allow us to investigate materials not studied by Raevsky. The first experiments will be done in collaboration with Raevsky at VNIIEF and then a large suite of additional experiments will be conducted at LANL.

The Raevsky technique utilizes a flat metal plate with perturbations of known wavelength and amplitude machined into the surface. High explosive (HE) is used to generate either shock or shock-free planar loading of the plate. The amplitude of the Rayleigh-Taylor unstable perturbations is

measured from x-radiographs acquired as a function of time (Figure 2). This technique can be used to generate pressures in the metal sample in excess of 80 GPa with strain rates ranging from 10^4 to 10^{10} s^{-1} .

The preliminary experiments to be performed at VNIIEF will use diagnostics and well-characterized copper samples from LANL. These experiments will duplicate exactly those previously performed by Raevsky and, as a result, will allow for a direct comparison to the reported Raevsky data. This comparison is essential, for if LANL is to utilize the Raevsky data for model validation purposes, we must corroborate the results and analyze their uncertainties. We currently lack information about repeatability of sample preparation, drive conditions, and absolute peak pressure. It is for this reason that LANL will supply the samples and field a high-precision velocity-measurement diagnostic. Further, the reported accuracy of perturbation amplitudes as determined from radiographic analysis seems to be unrealistically high based upon the resolution limitations present in the VNIIEF x-ray system. The LANL x-ray system to be fielded will provide multiple radiographs per experiment with a small improvement in amplitude resolution. Successful completion of these joint experiments will allow us to define a level of confidence in the reported Raevsky

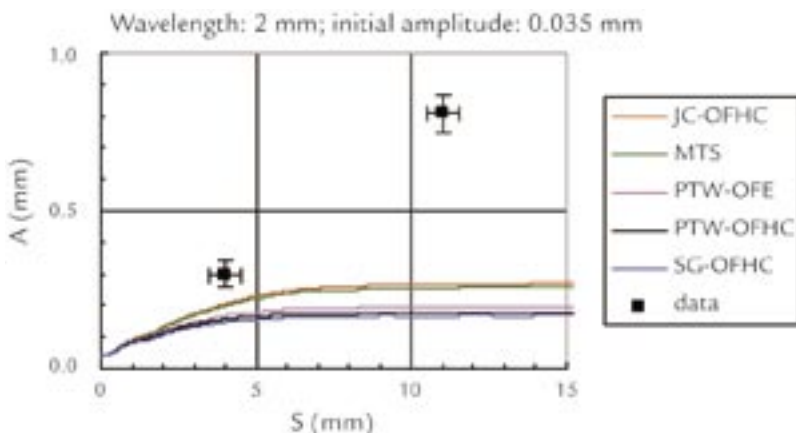


Figure 1. Perturbation amplitude versus the distance traveled by the copper plate due to shock-free loading to a peak pressure of 40 GPa: comparison of numerical simulations using the MTS, PTW, SG, and Johnson-Cook (JC) strength models to Raevsky's data.

data. The shock-free copper experiments will be continued at LANL to obtain a complete validation data set throughout the range of conditions where no other reliable data are available. The HE arrangement and quantity will be altered to control the strain rate and peak pressure through the range 10^5 – 10^8 s^{-1} and 20–70 GPa, respectively. Sample strain (up to ~250%) will be controlled through the wavelength and amplitude of the perturbations. Repeatability of the drive conditions and sample preparation will be ensured with sample velocimetry and material characterization. Amplitude growth will be measured via multiple repetition, low-energy flash x-radiography and will provide the measurable quantity to compare with hydrodynamic computations.

The results of hydrodynamic code simulations using the generalized PTW model will be compared to the extensive validation data set obtained at LANL and VNIIEF. Progressively more realistic representations of shear bands will be incorporated in the generalized model until good agreement with the data is achieved. We should emphasize that the Raevsky technique is currently the only means of obtaining accurate validation strength data at plastic strain-rates exceeding 10^5 s^{-1} , rates that are typical of explosively driven systems and high-velocity impacts.

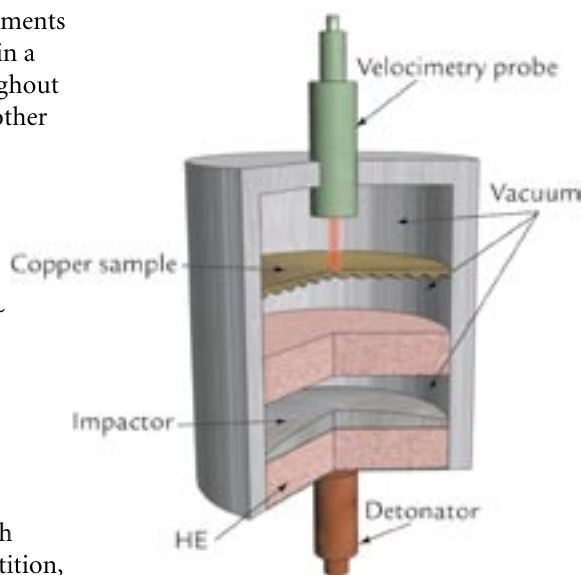


Figure 2. A schematic illustrating the Raevsky design for shock-free instability growth experiments. The radiographic line-of-sight is perpendicular to the plane of the paper.

References

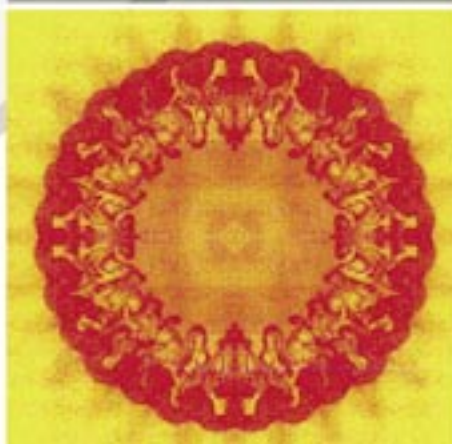
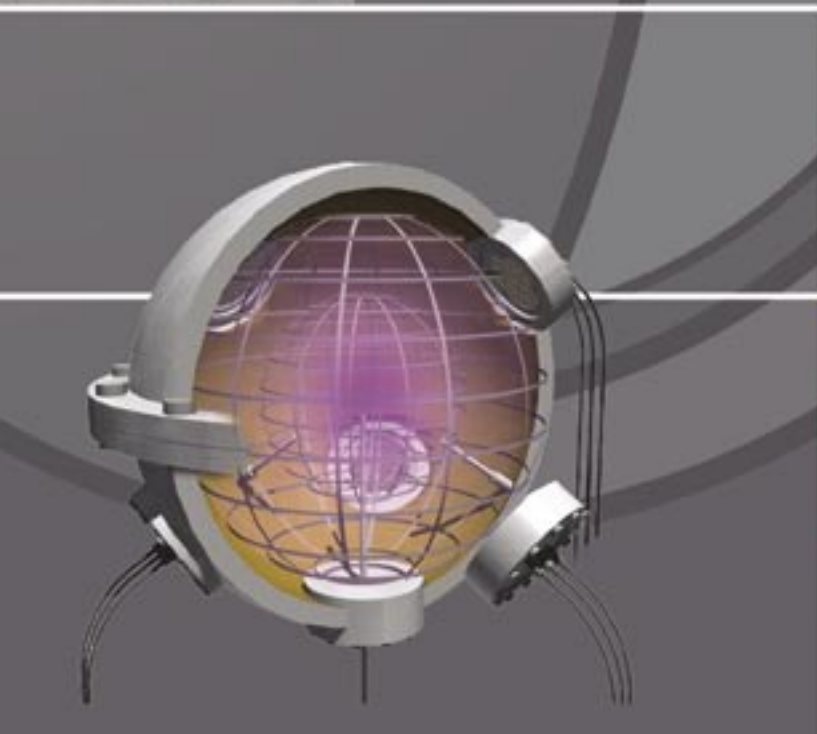
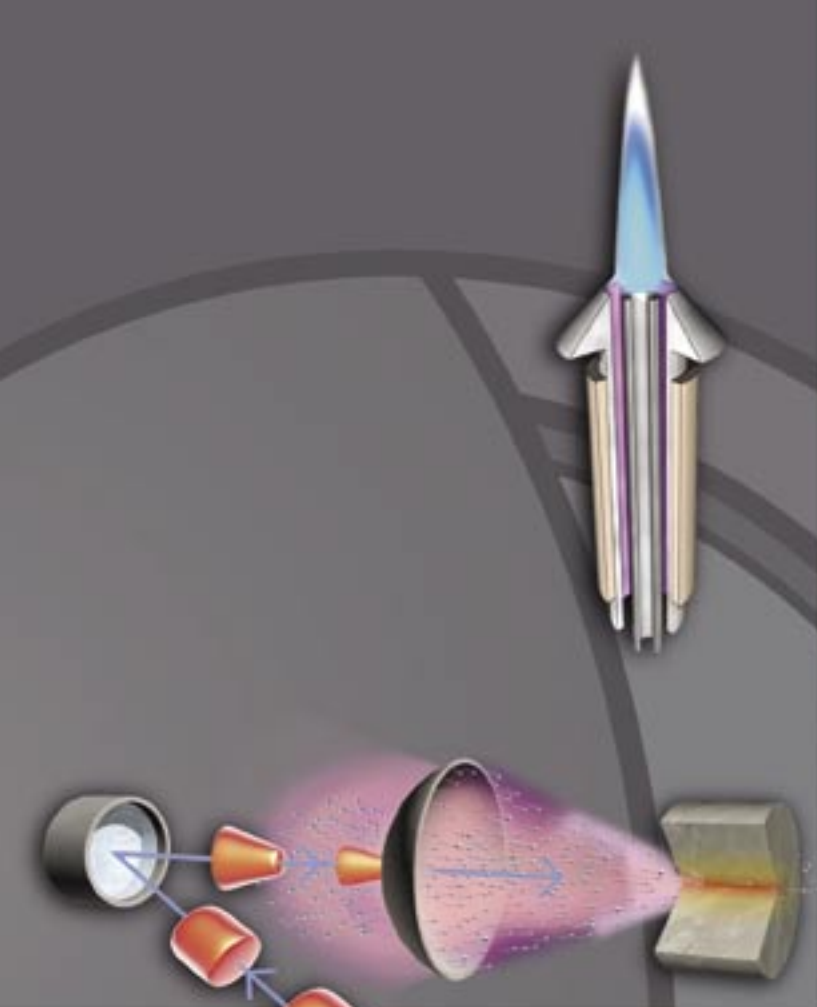
1. P.S. Follansbee and U.F. Kocks, "A constitutive description of the deformation of copper based on the use of the mechanical threshold stress as an internal state variable," *Acta Metallurgica* **36**, 82–93 (1988).
2. D.L. Preston, D.L. Tonks, and D.C. Wallace, "Model of plastic deformation for extreme loading conditions," *Journal of Applied Physics* **39**, 211–220 (2003).
3. R.F. Davidson and M.L. Walsh, "Constitutive modeling for hypervelocity cratering," *AIP Conference Proceedings* **370**, 1159–1162 (1996).
4. D.J. Steinberg, S.G. Cochran, and M.W. Guinan, "Constitutive model for metals applicable at high-strain rate," *Journal of Applied Physics* **51**, 1498–1504 (1980).
5. V.A. Raevsky, All-Russian Institute of Experimental Physics (VNIIEF), Report to LANL on Task 3.1 under Agreement 37713-000-02-35, (2003).
6. V.A. Raevsky, All-Russian Institute of Experimental Physics (VNIIEF), Final Report to LLNL under Agreement B512964, (2002).

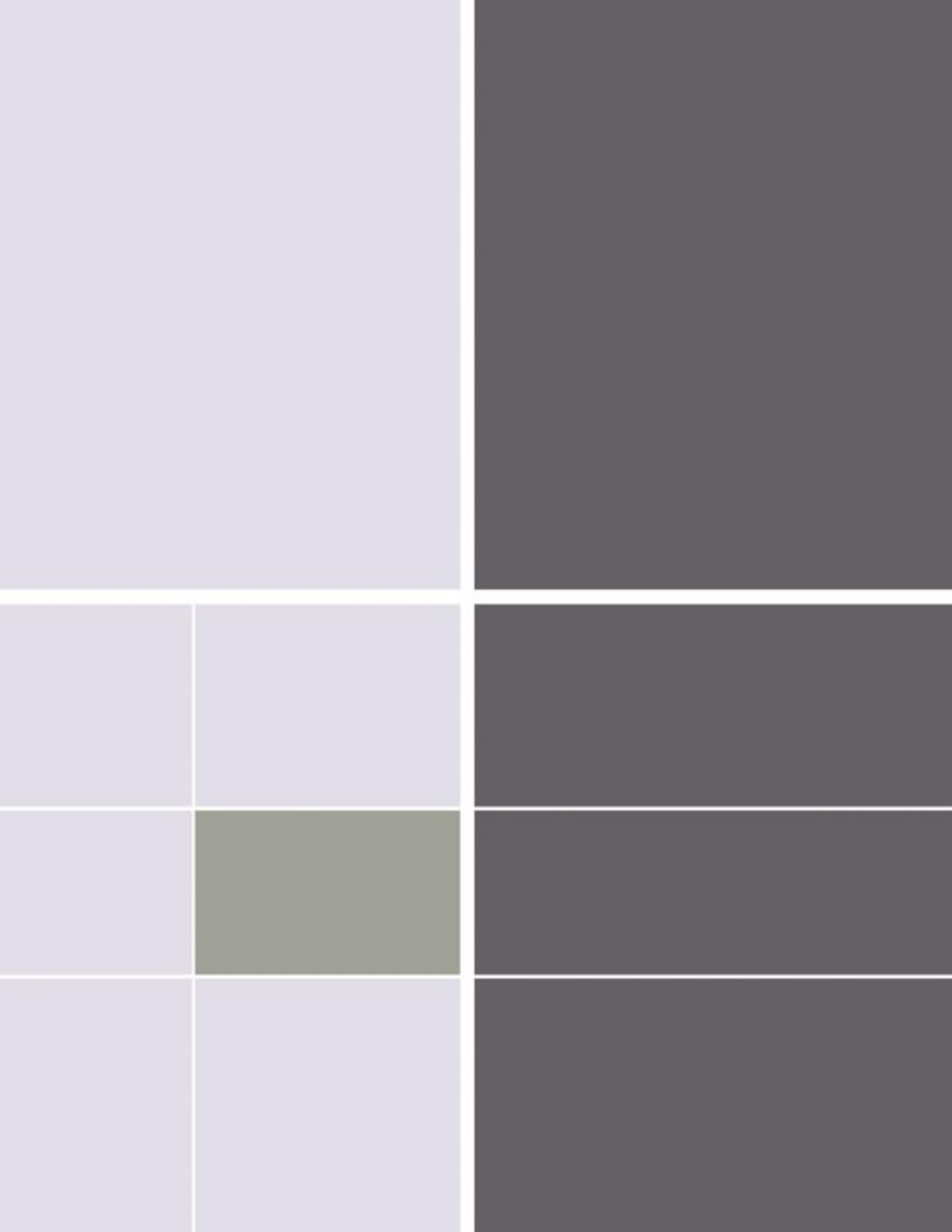
Acknowledgment

We would like to thank Dr. Victor A. Raevsky and his collaborators at the VNIIEF for several very informative discussions of their perturbation growth experiments.

For further information, contact Dean Preston, 505-667-8968, dean@lanl.gov.

Plasma Physics Research Highlights





Understanding Mix in Inertial-Confinement Fusion

G.A. Kyrala, C.R. Christensen (P-24), M.A. Gunderson, D.A. Haynes, D.C. Wilson (X-2)

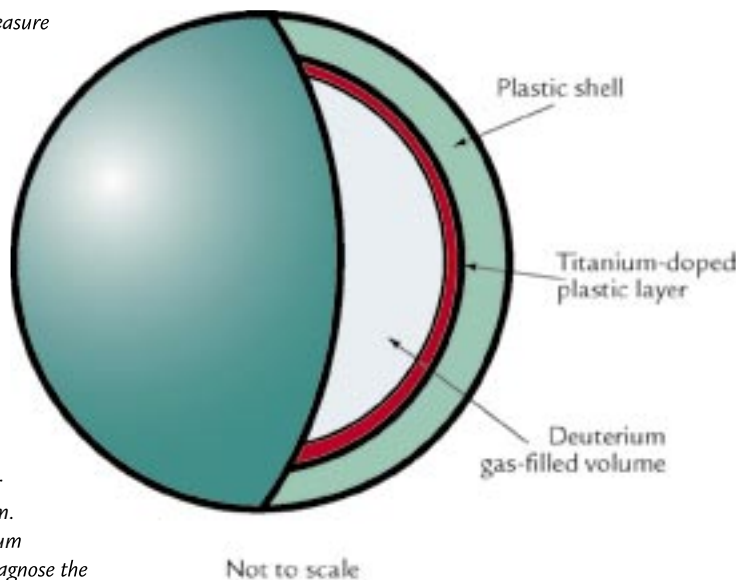
From the distant twinkle of the stars to the glowering fire of New Mexico at midday, fusion powers the universe. The Plasma Physics group (P-24) is at the forefront of the quest to capture this clean, safe, inexhaustible energy source here on earth.

In the inertial-confinement fusion (ICF) approach to fusion research, powerful lasers squeeze tiny capsules (Figure 1) filled with deuterium and tritium (rare forms of hydrogen) to enormous density and temperature to release huge amounts of nuclear energy and harmless helium gas: deuterium + tritium \rightarrow helium + neutron. This reaction could produce a megawatt of power (the same as a typical power plant) by burning only six millionths of an ounce of fuel per hour. The fuel is separated from seawater and is considered inexhaustible on conceivable time scales.

Mixed Impurities Reduce Nuclear Yield

One unsolved difficulty standing in the way of achieving fusion power is the problem of mix. During ICF implosions, internal temperatures can be around 140 million degrees Celsius, which is hotter than the core of the sun. The density can be 10,000 times what it would be at atmospheric pressure. Under these conditions, the material that forms the shell of the capsule (as well as the hydrogen fuel) is stripped of its electrons and becomes a highly reactive state of matter called a plasma. If this material mixes into the fuel, it interferes with fusion for several reasons. The heavier atoms of the shell are copious radiators, like a miniature version of the carbon arc

Figure 1. Researchers measure the spatial and temporal profiles of radiative emission from a thin titanium shell when it mixes during an ICF implosion. This measurement of the emission "color" and magnitude will constrain different mix models. The targets are shells of plastic with a titanium-doped layer on the inside surface of the shell. The target is filled with either 3 or 15 atm of deuterium. Emission from the titanium dopant will be used to diagnose the conditions in the core.



searchlights used to light up the sky at grand openings. When heated, the heavier elements release many electrons, increasing the particle density and contributing to the pressure of the hot, dense plasma resisting the force of the lasers. Thus, a capsule with a lot of mix cannot be squeezed down to the high fuel density and temperature that a clean capsule could. In addition, mix dilutes the fuel, so that within the 100 trillionths of a second or so that the burn takes place, fewer of the interparticle collisions are between the fuel nuclei, so

the burn gives less yield. For these reasons (i.e., radiating away the energy needed for heating, interfering with compression, and diluting fuel), mix diminishes the amount of energy we get from ICF implosions. To obtain a practical energy source to replace fossil fuels, the fusion reaction must produce enough energy beyond what is required to power the lasers used to implode the fuel capsules so that the scheme will be economically attractive. Mix diminishes energy output, so it's an important part of the economic equation.

RESEARCH HIGHLIGHT PHYSICS DIVISION

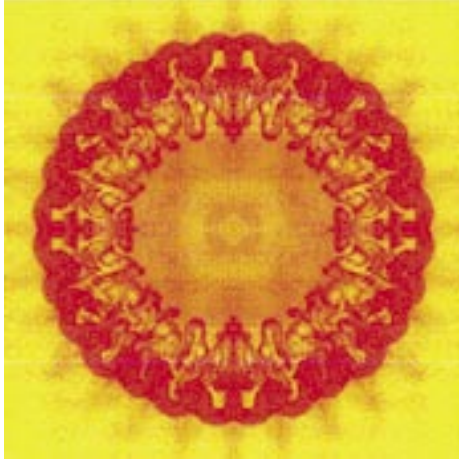


Figure 2. A supercomputer calculation of turbulent mix in an ICF capsule. The shell material is shown in red; the yellow in the center depicts the fuel. Turbulence develops during the implosion under the influence of hydrodynamic instabilities.

Mix occurs in ordinary states of matter (liquids or gases) because the molecules or atoms are in ceaseless random movement. The nuclei and electrons that comprise a plasma are in violently agitated motion with the particles traveling long distances without colliding. Thus, mix produced by random motion is greatly enhanced. Unfortunately, this component is only a miniscule part of the problem. Figure 2 depicts the results of a supercomputer simulation at a point in time midway during an ICF implosion (not necessarily our particular experiment). Turbulence develops as the capsule converges under the pressure from the lasers. Anyone who has dropped food coloring into water has seen these turbulent swirls and eddies. Similar behavior can be seen in the smoke from a smokestack or in a pot of boiling water. In ICF, the growth of turbulence is much more virulent, because the interface between a lighter material and a heavier material that accelerates it is inherently unstable. Many theories exist that attempt to model this turbulence behavior. They are difficult to verify in the ICF regime because present diagnostics cannot see the individual swirls looking through the edge of the spherical capsule, which is less than a millimeter in diameter.

Thus, while it is probably not possible to eliminate mix entirely, it is crucial to understand it. This understanding will enable us to mitigate the problem as much as we can and also to direct future research based on correct predictions.

P-24 Implosion Experiments Capture Images of Mix

Recent experiments performed by P-24 with collaborators from Applied Physics Division use a thin layer of titanium on the inside surface of a capsule (Figure 1) to image mix in the x-ray region. Titanium (22 electrons per atom) is used as the tracer element because it typically keeps at least one electron throughout the implosion, even at the core. Therefore, it still radiates efficiently at these high temperatures. The distribution of different “colors” of x-ray emission depends on the density and temperature in whatever local vicinity the titanium atoms find themselves.

Even if we cannot image the individual eddies, our results can still be used to reject models that do not match the energy distribution of the titanium emission versus radius and time.

Figure 3. Time history of the implosion. Time increases from right to left along a row, then from top to bottom. The circular images in the top two rows show the implosion of the 860 μm diam capsule during the time when the driving laser is on. Sixty laser beams with 22 million million watts (terawatts) of power produce an irradiance of a PW/cm^2 (a petawatt or a thousand million million watts per square centimeter) during a pulse lasting a billionth of a second. For comparison, the irradiance of the sun on the earth is $0.1 \text{ W}/\text{cm}^2$. The capsule is big enough in the beginning that the images for successive times overlap. The third row shows the inertial phase—the lasers are no longer on, but the capsule continues to implode. The fuel is ultimately compressed to 138 times its original density. Nuclear burn of the fuel begins 2200 ps after the start of the laser pulse. The last row shows an outgoing shock wave interacting with the still imploding outer part of the shell.

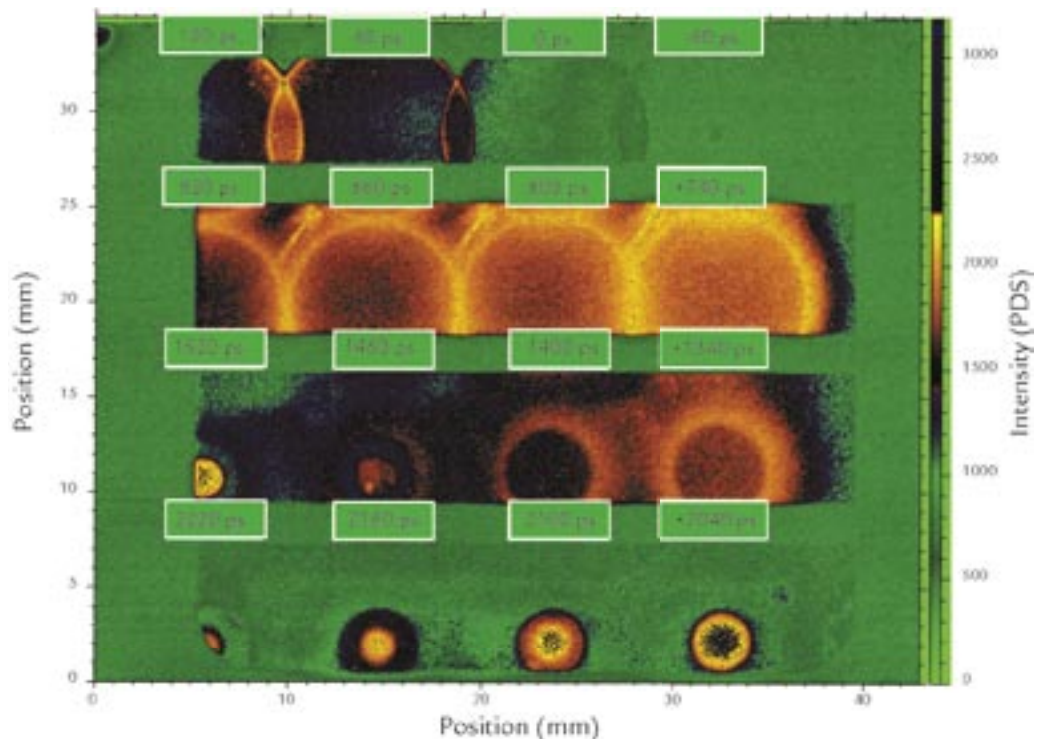
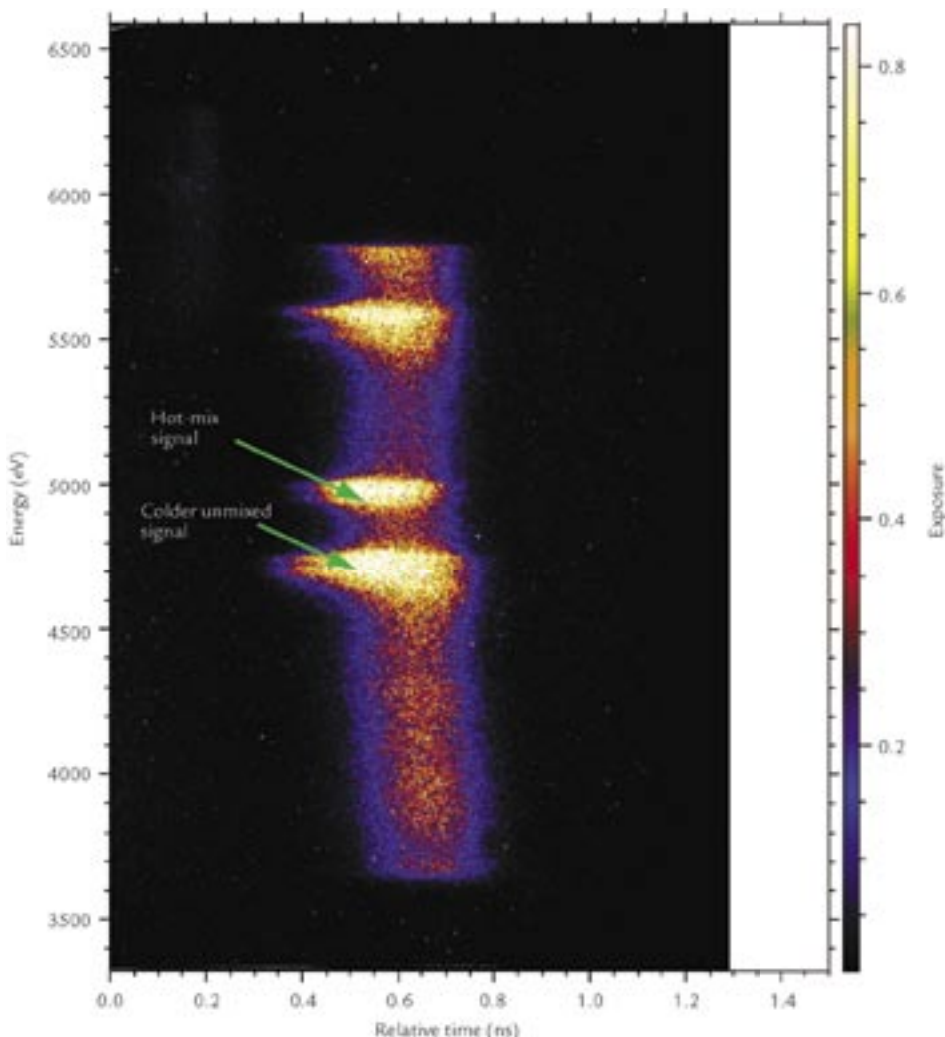


Figure 4. This time-dependent spectrum obtained in an experiment at the Omega laser facility shows the history of mixing of titanium from the shell during an implosion. Time is along the horizontal axis; x-ray radiation from the implosion is spread out along the vertical axis by a diffracting crystal, which disperses the x-rays according to their energy. Color on this plot is used to indicate the relative intensity (exposure) at each energy. The bright narrow band at ~ 5000 eV is the hydrogen-like titanium alpha line, and the helium-like line appears at ~ 4700 eV. The ratio of the signals in these lines changes as the titanium makes its way into the hot center.

Figure 3 shows x-ray framing camera images from our experiments. A framing camera produces a “movie” of the implosion, much like a movie camera produces a reel of film. However, in a framing camera, the film remains motionless, and the sensitive area that forms an image at any instant is determined electronically. The earliest picture is at the top right. As time progresses, the picture moves to the left and then down to the right edge of the next row. The time interval between two successive pictures is 60 ps, which corresponds to 17 thousand million frames per second. These images show the implosion, stagnation, and explosion of a capsule. The titanium shows up as brighter areas on the film. The interpretation is not simple because of the propagation of shocks. The increased noise on the film at stagnation is due to neutrons produced by the burn.

The time-resolved emission spectrum shown in Figure 4 is produced by a flat crystal located in front of a streak camera. From top to bottom, the radiation is separated by energy, or “color.” This is similar to the bands of colored light seen on a compact disc as it is tilted away from a light source. In our experiments, the different “colors” of light represent actual x-rays of different energies; therefore, a crystal is used to spread out the different energies. From left to right, the image



is swept in time. The camera puts the information onto an electron beam, which makes a picture from left to right in the same way that a television screen does. This image enables us to calculate the ratio of the titanium hydrogen-like alpha line (i.e., a transition from the second lowest atomic shell to the innermost shell when the electron making the transition is the last remaining one) to titanium helium-like alpha (i.e., the same transition when the atom still has one other electron that does not participate). The ratio of emission amplitudes in the two x-ray lines is important because the line from the hydrogen-like atoms is radiated only from the hottest part of the core. The ratio as a function of time allows us to watch the mixed material migrating into the center.

Conclusion

Our experimental series has just begun, so we are only beginning to interpret the implications for mix. We plan to carry these experiments further to measure not only where the mix occurs but also how much material is mixed into the fuel. We will use a series of capsules with the titanium layer buried successively deeper from the inside surface of the plastic. At the point in this series at which we no longer see a titanium signal, we will know that the thickness of the layer participating in mix is less than the burial depth. We continue to formulate refinements in the design of these exciting experiments.

Plasma Physics Research Highlights

Suggestions for Further Reading

1. D.K. Bradley *et al.*, “Measurements of core and pusher conditions in surrogate capsule implosions on the OMEGA laser system,” *Physics of Plasmas* **5**, 1870–1879 (1998).
2. D.D. Meyerhofer *et al.*, “Inferences of mix in direct-drive spherical implosions with high uniformity,” *Plasma Physics and Controlled Fusion* **43**, A277–A286 (2001).
3. V.A. Smalyuk *et al.*, “Hydrodynamic growth of shell modulations in the deceleration phase of spherical direct-drive implosions,” *Physics of Plasmas* **10**, 1861–1866 (2003).
4. S.P. Regan *et al.*, “Shell mix in the compressed core of spherical implosions,” *Physical Review Letters* **89**, 085003-1–085003-4 (2002).
5. M. Gunderson *et al.*, “Utilizing emission spectroscopy to study time-dependent mix,” European Conference on Laser Interaction with Matter, Los Alamos National Laboratory report LA-UR-04-6088.

Acknowledgment

This work was performed at LANL under the auspices of the U.S. DOE under contract No. W-7405-Eng-36. Experiments were performed on the Omega laser at the Laboratory for Laser Energetics (University of Rochester). General Atomics fabricated our capsules.

For further information, contact George Kyrala, 505-667-7649, gak@lanl.gov.



The World's Greatest Science Protecting America

Los Alamos National Laboratory, an affirmative action/equal opportunity employer, is operated by the University of California for the U.S. Department of Energy under contract W-7405-ENG-36.



Beryllium Ablator Microstructure and Stability Experiments

J.A. Cobble, T.E. Tierney, D.C. Swift (P-24), N.M. Hoffman, D.L. Tubbs (X-1),
A. Nobile, R.D. Day (MST-7)

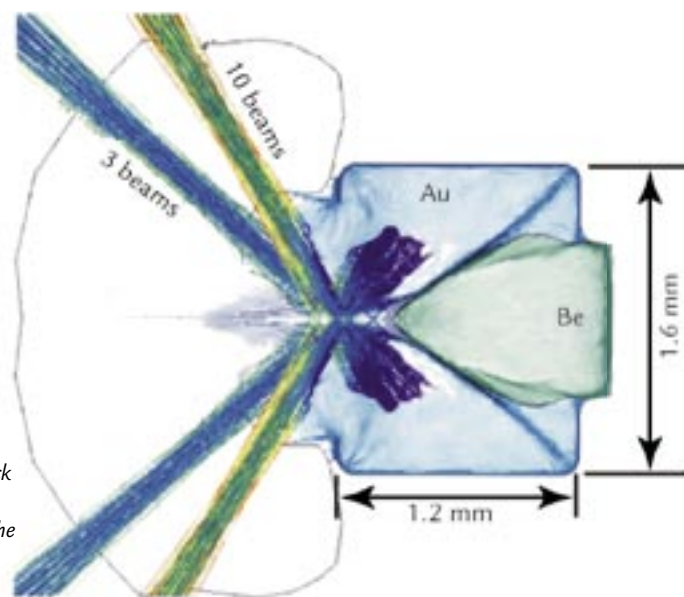
Controlled fusion in the laboratory remains the unfulfilled grand challenge of the nuclear age.

Fusion ignition of an inertially confined fuel capsule is a demanding task.¹ As in building a fire, the first task is assembling the fuel mass; however, for inertial-confinement fusion (ICF), this is extremely more difficult than collecting firewood.

The fusion fuel must be compressed to a density of $\sim 400 \text{ g/cm}^3$, which is over 30 times the density of solid lead and must be maintained at this density while its temperature is raised to over 200,000,000 K. Fuel assembly begins with as high a density fuel as possible—in this case, a thin shell of cryogenic deuterium-tritium (DT) ice at $\sim 18 \text{ K}$. The surface of the shell, both inside and outside, must be smooth to $\sim 1 \text{ }\mu\text{m}$,² and the radiation drive, which compresses the fuel, must be uniform to better than 1%.¹ These specifications are necessary to prevent hydrodynamic instabilities, which, while the irradiated capsule wall is compressing the fuel within, can rip the wall apart, release the fuel, and mix wall material with the fuel that remains in the core at the central hot spot. Only the highest quality compression will result in the density and the temperature of fuel necessary for ignition.

The first ablator material to be considered for the capsule wall was plastic. However, the technical hurdles to be overcome to field a plastic shell containing cryogenic DT ice are immense and the cost is prohibitive ($\sim \$150$ million). An alternate to plastic, beryllium has higher density, which leads to shorter laser drive for ignition; lower opacity, which leads to a higher implosion velocity; higher tensile

Figure 1. A gold vacuum hohlraum with laser beams entering from the left. The 800 μm diam beryllium package is centered on the back wall to the right. Gold and beryllium plasmas are filling the target.



strength, which allows a DT-filled capsule to be handled at room temperature; and higher thermal conductivity, which also relaxes cryogenic requirements.² However, crystalline beryllium, a naturally anisotropic material, supports different sound speeds depending on the direction of propagation. As long as a beryllium wall remains in the solid state during compression for fuel assembly, velocity shear at the beryllium-DT interface could lead to unfavorable hydrodynamic effects, primarily the classical Rayleigh-Taylor (RT) instability.³ Physics Division

and Applied Physics Division are collaborating in experiments to determine the magnitude of this potential problem. Meanwhile, Material Science and Technology Division is working to reduce the size of beryllium grains so that the number of grains in the wall with random orientation smoothes the effect of non-uniform velocity fields. Eventually during the radiation drive, the shock heating of the beryllium will cause melt. Then, the question becomes whether the material retains sufficient memory of RT behavior to spoil the compression.

RESEARCH HIGHLIGHT

PHYSICS DIVISION

Plasma Physics Research Highlights

For ignition at the National Ignition Facility (NIF), the early-time radiation pressure on the beryllium capsule will be 1–2 Mbar, exactly in the region for beryllium melt. Thus, experimental verification of beryllium behavior under various drive conditions is important to the success of future ignition experiments at NIF. We are therefore conducting beryllium ablator microstructure and stability experiments at the University of Rochester's Omega laser. Our main objective is to measure RT-instability growth rates in beryllium, first in machined sinusoidal perturbations and then from individual grains of various preselected sizes with “face-on” x-ray radiography. RT-instability growth is to be stimulated by laser-driven radiation in a gold vacuum hohlraum for as many growth times as needed to achieve detectability. We adopted the preliminary goals of

- (1) fabrication, utilization, and characterization of a relatively long (~ 6 ns) Omega pulse shape (to enhance RT-instability growth),
- (2) characterization of the hohlraum x-ray radiation drive to verify our ability to produce a first shock of ~ 1 Mbar pressure,
- (3) an assessment of the rate of influx of gold from the hohlraum wall during the drive, and
- (4) acquisition of face-on x-ray radiographs to assess requirements for effective diagnoses.

Experimental Rational and Results

Omega experiments typically last from 0.5–3 ns, which is insufficient time to detect microstructure-induced RT-instability growth in the beryllium. However, the longer the laser pulse, the less energy that can be extracted because of conversion efficiency problems in generating the 351 nm laser light at Omega. Our aim was to stagger two separate laser pulse shapes to integrate the longer drive within our targets.⁴

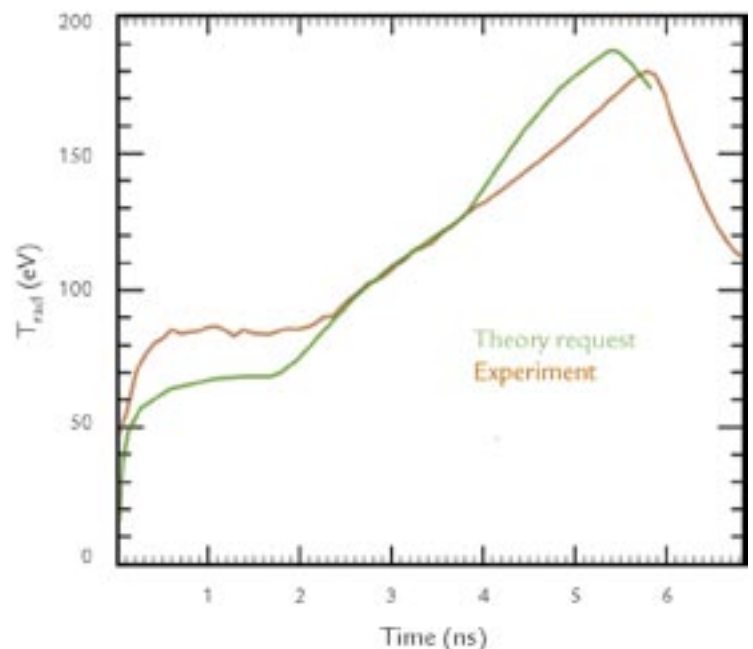
Then, after applying the appropriate laser drive to the hohlraum, we had to determine whether the measured radiation temperature, T_{rad} , and pressure, which drive the instability growth in the beryllium, matched theoretical predictions. Given the pulse length for heating the target, gold blowing in from the wall has sufficient time to stagnate on the hohlraum axis, blocking the later-arriving x-ray backlighter beam and hiding details of the RT-instability growth in beryllium, which has a much lower opacity than the gold. However, theoretical considerations suggest that radiation heating of the beryllium sample in the hohlraum could form a hot beryllium plasma bubble, putting pressure on the gold plasma and inhibiting its influx. Therefore, our final task was to qualify the ability of the vacuum hohlraum to maintain high visibility of the beryllium package within for face-on radiography.

Following initial laser profile design, we worked with Omega personnel to create two pulse shapes that when combined produced the desired ~ 6 ns laser drive. The integrated pulse consists of three beams carrying the “foot” of the drive for > 3 ns followed by ten 2.5 ns triangular-shaped beams, which carry

the bulk of the energy into the hohlraum. The timing of the foot drive and the triangular drive must be exact to within tens of picoseconds to maintain a smooth transition between the two sets of laser beams, which are symmetrically placed in azimuth around the wall of the hohlraum. Figure 1 indicates the placement of the laser pulses into the hohlraum target with a prediction, arising from a hydrodynamic model, for the position of the beryllium bubble with the application of over 4 kJ of laser energy.

T_{rad} was monitored by Dante, a ten-channel, filtered-x-ray-diode array.⁵ The results were consistent from shot to shot and are illustrated in Figure 2 with the desired radiation drive. Although it appears that T_{rad} is too high initially, the Dante measurement is increasingly less reliable below ~ 100 eV. For that reason, we also employed VISAR, a velocity interferometry system for any reflector⁶, to measure the free surface velocity of the beryllium sample, the shock-break-out time, and the radiation pressure. The ongoing VISAR analysis shows that during the first 3 ns, the radiation pressure is indeed about 1 Mbar.

Figure 2. Comparison of requested and measured T_{rad}



A gated x-ray framing camera (XRFC) filtered for gold M-band emission at 2.5 keV was used to monitor influx of gold from the hohlraum walls over the course of the radiation drive. Axial images in Figure 3 show the radial progress of the gold. During the third nanosecond of drive (at 10.5 mm on the y axis of Figure 3), the slowest component of the gold has moved $\sim 300 \mu\text{m}$ at a speed of $\sim 3 \times 10^7 \text{ cm/s}$. The fastest gold ions already appear to have stagnated on axis by 4 ns into the drive as shown by the black dot in the centers of the images. By 5 ns, the gold emission from the laser entrance hole (LEH), where the crossing laser beams have highest intensity, is heavy and uniform.

To assess the face-on radiography, we placed a gated axial XRFC opposite the LEH to the right of the beryllium sample in Figure 1 and, using M-band radiation from the LEH, backlit the beryllium, which for the first experiments was machined with a sine wave having a $100 \mu\text{m}$ period and an amplitude of $2.5 \mu\text{m}$. Figure 4 shows images from a single strip line from the XRFC taken at 5 ns into the laser pulse. The RT-instability growth of the sinusoidal variations has grown to the threshold of visibility as seen in modulations of the exposure, and an underexposed region near the hohlraum axis is revealed. Through analysis of parallax from the adjacent pinholes on the strip line, the center of mass of this quasi-opaque region is found to be one-quarter of the way back from the LEH—at exactly the position on axis where gold is not illuminated by laser beams. This observation provides evidence for an extensive beryllium bubble blowing out from the beryllium sinusoid, but which unfortunately does not reach far enough forward to prevent gold from obscuring the view.

Future directions

In the 20 laser shots for this campaign to date, we have learned that we can join different laser pulses together in a hohlraum to create a smoothly varying 6 ns radiation drive to study RT-instability growth in beryllium samples. Our first

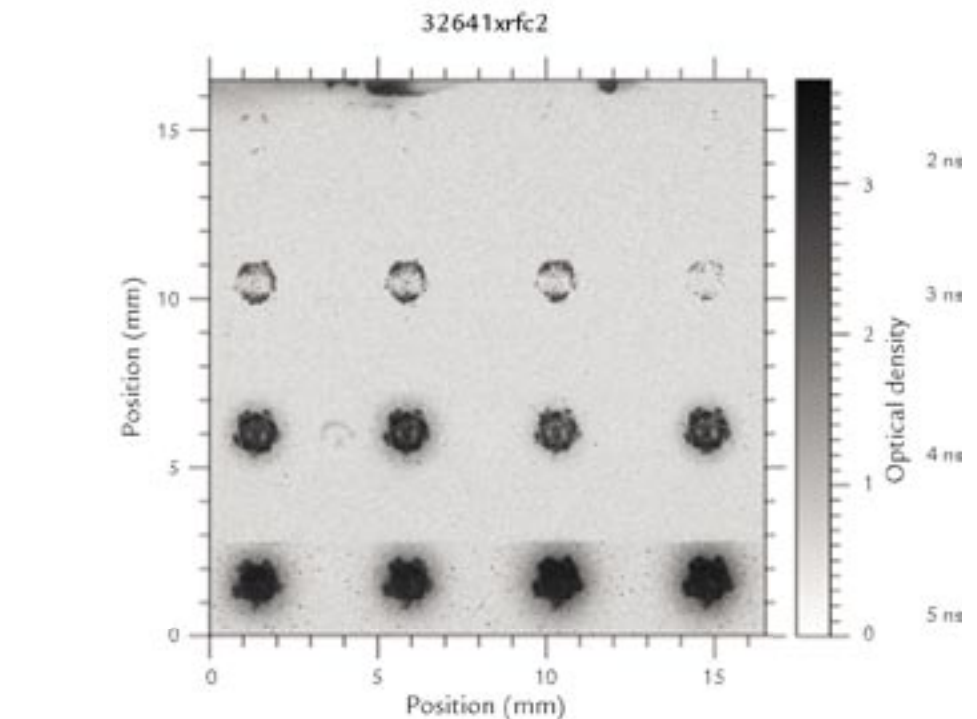


Figure 3. Gated XRFC images indicate the quasi-three-fold symmetry of the foot drive at 2 and 3 ns. (The time for each strip line of the imager is at the right in the figure. Time increases at $\sim 2 \text{ pt } 2 \pi \times 60 \text{ ps/frame}$, right to left.) The ten triangular-drive beams are paired, yielding quasi-five-fold symmetry later in time. These ten “turn on” at 3.5 ns.

effort has apparently resulted in a 1 Mbar drive, as measure by VISAR, which Dante confirms reaches $\sim 180 \text{ eV}$ at its peak, as required by theoretical demands. However, we have measured the influx of gold in a vacuum hohlraum and find that it is a threat to successful radiography. X-ray backlighting of sinusoidally perturbed beryllium samples has produced evidence

of RT-instability growth and of the presence of the beryllium bubble, which only partially inhibits gold plasma from encroaching into the center of the target. In the future, we hope to solve the gold influx problem with gas-filled targets, for instance, with 1 atm of CH_4 . Issues surrounding the gas-filled targets include the drive penalty for heating the gas—as

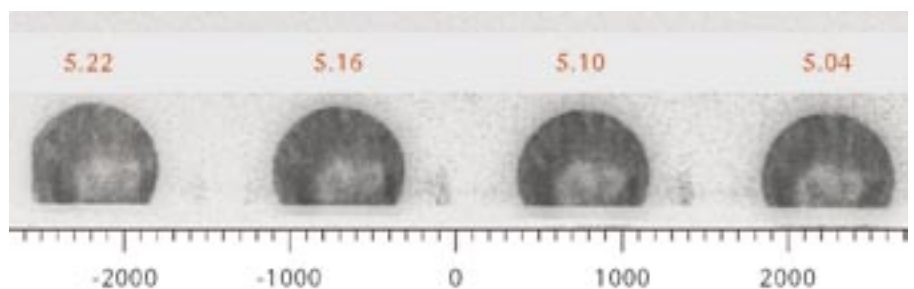


Figure 4. The 5 ns strip of the XRFC images for Omega shot No. 32652 shows the $100 \mu\text{m}$ sine wave in the beryllium sample and a region of quasi-opacity ($\sim 12\%$ transmission) shifting from frame to frame because of parallax. Gating times (ns) are in red; displacement (μm) is in object plane units.

Plasma Physics Research Highlights

much as a few hundred J—and possible laser-plasma instabilities. The latter may cause backscatter of 10% or more of the laser light away from the target. A drop in T_{rad} of ~ 10 eV is expected. The overall pulse duration might need to be shortened to boost the laser energy available for the required drive. Hopefully, laser energy will be available to evaluate a pulse shape for a 2 Mbar drive. We are encouraged that an Omega hohlraum environment can be created to validate beryllium as the material of choice for NIF ignition experiments.

Experiments at the Trident Laser Facility

Related laser-ablation experiments have been performed at the Trident Laser Facility at LANL to measure the strength of beryllium on a nanosecond time scale. The elastic and plastic response was monitored with VISAR from the sample surface and by *in situ* x-ray diffraction from the shocked beryllium. The effective strength was several times greater than that on the previously explored microsecond scales. These experiments also allow us to measure spatial variations in response caused by the microstructure of the material. Together with the Omega results, we are obtaining the detailed understanding of beryllium properties needed to set requirements for indirect-drive ignition experiments on NIF.

References

1. J. Lindl, “Development of the indirect-drive approach to inertial confinement fusion and the target physics basis for ignition and gain,” *Physics of Plasmas* **2**, 3933–4024 (1995).
2. D.C. Wilson *et al.*, “The development and advantages of beryllium capsules for the National Ignition Facility,” *Physics of Plasmas* **5**, 1953–1959 (1998).
3. N.M. Hoffman *et al.*, “Microstructure, shock waves, and stability: The initiator of mixing?” *Bulletin of the American Physical Society* **48**(7), 255 (2003).
4. D.L. Tubbs and N.M. Hoffman, “3- ω laser pulse shapes for July 2003 beryllium ablator microstructure and stability (BAMS) experiments at Omega,” LANL memo X-1: 2003-005, March 28, 2003.
5. H.N. Kornblum *et al.*, “Measurement of 0.1–3 keV x-rays from laser plasmas,” *Review of Scientific Instruments* **57**, 2179–2181 (1986).
6. D.L. Paisley *et al.*, “High-speed optical and x-ray methods for evaluating laser-generated shock waves in materials and the corresponding dynamic material response,” *Proceedings of the International Society of Optical Engineering (SPIE)* **4183**, 556–565 (2001).

Acknowledgment

This work has been done under the auspices of the U.S. DOE. We acknowledge the expert assistance of many workers at the University of Rochester Laboratory for Laser Energetics, including resident staff from Lawrence Livermore National Laboratory.

For further information, contact James Cobble, 505-667-8290, cobble@lanl.gov.



The World's Greatest Science Protecting America

Los Alamos National Laboratory, an affirmative action/equal opportunity employer, is operated by the University of California for the U.S. Department of Energy under contract W-7405-ENG-36.



Ultra-High-Intensity Laser Physics at the LANL Trident Laser Facility

B.M. Hegelich, J.C. Fernández, J.A. Cobble, K.A. Flippo (P-24), B.J. Albright, E.S. Dodd, M.J. Schmitt (X-1), R. Perea (MST-7)

Modern ultra-high-intensity lasers are able to reach focal intensities of the order of 10^{18} – 10^{21} W/cm² where laser-plasma interactions become relativistic, and a variety of new effects emerge into a completely new regime of physics. These processes include relativistic self-focusing of the laser beam, which results in even higher intensities, laser-induced particle acceleration to MeV energies on a μ m scale, x-ray lasers, laser-induced nuclear physics, and even the production of antimatter and other exotic particles. These effects can be applied to a variety of physics studies and can potentially be used for a number of applications. Concepts under consideration are next-generation accelerators, the jump-starting of inertial-confinement fusion with fast ignition, various medical applications, and laboratory astrophysics. One of the three beams of the Trident laser facility at LANL has been converted to deliver ultrashort laser pulses at the above-mentioned intensities so that researchers can participate in this exciting new field at the forefront of today's physics. This beam is used to carry out a program that investigates the acceleration of ion bunches to MeV energies and MA currents and the interaction of these ions with different targets.

High-Irradiance Laser-Matter Interactions

An ultra-high-intensity laser pulse pointed at a solid target always interacts with a plasma because of its finite contrast ratio. Even in a laser with a relatively excellent contrast of $\sim 10^{-7}$ there will be a “pre-

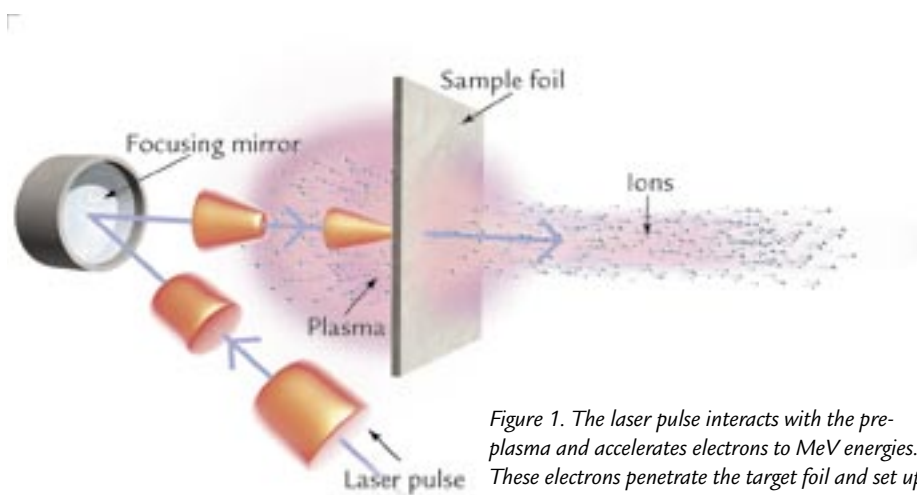


Figure 1. The laser pulse interacts with the pre-plasma and accelerates electrons to MeV energies. These electrons penetrate the target foil and set up an MV/ μ m quasi-static electric field that ionizes and accelerates the rear surface atoms.

pulse” at 1–2 ns ahead of the main pulse with an intensity above 10^{12} W/cm², which is high enough to instantly create a plasma. The main pulse will therefore always interact with a plasma and never with a solid target. Furthermore, at these intensities, the laser-plasma interaction is relativistic, i.e., the electrons gain energy on the order of their rest mass when moving in the electro-magnetic field of the laser pulse. The laser transfers energy to the electrons and accelerates them in the laser-propagation direction through the target to multi-MeV energies. This process is due to the $\mathbf{v} \times \mathbf{B}$ force from the magnetic component of the electromagnetic

field, which becomes nonnegligible when v approaches the speed of light. As illustrated in Figure 1, the electrons will penetrate a thin foil target, exit out the back surface, and set up a virtual cathode—a very strong electric field, exceeding field strengths of a few 10^{12} V/m (TV/m).

The electric field ionizes the rear surface and accelerates whatever ions are situated there to energies of many MeV. Protons have been accelerated to more than 60 MeV,¹ fluorine ions to above 100 MeV,² and lately high-Z palladium ions to 220 MeV.^{3,4} In many beam parameters, those ion pulses now exceed those of

RESEARCH HIGHLIGHT PHYSICS DIVISION

conventionally accelerated ions by orders of magnitude, exhibiting pulse durations in the subpicosecond range, beam currents up to MA, and a transverse emittance $\epsilon_t < 0.001 \pi \text{ mm mrad}$.⁵ A typical conventional accelerator like the CERN Super Proton Synchrotron (SPS) has an emittance of $\epsilon_t < 1 \pi \text{ mm mrad}$. These parameters have rekindled interest in laser-accelerated ion beams for applications like proton radiography⁶, isochoric heating⁷, fast ignition⁸, and next-generation accelerators. The major difficulty for all these applications to date has been the large energy spread of the laser-accelerated ions, which typically exhibit a Maxwellian-like energy spectrum as shown in Figure 2. At LANL, we have demonstrated for the first time that quasi-monoenergetic ion beams can be generated by controlled target treatment before irradiating the metal foil target with an ultra-high-intensity laser. Furthermore, we also show the acceleration of a single charge state

of one ion species directly in the forward target-normal direction. The accelerated C^{5+} ion bunch shown in Figure 3 exhibits a longitudinal emittance of $\epsilon_l < 2 \times 10^{-6} \pi \text{ eV s}$, exceeding that of conventional high-current accelerators by orders of magnitude. This new result shows the strong potential impact that ultra-high-intensity laser physics can have in many other areas of physics.

Accelerated Ions

Due to the vacuum conditions in ultra-high-intensity laser experiments, which typically are around 10^{-6} mbar, all target surfaces are coated with water vapor and hydrocarbon layers, e.g., pump oil. That means that no matter what target material is used, the outer layer always contains protons. Because of its low ionization potential and because protons exceed every other ion's charge-to-mass ratio by at least a factor of two, they are more efficiently produced and accelerated, drain the energy out of the acceleration process, and screen the accelerating electric field for the heavier particles. Accelerating other ions therefore requires the removal of the contaminating proton layers. This removal was demonstrated by Hegelich *et al.*² using the 100 TW laser at the École Polytechnique LULI research center with carbon and fluorine ions. To achieve our goal of mid- to high-Z ion acceleration at LANL's Trident laser facility, we implemented the same kind of cleaning techniques in our ultra-high-intensity laser experiments. Trident delivers pulses of up to 30 J in as short as 600 fs, which corresponds to a power of $\sim 30 \text{ TW}$. As such, Trident is currently the highest-energy subpicosecond laser in the U.S. The beam is aimed at an off-axis parabolic mirror within a vacuum chamber to focus the beam from its initial diameter of 6 in. down to a $20 \mu\text{m}$ spot on the target, achieving intensities in excess of 10^{19} W/cm^2 . A sketch of a typical setup is shown in Figure 4.

To clean the target, we rely on two methods: Joule heating using either a strong direct current that is passed through

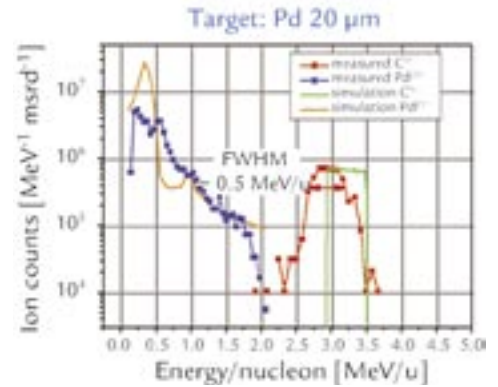


Figure 3. Measured ion energy spectra and simulations using BILBO.

the foil or a continuous-wave (cw) laser. Both methods are capable of heating the target to temperatures in excess of 1000°C , which remove all hydrogen-bearing contaminants. With no hydrogen present, remaining species on the rear surface are ionized by the electric field. The charge state with the highest charge-to-mass ratio is predominantly accelerated. Experiments on the LULI 100 TW laser and on the Trident laser successfully accelerated a wide range of low-Z ions to multi-MeV/nucleon energies. Figure 2(a) shows the spectra for helium-like beryllium, carbon, oxygen, and fluorine.

Moving from low-Z ions to mid- or high-Z ions proves to be more difficult. Although contaminants like water vapor can be cooked off by heating the target, heating cannot clean metal oxides, carbides, and nitrides on the surface—these contaminants usually have binding energies in the eV range. To overcome this problem we are working on two different approaches. The first approach is to use a second pulsed laser at relatively low intensity ($\sim 5 \times 10^{10} \text{ W/cm}^2$) to ablate the rear surface thus removing the contaminating oxides, etc. Although this approach worked in principle, the technical details are tricky and remain a subject of ongoing study. The second approach is to use a “magic” material that does not form oxides or other compounds. This approach is the easier solution, however, it limits the available target

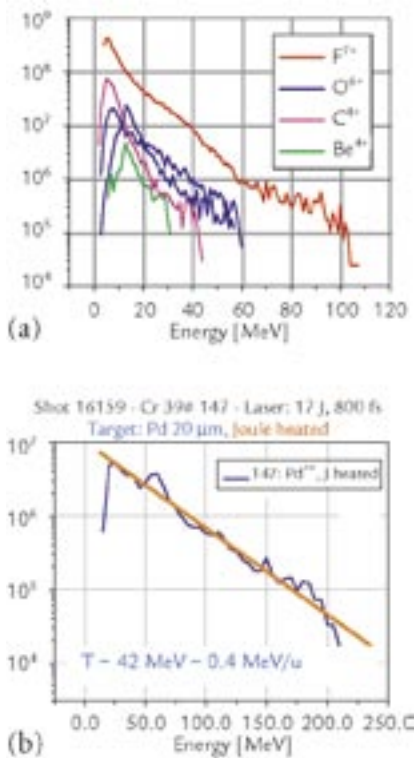


Figure 2. (a) Typical low-Z ion spectra from both the LULI 100 TW laser and Trident. (b) First mid-Z ion spectra [palladium(22^+), $Z = 46$] from Trident.

materials. One such “magic” material is palladium. With an atomic mass of 106, palladium ($Z = 46$) does not easily form oxides. As shown in Figure 2(b), we succeeded for the first time to accelerate a mid- Z material into a multi-MeV/ nucleon-ion bunch using an ultra-high-intensity laser. In future experiments, we hope to improve this result, increasing the energy and the particle number and achieving greater control of the beam properties, e.g., ballistic focusing as shown in Figure 3. Once these goals are achieved, the palladium beam can be used to study isochoric heating in matter, effectively recreating in the laboratory conditions that are otherwise only found in the interior of large Jovian-like planets.

Monoenergetic Ions and Modeling

As mentioned earlier, we were the first to accelerate a monoenergetic MeV-ion bunch with a laser. When heating the palladium target to remove the hydrogen, a thin monolayer layer of carbon atoms remained at the rear surface. Because these carbon layers are very localized, all carbon atoms see the same field at the peak of the

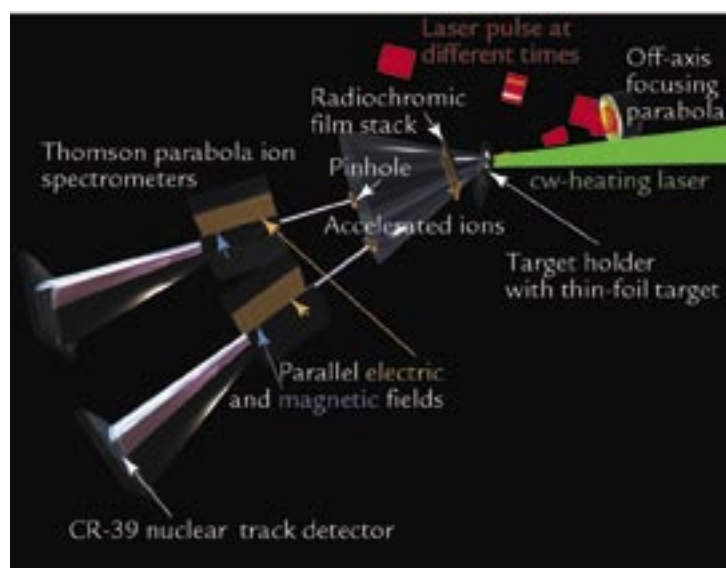


Figure 4. Typical setup of a laser-ion-acceleration experiment. The target is typically a $\sim 10 \mu\text{m}$ thin metal foil, the diagnostics consist of various films, track detectors, and spectrometers. A green cw laser is used to clean the target of hydrocarbon contaminants.

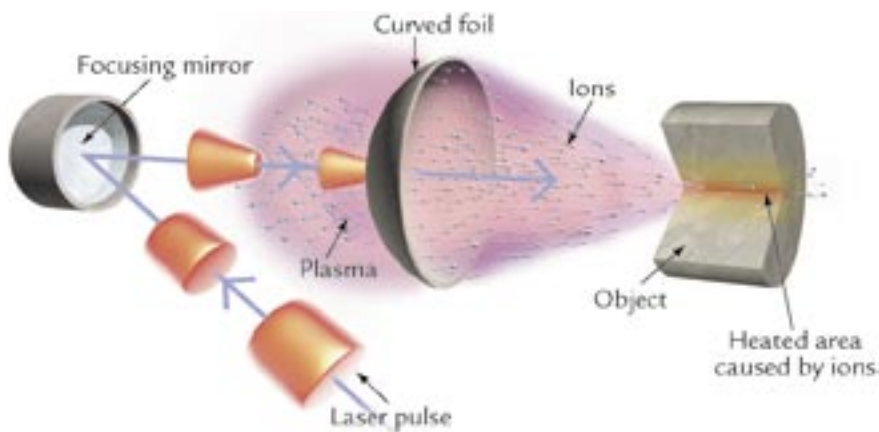


Figure 5. Ballistic focusing of a laser accelerated ion beam into a secondary target. The secondary target will be heated isochorically to high temperatures while remaining at high density, recreating conditions found in the core of Jovian-like planets.

pulse and are ionized to the same charge state and instantly accelerated. As the field decreases after ~ 100 fs, all the carbon atoms are at the front of the ion expansion, in a position trailing the hot electrons, which effectively conserves their volume in phase space. The full width half maximum of 0.5 MeV per nucleon in the Thomson parabola spectrum shows a longitudinal emittance of this C^{5+} bunch smaller than 2×10^{-6} eV seconds—about six orders of magnitude better than for the CERN SPS.

We have used the one-dimensional hybrid code BILBO (Backside Ion Lagrangian Blow-Off) to help us understand this result. BILBO solves a Vlasov-Maxwell system analytically, calculating the boundary conditions for a nonlinear Poisson solver. The solver yields the electron density

and electric fields and propagates the ions as kinetic particles. The code uses a threshold ionization model with atomic data for ionization energies of carbon and palladium and hot-electron-cooling models to account for the extraction of energy used to accelerate the ions. Using BILBO, we reproduced the measured spectra qualitatively (Figure 3) and seek to derive better models to understand and optimize beam production.

Conclusion

Future experiments will be directed towards better understanding of the underlying acceleration physics and towards the use of the accelerated ions for a number of different applications. Because of the modest integrated energy of the ions, they must be focused to one point, which can be achieved by using curved targets (Figure 5). The long-term goal of our project is to study transport and stopping mechanisms of high-current ion beams in cold, dense plasmas. These experiments require the use of Trident’s other beam lines to create the target plasma while the short-pulse beam generates the ion pulse. For these experiments and for other short-pulse physics applications, more energy in the short-pulse beam is desirable and in some cases even necessary. Therefore, the Trident

Plasma Physics Research Highlights

short-pulse arm will be upgraded over the next 18 months to deliver pulses of ~ 115 J in less than 500 fs. This 200 TW upgrade puts Physics Division even more firmly at the forefront of modern science and opens new opportunities for programmatic research. It keeps Trident among the best of the existing short-pulse lasers in the world and makes even more exotic new physics accessible.

References

1. R.A. Snavely *et al.*, "Intense high-energy proton beams from petawatt-laser irradiation of solids," *Physical Review Letters* **85**, 2945–2948 (2000).
2. B.M. Hegelich *et al.*, "MeV ion jets from short-pulse-laser interaction with thin foils," *Physical Review Letters* **89**, 085002-1–085002-4 (2002); [For nanosecond-laser work, resistive Joule heating was successfully accomplished by W. Ehler *et al.*, "Effect of target purity on laser-produced plasma expansion," *Journal of Physics D: Applied Physics* **13**, L29–L32 (1980).]
3. B.M. Hegelich *et al.*, "Spectral properties of laser accelerated mid-Z MeV/u ion beams," in *Proceedings of the 28th European Conference on Laser Interaction with Matter*, Rome, September 6–10, 2004.
4. J.C. Fernández *et al.*, "Laser-ablation treatment of short-pulse laser targets: Towards an experimental program on energetic-ion interactions with dense plasmas," in *Proceedings of the 28th European Conference on Laser Interaction with Matter*, Rome, September 6–10, 2004.
5. T.E. Cowan *et al.*, "Ultralow emittance, multi-MeV proton beams from a laser virtual-cathode plasma accelerator," *Physical Review Letters* **92**, 204801-1–204801-4 (2004).
6. J.A. Cobble *et al.*, "High resolution laser-driven proton radiography," *Journal of Applied Physics* **92**, 1775–1779 (2002).
7. P.K. Patel *et al.*, "Isochoric heating of solid-density matter with an ultrafast proton beam," *Physical Review Letters* **91**, 123004-1–123004-1 (2003).
8. M. Roth *et al.*, "Fast ignition by intense laser-accelerated proton beams," *Physical Review Letters* **86**, 436–439 (2001).

Acknowledgment

This work has been performed under the auspices of the U.S. DOE. We acknowledge support from 2004 Laboratory-Directed Research and Development/ Directed Research Proposal 20040064 and experimental run time at Ecole Polytechnique, Paris, France.

For further information, contact Manuel Hegelich, 505-667-6989, hegelich@lanl.gov.



The World's Greatest Science Protecting America

Los Alamos National Laboratory, an affirmative action/equal opportunity employer, is operated by the University of California for the U.S. Department of Energy under contract W-7405-ENG-36.



Inertial-Electrostatic-Confinement Fusion Device

*J. Park, S.M. Stange (P-24), R.A. Nebel (T-15),
K.M. Subramanian (University of Wisconsin)*

Inertial-electrostatic-confinement (IEC) systems provide an economical and technologically straightforward means to produce fusion reactions in a table-top device.^{1,2} IEC devices confine a plasma in a potential well created by electrostatic fields or a combination of electrostatic and magnetic fields. The fields can be produced either by grids or by virtual cathodes, typically in spherical or cylindrical geometry. The fields accelerate ions towards the center of the device, where fusion reactions can occur (Figure 1). The technological simplicity of the IEC system was the basis for its early success—it produced a steady-state neutron yield of 2×10^{10} neutrons/s in the late 1960s.³

Applications

One of the most promising applications for an IEC-based neutron source is the active nuclear assay of highly enriched uranium and high explosives (HE), such as landmines. High-energy neutrons (e.g., 14.1 MeV neutrons from deuterium-tritium [DT] fusion reactions) have the ability to penetrate shielded materials very effectively. For example, Monte Carlo neutron and photon (MCNP) transport-code calculations indicate that 14.1 MeV neutrons can penetrate soil as deep as 1 m and detect HE, such as landmines. We are currently working with a private company to develop a compact and economical intense neutron source based on the IEC system. The enhanced-detection capability of the IEC-based neutron source, compared to natural radiation sources, could provide cutting-edge technology for homeland defense and humanitarian causes.

Periodically Oscillating Plasma Sphere

Though useful for practical neutron sources, the existing IEC fusion devices suffer low fusion yields, $\sim 0.01\%$ of input power. This is because the Coulomb-collision cross section is much greater than the fusion-collision cross section by several orders of magnitude. The ion beams in the IEC device rapidly lose the energy by Coulomb collisions before producing fusion reactions, leading to a net loss in energy.

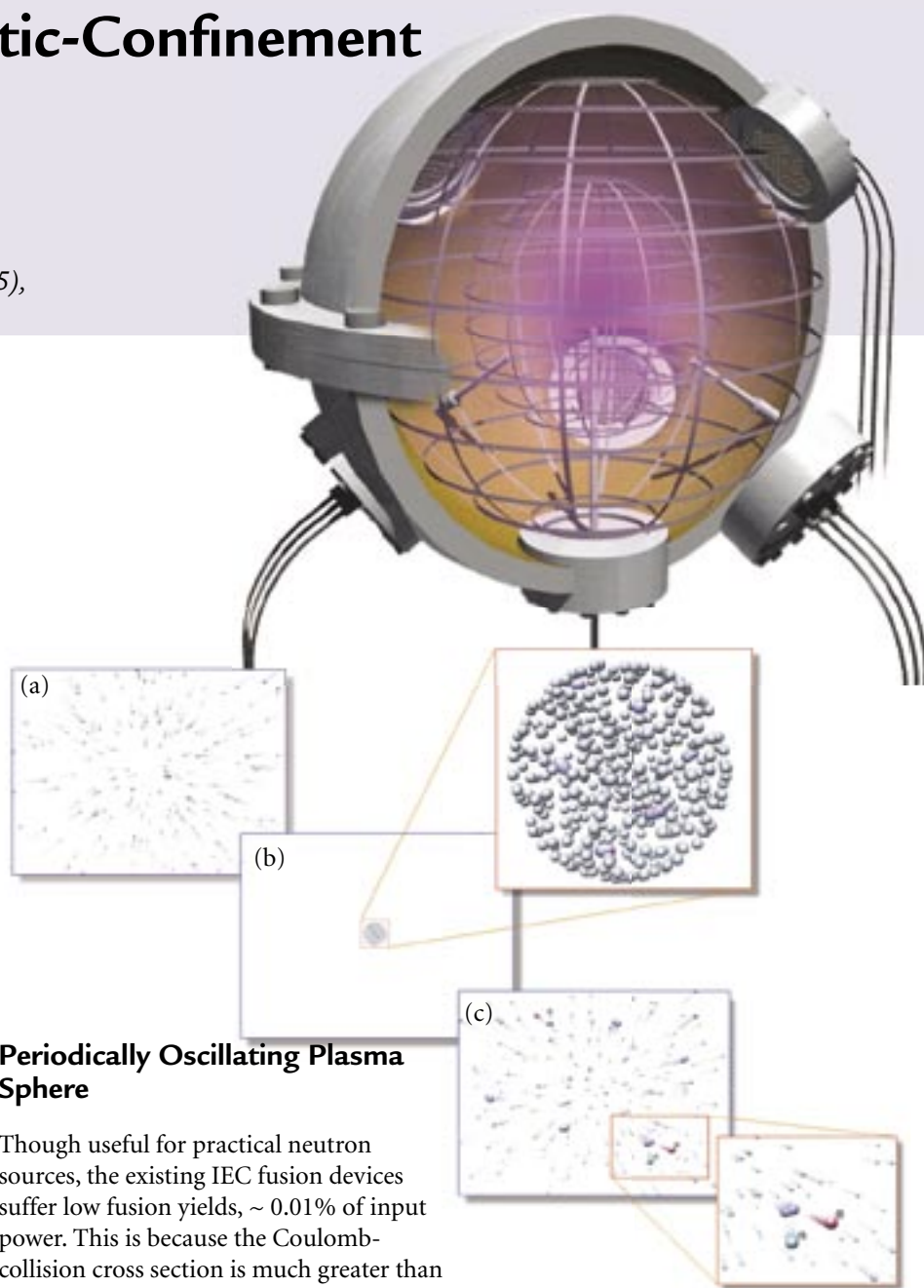


Figure 1. Grid-based IEC device. Fusion reaction occurs in the center region where the high-energy ions converge. The dynamics of a periodically oscillating plasma sphere (POPS) oscillation are shown as an (a) implosion, (b) compression, and (c) expansion.

RESEARCH HIGHLIGHT
PHYSICS DIVISION



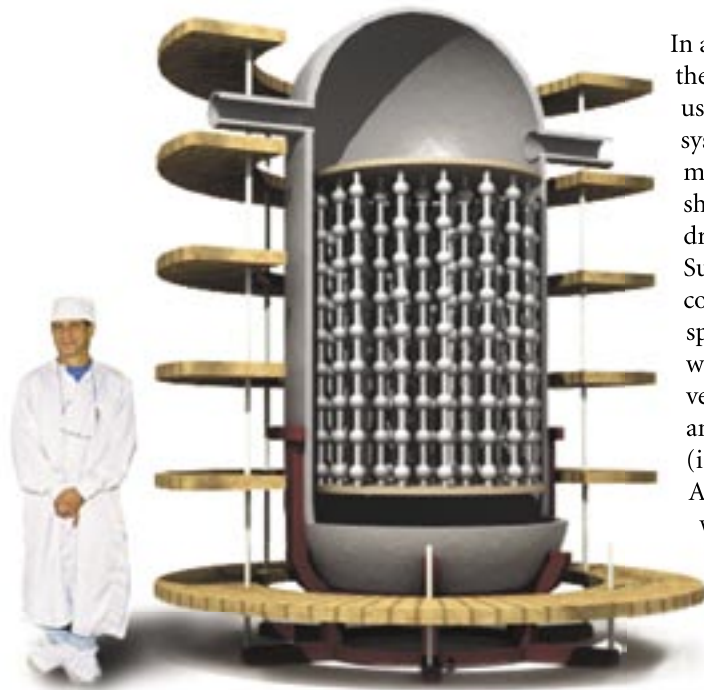


Figure 2. Penning trap modular IEC device for a high mass power density fusion reactor.

A new electrostatic plasma equilibrium that should mitigate this problem has been proposed by LANL theorists⁴ and recently confirmed experimentally.⁵ This concept requires uniform electron injection into the central region of a spherical device to produce harmonic oscillator potential. An ion cloud (referred to as the Periodically Oscillating Plasma Sphere, or POPS) in such an environment will undergo harmonic oscillation with an oscillation frequency independent of amplitude. Tuning the external radio-frequency (rf) electric fields to this naturally occurring mode allows the ion motions to be phase-locked. This simultaneously produces very high densities and temperatures during the collapse phase of the oscillation when all the ions converge into the center. Solutions to POPS oscillation have the remarkable property that they maintain equilibrium distribution of the ions at all times. This would eliminate any power loss due to Coulomb collisions and would greatly increase the neutron yield up to more than 100%, resulting in a net energy gain for fusion-power generation.

In a practical embodiment, the POPS system would use a massively modular system to achieve high-mass-power density as shown in the conceptual drawing in Figure 2. Such a device would contain thousands of tiny spherical IEC reactors within a single reactor vessel to produce a large amount of fusion power (i.e., $\sim 100\text{--}1000\text{ MW}$). A modular IEC device would have very high-mass-power density, comparable to a light-water reactor, while maintaining conventional wall loads ($\sim 1\text{ MW/m}^2$) and being economically competitive with other sources of power.

First Experimental Confirmation POPS Oscillation

The POPS oscillation has been experimentally measured for the first time, confirming the scientific basis for a POPS-based fusion device. The harmonic

potential well is created by electron injection.⁶ Ions in the potential well undergo harmonic oscillation. By applying rf fluctuation to the grid voltage, we were able to phase-lock the POPS oscillation and to measure the resonance behavior of the ions. Mathematically, ion dynamics during the driven POPS oscillation are equivalent to the driven harmonic oscillator as described by the Mathieu equations. The ions can gain a large amount of energy from a small external perturbation when the driving frequency is equal to the resonance frequency. The ion orbits become unstable, and ion loss from the potential well is enhanced. In the experimental setting, the enhanced ion loss compensates the background ionization and extends the lifetime of the potential well. On the other hand, rf fluctuation outside the POPS resonance frequency makes little impact to the ion loss. This resonance behavior of ion dynamics is shown in Figure 3, where the temporal variation of the plasma response is measured for various rf frequencies. Without rf fluctuation, the lifetime of the potential well is very short, $\sim 0.5\text{ ms}$, due to significant background ionization. By applying small rf fluctuation ($\sim 4\text{ V}$ amplitude compared to a direct-current [dc] bias voltage of 250 V) at POPS frequency, the lifetime increases greatly

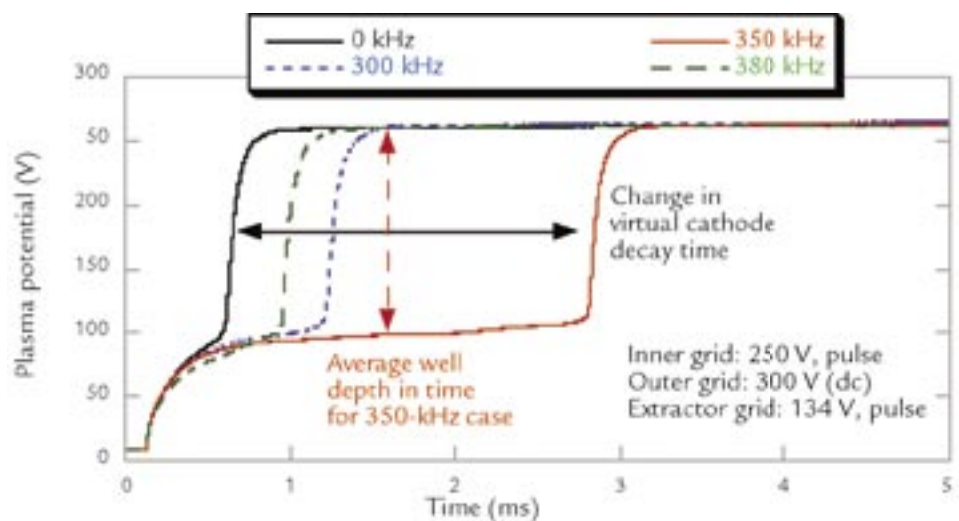


Figure 3. Temporal evolution of plasma potential at the center. The potential well lifetime is extended by applying rf fluctuation to the inner grid bias voltage at POPS frequency.

to ~ 2.5 ms. In comparison, rf fluctuation outside the resonance frequency changes the lifetime only slightly.

The frequency at which the POPS oscillation is found scales as $f_{POPS} = (\sqrt{2/\pi}) * (V_{well}/r_{well}^2 M_{ion})^{0.5}$. In using a harmonic-oscillator analogy, the ion mass provides the inertia, whereas the curvature of potential well is equal to the coefficient of the restoring force. Because this was the first time that the POPS oscillation has ever been experimentally observed, extensive efforts were made to verify the POPS frequency scaling as a function of the well depth and the ion mass. As shown in Figure 4, excellent agreement was obtained between the experiments and the theory, confirming that the observed resonance is the ion mode associated with the POPS oscillation. The potential well depth was controlled by varying the dc component of the inner-grid bias, whereas the well radius is fixed by the inner-grid dimension. Note that the well radius was estimated as $r_{well} = r_{grid} + \lambda_{Deff}$ where λ_{Deff} is the effective Debye length to account for the Debye shielding. We also varied the fill gas, using three different ion species, H_2^+ , He^+ , and Ne^+ to investigate the POPS frequency scaling.

Particle Simulation of POPS Plasma Compression

One of the most significant issues facing a fusion device based on POPS is the plasma compression, which determines the achievable fusion rates. In the case of deuterium-deuterium (DD) fuel, a radial plasma compression of 25 is sufficient for active nuclear assay, whereas the neutron tomography would require a compression of 100. In comparison, a practical fusion-power plant would require a compression of 2000 for DD fuel but less than 100 for DT fuel. One factor that greatly affects the compression ratio is the extent of space-charge neutralization. Inadequate space-charge neutralization can cause self-repulsion of the ion cloud during the collapse phase, limiting the compression.

A gridless particle code of one dimension in space and two dimensions in velocity space has been developed to investigate the space-charge neutralization during POPS compression.⁷ Figure 5 shows the radial profiles of ion density and plasma potential during POPS compression. The results in the left are from the expansion phase of POPS oscillation. The ion density profile is Gaussian in space, and the plasma potential profile matches the required harmonic oscillator potential for ions, produced by constant electron injection. In the middle, the ion density and the plasma potential during the collapsed phase of POPS oscillation are shown. A large distortion of plasma potential is due to the insufficient space-charge neutralization and ion self-repulsion during the POPS compression. This has limited the radial plasma compression to only 6.3. In comparison, the results on the right come from the case where we modulate the initial velocity distribution of injected electrons as a function of time to improve

the space-charge neutralization. This simple remedy helped to improve the space-charge neutralization in the core during the collapse phase. A radial plasma compression of 19 has been obtained, resulting in the ion-density enhancement of $\sim 10,000$ in the core as compared to the expansion phase. Currently, we are investigating a method, proposed by Louis Chacon (Plasma Theory Group, T-15), to correctly modify the injected electron distribution to eliminate the space-charge neutralization problem and to improve the plasma compression.

Conclusion

The IEC Team in our Plasma Physics Group (P-24) and T-15 is working on developing practical fusion devices based on an IEC scheme. The recent experimental confirmation of the POPS oscillation and successful plasma compression in a particle simulation has provided solid scientific foundation for

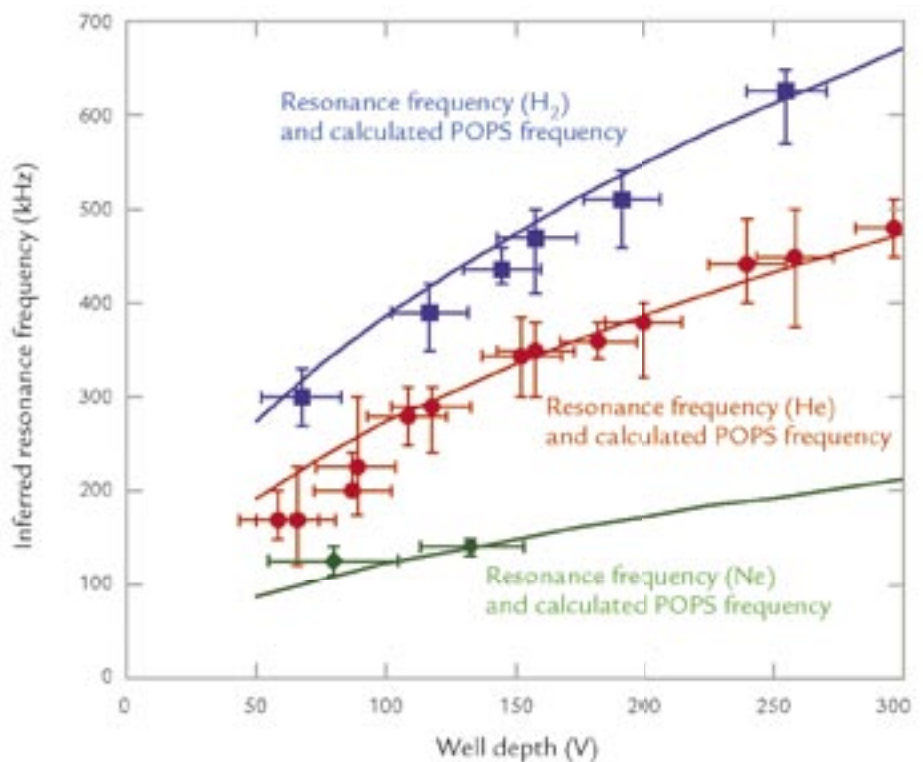


Figure 4. Comparison between the experimentally measured resonance frequencies due to POPS oscillation (points) and the theoretical calculations (lines) as a function of potential well depth and ion mass.

Plasma Physics Research Highlights

further exploration of this promising fusion device concept. This exploration will include direct experimental measurement of plasma compression and fully two-dimensional particle simulations of POPS dynamics. Successful plasma compression of at least 50 will be followed by a demonstration of nuclear fusion reactions using POPS.

References

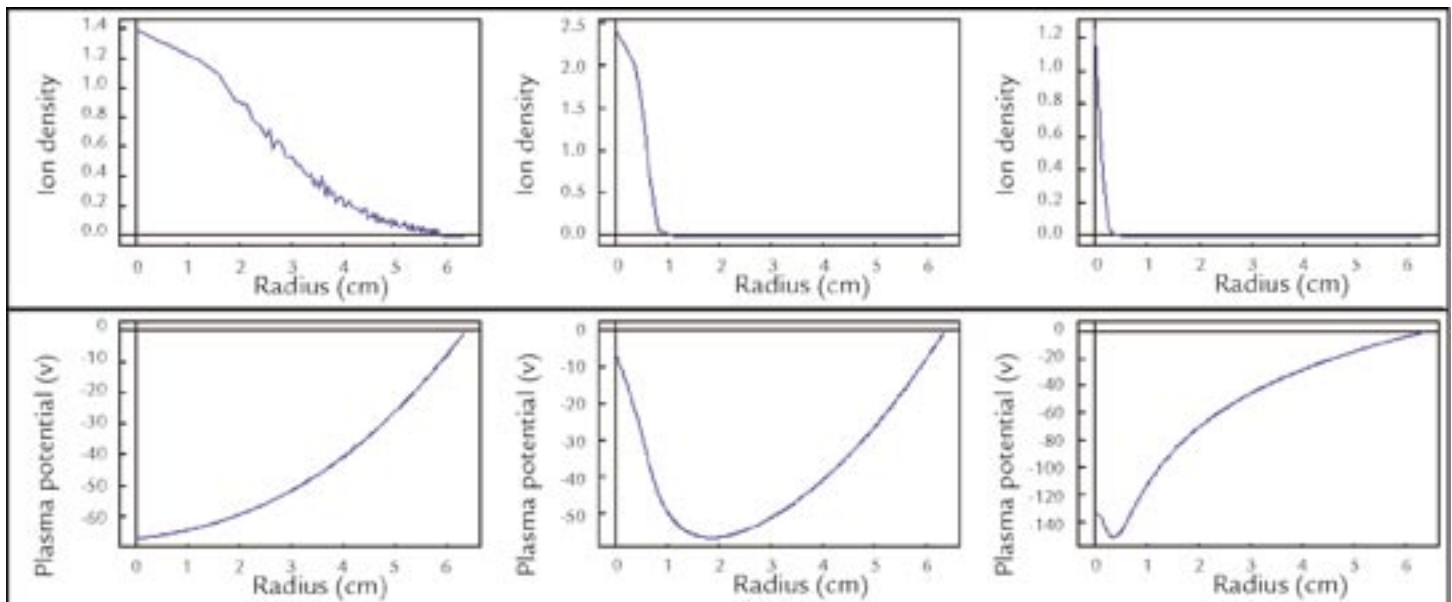
1. W.C. Elmore, J.L. Tuck, and K.M. Watson, "On the inertial-electrostatic confinement of a plasma," *Physics of Fluids* **2**, 239 (1959).
2. P.T. Farnsworth, "Electric Discharge Device for Producing Interactions Between Nuclei," U.S. Patent No. 3,358,402, issued June 28, 1966, initially filed May 5, 1956, reviewed Oct. 18, 1960, filed Jan. 11, 1962.
3. R.L. Hirsch, "Experimental studies of a deep, negative, electrostatic potential well in spherical geometry," *Physics of Fluids* **11**, 2486 (1968).
4. R.A. Nebel and D.C. Barnes, "The periodically oscillating plasma sphere," *Fusion Technology* **38**, 28 (1998).
5. J. Park *et al.*, "First experimental confirmation of periodically oscillating plasma sphere (POPS) oscillation," submitted to *Physical Review Letters*.
6. J. Park *et al.*, "Experimental studies of electrostatic confinement on the INS-e device," *Physics of Plasmas* **10**, 3841–3849 (2003).
7. R.A. Nebel *et al.*, "Theoretical and experimental studies of kinetic equilibrium and stability in the virtual cathode of the intense neutron source (INS-e) device," submitted to *Physics of Plasmas*.

Acknowledgment

This work is supported by the DOE Office of Science/Fusion Energy Sciences Innovative Confinement Concepts Program. The authors gratefully acknowledge Carter Munson (P-24), Martin Taccetti (Hydrodynamics and X-ray Physics Group, P-22), Dan Barnes (Coronado Consulting), Martin Schauer (Neutron Science and Technology Group, P-23), and John Santarius (University of Wisconsin) for many invaluable discussions on this project; Dave Beddingfield (Safeguards Science and Technology, N-1) for conducting MCNP calculations; Tom Intrator (P-24) for providing us with thoriated tungsten wire; and N-1 and the Nuclear Nonproliferation Division management for providing the facility for this experiment.

For further information, contact Jaeyoung Park, 505-667-8013, jypark@lanl.gov.

Figure 5. Radial profile of ion density and plasma potential during POPS oscillation from the one-dimensional particle code. The profiles on the left (top and bottom) come from the expansion phase, whereas the profiles in the center (top and bottom) and on the right (top and bottom) come from the collapsed phase. See the main text for a detailed description.



The World's Greatest Science Protecting America

Los Alamos National Laboratory, an affirmative action/equal opportunity employer, is operated by the University of California for the U.S. Department of Energy under contract W-7405-ENG-36.



Plasma-Enhanced Combustion of Propane using a Silent Discharge

L.A. Rosocha, Y. Kim, S. Stange, V. Ferreri (P-24),
D.M. Coates (P-DO), D. Platts (P-22)

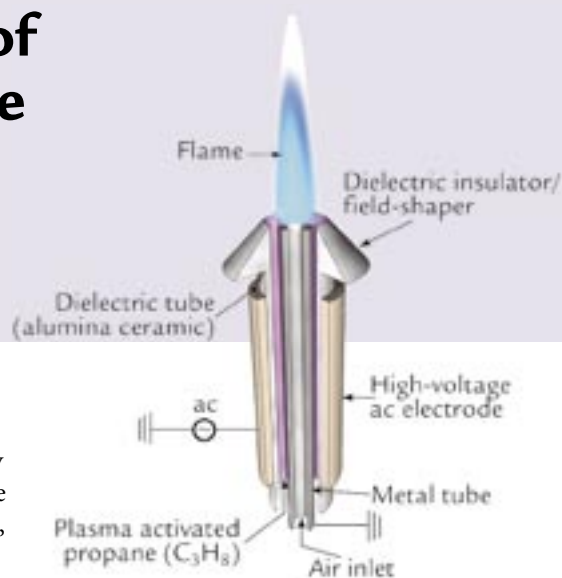


Figure 1. Schematic diagram of the experimental setup for blowout and combustion product studies, employing a coaxial DBD reactor.

As a primary objective, researchers in Physics (P) Division's Plasma Physics Group (P-24) want to minimize U.S. energy dependency on foreign resources through experiments incorporating a plasma-assisted combustion unit. Under this broad category, researchers seek to increase efficiency and reduce NO_x/SO_x and unburned hydrocarbon emissions in internal-combustion engines, gas-turbine engines, and burner units. To date, the existing lean-burn operations, consisting of a higher air-to-fuel ratio, have successfully operated in a regime where reduced NO_x/SO_x emissions are expected and have also shown increased combustion efficiency (less unburned hydrocarbon) for propane. By incorporating a lean-burn operation assisted by a nonthermal-plasma (NTP) reactor, the fracturing of hydrocarbons can result in increased power, combustion efficiency, and stability in the combustion system.

NTP units produce energetic electrons but avoid the high gas and ion temperatures involved in thermal plasmas. One NTP method, known as a silent discharge, allows free radicals to act in propagating combustion reactions, as well as intermediaries in hydrocarbon fracturing. Using NTP units, researchers have developed a fuel activation/conversion system that can decrease pollutants while increasing fuel efficiency, thus providing a path toward future U.S. energy independence.

Background

Combustion processes impact many aspects of modern life. They provide propulsion for automobiles, aircraft, and ships; generate electricity; and heat homes, water, and commercial buildings. Maximizing the efficiency of these combustion processes to conserve fuel and reduce pollution is of vital importance.

Over the past five decades, many attempts have been made to improve combustion using an electric field, which can affect flame stability, flame propagation speed, and combustion chemistry.^{1,2} However, the magnitude of the electric field in these experiments was insufficient to generate plasma. Thermal plasmas, which are usually less efficient and selective in directing electrical energy into the promotion of chemical reactions, have been applied to combustion over the past three or more decades with some success³, in particular, to convert air-fuel mixtures (into H_2 and CO)⁴, to increase internal-combustion engine efficiency, and to reduce NO_x .

NTPs are potentially more useful tools for promoting combustion. In NTPs, the electrons are energetic ("hot"), whereas ions and neutral gases are near ambient temperature ("cool"), which results

in little waste enthalpy (heat) being deposited in a process gas stream. Typical electron temperatures in such plasmas are at about a few electron volts, which is sufficient to break down the fuel and to produce free radicals.⁵ We consider the silent electric discharge⁶, also known as a dielectric barrier discharge (DBD), as a very promising candidate for combustion enhancement. In 1983, Inomata *et al.*⁷ demonstrated increases in flame speed when a DBD is applied upstream of a methane-air flame. More recent work performed by Cha *et al.*⁸ showed that applying a DBD to the flame region results in a decrease in flame length and reduced soot formation.

Our new technology, based on NTPs, pretreats fuels (not fuel-air mixtures) just before combustion.⁹ In our technique, fuels are broken down (cracked) into smaller molecular fragments, boosted

RESEARCH HIGHLIGHT

PHYSICS DIVISION

into reactive excited states, or made into “free-radicals.” The “activated” fuel is then mixed with air and combusted. This technology allows for very “lean-burn” modes of combustion highly desirable for reduction of NO_x . “Proof of principle” has been demonstrated in experiments using propane as the fuel in a flame-based burner. We investigated the effects of the plasma on combustion by examining combustion stability under lean-burn conditions, observing increases in flame propagation speed by photography, and sampling and analyzing the gas residues from combustion.

Hypothesis for NTP Combustion Enhancement

Conventional propane-air combustion begins with spark ignition, whereby a spark thermally decomposes the propane-air mixture to produce free radicals and other reactive species. Burning then continues by the propagation of the reactive species generated by the heat of combustion. The overall combustion reaction rate is usually determined by how efficiently new reactive species are generated in the propagating flame front. However, the self-generation of reactive species is sometimes insufficient to sustain combustion under certain conditions, for example, during lean-burn operation.

NTP “activation” can be used to continuously convert atomized-liquid or gaseous fuels into reactive species, so that

combustion does not rely on the self-generation of reactive species. The main possible mechanisms for fuel-cracking and fuel-activation (creation of more reactive species) are based on electron-impact processes, such as dissociation, dissociative ionization, vibrational excitation, and electronic excitation of the parent fuel molecule. Under an electron impact, propane is also ionized into multiple species, and these species then further fragment into smaller molecular ions.

Experimental Setup

We used two different NTP/DBD reactors for our investigations: one for lean-burn operation and exhaust-gas species determination and a second for flame-propagation observations. A schematic diagram of the first experimental setup⁹ is shown in Figure 1. Air flows through a grounded tubular inner electrode (diameter of 0.96 cm). Propane (C_3H_8) flows through the annular gap between the inner electrode and an alumina ceramic tube (inner diameter of 1.9 cm). The ceramic tube is surrounded by a cylindrical metal outer electrode, which is powered by a high-voltage alternating-current transformer operated at about 450 Hz to match our propane DBD reactor. An NTP was formed in the propane stream, thus activating the fuel. The inner electrode is shorter than the ceramic tube, so there is a region (of variable length, but generally < 14 mm) where the fuel and air partially mix before being ignited. A ceramic nose-cone shapes the electric field at the end of the reactor to prevent arcing.

We used the reactor shown in Figure 2 for our flame-velocity observations.¹⁰ In this experiment, the outer, high-voltage electrode was a piece of copper mesh. The mesh surrounded a quartz tube with an inner diameter of 12.5 mm. The inner electrode was a grounded stainless-steel tube having an outer diameter of 9.5 mm. Propane flowed in the annular region between the inner electrode and the quartz tube, while the air flowed down the center

of the inner electrode. The ends of the electrodes and the end of the quartz tube were separated by a 6 cm mixing region. By using a relatively long mixing region, we were able to eliminate any effects of the electric field on the flame. The air- and propane-flow rates were set to 4.6 and 0.3 lpm, respectively, to fix the equivalence ratio at 1. At an equivalence ratio of 1, combustion is stoichiometric, or ideal, so the propane should be entirely consumed.

The power deposited into the plasma was measured using Lissajous diagram techniques (charge-voltage plot).¹¹ Other diagnostics included two thermocouples to measure inlet and outlet gas temperatures, a digital camera to take photographs of the flame, and a residual-gas analyzer (RGA) equipped with a quadrupole mass spectrometer to measure the partial pressures of combustion by-products.

Experimental Results

Influence of Plasma on Flame Blowout Limits. We conducted blowout tests by holding the propane flow constant and increasing the air-flow rate until the flame blew out.¹² The blowout air-flow rate is an indicator of flame stability, and a high-blowout air-flow rate shows that combustion continues to occur under lean-burning conditions. Figure 3 shows the minimum blowout air-flow rates of an inverse, partially premixed flame for propane-flow rates between 0.2 and 0.8 lpm. The number associated with each data point in the plot corresponds to the equivalence ratio ϕ ¹³,

$$\phi = \frac{15.6 \times (\text{propane flow rate})}{(\text{air flow rate})}, \quad (1)$$

which is a standard measurement of combustion. In the absence of a plasma, the blowout limit of a propane flame increases with the propane-flow rate and begins to saturate at a propane-flow rate of 0.6 lpm. When 10 W discharge power is applied to the fuel, the blowout limit shows a large increase for low propane flow (and low equivalence ratio). However,

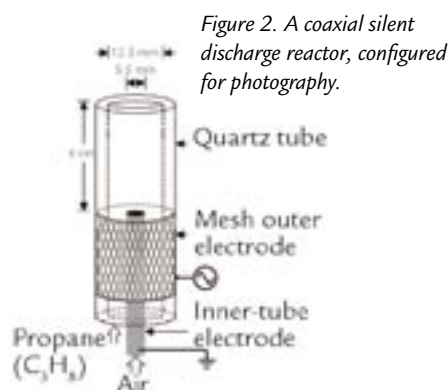


Figure 2. A coaxial silent discharge reactor, configured for photography.

the plasma benefit decreases as the propane flow increases, and for propane flow > 0.6 lpm, the blowout rate actually decreases in the presence of a plasma. This is not necessarily detrimental because low-equivalence-ratio systems show large decreases in pollutant production, especially NO_x , and are of great practical interest. In this experiment, the discharge power was held constant (10 W) while the propane-flow rate was increased. Thus, the discharge energy density ϵ ,

$$\epsilon = \frac{\text{discharge power}}{\text{gas flow rate}}, \quad (2)$$

deposited into the propane decreased as the propane-flow rate increased. For example, at a propane-flow rate of 0.3 lpm, the discharge energy density was equal to 2 kJ/L, whereas at a propane-flow rate of 0.8 lpm, the discharge energy density fell to 0.75 kJ/L. Thus, the magnitude of the discharge energy density seems to affect the blowout limit of a propane flame. More experiments will be performed to correlate the combustion enhancement with the discharge energy density.

Combustion By-products. The concentrations of gaseous products of combustion were measured with the RGA. Mass fragments of particular interest are atomic masses 26 (C_2H_2), 27 (C_2H_3), 39 (C_3H_3), and 43 (C_3H_7). During operation, the flame was ignited and allowed to burn without plasma for two minutes. Then the power supply was turned on, and the activated fuel burned for two minutes. This procedure was repeated several times to test the repeatability of any enhanced combustion provided by the plasma.

Figure 4 shows typical data (with one mass fragment, $M = 43$ shown).¹² The partial pressure of the propane fragments decrease while water and carbon dioxide (both common hydrocarbon combustion products) increase when the plasma is turned on. The plateaus at the end of the traces are the result of extinguishing the flame—these are the partial pressures in the absence of any combustion. It is clear that the plasma significantly decreases

the partial pressure of unburned hydrocarbons, indicating that propane is being burned more completely.

Flame Propagation Speed.

The photographs displayed in Figure 5 were taken with a Canon PowerShot S45 digital camera with ISO 400, a focal length of 17.5 mm, an aperture of f/8.0, and a shutter speed of 0.8 s.¹⁰ The images focus on the propane-air mixing region—the end of the quartz tube is visible at fiducial (1), and the purple glow at fiducial (2) is the edge of the outer electrode.

The progressively higher-power propane plasma's effect on the flame is shown in Figure 5. Figure 5(a) shows a propane-air flame in the absence of plasma. The application of even a relatively low-power 4 W plasma, as shown in Figure 5(b), improves the flame symmetry, a marker of stability. In both 5(a) and 5(b), the flame propagates upward only, although at an equivalence ratio of 1, it can theoretically propagate downward.¹⁴ The latter indicates that the flame propagation rate is insufficient to overcome the upward flow of the propane-air mixture. When a 6 W propane plasma is created, as shown in Figure 5(c), the flame begins to propagate downward. As larger fields are applied to the propane gas, creating higher-power plasmas, downward propagation becomes increasingly pronounced, as shown in Figures 5(d)–(f). The changes in the flame's ability to propagate downward suggest that the flame-propagation rate increases with plasma power.

The flame propagates more quickly because it is igniting and burning faster. This combustion enhancement may result from the improved cracking of propane, the creation of reactive radicals, or

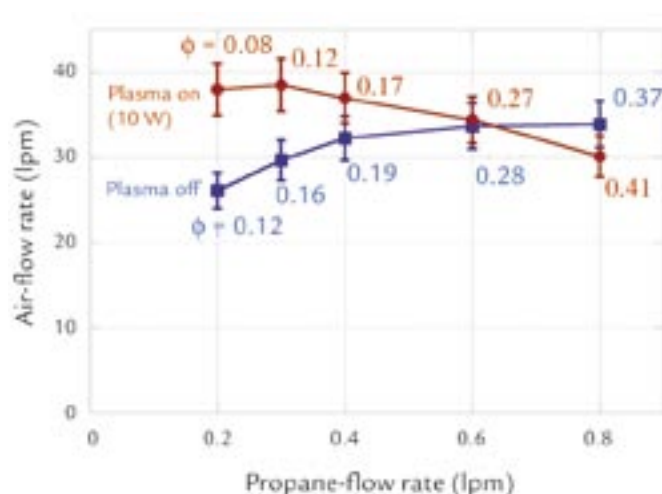


Figure 3. Effect of plasma on the blowout air-flow rate for propane flame. Combustion enhancement is indicated by the increment of the blowout limit when the plasma is on.

hydrogen generation. As discussed above, all of these factors likely play a role in combustion enhancement, but the relative importance of each is unknown. In the near future, we plan to use mixing regions of varying lengths to better understand the role of reactive radicals.

Conclusion

We have shown that silent-electrical-discharge-generated NTP can be used to activate propane fuel, significantly enhancing combustion in an activated propane-air mixture, as determined by mass spectrometric measurements of combustion-effluent gas concentrations. The plasma energy density required to achieve such enhancement is modest, of order 100s of J/L. Also, visual observations of activated propane-air flames indicate an increased spatial stability of the flame, increased blowout limits (leaner burn), and increased flame propagation speed. If applications to other fuels (e.g., gasoline, diesel, jet fuel) are successful, NTP-assisted combustion may prove to be highly beneficial to the energy needs of modern society.

References

1. J. Lawton and F.J. Weinberg, *Electrical Aspects of Combustion* (Clarendon, Oxford, 1969).
2. H.C. Jagers and A. von Engel, "The effect of electric fields on the burning velocity of various flames," *Combustion and Flame* **16**, 275–285 (1971).
3. F.J. Weinberg, Ed., *Advanced Combustion Methods* (Academic Press, London, 1986).
4. L. Bromberg *et al.*, "Emissions reductions using hydrogen from plasmatron fuel converters," *International Journal of Hydrogen Energy* **26**, 1115–1121 (2001).
5. L.A. Rosocha, "Processing of hazardous chemicals using silent electrical discharge plasmas," in *Environmental Aspects in Plasma Science*, W. Manheimer, L.E. Sugiyama, and T.H. Stix, Eds., (American Institute of Physics Press, Woodbury, New York, 1997).



Figure 5. Increasing the plasma power causes an increase in flame propagation speed, indicated by the movement of the flame towards the electrodes. Figure (a) shows combustion without a plasma. The other images show the effect of plasmas having powers of (b) 4 W, (c) 6 W, (d) 8 W, (e) 10 W, and (f) 12 W. The numbers indicate regions of interest of the apparatus: (1) is the top of the quartz tube and (2) is the top of the outer electrode. The mixing region lies between them.

6. U. Kogelschatz, "Dielectric-barrier discharges: Their history, discharge physics, and industrial applications," *Plasma Chemistry and Plasma Processing* **23**, 1–46 (2003).
7. T. Inomata *et al.*, "The application of silent electric discharges to propagating flames," *Combustion and Flame* **50**, 361–363 (1983).
8. M.S. Cha *et al.*, "Interaction between a non-thermal plasma and a flame," in *Proceedings of the 30th International Conference Plasma Science*, Cheju, Korea, June 2–5, 2003.
9. L.A. Rosocha *et al.*, "Plasma-enhanced combustion of propane using a silent discharge," *Physics of Plasmas* **11**, 2950–2956 (2004).
10. S. Stange *et al.*, "Flame images indicating combustion enhancement by dielectric barrier discharges," in *IEEE Transactions on Plasma Science* (to be published, February 2005).
11. T.C. Manley, "The electrical characteristics of the ozonator discharge," *Transactions of the Electrochemical Society* **84**, 83–95 (1943).
12. Y. Kim, S. Stange, and L.A. Rosocha, "Combustion enhancement of propane by dielectric barrier discharges," in *Proceedings of the 4th International Symposium on Non-Thermal Plasma Technology for Pollution Control and Sustainable Energy Development*, (Panama City Beach, Florida, May 10–14, 2004) pp. 221–225.
13. N.O. Nylund and A. Lawson, *Exhaust Emissions from Natural Gas Vehicles* (International Association for Natural Gas Vehicles, Sigma Group, Takapuna, New Zealand, 2000).
14. A.G. Gaydon and H.G. Wolfhard, *Flames: Their Structure, Radiation, and Temperature* (Chapman and Hall, London, 1970).

Acknowledgment

The authors wish to express their appreciation to Margaret Harris and Andrew Jensen (student interns) for technical assistance with this work and to P Division and Technology Transfer Division for financial support for this project.

For further information, contact Louis Rosocha, 505-667-8493, rosocha@lanl.gov.

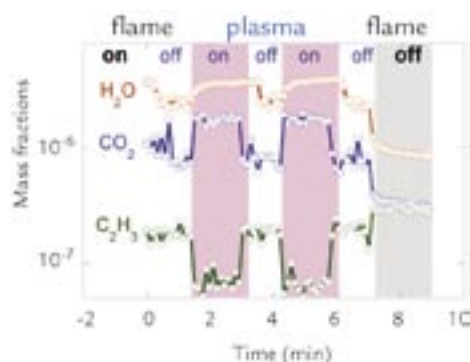


Figure 4. Mass spectrometer data for propane combustion fragments. Combustion enhancement is indicated by the reductions in unburned hydrocarbon and increases in water and carbon dioxide when the plasma is on.

Angular Momentum Transport and Dynamo Studies in the Flowing Magnetized Plasma Experiment

Z. Wang, S.C. Hsu, C.W. Barnes (P-24), K. Noguchi (T-CNLS, now Rice University), D.C. Barnes, H. Li (X-1), X.Z. Tang (T-15), S.A. Colgate (T-6)

Angular momentum transport and dynamo effects are two plasma physics problems that bear on fundamental unsolved astrophysical mysteries. Understanding angular momentum transport in weakly magnetized plasmas is important in determining, for example, the details of how galaxies form and evolve starting from nebulous clouds of matter. A solution to the dynamo problem will tell us how magnetic fields in the galaxy are created and amplified. Researchers in Physics Division's P-24 Plasma Physics Group have developed a laboratory plasma experiment to investigate these two plasma physics problems.

The problem of angular momentum transport is critical for understanding the rate at which matter collapses gravitationally to form compact objects, such as black holes, in the universe. If this happens too quickly, there will be far too many black holes in the universe; however, if this happens too slowly, then galaxies and stars and planets would never form. Because angular momentum conservation is a robust principle in physics, gravitationally collapsing globs of matter tend to become spinning disks in order to conserve their initial angular momentum. These "accretion disks" are ubiquitous in the universe and exist in the centers of galaxies (Figure 1), around binary star systems, and are an evolutionary step in the formation of solar systems. For matter to "accrete" or fall inward toward the gravitational center of a system, the angular momentum must be transported away via friction within the accretion disk plasma. However, for decades the rate at

which matter spiraled inward for many accretion disk systems was a mystery because of the inconsistency between the amount of friction thought to exist and the observationally inferred rates of accretion. The rate of interparticle collisions in disks generally cannot account for the necessary frictional forces. However, in the early

1990s, Balbus and Hawley¹ realized that a weak magnetic field in an accretion disk can lead to a plasma instability, the magnetorotational instability (MRI), which was first discovered in the 1950s. This instability could create magnetic turbulence, which can lead to the necessary frictional forces needed for the mass

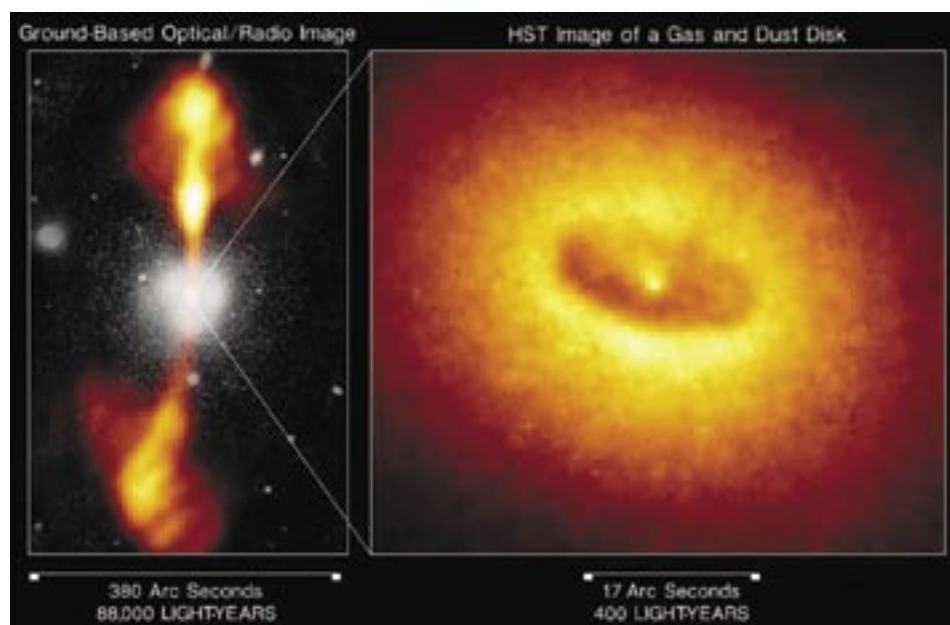


Figure 1. (a) Ground-based composite optical/radio view of elliptical galaxy NGC4261 with opposed jets emanating from galactic nucleus. (b) Hubble Space Telescope image of the core of NGC4261, showing a giant disk of cold gas and dust fueling a possible black hole. The dark, dusty disk represents a cold outer region that extends inwards to an ultrahot accretion disk within a few hundred million miles of the suspected black hole. (Credits: National Radio Astronomy Observatory, Caltech; Walter Jaffe/Leiden Observatory; Holland Ford/JHU/STScI; and NASA)

RESEARCH HIGHLIGHT PHYSICS DIVISION

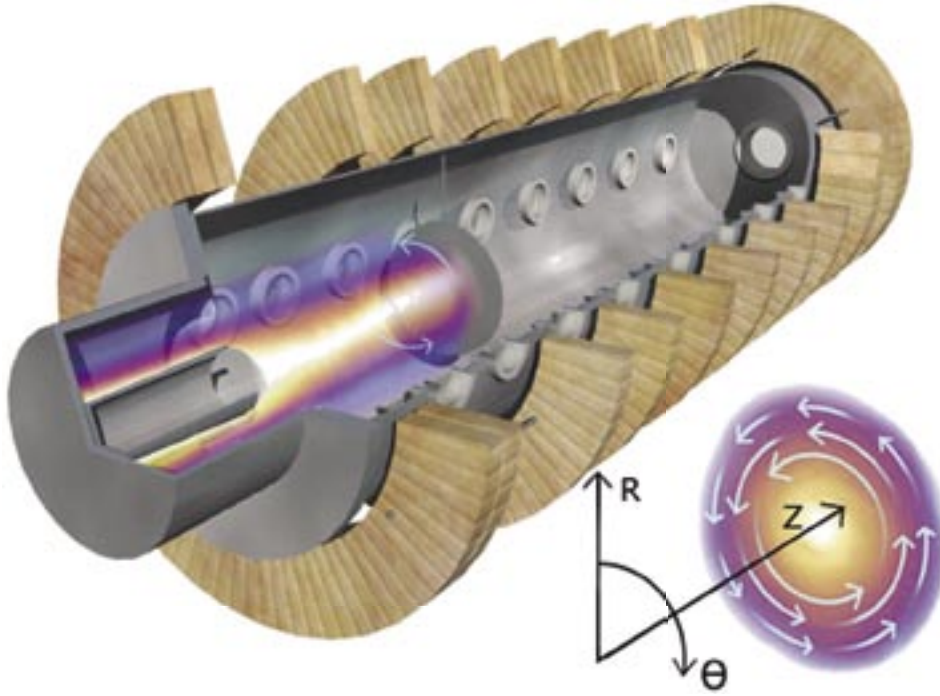


Figure 2. The FMP experimental setup consists of a coaxial plasma gun (front, left) mounted on one end of a large, cylindrical metal vacuum chamber surrounded by magnetic coils. The circular plate inside the chamber can be biased to different voltages, providing axial plasma confinement and some control over the potential profiles inside the plasma, which affects the azimuthal plasma rotation profile. A cylindrical coordinate system is used.

in an accretion disk to fall towards the central object. Over the past decade, much theoretical and computational research has advanced our understanding of the MRI and its ability to lead to increased friction in rotating disks of plasma. However, this instability has not been observed yet in plasma experiments, providing a strong motivation for this work.

The dynamo problem is another astrophysical holy grail: how are magnetic fields created and amplified on galactic scales to their observed values? Many kinds of dynamos exist, but the kind we are concerned with here involves conversion of kinetic energy in plasma flows to magnetic field energy via electrical currents created by the flowing plasma.² This process is thought to occur in galactic accretion disks, which can be thought of as magnetic engines that fill intergalactic space with magnetic energy. Again, much theoretical and numerical simulation

research has been done on the dynamo problem in recent decades, with very little experimental verification and tests. Recently, however, dynamo action was observed in a liquid-metal experiment.³ The experiments in P-24 will try to create dynamo action in a plasma experiment for the first time.

Experimental Setup

In P-24's Flowing Magnetized Plasma (FMP) experiment, researchers generate a plasma using a "coaxial gun" source, which was recycled from magnetic fusion energy research at LANL in the 1980s. The coaxial gun, which consists of two concentric cylinders, is mounted on one end of a large, cylindrical metal vacuum chamber, as seen in Figure 2. Gas is injected into the unit, and a voltage of up to 1 kV is applied across the gap between the cylinders. The gas then breaks down into a plasma as electric current up to 200 kA

flows from one gun electrode through the plasma to the other electrode. The plasma flows down the long axis of the vacuum chamber and rotates azimuthally due to electromagnetic forces. By controlling the plasma density and temperature, the plasma rotation profile, and the magnetic field strength, the experiment is expected, based on numerical calculations, to operate in regimes in which both the MRI and dynamo can be observed and studied.

Experimental measurements of magnetic field, electron density and temperature, and ion-flow speeds are required to characterize the plasma configurations created by the coaxial gun and to detect the MRI and dynamo processes. Various diagnostics are installed on the vacuum chamber to make these measurements, including

- (1) edge and internal magnetic probe coils to measure all three components of the magnetic field,
- (2) a triple Langmuir probe to measure electron temperature and density and floating electric potential,
- (3) a Mach probe to measure ion-flow speed,
- (4) a charge-coupled device camera to capture movie sequences of plasma evolution as seen in visible light emission, and
- (5) a spectroscopy system to measure ion temperature and flows via Doppler broadened emission lines.

More sophisticated probe arrays are being built by summer students to provide better diagnosis capability for the experiment.

Initial Experimental Data on FMP Plasmas

The first FMP plasma was achieved in September 2003. Coaxial-gun plasmas were created using a new low-voltage technique⁴, allowing longer plasma pulse durations for a given stored energy. Our first goal—to create and characterize the necessary plasma conditions to observe the MRI—requires the establishment of a

Angular Momentum Transport and Dynamo Studies in the Flowing Magnetized Plasma Experiment

rotating plasma within a certain range of density, temperature, magnetic field, and lifetime values. These ranges of values were determined from preliminary numerical calculations of the MRI, specifically for the geometry and conditions of the FMP experiment.⁵ These calculations also predict the initial growth rate of the instability and expected modifications to the profiles of the magnetic field and plasma pressure. The FMP diagnostics should be able to detect these signatures as the plasma transitions from a stable to unstable regime with respect to the MRI.

Camera images of the plasma evolution are shown in Figure 3. The images show that a plasma is generated in the gap between the coaxial gun electrodes. Then it flows out of the coaxial gun and quickly fills up the plasma chamber. An azimuthal rotation can also be detected from the

images. Various probes, which are scanned in the radial direction, provide profile information on magnetic field strength, ion-flow speed, and electron density and temperature.

The initial experimental data suggest that we may have a quasi-steady plasma equilibrium in which high magnetic pressure at larger radii balances the thermal plasma pressure and at smaller radii balances the rotational-kinetic pressure. The large magnetic pressure at large radii is related to a plasma “diamagnetic” effect in which the axial magnetic flux in the interior is reduced from its initial value by being expelled to the edge. The net reduction is known as the excluded flux. Diamagnetic effect is measured using two large single-turn pickup coils that encircle the plasma. The coils are at different axial positions.

The result is summarized in Figure 4. We observed that the total excluded flux is maximized when the initial axial magnetic field is around 100 G. From the measured excluded flux and a magnetohydrodynamic equilibrium model, we estimate the plasma β (ratio of the total thermal energy to magnetic field energy) is between 30%–60%. We have also observed growth of the local magnetic field (Figure 5), which will be investigated further in terms of both the MRI and dynamo.

Present experimental runs are now dedicated to characterizing the radial profiles of magnetic field, ion flow, and electron density and temperature more completely. This characterization will also be done for a variety of bias schemes on an internal bias plate in hopes of achieving the most desirable profiles for observing the MRI.

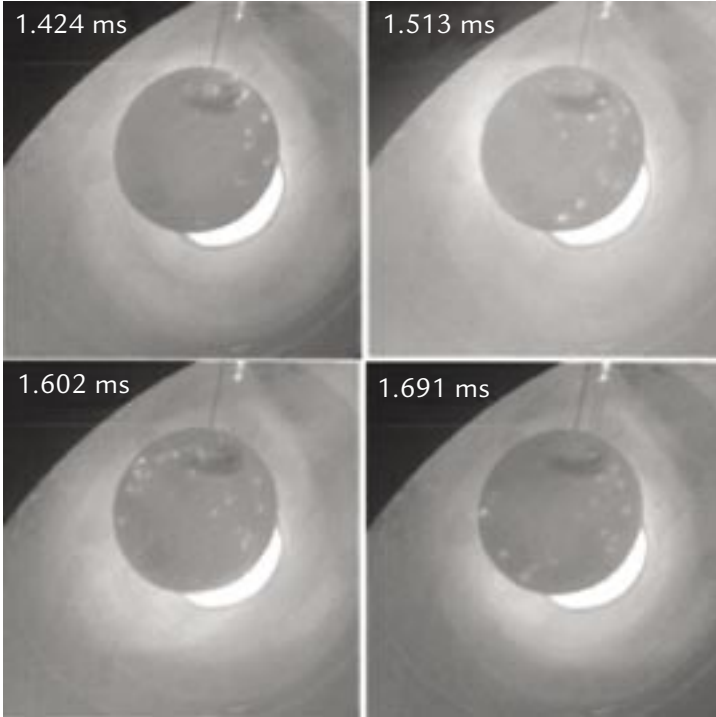


Figure 3. Evolution of an FMP plasma with a floating electrode (the black circle at center) located 1.5 m away from the coaxial gun (the brightest arc-shaped region corresponds to the coaxial gap between the coaxial electrodes). Volume light emission, as well as the bright spots on the floating electrode, appears to rotate from frame to frame. The vacuum axial magnetic field is 340 G; rotation frequency is 9.40 kHz (from magnetic probe measurements), which is slightly less than the interframe frequency of 11.2 kHz.

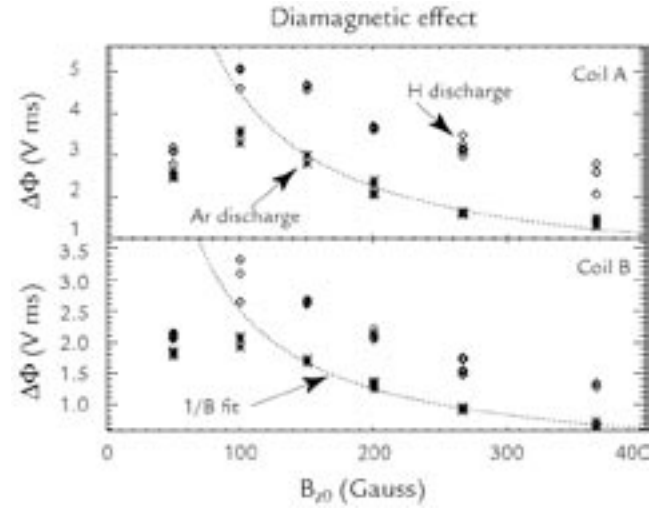


Figure 4. FMP plasma is globally diamagnetic. Axial magnetic flux (excluded flux) changes with initial axial magnetic field, which is verified at two axial (z) locations, and is labeled as Coil A for the top panel and Coil B for the bottom panel. In both panels, results for both argon (Ar, \bullet) gas and hydrogen (H, \circ) gas are shown. The excluded flux is maximal when the initial axial magnetic field is about 100 G. The corresponding plasma (β) is between 30%–60%. The discrepancy in excluded flux between hydrogen and argon is likely due to their mass difference, which will be further studied experimentally.

Plasma Physics Research Highlights

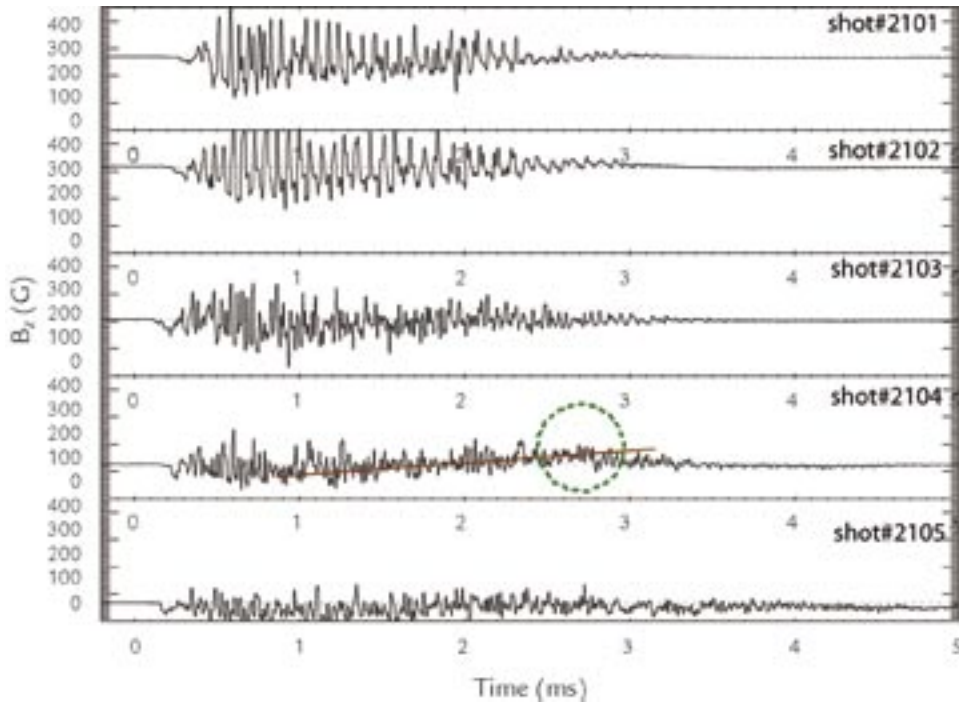


Figure 5. Study of local axial-magnetic-field (B_z) evolution under different vacuum axial-magnetic-fields ranging from 60 G to 320 G for the same coaxial-gun conditions using hydrogen plasmas. It appears that local B_z can grow on the millisecond time scale. Several mechanisms, including MRI and dynamo in high- β plasmas, are considered as candidates to explain this new observation.

Future Work

We plan to deduce the viscous damping term in the plasma force equation by measuring all of the other terms in the equation. This deduced viscosity will be compared to the theoretical value of viscosity based simply on Coulomb collisions between plasma particles. If the MRI is active, then we should expect that the experimentally deduced value for viscosity is higher than the classical value. Both MRI and dynamo will be studied by controlling flow profiles.

References

1. S.A. Balbus and J.F. Hawley, "Instability, turbulence, and enhanced transport in accretion disks," *Reviews of Modern Physics* **70**, 1–53 (1998).
2. Z. Wang *et al.*, "Laminar plasma dynamos," *Physics of Plasmas* **9**, 1491–1494 (2002).
3. A. Gailitis *et al.*, "Detection of a flow induced magnetic field eigenmode in the Riga Dynamo Facility," *Physical Review Letters* **84**, 4365–4368 (2000).
4. Z. Wang *et al.*, "A Penning-assisted sub-kilovolt coaxial plasma source," submitted to *Journal of Applied Physics* (2004).
5. K. Noguchi and V.I. Pariev, "Magnetorotational instability in a Couette flow of plasma," in *American Institute of Physics Conference Proceedings* **692**, 285–292 (2003).

Acknowledgment

This work is supported by Laboratory-Directed Research and Development/Exploratory Research funding.

For further information, contact Zhehui Wang, 505-665-5353, zwang@lanl.gov.

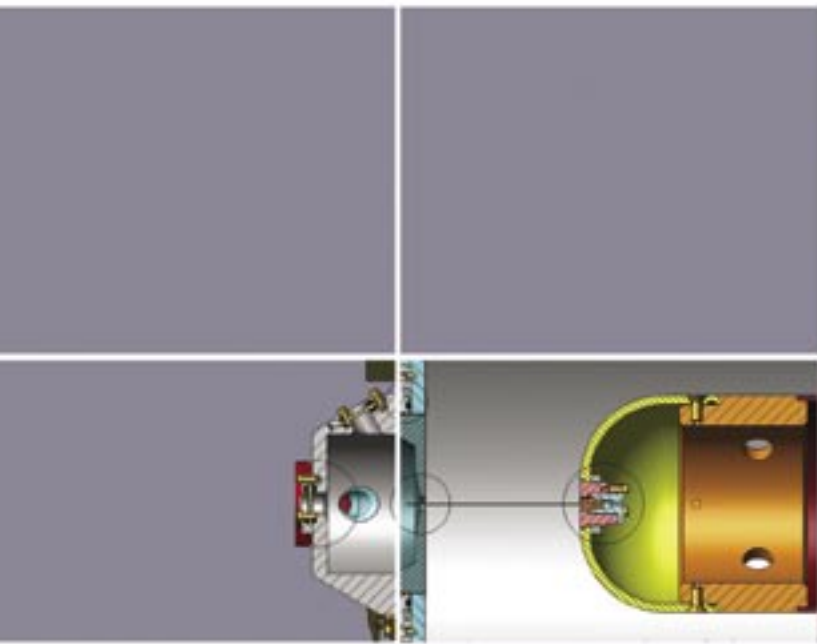
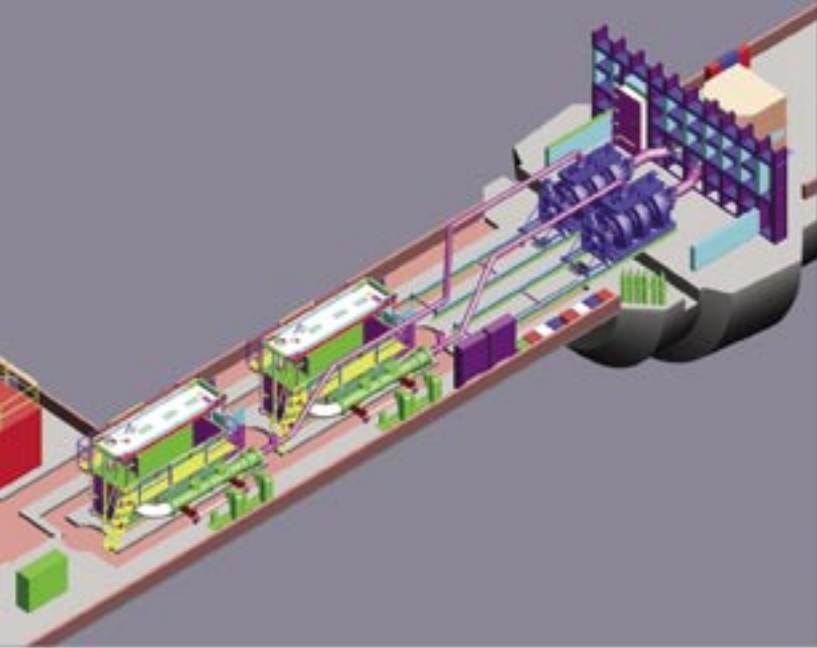


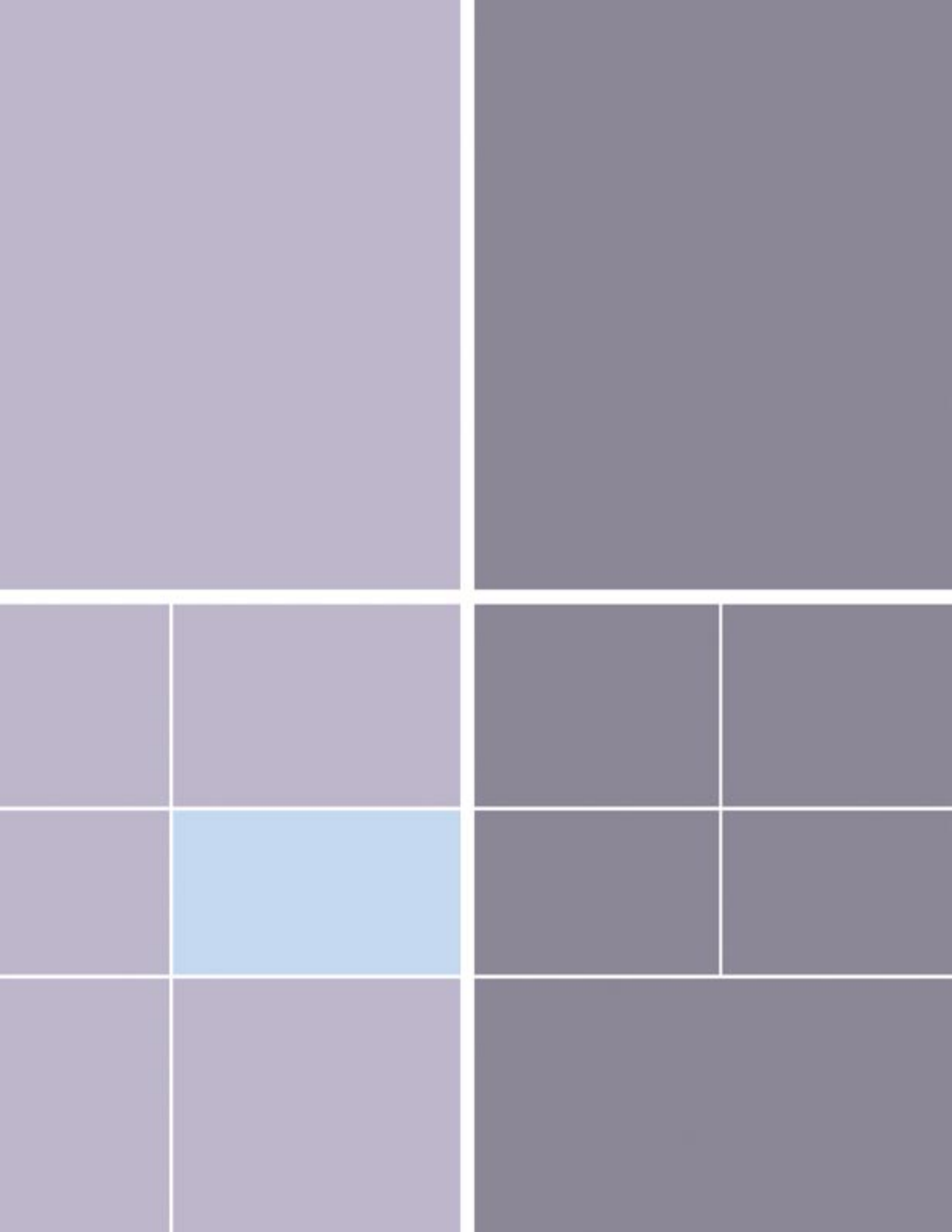
The World's Greatest Science Protecting America

Los Alamos National Laboratory, an affirmative action/equal opportunity employer, is operated by the University of California for the U.S. Department of Energy under contract W-7405-ENG-36.



Instrumentation Research Highlights





Design Feasibility and Cost Estimate for a Single-Axis, Multipulse Proton Radiography Facility

J.A. McGill, C.L. Morris (P-25), P.L. Colestock (ISR-6), F. Neri, L.J. Rybaryk (LANSCE-1), M.E. Schulze (DX-6), H.A. Thiessen (X-4), N.S.P. King (P-23)

A recent study motivated by the success of proton radiography (pRad) experiments done at Brookhaven National Laboratory (BNL) has examined the design parameters and estimated the costs of proton synchrotrons at both 10 and 20 GeV, which can be applied to quantitative radiography for the weapons stockpile. Potential sites and capabilities at LANL or the Nevada Test Site (NTS) were studied, and design feasibility and cost estimates were completed. The goal of the study was to present options for a new hydrotest capability that provides better position resolution, a factor of 10–100 higher effective dose¹, and up to ten time frames.

The choice of the two energies is driven by the classified results of static experiments performed using 24 GeV/c and 7.5 GeV/c beams from the Alternating Gradient Synchrotron (AGS) at BNL. These experiments showed that the lower energy is sufficient for measuring weapons-physics processes in scaled experiments, which are important to certification²; and the higher energy is suitable for full-scale hydrotesting on the largest stockpiled systems, with significantly enhanced physics returns³.

The Potential Sites

The prospective LANL site was selected to take advantage of the existing accelerator infrastructure at the Los Alamos Neutron Science Center (LANSCE). The 800 MeV LANSCE linear accelerator could be used as an injector, saving the time and money that would be needed to build and commission a new accelerator. In

addition, the existing infrastructure of trained people and equipment would simplify commissioning a new accelerator. However, the current site-wide authorization basis would preclude using pRad to diagnose dynamic experiments with plutonium, a key requirement for certification.

The potential NTS site studied was selected to take advantage of the U1a firing site and its authorization basis for plutonium experiments. Although the underground construction required at U1a would be more expensive than the site at LANL, and an injector would have to be designed and constructed, once the machine was completed, it would be relatively straightforward to implement an authorization basis for experiments with plutonium.

The requirements for these machines were synthesized from a combination of the results from the AGS experiments and from requirements studies carried out over the last decade.⁴ They are listed in Table 1.

The number of pulses is driven by the need to measure density at several times normal to infer criticality. Extensive studies by Buescher, Hopson, and Slattery have shown that four pulses spaced at a minimum of 200 ns are sufficient. We have added a fifth

time to the design requirements so that early time phenomena can be studied simultaneously and critically. Up to 10 pulses can be used for the 20 GeV ring studied here, limited by the circumference of the synchrotron. The 10 GeV ring can provide up to 6 pulses at 200 ns spacing. The proton dose in Table 1 is twice what has been used in validation experiments described below. This is enough beam to allow a two-Gaussian imaging mode, in which part of the beam is used to image small radii in the object and another part of the beam is used for full-field imaging.

pRad

Transmission radiography measures the transmission of a penetrating beam through an object and uses the attenuation to measure the areal density profile (thickness) of the object. Typically, the information is used to qualitatively determine the internal structure of the object. Hydrotesting involves imploding

Table 1. Machine requirements

Number of pulses	> 5
Minimum pulse spacing	~ 200 ns
Protons per pulse	2×10^{11}
Time format	Individual pulse extraction

RESEARCH HIGHLIGHT
PHYSICS DIVISION



Instrumentation Research Highlights

a primary from a weapon, in which the nuclear fuel has been replaced with a surrogate in order to not produce a nuclear yield. One goal of hydrotest radiography is to measure densities at late times in the implosion to benchmark numerical simulations that can be used to predict the explosive yield of nuclear systems. Until recently, the only diagnostic available for late-time hydrotesting was flash x-radiography.

With the cessation of underground testing, considerable effort has been expended to improve x-ray technology. The most recent manifestations of this effort are the first axis of the Dual-Axis Radiographic Hydrodynamic Test (DARHT) facility and the ARIX facility.⁵ These machines produce the largest doses and smallest spot sizes ever achieved with flash x-radiography. Nevertheless, in order to answer questions about stockpile performance and long-term stockpile certification, researchers require data that flash x-radiography cannot provide.⁴ Transmission radiography is described by the Beer-Lambert law.⁶ The solution to the differential equation,

$$\frac{dN}{dz} = -\lambda N \text{ is } N = N_0 e^{-\frac{z}{\lambda}}, \quad (1)$$

where λ is the mean-free path of the probe, z is the distance traversed, N_0 is the incident number of particles, and N is the number surviving after a distance (z). For objects of composite materials, z/λ becomes a summation or an integral, but the analysis below remains the same. In quantitative radiography the thickness of an object can be measured as:

$$\frac{l}{\lambda} = -\ln\left(\frac{N}{N_0}\right), \quad (2)$$

where l is the total amount of material traversed. Experimentally, one must consider details that are not reflected in the above equations such as the source spectrum (because λ is a function of energy), and backgrounds, which always seem to be a problem.

In spite of the simplified treatment, it is instructive to calculate the uncertainty on the measurement of thickness Δl , under the assumption that the only source of noise is the Poisson (counting) statistics of the transmitted beam:

$$\frac{\Delta l}{\lambda} = \frac{1}{\sqrt{N}}. \quad (3)$$

The mean-free path, λ , can be chosen to minimize Δl for a given object. Setting $\frac{d(\Delta l)}{d\lambda} = 0$, and solving for $\frac{\lambda}{l}$ gives $\frac{\lambda}{l} = \frac{1}{2}$.

That is, the optimum thickness determination per unit dose occurs at twice the mean-free path. In the case of x-rays, λ is a strong function of x-ray energy. The mean-free path reaches a maximum energy value where the likelihood for pair-production (which is rising with energy) becomes comparable to Compton scattering (which is falling with energy). The maximum mean-free path is weakly dependent on z , the nuclear charge. It occurs at an energy near 4 MeV, and is about 22 gm/cm² or a little over a centimeter of uranium. This maximum x-ray, λ , is far from the optimum for hydrotest experiments.

An alternative is provided by hadronic rather than electromagnetic probes. The absorption cross section, σ_A , for hadrons on a nucleus with atomic number A is well-approximated by:

$$\sigma_A = \pi r_A^2, \quad (4)$$

where $r_A \approx 1.2A^{1/3}$ fm. Using $\lambda = \frac{1}{\rho\sigma_A}$ gives an estimate of the hadronic mean-free path in uranium of 220 gm/cm², or 11.6 cm. The tabulated value is 199 gm/cm².^{2,7} Measurement of thickness is optimized at around 23 cm of uranium. This is much better matched to hydrotest radiography than the x-ray mean-free path. Consequently, the same statistical information can be obtained with a much lower incident flux of hadrons than with high-energy x-rays.

Advantages of pRad

It is possible to take advantage of the long hadronic mean-free path by using high-energy protons as a radiographic probe. High intensities are available in short pulses using current accelerator technology. Because the protons are charged, a proton beam can be distributed across a radiographic object and focused onto downstream detectors using electromagnets.⁸

In a set of experiments performed using the AGS at BNL, data were taken on a set of test objects to validate pRad and to compare it to x-radiography from DARHT. In all cases that have been studied, the qualities expected from pRad have been verified, and in all comparisons, even modest pulses of 10¹⁰ protons have been observed to provide a radiographic advantage over DARHT performance by a factor of between 10 and 100 in units of dose.

Even more significantly, pRad has been demonstrated to be quantitative at the percent level, and in high-fidelity mockups of hydrotest experiments, pRad demonstrates the capability to measure some of the underlying physics of cavity shape and mix, topics that have been identified as requirement drivers for hydrotest radiography.

The costs are based on a model developed in the Advanced Hydrotest Facility (AHF) project, and are expected to be accurate to $\pm 20\%$. It must be emphasized that this study is intended only to show the outlines of a facility that would provide the high-quality radiography discussed above and a rough cost estimate for such a facility. A more definitive design and estimate will be produced during conceptual design.

Scope and Cost

The goals of the accelerator complex are to satisfy the parameters in Table 1. The most demanding machine is the 20 GeV main ring synchrotron, common to both the LANL and the NTS sites. The alternative, a 10 GeV ring, has been studied only to

Design Feasibility and Cost Estimate for a Single-Axis, Multipulse Proton Radiography Facility

Table 2. Parameters of the strawman 20 GeV lattice

Circumference	608 m
Number of Dipoles	56
Dipole length, field, gap	5.0 m., 1.56 T, 5 cm
Number of Quads	76
Quad length, Gradient, aperture	0.8 m., 11.3 T/m, 10 cm
Transition gamma	5.73
Admittance (normalized)	16π mm-mr

Table 3. Parameters for the 10 GeV Ring

Circumference	392 m
Number of Dipoles	40
Dipole length, field, gap	4.0 m., 1.43 T, 5 cm
Number of Quads	56
Quad length, Gradient, aperture	0.6 m., 8.5 T/m, 10 cm
Transition gamma	4.22
Admittance (normalized)	16π mm-mr

the level of detail necessary to show its proof of principle. Capture, ramp, and acceleration have been studied for the 20 GeV ring, assuming injection could be provided by LANSCE's 800 MeV linac, or from the 500 MeV "green-field" injection complex at NTS. Detailed studies of the dynamics in the 10 GeV machine have only been done assuming injection from the LANSCE linac.

A 500 MeV booster synchrotron injects the larger machine (either 10 or 20 GeV) for the NTS siting option. The booster is injected by a small commercially available 11 MeV H(-) linac. As with the larger machines, the dynamics of the booster have been studied to such detail that its final design can be bounded, and to provide a reasonable estimate of its cost.

The overall layout of the ring is a racetrack design as shown in Figure 1. The pair of long straight sections provide for injection, extraction, and acceleration. Parameters of the Main Ring are in Table 2. The 10 GeV design is conceptually similar to the 20 GeV design, and results in an overall smaller circumference (Figure 2). The reduction in size is not precisely a factor of two from the 20 GeV case owing to the required straight sections and other infrastructure for injection and extraction. The ring's parameters are given in Table 3. The accelerators proposed here are well within the parameters of other accelerator projects that have been proposed and/or built. The reported (or estimated) costs of these accelerators vary considerably from site to site; nevertheless a reasonable estimate can be made, accurate to probably 20%. The costs of several synchrotron

projects were studied in the AHF project. Those costs were summarized and reported by Prichard⁹ and incorporated into a model for costing synchrotrons. The model uses gross measures, such as total weight of dipole and quadrupole magnets, total amount of direct-current power, total length of beam pipe vacuum, etc. Cost rates are applied to generate a total equipment cost. Factors are applied for overheads, design costs, and contingency, to arrive at the total project cost (TPC) for the accelerator equipment. A similar breakdown is done for the balance of plant, and cost loading factors specific to the civil construction process is applied. The result of the two exercises is an estimated TPC.

References

1. C.L. Morris *et al.*, to be published in DDR 2003.
2. S. Sterbenz *et al.*, Nuclear Explosives Design Physics Conference, Los Alamos, 2003
3. C.L. Morris *et al.*, to be published in DDR 2003.
4. J. Hopson, K. Buescher, and W. Slattery have done extensive work on establishing and quantifying a criticality requirement.
5. C. Ekdahl, "Modern Electron Accelerators for Radiography," *IEEE Transactions on Plasma Science*, **30** 254–261 (2002).

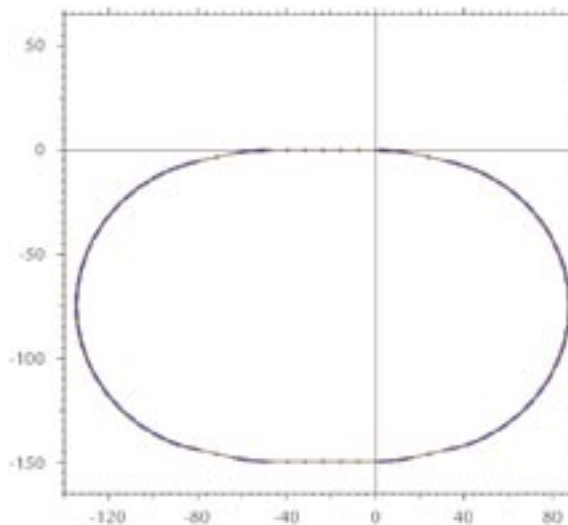


Figure 1. Concept for a 20 GeV ring design. The design is composed of two circular arcs coupled by matching sections into straight sections.

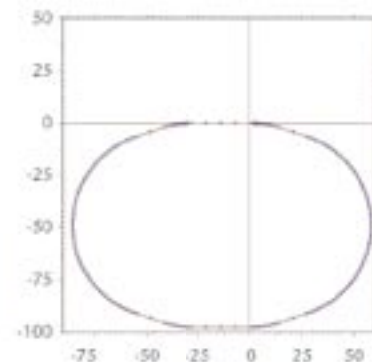


Figure 2. Concept for a 10 GeV ring design similar to that of the 20 GeV ring, but with a shorter circumference.

Instrumentation Research Highlights

6. A. Beer, *Annals der Physik Chemie* **86**, 78 (1952).

7. Particle Data Group, *The European Physical Journal C* **v3**, 1 (1998).

8. A. Gavron *et al.*, “Proton radiography,” Los Alamos National Laboratory document LA-UR-96-420.

9. B. Prichard, AHF Tech. Note 619, *A costing formula for proton synchrotrons*, 2003.

Acknowledgment

For further information, contact Chris Morris, 505-667-5652, cmorris@lanl.gov.

Table 4. Summary of costs for the various options

Cost Element	20 GeV Ring		10 GeV Ring	
	NTS	LANL	NTS	LANL
Equipment				
Linac	\$7.8		\$7.8	
Booster	\$16.2		\$16.2	
Main Ring	\$64.7	\$64.7	\$45.2	\$45.2
Transfer Lines	\$3.4	\$7.4	\$3.4	\$7.4
Firing Site & Detectors	\$7.6	\$7.6	\$7.6	\$7.6
Balance of Plant	\$260.2	\$83.7	\$225.1	\$69.0
Total	\$ 359.9	\$ 163.4	\$ 305.3	\$ 129.2
Costs are in \$M, FY07, The NTS costs have been validated by independent estimates made by Bechtel Nevada.				



Figure 3. A possible site for the 20 GeV ring, shown overlaid on the LANL Technical Area 53 site.

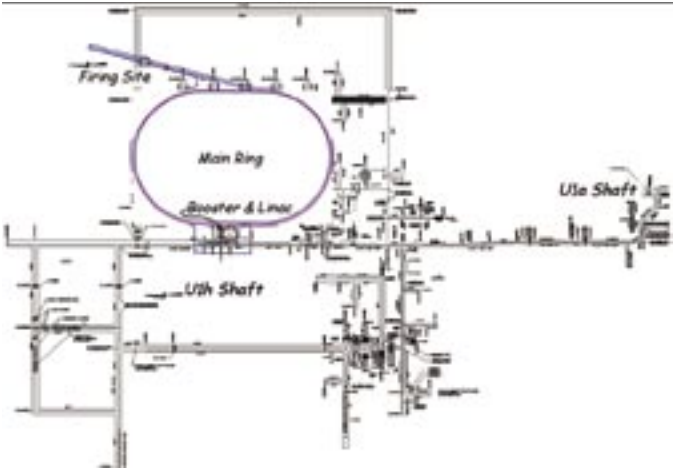


Figure 4. A possible layout of the accelerator complex, overlaid on the NTS U1a complex. There are no pre-existing facilities at the NTS to work around, so the accelerators and firing site can be positioned next to each other (allowing for operational considerations).



The World’s Greatest Science Protecting America

Los Alamos National Laboratory, an affirmative action/equal opportunity employer, is operated by the University of California for the U.S. Department of Energy under contract W-7405-ENG-36.



Cygnus—A New Radiographic Diagnostic for Subcritical Experiments

J.R. Smith, R.L. Carlson (P-22), R.D. Fulton (P-23), J.R. Chavez, P.A. Ortega, R.G. O'Rear, R.J. Quicksilver (DX-3), B. Anderson, D.J. Henderson, C.V. Mitton, R. Owens (BN), S. Cordova, J.E. Maenchen, I. Molina, D. Nelson, E. Ormond (SNL)

The subcritical experiment (SCE) program was initiated after the 1992 moratorium on underground nuclear testing in support of stockpile stewardship.¹ The dynamic material properties of plutonium are a major topic of exploration for the SCE program. In order to provide for a multilayered containment of plutonium, the SCEs are executed in the U1a underground tunnel complex at the Nevada Test Site (NTS). We developed Cygnus, a new radiographic x-ray source, for diagnostic support of the SCE program at NTS. We took the name Cygnus from the binary star Cygnus X-1, located in the constellation Cygnus, which is a strong x-ray source. For the special conditions related to this application, we emphasize design in areas affecting machine placement, remote operation, and reliability.

Typically, SCEs have been limited to surface diagnostics such as interferometry and pyrometry. The interferometry system commonly used on SCEs is called VISAR (velocity interferometer system for any reflector). We developed x-ray radiography to complement the existing surface diagnostics, provide a more extensive spatial view (albeit temporally limited), and provide internal (penetrating) measurements. The Stallion series of SCEs consists of four shots: Vito, Rocco, Mario, and Armando.² Armando was the initial experiment for Cygnus radiography. The Rocco, Mario, and Armando tests use identical physics packages, permitting the use of Armando radiographic results as a confirmation of VISAR measurements. The main x-ray source requirements for an SCE involve

spot size, intensity, penetration, and duration. The Cygnus source meets the following design specifications: ~ 1 mm diameter, 4 Rads dose at a distance of 1 m, ~ 2.25 MeV endpoint energy, and < 100 ns pulse length. Two Cygnus sources (Cygnus 1, Cygnus 2) were fielded on Armando providing two radiographic views separated in space by 60° and in time by 2 μ s.

Cygnus Design and Layout

A multiorganizational team (LANL, Bechtel Nevada, Sandia National Laboratories, Naval Research Laboratory, and Titan/Pulse Sciences Division [Titan/PSD]) was formed to design a prototype x-ray machine in response to the programmatic need for fielding a radiographic diagnostic on SCEs. The design concept is based on three criteria:

- (1) it must fulfill the radiographic source requirements as previously stated;
- (2) it must accommodate the U1a tunnel environment in terms of footprint, operations, and safety; and
- (3) it must be reliable.

To satisfy the first criterion, the key is use of the rod-pinch diode that is a low-impedance, high-dose diode.³ This approach yields a smaller source size

in comparison with other diode types. We met the footprint component of the second criterion by using a modular pulsed-power design where the energy storage unit (Marx) is independently located with respect to the inductive voltage adder (IVA), which are both connected by a coaxial water-transmission line. We achieved the reliability criterion by using proven pulsed power elements, extraordinarily conservative mechanical and pulsed-power designs, and an extensive test program.

The overall Cygnus layout in Figure 1 shows the two sources as fielded at NTS/U1a. Proceeding downstream, the major elements are: Marx generator, pulse-forming line, water-transmission line, IVA, and rod-pinch diode. Not shown is the high-voltage trigger generator used to initiate the Marx pulse. Titan/PSD integrated these pulsed-power elements into a design for the Cygnus system.⁴

Cygnus Test Plan and Deployment

Cygnus Prototype Tests at LANL. The “demonstration test” for Cygnus was performed at LANL. This test involves assembly of a prototype machine and testing via a series of shots designed to prove that the Cygnus design would meet or exceed x-ray source requirements

RESEARCH HIGHLIGHT

PHYSICS DIVISION



Instrumentation Research Highlights

(diameter, dose, endpoint energy, and pulse length), as well as operational requirements (reliability, reproducibility). A total of 118 prototype test shots were completed.

Shot analysis shows design specifications for the source were met or exceeded.⁵ Successfully demonstrating that the prototype machine meets all design criteria and provides an acceptable level of reliability, we proceeded with the project along the following paths:

- (1) Promotion of the existing machine from prototype to field status (i.e., a source suitable for use on a SCE shot) and designation as Cygnus 1. Relocation of Cygnus 1 to a LANL firing site (R-306) for extended testing.
- (2) Approval of fabrication and testing of a second source (Cygnus 2) at Titan/PSD.

Cygnus 1 Field Tests at LANL. Cygnus 1 was moved to the LANL firing site for the extended testing phase. At this site, a structure was built to replicate underground installation at U1a for the express purpose of certifying the instrument in a realistic environment. Matching R-306 and U1a features include: wall and ceiling dimensions; bulkhead wall construction; electrical-utility placement; and installation of a camera house, camera monitoring system, and a remote control system. We completed 202 shots at R-306.

The R-306 tests show that Cygnus 1 was

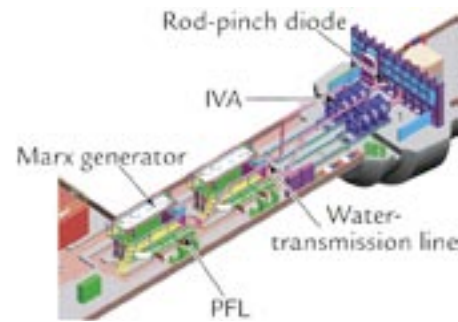


Figure 1. Cygnus 1 and 2 as fielded at NTS/U1a.

suitable for installation and operation in the U1a environment, did not produce levels of radiation adverse for operation of other planned diagnostics or systems, and produced images with the desired spatial quality and intensity. Therefore, Cygnus 1 was approved for underground installation at U1a.

Cygnus 2 Construction at Titan/PSD. Titan/PSD was contracted to deliver a second machine, Cygnus 2, which is similar to Cygnus 1 with the exception of a longer coaxial transmission line. Assembly and testing of Cygnus 2 paralleled with testing of Cygnus 1 at R-306. Testing at PSD consisted of 410 shots. Cygnus 2’s performance during the acceptance tests was similar to that of Cygnus 1, and the machine was ultimately approved for installation at U1a.⁶

Cygnus 1/Cygnus 2 Deployment at NTS/U1a. Figure 1 shows Cygnus 1 and 2 in the U1a.05 drift. Note that placing the Marx

tanks end-to-end and the IVAs side-to-side accommodates the tunnel dimensions. The rod-pinch diodes are oriented with a 60° included angle. A bulkhead containment wall separates the zero room, which houses the experiment, from the Cygnus machine area. The test object is contained in a 3 ft diam vessel, thereby permitting reuse of the zero room. The camera system is protected in a camera room that has 1 in. thick steel walls. Tungsten collimators are placed in the bulkhead wall and camera room wall to reduce image “noise” from scattered x-rays. Both Cygnus machines may be monitored and controlled either from a screen room located in the .05A drift alcove, or from a diagnostic trailer on the surface. A total of 237 shots, the sum of shots from both machines, were fired at U1a.

Table 1 gives a breakdown of the number of shots completed for each facility as well as for each source. The total shot number (967) is an indication of the considerable effort given in this endeavor.

Cygnus Reliability is a Key Operational Element

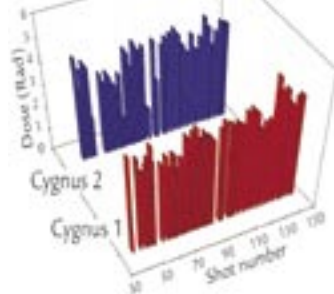
The risk inherent in the execution of a SCE is that a high-stakes package is expended in a single event where there is no reprieve from equipment failure. In this respect, an SCE is similar to a NASA rocket launch. On command, Cygnus must reliably deliver x-rays at a specified time. Because Cygnus radiography is the primary diagnostic for Armando, and therefore a key metric for its success, pressure to guarantee high reliability was intense. We were

especially concerned with two catastrophic failure modes for Cygnus that would result in losing the radiographic image. Just as in the rocket-launch scenario, a critical time in the SCE countdown specifies a “point of no return” where the event cannot be stopped. Both Cygnus failure modes correspond to malfunctions that occur after this critical time. The first failure mode is due to either a trigger

Table 1. Cygnus shot record

	LANL TA-3/SM-316				LANL TA-15/R-306				Titan/0PSD				NTS/U1a				Total
	MRX	PFL	LAD	RPD	MRX	PFL	LAD	RPD	MRX	PFL	LAD	RPD	MRX	PFL	LAD	RPD	
Cygnus 1	5	7	46	60	31	0	102	69					54	0	11	58	443
Cygnus 2									85	217	108	0	52	0	16	46	524
Total	118				202				410				237				967
The four shot modes are:																	
MRX = Marx resistive load									LAD = large-area diode								
PFL = pulse-forming-lines resistive load									RPD = rod-pinch diode								

Figure 2. Thermoluminescent dosimetry results for Cygnus 1 and 2 at U1a. Note, shot #100 is the confirmatory shot, and shot #144 is the Armando shot.



generator or Marx generator *prefire*, resulting in premature radiation. The second failure mode is a *no-fire* situation, where the Marx fails to breakdown on command due to either a trigger failure or Marx failure, resulting in no radiation.

The three provisions below were implemented to enhance the probability for success.

Readiness. Historically, the Cygnus trigger generator and Marx generator components have exhibited a tendency for failure. In order to check these components, as well as the control and data acquisition systems, we instituted a preliminary shot procedure. This involves firing a dual-resistive load shot approximately 15 to 30 minutes before the planned radiography shot. This procedure is very effective in discovering preshot personnel error or equipment failure and in assuring system readiness.

Prefire Protection. Although we thought that trigger-generator problems previously discovered during prototype tests were fixed, initially there were frequent trigger-generator prefires on both Cygnus machines at U1a. As a result, we sent the trigger generators to LANL for extensive evaluation, testing, and modification to remedy the problem. We implemented an additional level of precaution to prevent prefire: we turned on the trigger generator high-voltage power supply just before a shot (~ 10 s). This method minimized the exposure to prefire and worked well even with trigger generators prone to prefire. Dirty spark gaps, as was discovered early in the program, encourage Marx

generator prefire. Spark-gap purging is included as a command in the control software. It is done liberally (i.e., with significant gas flow) and often. Several Marx generator prefires occurred on Cygnus 1 just before the confirmatory shot. After the confirmatory shot, an inspection revealed the cause as several broken trigger resistors. After replacing the resistors, and during the period between the confirmatory shot (#100) and the Armando shot (#144), neither Cygnus machine experienced trigger-generator or Marx-generator prefires.

No-Fire Protection. Marx no-fires are typically caused by spark gap overpressure. Too much pressure leads to a no-fire, while too little pressure yields prefires. The Cygnus Marx pressures were set to favor the prefire case because there are no timely warnings for a no-fire, while the prefire has a good probability of occurrence before the critical time where the shot can be “saved.” We observed zero no-fire events on either machine.

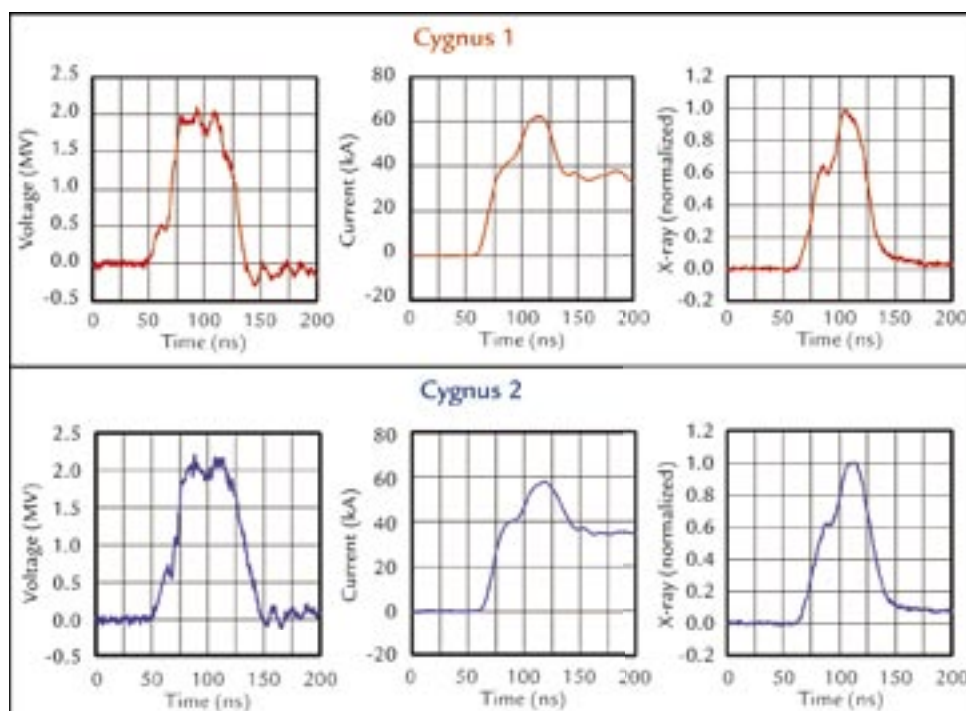
Cygnus Reproducibility is a Key Operational Element

Shot-to-shot reproducibility of x-ray parameters is an important demonstration that source quality is consistent and that good radiography performance will likely be delivered on the Armando shot. It is also important because reproducible shots are required to baseline other diagnostic systems (e.g., to produce a repeatable electromagnetic interference background) and adjust the camera imaging system (e.g., alignment, intensity).

Dose results for U1a shots are shown in Figure 2. The gaps in the data primarily represent nonradiation shots, either the Marx resistive load or large area diode test modes. The low-dose shots, most predominantly seen on Cygnus 2, were caused by alignment or vacuum problems in the diode. These problems had been fully addressed by the day of the confirmation shot.

The average dose for all rod-pinch shots in the time period from the confirmation shot to the Armando shot is: 4.4 ± 0.5 Rad

Figure 3. Diode voltage, diode current, and x-ray waveforms for the Armando shot #144.



Instrumentation Research Highlights

(Cygnus 1) and 4.1 ± 0.4 Rad (Cygnus 2). These measurements are standardized for a source-detector distance of 1 m, and for attenuation through 1 in. thick aluminum. Endpoint voltage is an indication of source penetration. The endpoint voltage for the same database as cited above is: 2.1 ± 0.1 MV (Cygnus 1) and 2.3 ± 0.1 MV (Cygnus 2). Reproducibility in Cygnus source intensity and penetration, shown by the standard deviation in dose and endpoint voltage above, easily satisfies the desired shot-to-shot performance.

Conclusion—Cygnus Succeeds on the Armando SCE

The Armando shot was executed on May 25, 2004. The efforts of more than three years of planning and testing are encompassed in Cygnus performance on this single shot. It is, therefore, appropriate to conclude by presenting Armando results. Diode voltage, diode current, and x-ray waveforms (Figure 3) are key indicators of Cygnus performance. By visual comparison of the Cygnus 1 and 2 waveforms, it is evident that both machines produced markedly similar results. Several quantitative measurements of Cygnus performance on the Armando shot are given in Table 2. The measurements are placed in three categories representing different facets of machine output: Cygnus diode, electrons, and x-rays. On the Armando shot, Cygnus 1 (Cygnus 2) satisfied source requirements as follows: ~ 1 mm x-ray source diameter, 4.5 (4.2) Rad dose, 2.1 (2.2) MeV endpoint energy, and 47 (48) ns pulse length. Additionally, the desired timing with a pulse separation of $2 \mu\text{s}$ was delivered. The success of Cygnus at U1a is a historical milestone that demonstrates the feasibility of fielding

Table 2. Armando shot summary

Shot #144	Cygnus Diode		Electrons		X-rays	
	Endpoint Voltage (MV)	Average Impedance (W)	Total # ($\times 10^{16}$)	Average Energy (MeV)	Dose (Rad)	Pulse Length (ns)
Cygnus 1	2.1	38	2.2	1.5	4.5	47
Cygnus 2	2.2	42	2.1	1.6	4.2	48

large and complex diagnostic systems downhole. Its success paves the way for Cygnus participation in future SCEs as well as promotes consideration of even larger radiographic facilities at U1a.

References

1. L.R. Veaser *et al.*, "Subcritical plutonium experiments at the Nevada Test Site," 1997–1998 *Physics Division Progress Report*, Los Alamos National Laboratory report LA-13606-PR (May 1999) pp. 94–101.
2. D. Fulton, M.D. Wilke, and N.S.P. King, "Dynamic material studies in subcritical experiments: Rocco, Mario, Vito, and Armando," *Physics Division Activity Report*, Los Alamos National Laboratory report LA-14112-PR (February 2003) pp. 23–26.
3. G. Cooperstein *et al.*, "Theoretical modeling and experimental characterization of a rod-pinch diode," *Physics of Plasmas* **8**, 4618–4636 (2001).
4. D. Weidenheimer *et al.*, "Design of a driver for the Cygnus x-ray source," *Proceedings of the 13th IEEE International Pulsed Power Conference*, R. Reinovsky, M. Newton, Eds. (IEEE, Piscataway, New Jersey, 2001), Vol. (1) pp. 591–595.
5. J.R. Smith *et al.*, "Performance of the Cygnus x-ray source," *Proceedings of the 14th International Conference on High Power Particle Beams*, T.A. Melhorn, M.A. Sweeney, Eds. (AIP, Melville, New York, 2002), Vol. (1), pp. 135–138.
6. V. Carboni *et al.*, "Pulse power performance of the Cygnus 1 and 2 radiographic sources," *Proceedings of the 14th IEEE International Pulsed Power Conference*, M. Giesselmann, A. Neuber, Eds. (IEEE, Piscataway, New Jersey, 2003), Vol. (2) pp. 905–908.

Acknowledgment

We gratefully acknowledge support for this work from many colleagues in Physics and Dynamic Experimentation Divisions at LANL, and from colleagues at Bechtel Nevada, Sandia National Laboratories, Titan/PSD, and Naval Research Laboratory. Special recognition is given for Nevada Operations and Bechtel Nevada support at NTS which was instrumental in fielding Cygnus at U1a. This work was sponsored by the U.S. DOE.

For further information, contact
John R. Smith, 505-665-8546,
smith@lanl.gov.

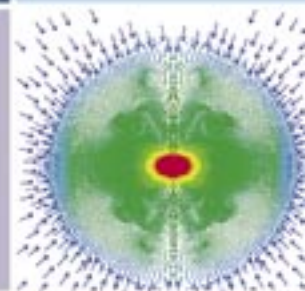
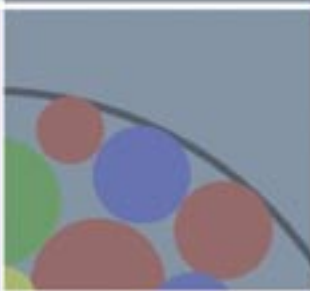
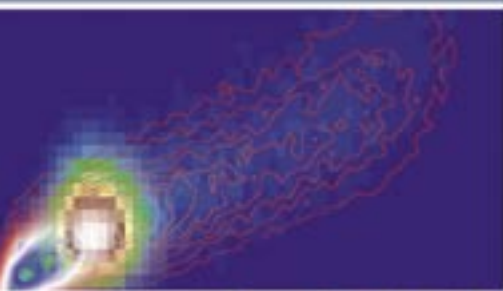
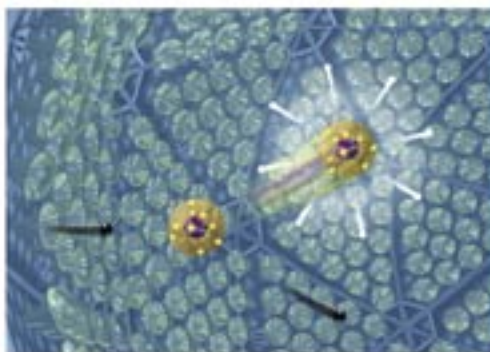
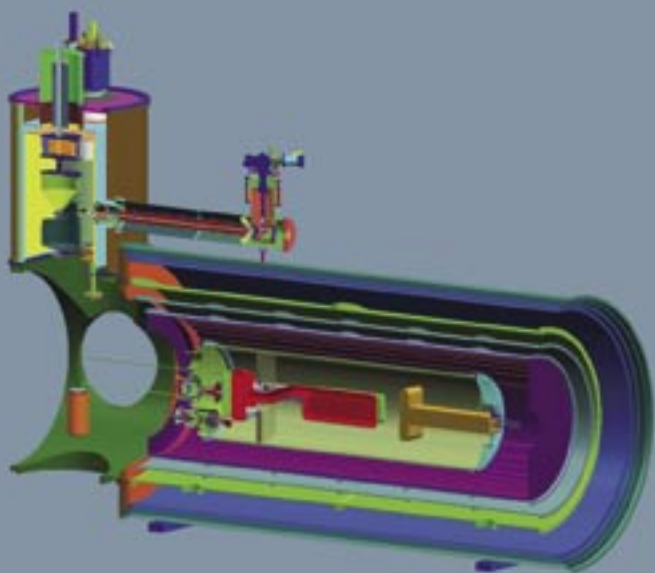


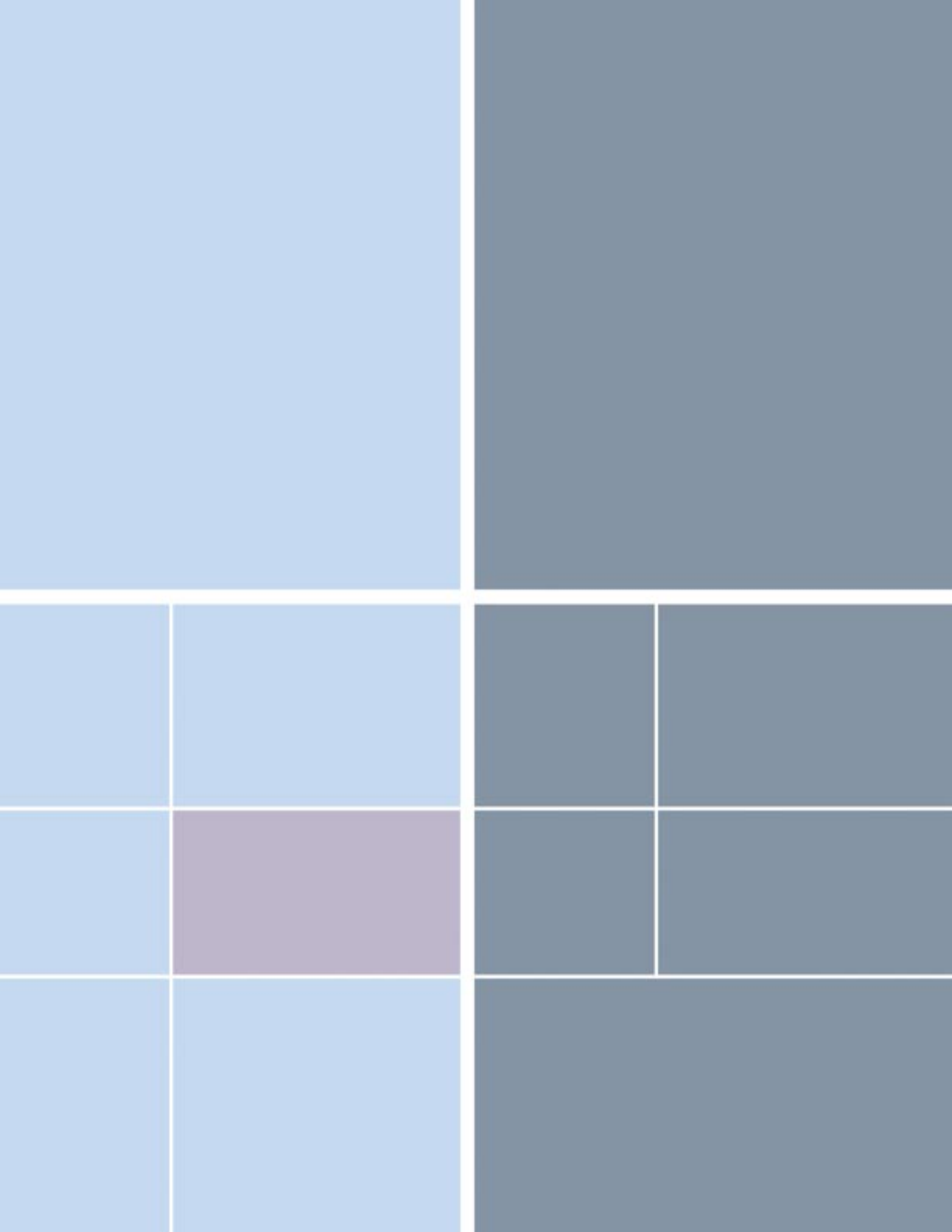
The World's Greatest Science Protecting America

Los Alamos National Laboratory, an affirmative action/equal opportunity employer, is operated by the University of California for the U.S. Department of Energy under contract W-7405-ENG-36.



Nuclear Physics and Astrophysics Research Highlights



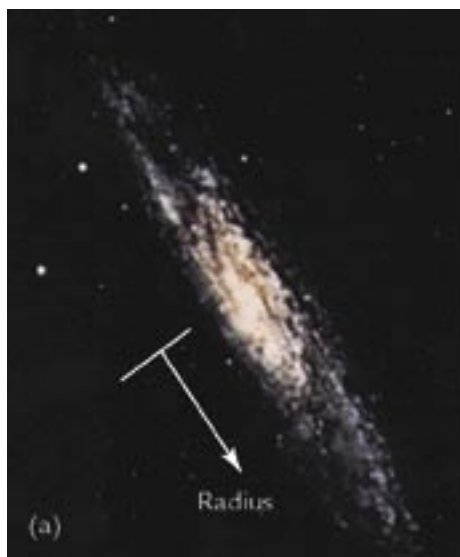


Detection of Dark Matter and Low-Energy Solar Neutrinos with Liquid Neon

M.G. Boulay, A. Hime, J. Lidgard, D.-M. Mei (P-23)

The origin of dark matter in our universe and the study of low-energy solar neutrinos are two of the foremost topics in particle astrophysics. It has long been known that much of our universe is composed of an undetected form of matter, known as *dark matter*. Initial evidence for dark matter came from rotation curves of galaxy clusters and galaxies, an example of which is shown in Figure 1(b). Objects at very large distances from galactic centers are found to have velocities too large to be gravitationally bound by only the visible matter in the galaxy. Additional matter must be present to account for the fact that these objects are indeed bound by gravitational forces. A currently favored hypothesis is that dark matter consists of a new type of particle, a weakly interacting massive particle (WIMP), which has so far remained undetected.

Current searches for dark matter attempt to detect WIMPs from our galaxy's dark-matter halo through their elastic scattering on target nuclei. Because the interaction between WIMPs and matter is extremely weak, event rates in terrestrial detectors are low. Current experimental searches are limited by the total mass of target material achievable, with limits on the WIMP interaction rate on the order of events per kilogram of detector material per day. Extreme care must be taken to reduce sources of background contamination in these experiments. The goal for next-generation experiments is to improve sensitivity by several orders of magnitude, with target masses on the order of tons.



Distribution of dark matter in NGC 3198

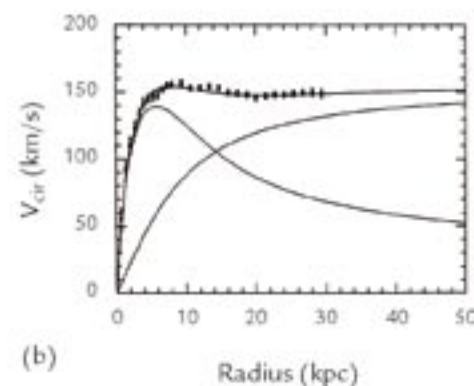


Figure 1. (a) Optical image of galaxy NGC 3198.¹ "Radius" is the distance from the galactic center. (b) Distribution of velocities versus radius.² The curve labeled "disk" shows the contribution from visible objects in the galactic disk. The curve labeled "halo" shows the contribution from a dark-matter halo required to explain the experimental result.

Since the experimental discovery of the neutrino by a team of LANL researchers, the field of neutrino physics has become rich with new insights into the fundamental properties of the neutrino. A wide range of the solar neutrino spectrum (Figure 2) has been probed by solar-neutrino experiments during the past four decades. LANL has played a leading role in the Sudbury Neutrino Observatory (SNO), recent results of which have conclusively

shown that electron neutrinos (ν_e) emitted in the sun undergo transformation into other neutrino flavors (ν_μ, ν_τ), solving a decades-old problem of missing solar neutrinos.^{3,4} Future experimental efforts on solar neutrinos will focus on very precise measurements of the lowest-energy solar neutrinos. The flux of pp neutrinos is very well predicted by standard models of solar evolution and is tightly constrained by the observed solar luminosity.

RESEARCH HIGHLIGHT

PHYSICS DIVISION

Nuclear Physics and Astrophysics Research Highlights

Measurement of this component of the solar spectrum with high precision and in real time will shed light onto both the solar models and the fundamental properties of the neutrinos themselves.

Cryogenic Low-Energy Astrophysics with Neon

The CLEAN (Cryogenic Low-Energy Astrophysics with Neon) experiment (Figure 3) will be sensitive to the low-energy pp solar neutrinos (ν_x) and to WIMP particles (χ) through their elastic scattering from electrons and neon nuclei, respectively:

$$\nu_x + e^- \rightarrow \nu_x' + e^- \quad (1)$$

$$\chi + \text{Ne} \rightarrow \chi' + \text{Ne}' \quad (2)$$

The recoiling electrons (ν_x') or neon nuclei (Ne') lead to the production of scintillation photons in the liquid neon (approximately 15,000 photons per MeV of kinetic energy), which can then be detected by the photomultiplier tubes (PMTs). The concept of a liquid-neon scintillation detector on which this work is based was first put forward by McKinsey and Doyle.⁶ The proposed experiment consists of a large volume of liquid neon surrounded by 1842 PMTs

that detect scintillation photons produced by the recoiling electrons (e^-) or Ne' from reactions (1) and (2). A key to the CLEAN experiment is the difference in emission times of scintillation photons from reactions (1) and (2), allowing discrimination between these two reactions. At the projected sensitivity of the CLEAN experiment, low-energy solar neutrinos occur at rates much greater than the WIMP scattering rates, and separating these event types is critical to the success of the experiment. CLEAN is projected to measure the dominant pp component of the solar-neutrino flux with 1% precision.

To evaluate the detector's capability, we performed detailed Monte Carlo simulations. Nominal properties associated with the production and propagation of scintillation photons (scintillation yield, scattering lengths, etc.) and PMTs with currently achievable background levels were assumed in the simulation. PMT glass contains small traces of uranium, thorium, and potassium, which can decay and generate scintillation photons that could then be mistaken for signal events. Many of the properties of scintillation light in neon are not well known, and part of the current experimental program at LANL is to improve our knowledge of these.

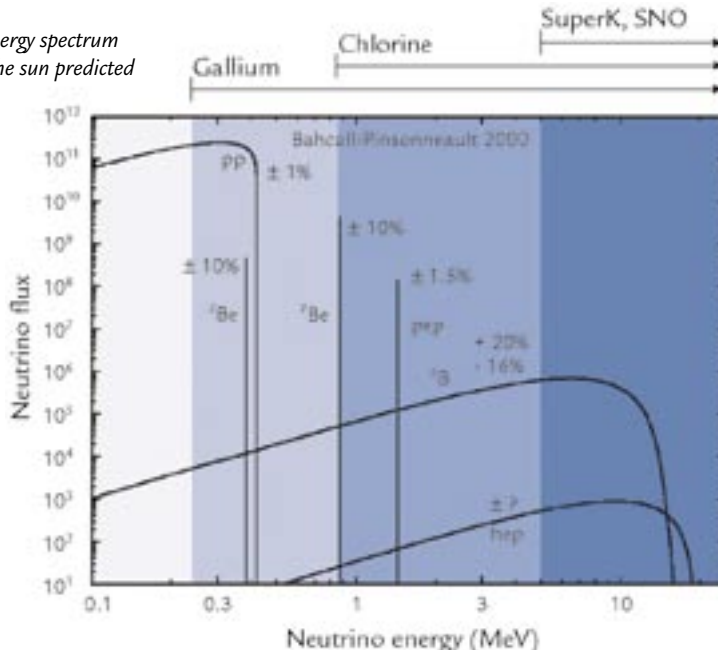
Scintillation-Event-Position Reconstruction

Scintillation events from radioactive decays in the PMTs or other sources of radioactivity external to the neon are a potential background to the solar-neutrino or WIMP scintillation signals. Reducing this background to an acceptable level requires the reconstruction of scintillation-event positions based on the PMT data, which samples the scintillation photons. We have developed a new position reconstruction algorithm based on our detector simulation. The algorithm shows significant improvement over earlier geometrical reconstruction algorithms by including PMT timing information (Figure 4). The reconstruction of scintillation-event positions is critical to the success of CLEAN because it allows us to use a large target mass of neon necessary for WIMP sensitivity with a very low-energy threshold (approximately 12 keV) essentially free of PMT backgrounds.

Background Contamination

Purification of the neon is expected to reduce background contamination from internal sources of radioactivity significantly because at the very low temperature of liquid neon most impurities will bind efficiently to carbon and can thus be removed by cold traps. The PMTs and associated hardware will contain the largest amount of radioactive contamination near the inner detector volume, and these are mitigated by applying position reconstruction algorithms described above. The dominant internal source of background for CLEAN is expected to be krypton-85 because it has a relatively short half-life (approximately 11 years), decays through e^- emission with energies in the same range as the ν_x neutrinos (Q -value = 687 keV), and is present in the atmosphere. Several other naturally occurring radioactive contaminants will need to be removed from the neon to achieve acceptable background levels for neutrino detection.

Figure 2. The neutrino energy spectrum from fusion reactions in the sun predicted by Bahcall and Pinsonneault.⁵ Solar neutrino experiments have detected neutrinos over most of the energy range. The gallium and chlorine experiments have measured integral fluxes of neutrinos with radiochemical techniques; SNO and SuperK have detected the higher-energy neutrinos in real time. The goal for next-generation experiments is to measure with high precision and in real time the lowest-energy solar neutrinos.



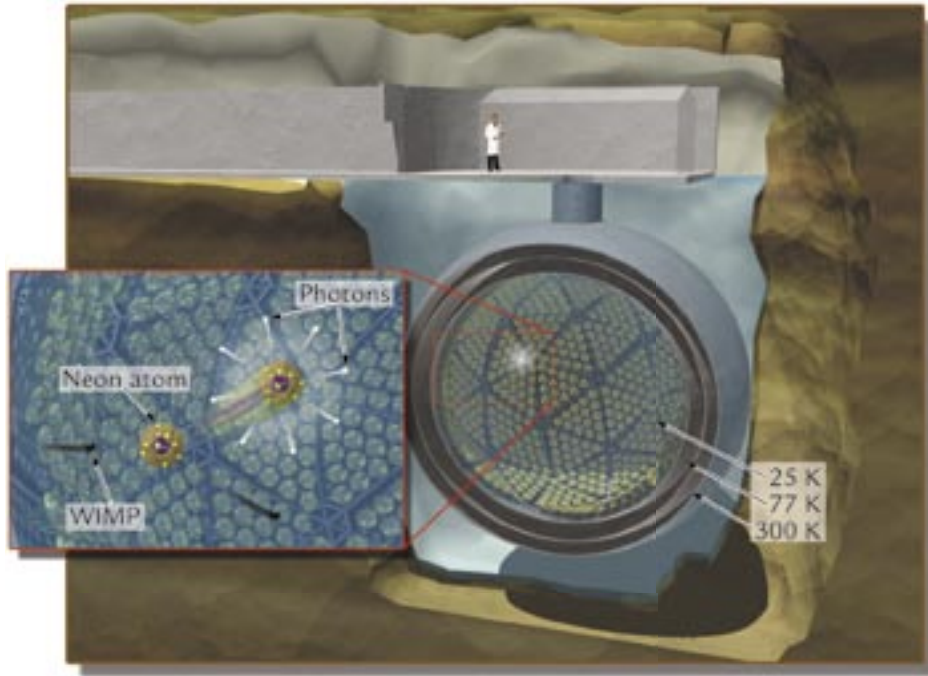


Figure 3. The CLEAN experiment. A spherical array of 1842 PMTs look inward into a large volume of liquid neon (at approximately 25 K). Elastic scattering of neutrinos or WIMP particles from electrons or neon nuclei (respectively) lead to the production of scintillation photons, which are then detected by the PMTs. Data from the PMTs are then used to reconstruct the event position and energy and statistically separate neutrino interactions, WIMP interactions, and background events.

Conclusions

We have demonstrated the possibility for a simultaneous dark-matter and low-energy neutrino experiment using liquid neon, assuming nominal scintillation characteristics and background contamination levels. Assuming the required background contamination levels can be achieved, the large target mass possible with neon may lead to the best sensitivity for detecting dark-matter particles. The current research and development program at LANL focuses on providing precise measurements of some of the fundamental scintillation properties in liquid neon and achievable background contamination levels, both of which are critical to the feasibility of the experiment. A test cell of approximately 5 kg of neon is being designed to measure the precise scintillation time distribution for both electron and nuclear recoils in liquid neon. A system currently under construction will clean neon gas of impurities using cold traps, with the goal of ultimately demonstrating the background requirements needed for the full-scale detector. Studies are under way to design a small-scale prototype that could be used to further assess scintillation and background properties and provide initial limits on WIMP interactions.

Projected Sensitivity

By evaluating the detector response from Monte Carlo simulations and including the effects of background contamination from PMTs, internal radioactivity, and solar neutrinos, we have evaluated the ultimate sensitivity to WIMP dark matter (see Figure 5). The cross sections (interaction strength) for WIMP-nucleon interactions and the WIMP's mass are both unknown, and both affect the signal seen in CLEAN so that the sensitivity depends on these two parameters. For a 300 cm radius detector, we find an experimental sensitivity to dark matter that is several orders of magnitude better than current searches and competitive with proposed searches.

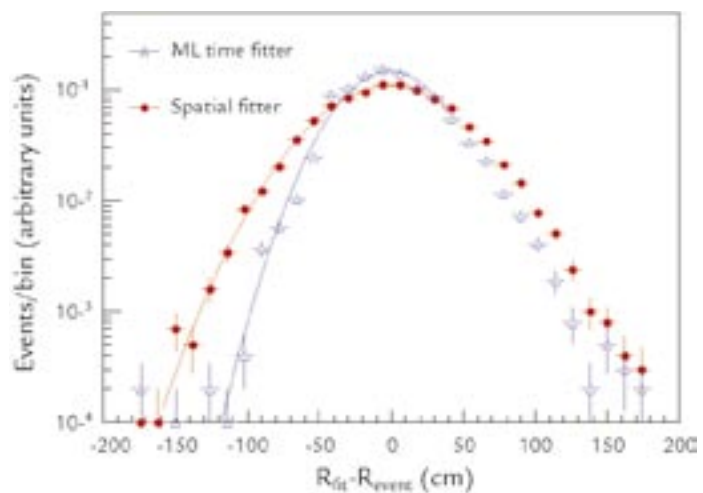


Figure 4. Reconstructed position distributions for simulated low-energy events in CLEAN. Shown are the differences between the reconstructed event radius and the true event radius, which is simulated at the PMTs. The improved reconstruction algorithm, including PMT time information, significantly improves position resolution and allows us to use a much larger volume of neon for analysis of dark-matter interactions.

Nuclear Physics and Astrophysics Research Highlights

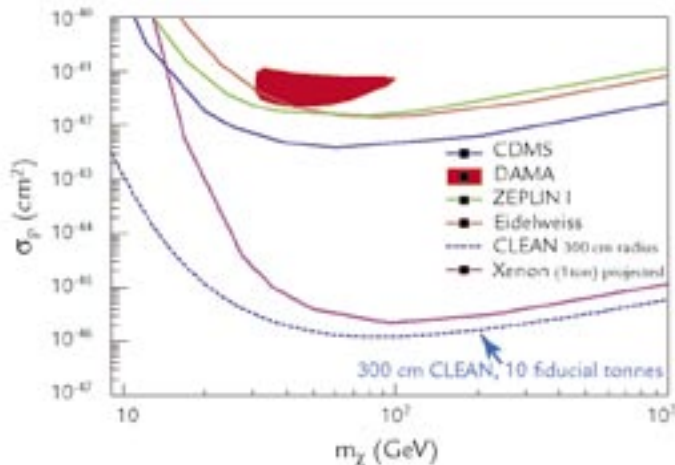


Figure 5. Projected sensitivity to dark-matter interactions with CLEAN and other experimental searches. The curves indicate combined exclusion regions for the WIMP's mass (m_χ) and for the WIMP-nucleon interaction strength (σ_p). The current best experimental sensitivity is from the Cryogenic Dark Matter Search (CDMS) experiment. CLEAN is projected to improve this sensitivity by four orders of magnitude. A combination of parameters above the sensitivity limit would be seen as evidence for WIMP particles in CLEAN. Data for other experiments are adapted from Reference 7.

References

1. Image of NGC 3198 adapted from *The Galaxy Catalog*, http://www.astro.princeton.edu/~freil/Gcat_html/Catalog/CJpeg/n3198.jpg.
2. T.S. van Albada *et al.*, "Distribution of dark matter in the spiral galaxy NGC 3198," *The Astrophysical Journal* **295**, 305–313 (1985).
3. S.N. Ahmed *et al.*, (SNO Collaboration), "Measurement of the total active 8B solar neutrino flux at the Sudbury Neutrino Observatory with enhanced neutral current sensitivity," *Physical Review Letters* **92**, 181301-1–181301-6 (2004).
4. A. Hime *et al.*, "The Sudbury Neutrino Observatory—Taking physics beyond the standard model," Los Alamos National Laboratory report LA-14112-PR (2003).
5. J.N. Bahcall, M.H. Pinsonneault, and S. Basu, "Solar models: Current epoch and time dependences, neutrinos, and helioseismological properties," *Astrophysical Journal* **555**, 990–1012 (2001).
6. D.N. McKinsey and J.M. Doyle, "Liquid helium and liquid neon-sensitive, low background scintillation media for the detection of low energy neutrinos," *Journal of Low Temperature Physics* **118**, 153–165 (2000).
7. SUSY/Dark Matter Interactive Direct Detection Limit Plotter, <http://dmttools.berkeley.edu/limitplots>.

Acknowledgment

This work is supported with funds from the LANL Laboratory-Directed Research and Development program.

For further information, contact Mark Boulay, 505-665-3821, mboulay@lanl.gov.



The World's Greatest Science Protecting America

Los Alamos National Laboratory, an affirmative action/equal opportunity employer, is operated by the University of California for the U.S. Department of Energy under contract W-7405-ENG-36.



Research and Development Progress toward a New Search for the Electric Dipole Moment

M. Cooper (P-25), S. Lamoreaux (P-23) representing the EDM Collaboration

A nonzero electric dipole moment of the neutron (nEDM) would be an exciting discovery because it would either solve the “strong *CP*” problem (see below) or reveal new physics beyond the standard model of electroweak interactions. In the neutron, an EDM would arise from a slight separation of positive and negative charges along the spin axis. Such a separation allows for an interaction with an applied electric field that has space-time transformations that break the time-reversal symmetry (*T*). Symmetries of nature have their origin in conservation laws. No such law exists for the strong interaction, the origin of the nuclear force, and time reversal is expected to be broken. However, extremely sensitive searches for a nonzero nEDM have given null results. Furthermore, great experimental effort has been devoted to the search for a particle called the axion that could be the signature of an undiscovered conservation law; these searches have also provided negative results. A substantially more sensitive search for a nEDM would sharpen this conflict in our understanding.

A nonzero value for the nEDM is expected to arise at a very small value ($\sim 10^{-31}$ e·cm) due to the violation of time reversal discovered in the strange- and bottom-quark systems. Between this (nearly) immeasurably small value and the current experimental limit of 6×10^{-26} e·cm,¹ there exists a window for discovery of new phenomena in the standard model. Physicists have two exciting motivations to look for the nEDM: the highly popular idea of supersymmetry, which remains to be proven, predicts a value in the range

10^{-26} – 10^{-28} e·cm; the dominance of matter over antimatter in the universe resists quantitative explanation, and another source of *T* violation could resolve this puzzle.

An international team of scientists has proposed a new method to search for the nEDM that promises to increase sensitivity by two orders of magnitude.² To measure a nEDM, polarized neutrons are placed in a weak magnetic field and strong electric field. The magnetic field causes neutron precession about the field direction with a predictable frequency. An EDM slightly modifies the frequency in proportion to the value and sign of the applied electric field. In the new method, a small quantity of another species, polarized helium-3, is placed in the same container as the neutrons. The helium-3 has a very similar magnetic dipole moment to the neutron but is known not to have an EDM greater than 10^{-29} e·cm. The helium-3 precession occurs at nearly the same rate as the neutron precession, and any shift of the neutron frequency with respect to the helium-3 frequency that is proportional to the electric field will be the signature of an nEDM.

Both the neutrons and helium-3 are contained in a measurement cell filled with superfluid helium-4. Neutrons can

be bottled in a cell if their energy is low enough for them to be reflected by the Fermi potential of the walls; they are called ultracold neutrons (UCNs). UCNs are produced³ in the cell by down scattering cold neutrons off the helium-4. The cross section for absorption of neutrons by helium-3 is highly spin-dependent, and the helium-3 serves as an analyzer of the relative precession frequency between the two species. If a neutron is absorbed, the reaction products lose their kinetic energy in the helium-4, which in turn scintillates. The detection of this scintillation light measures the beat frequency between the two species. As a control measurement, the precession frequency of the helium-3 is measured with superconducting quantum interference devices. The helium-3 is referred to as a comagnetometer because it occupies the same volume as the neutrons and measures the magnetic field.

The proposal has been reviewed by the Nuclear Science Advisory Committee and has been deemed to be the experiment with the greatest discovery potential for the new fundamental-neutron-science beam line at the Spallation Neutron Source.⁴ The committee recommended a vigorous program of research and development (R&D) to validate the measurement technique and to work out the most significant engineering challenges

RESEARCH HIGHLIGHT PHYSICS DIVISION



Nuclear Physics and Astrophysics Research Highlights

as well as eventual funding for the project. In order to control a variety of systematic errors that could produce a false result, the experimental apparatus must meet stringent design requirements. Significant progress has been made towards validation of the method.

The Electric Field

Whereas the sensitivity of the measurement is proportional to the magnitude of the electric field, this experiment has a goal of $50 \text{ kV}\cdot\text{cm}^{-1}$, roughly five times that of previous measurements. Liquid helium-4 is a very good dielectric, i.e., will break down only at quite a high voltage. However, all previous measurements of its dielectric strength were performed with small surface areas and small gaps between the electrodes. The proposed experiment will have electrodes exceeding 600 cm^2 and a separation of 7.5 cm. We felt it necessary to demonstrate that we can achieve the desired voltage because the breakdown voltage is believed to scale as the square root of the separation.

A full-scale apparatus has been built at LANL to measure the dielectric strength in the relevant geometry. The electrodes are constructed so that the gap between them is variable. The high-voltage electrode is charged to about 50 kV with a power supply and then disconnected from the supply. As the electrode gap is increased, the voltage is multiplied to keep the field constant. Figure 1 shows a plot of the breakdown voltage as a function of separation. The curve in the figure is the breakdown voltage calculated assuming a square-root-of-the-gap dependence. The curve is normalized to the work of other investigators, all of which occurred below 10 mm. Our value of $570 \pm 70 \text{ kV}$ is the point at 73 mm. The voltage was stable for 11 h. In order to achieve $50 \text{ kV}\cdot\text{cm}^{-1}$ in the actual experiment, a larger variable capacitor will be attached in parallel with the fixed electrodes of the measurement cell.

The sign of the change in precession frequency with electric field for a real EDM should reverse if the sign of the field is reversed. Furthermore, at the very highest densities of UCNs, ionization produced by the decay or absorption of neutrons will discharge the electrodes slowly during the measurement. Thus, the value of the electric field needs to be known for both polarities. As part of our collaboration, Berkeley has proposed to use the Kerr effect to make an *in situ* measurement of the electric field. The Kerr effect is the rotation of polarized light passing through a high electric field. The size of the effect is proportional to the square of the electric field, and the proportionality constant is called the Kerr constant. Figure 2 shows the first measurement of the Kerr effect in superfluid liquid helium-4. The quadratic dependence is clear. The extracted value⁵ of the Kerr constant is $(1.43 \pm 0.02^{(\text{stat})} \pm 0.04^{(\text{sys})}) \times 10^{-20} (\text{cm/V})^2$ at $T = 1.5 \text{ K}$. The measurement at each voltage was made with roughly 3.5 cm of liquid helium-4 and took 1000 s. With a 50 cm path that is expected in the real application, the time for a measurement should be short enough to meet our needs.

The Magnetic Field

To preserve the polarization of the neutrons and the helium-3, magnetic-field uniformity must be 10^{-3} . The measurement cell must be shielded against μG external fields. The scheme

we have selected consists of a multilayer shield of highly permeable material that surrounds a superconducting shield. The constant field is produced by a $\cos\theta$ coil inside the superconducting shield. The magnetic-field boundary conditions of the superconducting shield are incompatible with the coil. The coil will produce a very uniform field if it is wound inside an additional ferromagnetic layer. Because the experiment runs at cryogenic temperatures, it is necessary to select a ferromagnetic material that preserves its permeability at such temperatures. We have studied Metglas, a commercially available amorphous metal. Figure 3 shows the measured inductance of the Metglas as a function of temperature to be sufficient to meet our needs.

The Helium-3 Comagnetometer

The handling of the polarized helium-3 requires many complicated steps. We must

- produce highly polarized helium-3,
- inject it into a superfluid helium-4 bath while maintaining the polarization,
- maintain the polarization during the measurement, and
- remove the helium-3 once it depolarizes.

Figure 1. The breakdown voltage for liquid helium versus electrode separation.

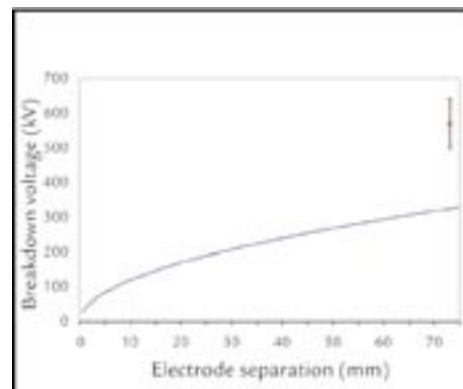
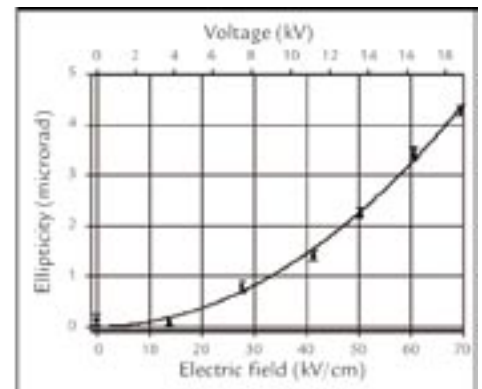


Figure 2. The Kerr effect in liquid helium at $T = 1.5 \text{ K}$: induced ellipticity as a function of the electric field between the electrodes. The potential difference between the electrodes is shown on the upper scale.



The production step is accomplished with an atomic beam source. Helium-3 atoms at 1 K are injected into a quadrupole magnet. This magnet configuration produces a gradient field that is appropriate to focus only one spin through the apparatus. The other spin is removed with vacuum pumps. This type of device is known to produce very high polarization but sufficient intensity to meet our needs.

An atomic beam source has been built at LANL to verify its performance. In order to know the polarization, a second quadrupole magnet has also been built to act as an analyzer of the emitted atomic beam. The two magnets are separated by a region where radio frequency coils can manipulate the spins to measure the polarization. The polarization of the source has been measured to be $99.5 \pm 0.25\%$. The flux was approximately 4×10^{14} atoms/s.

The polarization must be maintained until the measuring cycle is complete. The problem has been broken into two parts, one where the atoms are injected into the system and one where the polarization is maintained in the measurement cell. The former is the subject of future R&D. The polarization relaxation time depends on the wall material of the container. The mechanisms for depolarizing the atoms vary significantly over the temperature range between 0.1–4.3 K. The expectation is that the relaxation time will decrease

as the temperature is lowered to 1 K and then rise rapidly below 1 K. The operating temperature of the experiment is 0.3 K. The cell walls have been chosen to be deuterated styrene impregnated with a deuterated wavelength shifter in order to minimize UCN absorption on the walls and to aid in the detection of the scintillation light.

Duke University is studying relaxation times at temperatures above 2 K. An ideal relaxation time is in excess of 8 h, which implies a depolarization of a few percent during an EDM measuring cycle. The Duke investigators are comparing the relaxation times in glass cells to those in cells where beads coated with deuterated styrene have been added. Thus far, they have achieved times in excess of 7 h in pure glass cells. They see no degradation when the coated beads are added.

The EDM collaboration has measured the diffusion coefficient for helium-3 in superfluid helium-4 between 0.45–0.95 K.⁶ The measurement was carried out at Los Alamos Neutron Science Center employing neutron tomography. The results are shown in Figure 4. The measurement verifies predictions that the diffusion coefficient varies as T^{-7} below 0.7 K and allowed us to determine the temperature where the ballistic velocity of neutrons equals the diffusion velocity of the helium-3. Between 0.1–0.6 K, the average

velocity of the helium-3 is sufficient to allow escape from the superfluid helium-4. This realization leads towards the possible design of a system to remove depolarized helium-3 from a mixture by simply pumping on the bath.

The heat-wind technique can produce our initial charge of ultrapure helium-4 ($< 10^{-13}$ atoms of helium-3).⁷ Phonons couple strongly to helium-3 and weakly to helium-4. The phonons can be used to blow the helium-3 away from a source of heat. When liquid helium-4 at ~ 1 K is passed through a capillary tube surrounded by a resistive heater, only pure helium-4 passes. A cryostat designed for this purification process has been built at the Hahn-Meitner Institut and was operated at LANL. The first sample has been analyzed at Argonne National Laboratory and shown to have a purity of at least 10^{-12} .

Neutron Absorption Identification

The possibility to identify neutron absorption in liquid helium-4 has been reported by the method of after-pulses.⁸ If the scintillation light produced by other mechanisms can be discriminated against, the scintillation signal has the possibility of being nearly background free, increasing the sensitivity of the measurement. The method of after-pulses consists of plotting the number of single photoelectrons detected in the 10 μ s following the main scintillation pulse plotted versus the total scintillation light. The events due to absorption produce more highly ionizing particles than background beta particles. Both the highly ionizing particles and betas excite dimers in the helium-4, but the absorption events have a longer de-excitation time and thus, more late after pulses. Figure 5 shows the effect in data taken by the collaboration at the Hahn-Meitner Institut. These data show the promise of greatly reducing a variety of backgrounds in the experiment.

Figure 3. The inductance of Metglas versus temperature.

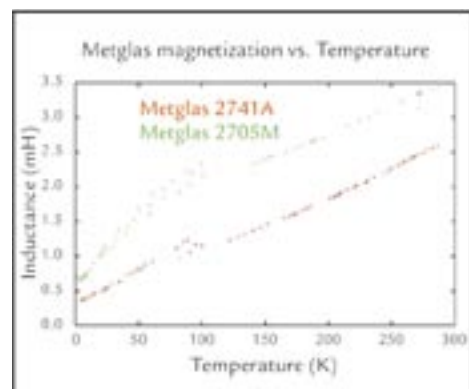
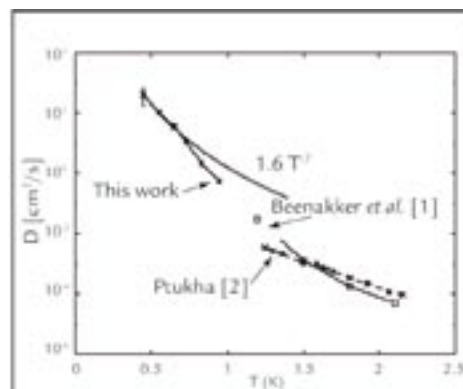


Figure 4. A comparison of our results for the mass diffusion coefficient D of helium-3 in superfluid helium-4 below 1 K with those of previous workers at higher temperatures.



Nuclear Physics and Astrophysics Research Highlights

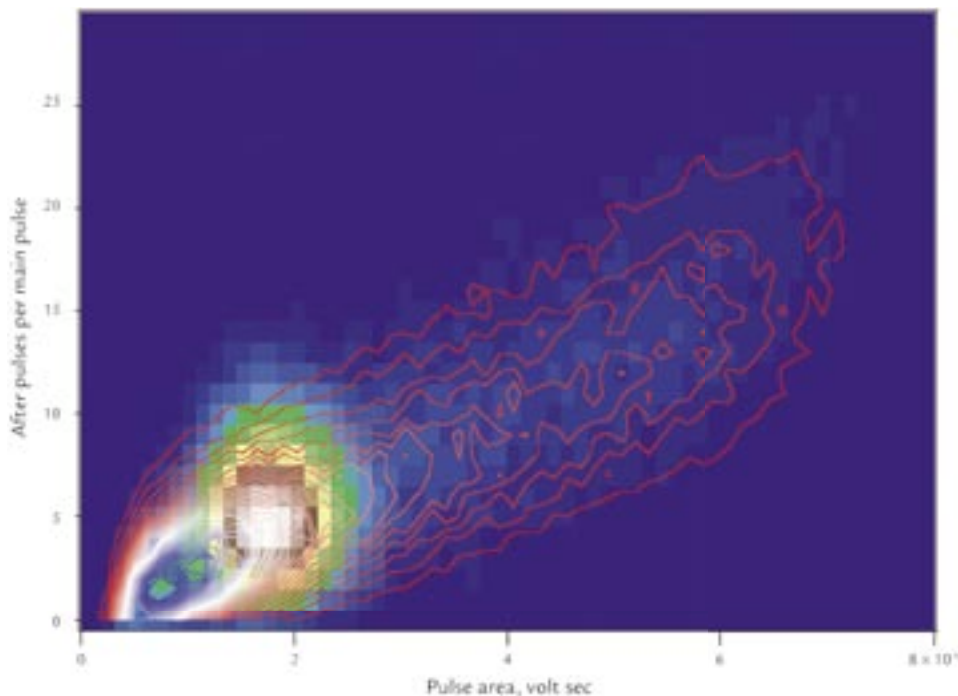


Figure 5. The separation between helium-3 absorption of neutrons and betas at 300 mK: number of after-pulses as a function of pulse height. The image plot is the absorptions and the contour plot is the betas.

Future R&D

A challenging task is to build a single piece of apparatus to contain all these different elements simultaneously that may be assembled and serviced. The engineering staff at LANL has made great progress toward reaching a reference design.

The EDM Collaboration has made great strides in developing a new experiment for a nEDM search. The collaboration has many other projects underway. Most of the crucial performance criteria of the detector components have been demonstrated. The future R&D is focused on bringing new concepts to the experiment to reduce backgrounds and systematic errors.

References

1. P.G. Harris *et al.*, "New experimental limit on the electric dipole moment of the neutron," *Physical Review Letters* **82**, 904–907 (1999).
2. R. Golub and S.K. Lamoreaux, "Neutron electric-dipole moment, ultracold neutrons and polarized ^3He ," *Physics Reports* **237**, 1–62 (1994); M.D. Cooper *et al.*, "A new search for the neutron electric dipole moment," Los Alamos National Laboratory report LA-UR-02-2331 (April 2002).
3. E. Golub and J.M. Pendlebury, *Contemporary Physics* **13**, 519 (1972).
4. Report to NSAC, Subcommittee on Fundamental Physics with Neutrons (2003) 1.
5. A.O. Sushkov *et al.*, "Kerr effect in liquid helium at temperatures below the superfluid transition," *Physical Review Letters* **93**, 153003–1–153003–4 (2004).
6. S.K. Lamoreaux *et al.*, "Measurement of the ^3He mass coefficient in superfluid ^4He over the 0.45–0.95 K temperature range," *Europhysics Letters* **58**, 718–724 (2002).
7. P.V.E. McClintock, "An apparatus for preparing isotopically pure ^4He ," *Cryogenics* **18**, 201–208 (1978).
8. K. Habricht, PhD Thesis, Technischen Universtat Berlin (1998).

Acknowledgment

The authors would like to acknowledge the participation of our LANL colleagues and our offsite collaborators from the University of California, Berkeley; California Institute of Technology; Duke University; Hahn-Meitner Institut; Harvard University; Hungarian Academy of Sciences; University of Illinois, Urbana-Champaign; University of Kentucky; Air Liquide, Advanced Technology Division; University of Leiden; National Institute of Standards and Technology, Gaithersburg; North Carolina State University; Oak Ridge National Laboratory; Simon-Fraser University; and Yale University. It is only through broad international collaboration that this experimental effort has achieved the results that it has.

Some aspects of this work are funded by LDRD funds from LANL, and other aspects are funded by a grant from the U.S. DOE.

For further information, contact Martin Cooper, 505-667-2929, mcooper@lanl.gov.



The World's Greatest Science Protecting America

Los Alamos National Laboratory, an affirmative action/equal opportunity employer, is operated by the University of California for the U.S. Department of Energy under contract W-7405-ENG-36.



The Highest Energy Emission from Gamma-Ray Bursts

B.L. Dingus (P-23), M.M. González (P-23/University of Wisconsin), Y. Kaneko, R.D. Preece, M.S. Briggs (University of Alabama, Huntsville), C.D. Dermer (Naval Research Laboratory)

Astrophysical sources of gamma rays are the most extreme physical laboratories in the universe.

Gamma rays, the highest-energy light, are produced by particles that are accelerated to relativistic energies. The highest-energy gamma rays are produced by the highest-energy particles and hence are excellent probes of these extreme environments.

Gamma-ray bursts top the list of extreme astrophysical sources. The release of energy in a gamma-ray burst exceeds that of a supernova. Almost all of that energy shows up from within a fraction of a second to a few minutes and emits almost entirely in gamma rays. It is likely that the formation of black holes produces gamma-ray bursts.

While gamma-ray bursts occur about once per day in the universe, they are very difficult to detect due to their short duration and unpredictable location. Special wide-field-of-view gamma-ray detectors must be used. These detectors must be above the Earth's atmosphere except for detecting gamma rays at the very highest energies, such as above about 0.1 TeV (Teraelectronvolt = 10^{12} eV, which is about one trillion times the energy of visible-light photons).

Researchers in Neutron Science and Technology (P-23) have found a new high-energy feature in a gamma-ray burst that was detected by NASA's Compton Gamma-Ray Observatory. This feature points to interesting possible observations with Milagro, a high-energy detector located at LANL, which is operated by P-23 in collaboration with the University of Maryland, University of California -Irvine, -Santa Cruz, -Riverside, University

of New Hampshire, New York University, Michigan State University, and George Mason University.

Producing the Highest-Energy Gamma Rays

The easiest way to produce light is by heat. For example, an incandescent light bulb heats up a filament, which then glows. On a larger scale, the light that is detected from the cosmic microwave background is due to the heat left over from the big bang. The wavelength of the light, which is another way of characterizing the energy of the photons, is related to the temperature of the source. A light bulb filament is 3000 K and produces visible photons, whereas the universe is 2.73 K and produces microwave photons. In order to produce gamma-ray photons, the temperature would have to be greater than 10^{13} K. Such high temperatures are unknown; in addition the distribution of gamma-ray energies is not consistent with such a thermal model.

Therefore, gamma rays require a more difficult mechanism to produce them. Charged relativistic particles are the key because they must emit gamma rays when they interact with magnetic fields, photons, or matter. These mechanisms are well studied with accelerators on Earth,

such as the one at the Los Alamos Neutron Science Center. We can relate the energy of the gamma ray with the energy and type of the accelerated particle, the type of interaction, and the characteristics of the astrophysical medium. This description has many free parameters, so the more features we can observe, the better we can constrain the models of these sources. The features that we observe are the distribution of the energies of the gamma rays and how they vary with time. The maximum energy of the gamma rays detected is one of the easiest constraints to interpret. For example, the energy of the particle that produces the gamma ray must be larger than or approximately the same as the energy of the gamma ray for all types of these interactions.

Gamma-Ray Bursts

The origin of these powerful explosions is actively being debated. The duration is often as short as a few milliseconds and thus requires a very compact emission region. Also, the total energy released is so large that it exceeds the output of our sun during its entire lifetime. These characteristics have led researchers to believe that the astrophysical source must involve the creation of a black hole.

RESEARCH HIGHLIGHT
PHYSICS DIVISION



Nuclear Physics and Astrophysics Research Highlights

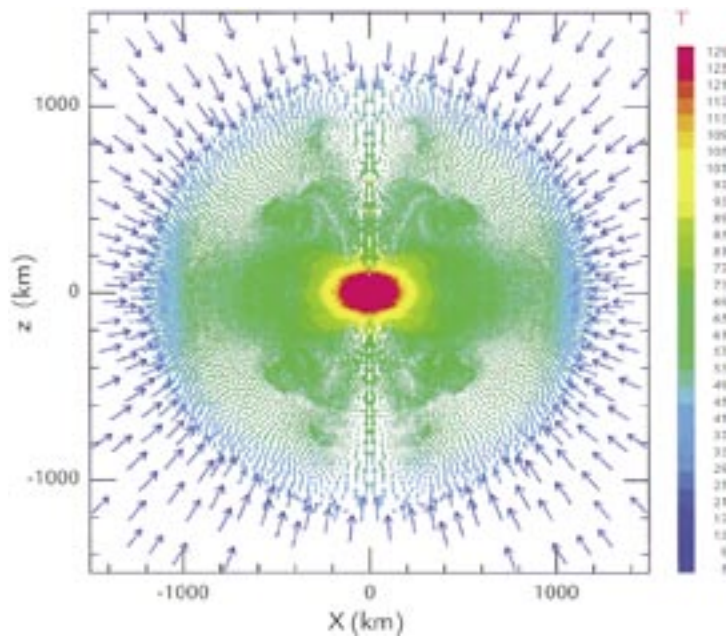


Figure 1. A computer simulation by Fryer, Woosley, and Heger of the collapse of a rotating massive star which is 1.5 s from forming a black hole. Color gives temperature in 10^9 K, and the arrows show the direction and magnitude of the particle velocity.

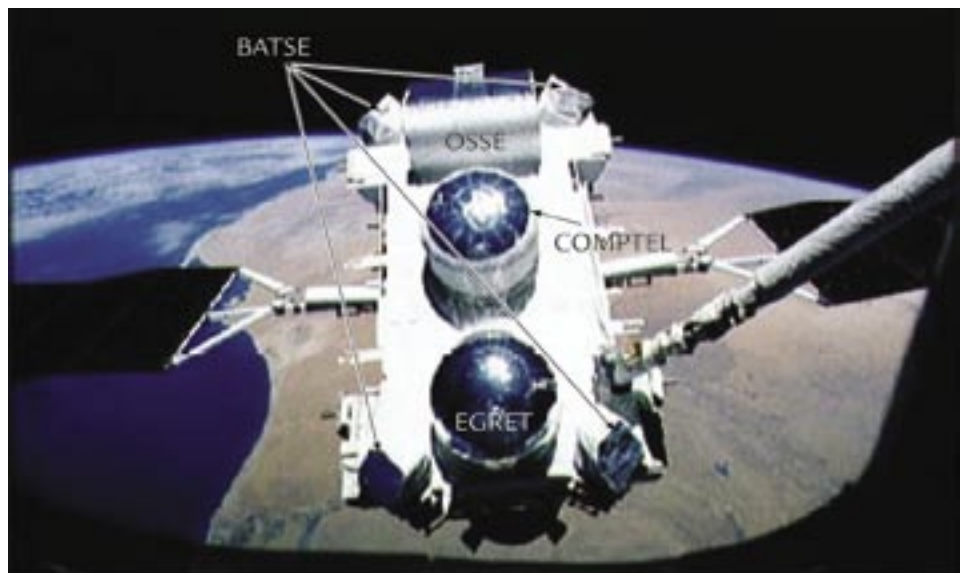
The details about how the birth of a black hole can cause a jet of relativistic particles to be accelerated involve fascinating but difficult physics. The conditions of such large gravitational and electromagnetic fields cannot be replicated on Earth. Researchers, such as Chris Fryer and Alex Heger of the Theoretical Astrophysics Group (T-6), are attempting to use computer simulations of the fundamental physics in this extreme environment to replicate these phenomena as shown in Figure 1.¹ These simulations cannot be exact due to the complexity of the problem and have yet to produce a complete understanding. These theories need more data from observations both in space and on the ground to provide constraints to the computer models.

Detecting Gamma Rays

Gamma rays are photons of light at an energy a few times 10^4 eV to greater than 10^{13} eV. This broad energy range requires different types of detectors. Below about 10^{11} eV gamma rays will not penetrate the Earth's atmosphere, so a space-based observatory is needed. NASA's Compton Gamma-Ray Observatory, shown in Figure 2, had four gamma-ray detectors covering different energy ranges with different fields of view.

Gamma rays cannot be focused onto small detectors as is done for visible photons with large mirrors. Instead, large detectors are required to cause the gamma rays to interact, turning their energy into ionizing radiation, which can be recorded.

Figure 2. Compton Gamma-Ray Observatory being deployed, as seen from the space shuttle. The four detectors, BATSE, OSSE (Oriented Scintillation Spectrometer Experiment), COMPTEL (Imaging Compton Telescope), and EGRET, are labeled.



Astrophysical sources produce fewer high-energy gamma rays than low-energy gamma rays, thus larger detectors are required for higher-energy gamma rays. Due to the high cost of putting large detectors into space, the maximum energy of detectable gamma rays is limited. However, above 10^{11} eV, gamma rays produce showers of particles in the Earth's atmosphere that are detectable on the ground. Milagro, a gamma-ray observatory located at LANL, is the first large-field-of-view gamma-ray detector sensitive down to nearly 10^{11} eV. The large field of view is crucial to observing short duration, randomly and rarely occurring, gamma-ray bursts. An artist's conception of the shower of particles impacting Milagro is pictured in Figure 3.

A New Feature in the Highest-Energy Gamma Rays from Gamma-Ray Bursts

The largest-field-of-view detector on NASA's Compton Gamma-Ray Observatory was BATSE (Burst and Transient Source Experiment). BATSE was sensitive to gamma rays of a few times 10^4 eV up to a few times 10^6 eV, and detected nearly 3000 gamma-ray bursts during the nine years of this mission. EGRET (Energetic Gamma-Ray Experiment Telescope) was the detector on

the Compton Gamma-Ray Observatory that was sensitive to the highest-energy gamma rays, but detected only the brightest burst observed by BATSE.

Researchers in P-23 collaborated with researchers at the University of Alabama in Huntsville and the Naval Research Laboratory to combine data from BATSE and EGRET to examine the distribution of the energy of gamma rays, known as the energy spectrum, from the brightest gamma-ray bursts detected by BATSE. Twenty-six bursts were selected and one burst was found to have a new feature at the highest energies. Most gamma-ray burst spectra can be characterized as a single broad bump peaking in the center of the BATSE energy range. The peak of the bump typically evolves with time to lower energies as the brightness of the burst decays.

The energy spectrum of one burst, GRB941017, had an additional feature in the spectrum and produced up to the highest energies detectable as shown in Figure 4.² This feature decays slower than the typical broad bump, which is also detected in this burst. The total energy in this new feature exceeds that of the broad bump by at least a factor of two. The peak energy of this feature is beyond the range of the EGRET detection and suggests researchers may require a more powerful astrophysical source.

This observation raises many questions: What fraction of gamma-ray bursts has such high-energy emission? How high in energy does this feature extend? And most importantly, what type of interaction is creating this second feature? Due to the different temporal evolution of the broad bump and the high-energy feature, different types of particles may be responsible for the two types of emission. The lowest-energy broad bump is likely due to electrons interacting with magnetic fields, and the highest-energy feature could result from protons interacting with the gamma rays of the broad bump. However, in order for protons to produce gamma rays, the energy of the protons must be nearly as large as the highest-energy

particles known. These particles are known as ultra-high-energy cosmic rays. If this explanation for the high-energy feature of GRB941017 is confirmed by future observations, the long standing mystery of the origin of cosmic rays would be solved.

Future Observations

On November 20, 2004 NASA launched a new satellite, Swift, which is dedicated to detecting gamma-ray bursts. Swift will only detect gamma rays up to a few times 10^5 eV but will localize the direction and the distance to their origin very well. Milagro will look for evidence of $> 10^{11}$ eV gamma rays in coincidence

with Swift's detections of gamma-ray bursts. A prototype version of Milagro was operational during the time when BATSE was detecting gamma-ray bursts and found evidence for one gamma-ray burst which also had much more power released at higher energies than at the energies detected by BATSE.^{3,4} Milagro is much more sensitive than this early prototype, and P-23 researchers are eagerly awaiting Swift's operation and more detections of the highest-energy gamma rays from gamma-ray bursts.

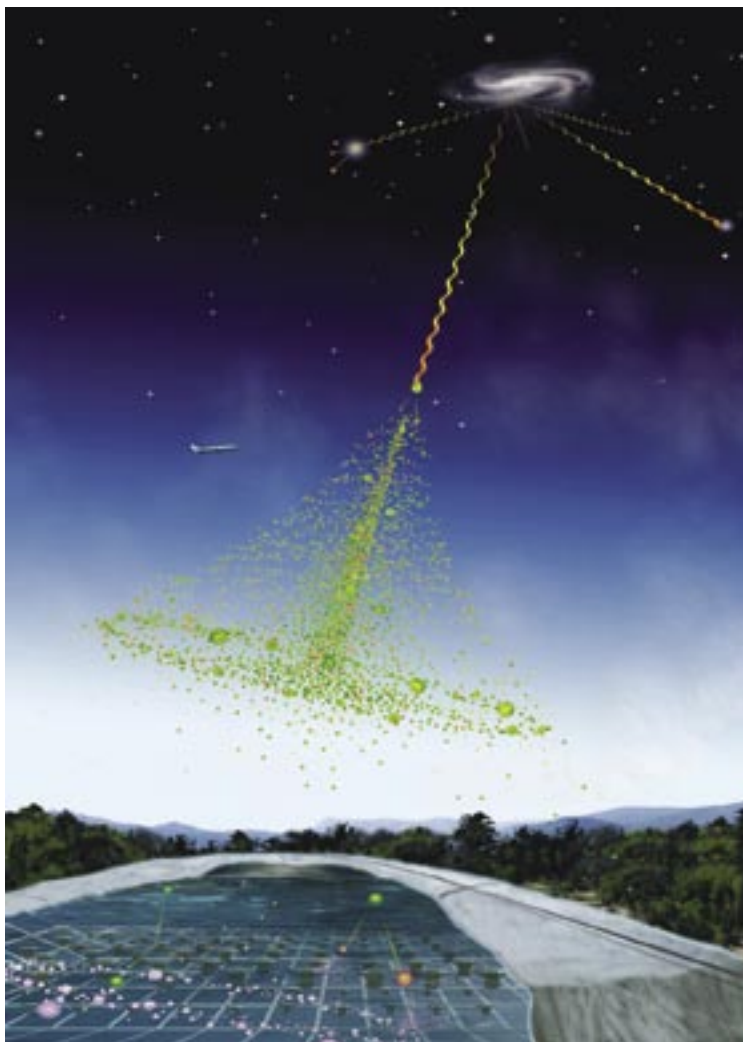


Figure 3. An artist's conception of an air shower about to be detected by the Milagro gamma-ray observatory located in the Jemez Mountains.

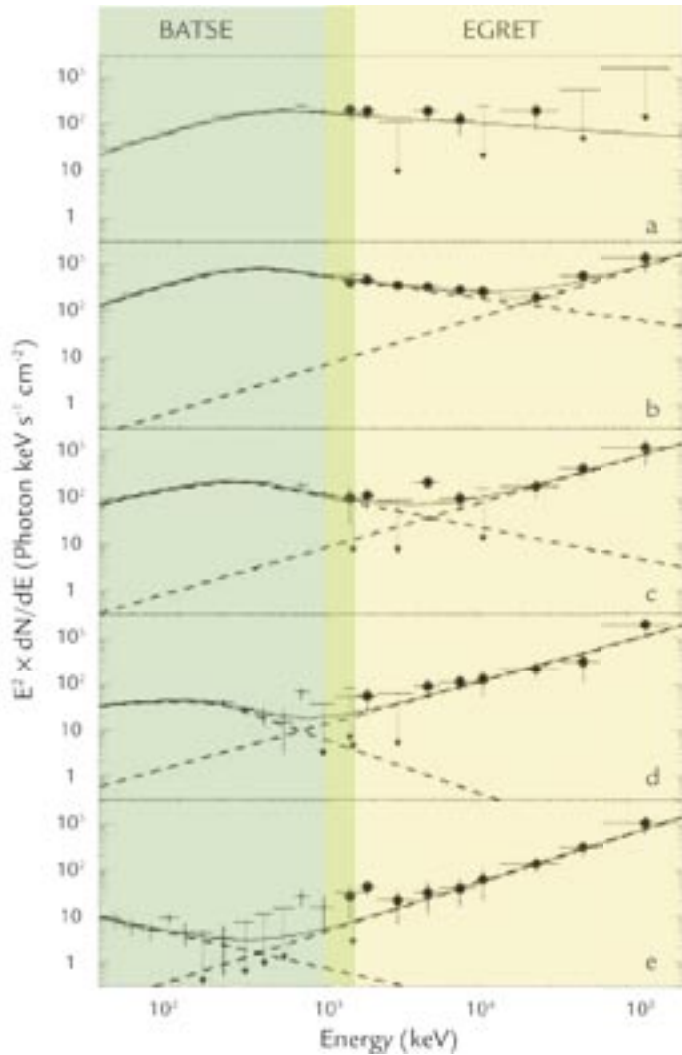


Figure 4. The energy spectrum from GRB941017 showing a new high-energy feature above 10^3 keV ($= 10^6$ eV). The five time intervals relative to the beginning of the burst were determined from the arbitrary time intervals of spectra collected by EGRET and are (a) -18 to 14 sec, (b) 14 to 47 sec, (c) 47 to 80 sec, (d) 80 to 113 sec, and (e) 113 to 211 sec. (Reprinted from Nature Publishing Group.)

References

1. C.L. Fryer, S.E. Woosley, and A. Heger, "Pair-instability supernovae, gravity waves, and gamma-ray transients," *Astrophysical Journal* **550**, 372–382, 2001.
2. M.M. Gonzales *et al.*, "A γ -ray burst with a high-energy spectral component inconsistent with the synchrotron shock model," *Nature* **424**, 749–751, 2003.
3. R. Atkins *et al.*, "Evidence for TeV emission from GRB 970417a," *Astrophysical Journal*, **533**, L119–L122, 2000.
4. R. Atkins *et al.*, "The high-energy gamma-ray fluence and energy spectrum of GRB 970417a from observations with Milagro," *Astrophysical Journal*, **583**, 824–832, 2003.

Acknowledgment

This work was supported by LANL Laboratory Directed Research and Development (LDRD) and Institute of Geophysics and Planetary Physics programs as well as NASA. Milagro has been supported by the National Science Foundation, DOE High Energy Physics, and LANL LDRD.

For further information, contact
Brenda Dingus, 505-667-0400,
dingus@lanl.gov.



The World's Greatest Science Protecting America

Los Alamos National Laboratory, an affirmative action/equal opportunity employer, is operated by the University of California for the U.S. Department of Energy under contract W-7405-ENG-36.



Muon Production with the PHENIX Muon Spectrometers and Color Glass Condensate

M.X. Liu, J.G. Boissevain, M.L. Brooks, P. Constantin, G.J. Kunde, D.M. Lee, M.J. Leitch, P.L. McGaughey, B. Norman, A.K. Purwar, W.E. Sondheim, H.W. van Hecke (P-25), J.P. Sullivan (ISR-1)

Understanding the substructure of nuclei is fundamentally important in nuclear physics. In modern theory, the strong nuclear interaction observed between nucleons (protons and neutrons) inside the nucleus is only a van-der-Waals-type residual force of a more fundamental interaction between the nucleon's constituents. This interaction involving quarks and gluons, collectively called partons, is referred to as quantum chromodynamics (QCD). Studying the parton distribution inside nuclei can shed light on why and how quarks and gluons are confined inside hadrons.

Our knowledge about parton distributions is mainly from deep inelastic lepton-nucleus scattering (DIS) experiments. In parton models, high-energy electron-nucleus scattering does not affect the nucleon as a whole, but just one of its constituents (Figure 1). Each constituent carries a fraction x of the nucleon's momentum with the probability density $f(x)$, also known as the parton density function (PDF).

In a naïve picture, the nucleus-parton distribution is simply the sum of the nucleon's PDFs inside the nucleus. However, the subject of this study is to see if internucleon interaction will eventually modify such distributions.

In a DIS scattering to the first order, an incoming lepton only couples with the charged quark or antiquark, not with a neutral-charged gluon. Using measured quark and antiquark distributions from DIS, one can calculate the gluon distribution employing QCD-based parton evolution equations. Figure 2

shows the gluon distribution inside the proton at a various probing energy scale represented as Q^2 . It is interesting to note that the rapid rise in the small- x gluon PDF predicted by QCD calculation will eventually violate unitarity and lead to a breakdown in the parton model picture of scattering off independent partons. At a sufficiently high density, it becomes possible for a second gluon to overlap in space with the first, leading to gluon fusion, thus limiting the achievable gluon density at small- x . This saturation is sometimes described as the formation of a color glass condensate (CGC).¹

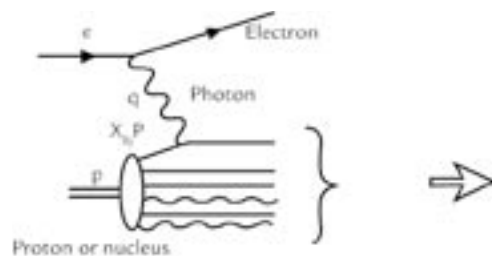


Figure 1. High-energy electron-nucleus interaction in the parton model. The incoming high-energy electron exchanges a virtual photon with a quark inside the nucleus. The collision probability is proportional to the quark density.

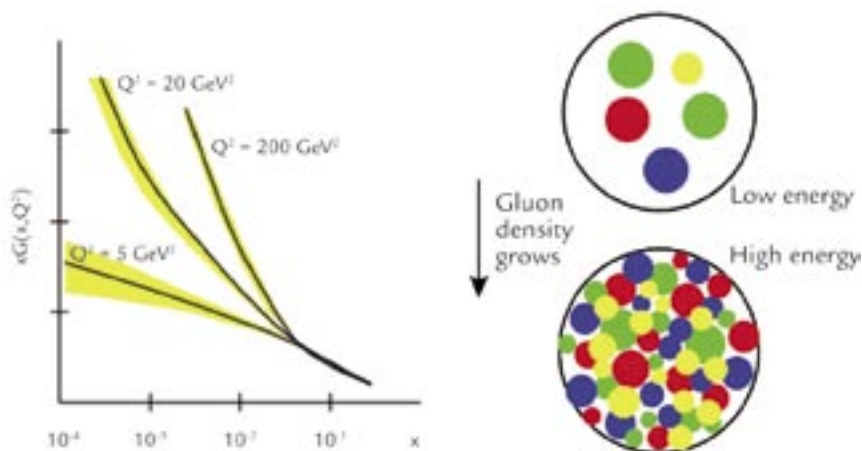


Figure 2. The gluon density $xG(x, Q^2)$ grows rapidly as collision energy increases.

RESEARCH HIGHLIGHT PHYSICS DIVISION

Nuclear Physics and Astrophysics Research Highlights

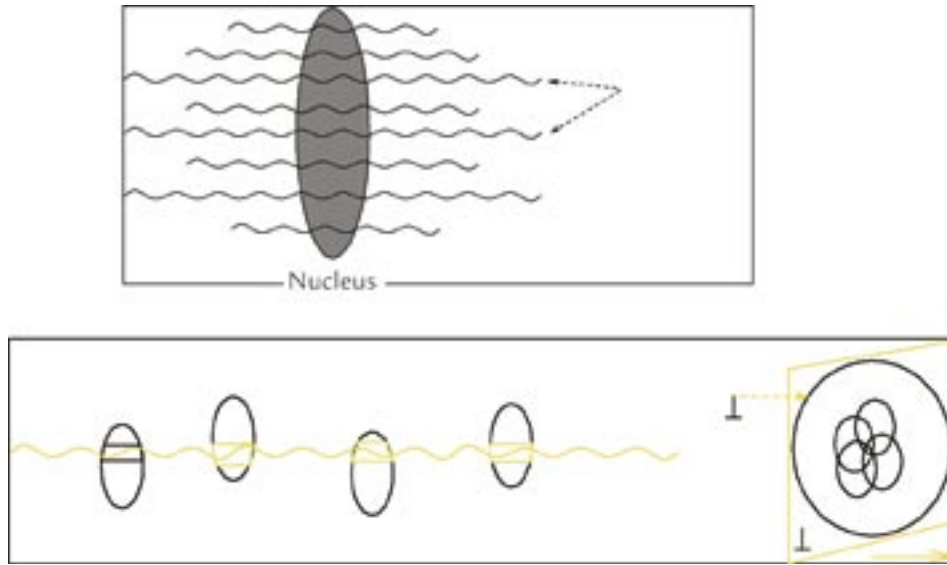


Figure 3. Small- x (or long-wavelength) gluons tend to overlap inside heavy nuclei and lead to gluon fusion.

One could expect that such saturation effects are particularly important for heavy nuclei where small- x gluons from different nucleons have a high probability to overlap in space (Figure 3).

The RHIC at BNL and the PHENIX Experiment

The Relativistic Heavy-Ion Collider (RHIC) at Brookhaven National Laboratory (BNL) collides two ion beams of various types, ranging from protons and deuterons to gold nuclei types, at energies of 100 GeV per nucleon. In such high-energy collisions, quarks and gluons interact directly, thus allowing us to directly probe the nucleus' parton distributions.

The PHENIX experiment at RHIC consists of a general-purpose detector that possesses unique attributes among the five RHIC experiments, including two spectrometers designed to measure high-energy muons over the forward and backward pseudorapidity range $1.2 < |\eta| < 2.4$. They are also the largest subsystems in the PHENIX experiment. The Subatomic Physics (P-25) PHENIX Team has led the design, construction, and operation of the muon spectrometers, and is now leading efforts to analyze the muon data. Figure 4

shows an artist's view of the PHENIX muon spectrometers.

PHENIX also has the ability to measure the centrality of individual ion-ion collisions, where centrality is a measure of the degree of overlap between the two colliding ions. One can compare particle production per nucleon-nucleon reaction in the head-on collisions with these in glancing ones. If there are no nuclear medium effects, i.e., the nucleus-parton distribution is simply the sum of the nucleons and there is no initial- and final-state interaction with nuclear medium, the particle yield per nucleon-nucleon collision will be independent of the collision's centrality.

Muon production in asymmetric deuteron-gold collisions at RHIC

In 2003, RHIC collided deuteron and gold nuclei at a center of mass energy of 200 GeV per nucleon pair. At this energy, most hadrons with a transverse momentum of $P_t > 2$ GeV arise from parton-parton interactions and can be used to probe the nuclear parton structure. Particle production in the deuteron direction (forward) is sensitive to small- x parton distribution in the gold nuclei, whereas particle production in the gold

direction (backward) is sensitive to the large- x parton distributions. It has been predicted that the gluon saturation at small- x in gold will suppress the particle production yield in the forward direction.¹ Very recently, other hadron-production mechanisms, such as quark recombination and coherent multiple-scattering models, could explain the observed suppression in the forward-rapidity region.²

The spectrometers were originally designed to measure muons, however, we recently developed new methods to expand the capability to include hadron measurement. In the following, we briefly discuss how to use muon spectrometers to measure hadrons in deuteron-gold collisions.

Due to the finite distance from the collision vertex to the hadron absorber in front of the muon tracking system, charged pions and kaons have a small probability to decay into a muon before the absorber, through decay modes such as $\pi^\pm \rightarrow \mu^\pm + \nu$, with the decay probability given by,

$$P_{\text{decay}} = 1 - e^{-\frac{L \cdot M}{\tau \cdot p}} \approx \frac{L \cdot M}{\tau \cdot p}$$

where $L \sim 40$ cm is the distance from the collision's vertex to the absorber and p , M , and τ are the momentum, mass, and proper lifetime of the particle. Collisions that occurred far from the absorber will have a higher probability to contain muons that originated from light meson decays than those that occurred close to the absorber. Figure 5 shows the normalized collision's vertex distribution for events with forward (positive z -direction) muons in deuteron-gold collisions. The large slope indicates a significant fraction of the muons are from pion and kaon decays.

In addition to muons from light meson decays, about 1% of hadrons from the collisions can also punch through the absorber and get into the muon spectrometer. These hadrons are identified by the muon identification (MuID) system. Most of the punch-through hadrons interact strongly and stop within

the first a few layers of the MuID absorbers while most muons will likely sail through all of the MuID absorbers.

Results

We studied the hadron production as a function of centrality and rapidity. Figure 6 shows the particle yield ratios per nucleon-nucleon collisions versus rapidity of the most central collisions (0%–20%) to peripheral collisions (60%–88%). Without nuclear medium effects, this ratio should be unity.

We observed suppression in charged hadron yield at forward rapidity and enhancement at backward rapidity in the ratio between central and peripheral deuteron-gold collisions. The forward suppression is consistent with the expectation of gluon shadowing or saturation in the small- x region in large nuclei. For a typical hadron of transverse momentum $p_t \sim 1.5$ GeV, the x -value probed in gold nuclei at the very forward rapidity $y \approx -2$ is estimated to be 2×10^{-3} , and at the very backward direction $y \approx -2$, the x -value is close to 1×10^{-1} . Further detailed comparisons with various theoretical approaches are necessary in order to discriminate between different models, such as CGC and parton recombination models. Currently, we have no sound theoretical understanding for the enhancement in the backward rapidity. Antishadowing (enhancement) in parton distribution at large- x or final-state multiple scattering could lead to such effects.

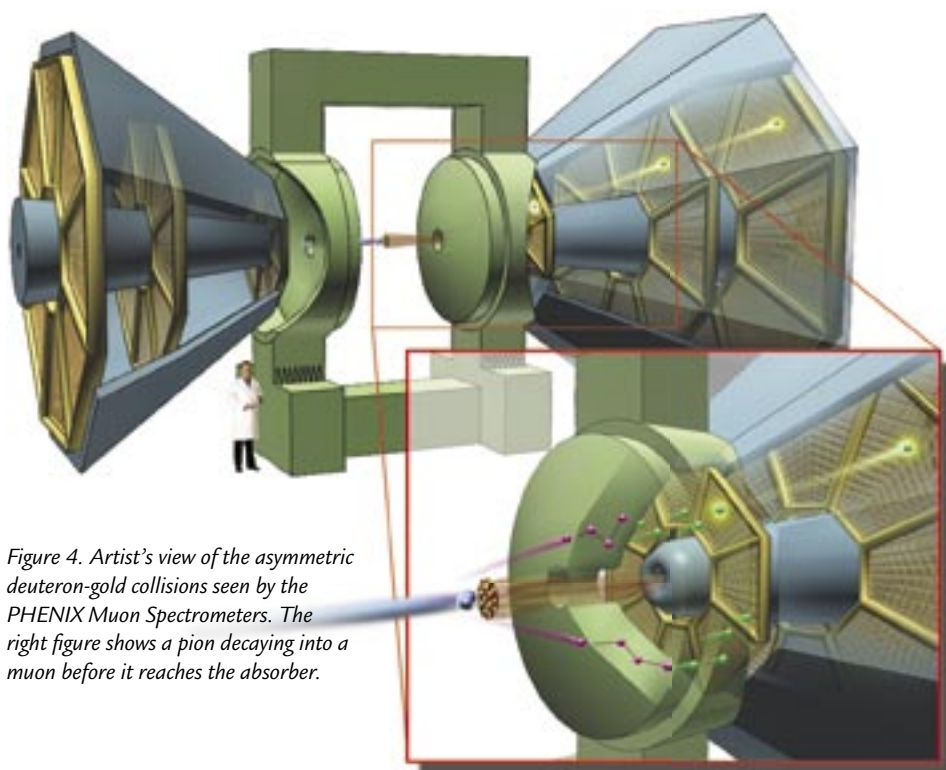


Figure 4. Artist's view of the asymmetric deuteron-gold collisions seen by the PHENIX Muon Spectrometers. The right figure shows a pion decaying into a muon before it reaches the absorber.

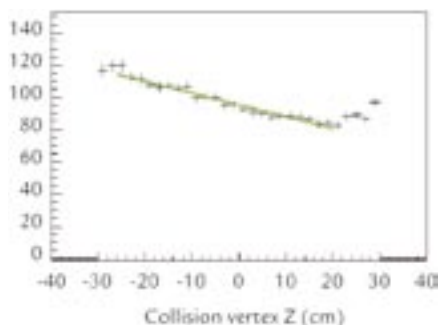


Figure 5. Normalized collision vertex distribution for muon events. The slope indicates that a significant fraction of muons is from pion and kaon decays.

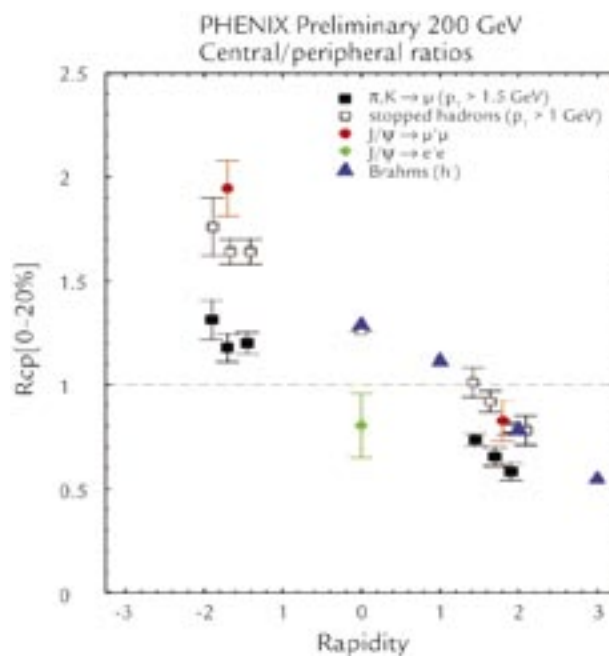


Figure 6. The ratio of particle yield per nucleon-nucleon reaction in the very central deuteron-gold collisions relative to the peripheral one.

Nuclear Physics and Astrophysics Research Highlights

Conclusion

We have studied high-energy particle production at the forward and backward directions in asymmetric deuteron-gold collisions at RHIC. The preliminary results are consistent with parton shadowing or CGC saturation models at small- x , and antishadowing or Cronin effects at large- x inside gold nuclei. In the near future, we expect to measure heavy flavor production in a similar kinematic region. Such measurements are particularly important since the final-state multiple scattering effect is expected to be minimal for heavy quarks, thus they could provide an unambiguous experimental test of various particle production models.

References:

1. L.D. McLerran and R. Venugopalan, "Computing quark and gluon distribution functions for very large nuclei," *Physical Review D* **49**, 2233–2241 (1994).
2. R. Hwa, C.B. Yang, and R.J. Fries, "Hadron production in the forward and backward rapidities in dAu collisions at RHIC," e-Print Archive preprint nucl-th/0410111, (13 Apr 04); J. Qiu and I. Vitev, "Coherent QCD multiple scattering in proton-nucleus collisions," e-Print Archive preprint hep-ph/0405068, (7 May 04).
3. M.X. Liu (PHENIX Collaboration) Talk at Quark Matter 2004 Conference, Oakland, CA, Jan. 2004; D. d'Enterria, "Hard spectra and QCD matter: experimental review," e-Print Archive preprint nucl-ex/0403047, (2 Jun 04); R.G. de Cassagnac, Talk at Quark Matter 2004 Conference, Oakland, CA, Jan. 2004; R.G. de Cassagnac, "J/ ψ production and nuclear effects for d + Au and p + p collisions in PHENIX, e-Print Archive preprint nucl-ex/0403030, (16 Mar 04).

Acknowledgment

We thank the staff of the Collider-Accelerator and Physics Departments at BNL for their vital contributions. We acknowledge support from the Department of Energy and NSF (U.S.A.), MEXT and JSPS (Japan), CNPq and FAPESP (Brazil), NSFC (China), IN2P3/CNRS, CEA, and ARMINES (France), BMBF, DAAD, and AvH (Germany), OTKA (Hungary), DAE and DST (India), ISF (Israel), KRF and CHEP (Korea), RMIST, RAS, and RMAE (Russia), VR and KAW (Sweden), U.S. CRDF for the FSU, US-Hungarian NSF-OTKA-MTA, and US-Israel BSF.

For further information, contact Ming Liu, 505-667-7125, mliu@lanl.gov.



The World's Greatest Science Protecting America

Los Alamos National Laboratory, an affirmative action/equal opportunity employer, is operated by the University of California for the U.S. Department of Energy under contract W-7405-ENG-36.



J/ψ and Charm Quark Production Measurements with the PHENIX Detector at RHIC

P.L. McGaughey, J.G. Boissevain,
M.L. Brooks, G.J. Kunde, D.M. Lee,
M.J. Leitch, M.X. Liu, B. Norman,
W.E. Sondheim, H.W. van Hecke (P-25),
J.P. Sullivan (ISR-1)

The Relativistic Heavy-Ion Collider (RHIC) facility at Brookhaven National Laboratory was designed to collide counter-rotating beams of gold atoms with velocities near the speed of light. When two gold atoms suffer a head-on collision at these high speeds, it is expected that a new phase of matter may be formed. This new type of matter, called the quark-gluon plasma (QGP), consists of quarks and gluons that are no longer bound inside the protons and neutrons contained in the gold atoms. Plasma formation can be understood by an analogy to boiling water. As liquid water heats, it begins to boil, evaporating to form a gas. Likewise, protons and neutrons heat up and begin to evaporate quarks and gluons.

The PHENIX Experiment and QGP Formation

The PHENIX experiment¹ at RHIC is designed to search for signatures of QGP formation. Matsui and Satz² have proposed that the J/ψ particle, which consists of a charm and anticharm quark bound together, is not formed in the presence of a QGP. Due to the relatively large size of the J/ψ, the attractive force between the two charm quarks can be greatly reduced by interference with the strong fields associated with the light quarks and gluons liberated in the plasma. This behavior is analogous to the Debye screening process in chemical solutions and atomic plasmas. The result is that the two charm quarks are unlikely to form a bound state. Instead, they combine individually with light quarks to form a pair of D mesons. Therefore, an



Figure 1. The PHENIX detector during construction. The central magnet is in the middle. The two muon magnets are the lampshade-shaped objects on the left and right.

experimental signature of QGP formation is the observation of a strong suppression of J/ψ production in central gold-gold collisions, relative to peripheral collisions. An increase in D meson production is also expected. However, because the total yield of D mesons is much larger than for the J/ψ, the latter effect will probably be too small to observe.

In order to quantify J/ψ suppression in the QGP, it is critical to understand J/ψ production in collisions where the QGP is not formed. Examples of these

are proton-proton and proton-gold collisions at similar energies. At RHIC energies, the production of charm quarks is dominated by the gluon fusion process $g + g \rightarrow c + \bar{c}$. Thus, charm production is sensitive to the gluonic content of the colliding nuclei. It's also known that J/ψ production is somewhat suppressed by the ordinary nuclear medium, relative to the proton, and that the level of suppression is dependent upon the momentum vector of the J/ψ. These nuclear effects have been characterized as initial-state effects, which refer to the modification of J/ψ formation

RESEARCH HIGHLIGHT

PHYSICS DIVISION

Nuclear Physics and Astrophysics Research Highlights

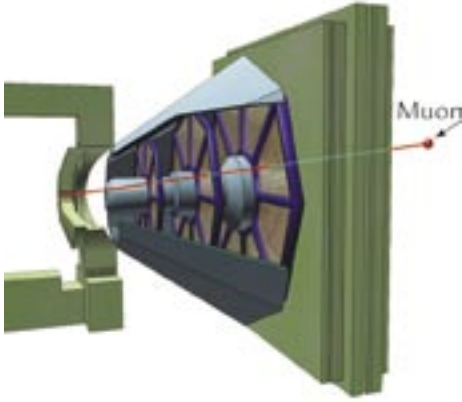


Figure 2. A schematic drawing of one muon arm, with the muon magnet and tracking chambers shown in blue. On the right is the muon identifier. A typical muon trajectory is drawn in red, traversing the arm from left to right.

in a nucleus, and final-state effects relevant to the propagation of the J/ψ through the nucleus. Initial-state effects can arise from changes in the gluon momentum distributions in a nucleus. Final-state effects include multiple scattering, energy loss, and dissociation of the J/ψ . It's important to measure open charm (D mesons) to help separate initial- from final-state effects, because D mesons suffer different final-state effects than the J/ψ .

The PHENIX experiment, shown under construction in Figure 1, consists of two central arms and two muon arms. Each muon arm consists of a tracking system, which measures the momentum vector of each muon, together with a muon identifier, which separates muons from other particles and provides the muon trigger for PHENIX. Our team led the design, construction, and operation of the muon tracking system over a period of more than ten years. Staff from Oak Ridge National Laboratory led the muon identification system effort. We also pioneered the use of cathode-strip-chamber technology for the high-precision tracking chambers used to accurately measure the muon trajectories and momentum. The muon arms measure the decay $J/\psi \rightarrow \mu^+ \mu^-$ over the rapidity range of $1.2 < |\eta| < 2.4$, while D mesons are detected via the semileptonic decay $D \rightarrow \mu + X$.

A schematic of the operation of a muon arm is given in Figure 2. A muon originating from the intersection point of the two gold beams (left side of drawing) travels through the steel of the central magnet into the muon lampshade magnet. Particles other than muons generally interact in the steel and are stopped there. Three stations of cathode strip chambers (vertical blue bars on the drawing) inside the magnet accurately measure the trajectory of each muon. Due to the presence of a large magnetic field inside the magnet, a muon follows a curved trajectory. By measuring this curvature, we determine both the muon's charge and momentum. After exiting the muon magnet, the muon encounters alternating layers of steel and Iarocci tube detectors in the muon identifier, which remove any remaining backgrounds due to particles other than muons. The depth of penetration is a rough measure of the muon's energy, which we use to provide a trigger to PHENIX, requesting that the data for this beam crossing be recorded.

Experimental Results

PHENIX has recently measured proton-proton, deuterium-gold³, and gold-gold collisions at energies of 100 GeV per nucleon. Preliminary results for the J/ψ differential cross section versus rapidity from proton-proton collisions are shown in Figure 3. The shape of differential cross section is consistent with predictions of perturbative quantum chromodynamics (QCD), based upon gluon fusion diagrams. The total cross section times branching ratio is $159 \text{ nb} \pm 8.5\%$ (fit uncertainty) $\pm 12.3\%$ (systematic uncertainty). These proton-proton J/ψ data serve as the baseline for extracting nuclear effects from the deuterium-gold data.

The ratio between the deuterium-gold and proton-proton J/ψ data versus rapidity is given in Figure 4. While the ratio is near one at backward (negative) rapidity, a significant suppression is observed at forward (positive) rapidity. The latter region corresponds to low-Bjorken- x (fraction of the proton momentum) values

for the gluons in deuterium, where we expect the gluons to be suppressed, due to the presence of the color glass condensate⁴ or as a result of other models of gluon shadowing. Also shown in Figure 4 are theoretical predictions of shadowing from Vogt⁵ and Kopeliovich⁶. The data favor less shadowing than in the Kopeliovich model, but the uncertainties are large.

Also of interest are the transverse momentum distributions of the J/ψ . The data are consistent with nuclear suppression at low p_T and enhancement at high p_T , similar to that seen previously by E866.⁷ This behavior, which is often referred to as the Cronin effect⁸, comes about from the multiple scattering of particles as they propagate through a nucleus, leading to an average increase in their transverse momentum.

PHENIX has the ability to measure the centrality of individual ion-ion collisions, where centrality is a measure of the degree of overlap of the two ions. Using the beam-beam Cerenkov counters located at small angles with respect to the two ion beams, the yield of produced particles is determined, which is directly correlated with the collision centrality. The centrality dependence of the J/ψ yield can then be computed. Shadowing of the gluons in gold is again observed, consistent with theory, with little centrality dependence. However, a strong increase with centrality is observed for the yield of J/ψ produced at backward rapidity, which is inconsistent with theory.

Open charm particles (D mesons) have been measured by both the PHENIX⁹ and the STAR¹⁰ experiments at central rapidity. Data is available from proton-proton and deuteron-gold collisions. Both experiments report total cross sections in reasonable agreement with predictions of perturbative QCD. The deuteron-gold data show no strong nuclear dependence, which is not surprising as these data do not correspond to the shadowing region and have poor statistics at high p_T . Open charm data from the muon arms are presently under analysis and will be able to address both the shadowing and high- p_T regions.

Data from gold-gold collisions is presently under intense study. Due to the large number of particle tracks in each muon spectrometer, track reconstruction is much more difficult than for the lighter ions. After we made significant upgrades to the reconstruction software, we are now able to reliably detect J/ψ particles in peripheral collisions. Figure 5 shows dimuon mass plots from each arm. The peaks with mass near 3.1 GeV correspond to the J/ψ. Further study of these data is required to determine and optimize the reconstruction efficiency versus centrality.

Conclusion

The PHENIX muon arm physics program is well underway after more than 10 years of design, construction, and installation. Both muon arms are completely functional and working within design specifications. The first measurements of J/ψ production in proton-proton and deuteron-gold collisions at RHIC energies have been presented and are providing important insight into the nature of gluon shadowing and the Cronin effect. An excellent set of data from gold-gold collisions has been recorded and the analysis is well underway. Within the near future, we should be able to determine if the J/ψ signal is suppressed enough in these collisions to indicate the formation of a quark-gluon plasma.

Figure 3. Rapidity distribution for J/ψ produced in proton-proton collisions at 200 GeV. The red points are from Run 3, which has the highest integrated luminosity to date.

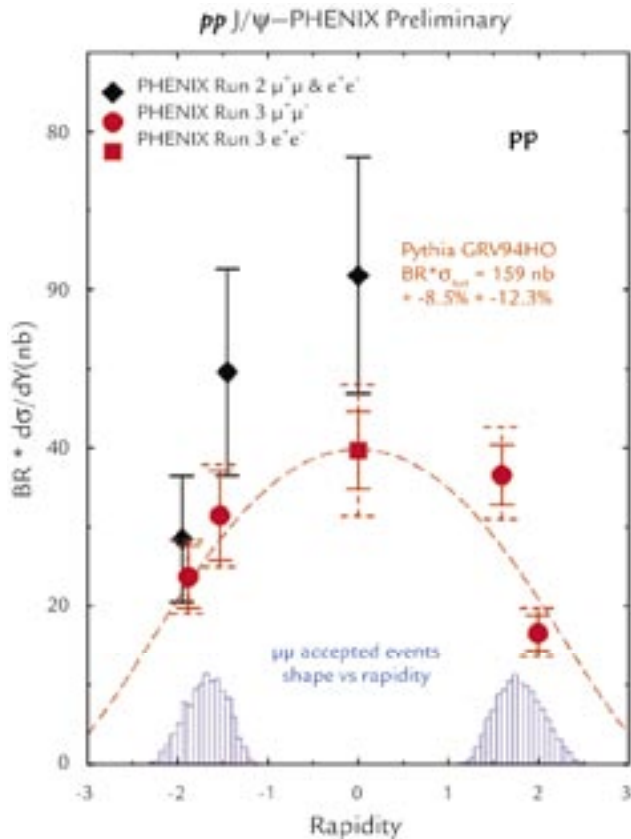
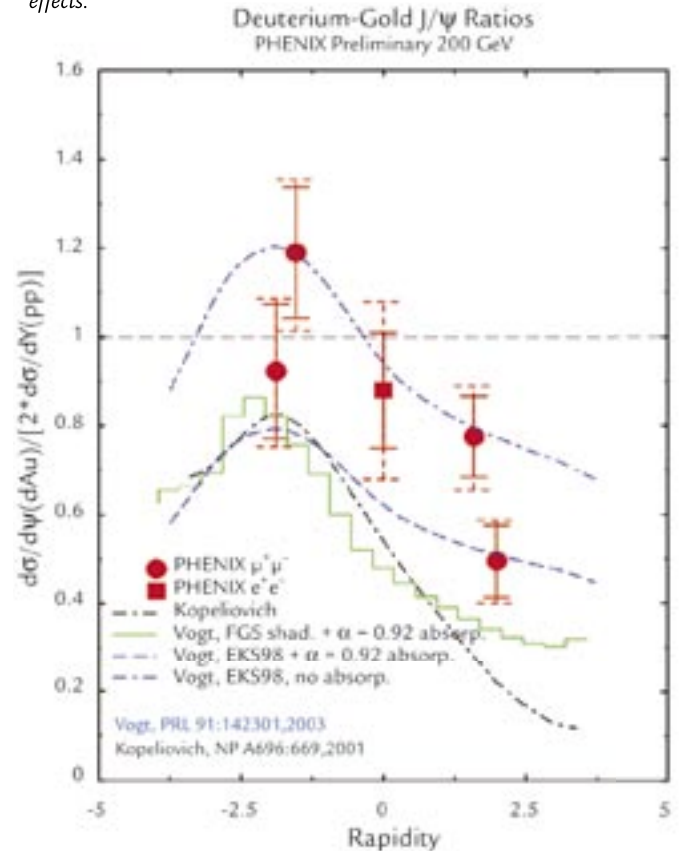


Figure 4. The ratio of J/ψ cross sections from deuteron-gold and proton-proton collisions. The data at positive rapidity correspond to the shadowing region. The colored curves are various theoretical predictions of nuclear effects.



Nuclear Physics and Astrophysics Research Highlights

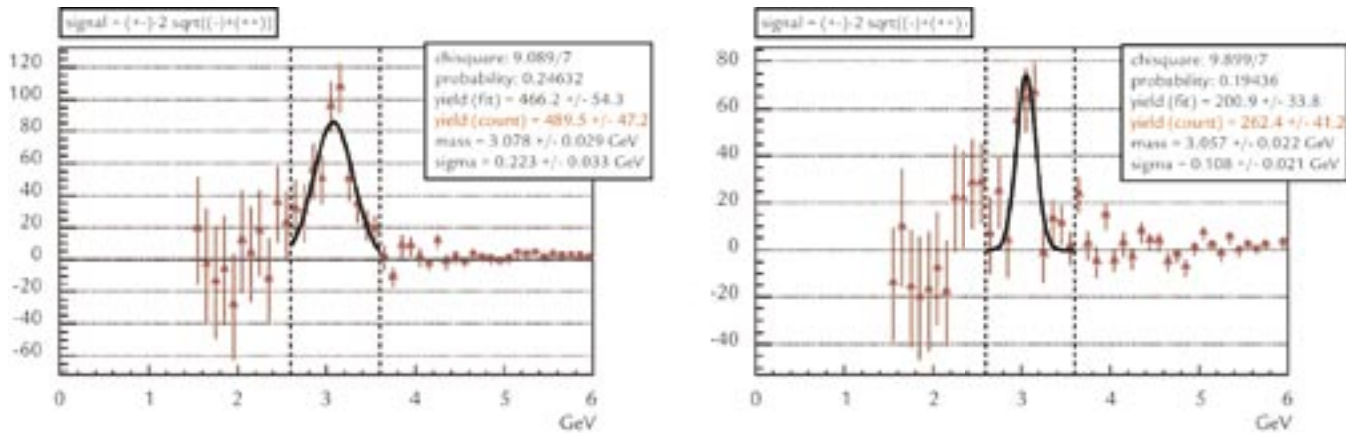


Figure 5. Preliminary dimuon mass distributions from peripheral gold-gold collisions after background subtraction. The left plot is for the south muon arm, while the right plot is for north. The peak corresponds to the J/ψ particle.

References

1. A web-based introduction to the PHENIX Experiment is located at: <http://www.phenix.bnl.gov/phenix/WWW/intro/>.
2. T. Matsui and H. Satz, " J/ψ suppression by quark-gluon plasma formation," *Physics Letters B* **178**, 416–422 (1986).
3. R.G. de Cassagnac, " J/ψ production and nuclear effects for d+Au and p+p collisions in PHENIX," *Journal of Physics G* **30**, S1342–S1345 (2004).
4. L. McLerran, "The quark gluon plasma and the color glass condensate: 4 lectures," *RHIC Physics Lectures*, e-Print Archive: hep-ph/0311028 (2003).
5. S.R. Klein and R. Vogt, "Inhomogeneous shadowing effects on J/ψ production in dA collisions," *Physical Review Letters* **91**, 142301-1–142301-4 (2003).
6. B. Kopeliovich, A. Tarasov, and J. Hüfner, "Coherence phenomena in charmonium production off nuclei at the energies of RHIC and LHC from pQCD, saturation and hydrodynamics," *Nuclear Physics A* **696**, 669–714 (2001).
7. E866/NuSea Collaboration, "Measurement of differences between J/ψ and ψ' suppression in p-A collisions at 800-GeV/c," *Physical Review Letters* **84**, 3256–3260 (2000).
8. J.W. Cronin, *et al.*, "Production of hadrons with large transverse momentum at 200-, 300-, and 400-GeV," *Physical Review D* **11**, 3105–3123 (1975).
9. S. Kelly, "The PHENIX measurement of heavy flavor via single electrons in p-p, d-Au, and Au-Au collisions at $\sqrt{s_{NN}} = 200 \text{ GeV}$," *Journal of Physics G* **30**, S1189–S1192 (2004).
10. A. Tai, "Measurement of open charm production in d+Au collisions at $\sqrt{s_{NN}} = 200\text{-GeV}$," *Journal of Physics G* **30**, S809–818 (2004); L. Ruan, "Open charm yields in 200-GeV p+p and d+Au collisions at RHIC," *Journal of Physics G* **30**, S1197–S1200 (2004).

Acknowledgment

This work was supported by the U.S. DOE and includes contributions from many members of the PHENIX Collaboration.

For further information, contact Patrick McGaughey, 505-667-1594, plm@lanl.gov.



The World's Greatest Science Protecting America

Los Alamos National Laboratory, an affirmative action/equal opportunity employer, is operated by the University of California for the U.S. Department of Energy under contract W-7405-ENG-36.



The NPDGamma Experiment

J.D. Bowman, M. Gericke, G.S. Mitchell, S.I. Penttila, G. Peralta, P.-N. Seo, W.S. Wilburn (P-23) representing the NPDGamma Collaboration.

The nature of weak interactions between strongly interacting hadrons is not well understood. The NPDGamma ($\bar{n} + p \rightarrow d + \gamma$) experiment¹ currently being commissioned at the Los Alamos Neutron Science Center (LANSCE), will study the parity-violating weak interaction between the most common hadrons: protons and neutrons. The hadronic weak interaction is observed in nuclei and nuclear processes², but interpretation of these experiments is difficult because of the complicated many-body dynamics of a nucleus. The goal of the NPDGamma experiment is to measure the parity-violating directional gamma-ray asymmetry in the reaction ($\bar{n} + p \rightarrow d + \gamma$) to an accuracy of 5×10^{-9} , which is approximately 10% of its predicted value.^{3,4} Such a result, in a simple system, will provide a theoretically clean measurement of the weak pion-nucleon coupling, thus resolving a long-standing question in nuclear physics.

In early 2004, all elements of the NPDGamma experiment were successfully commissioned, with the exception of the liquid-hydrogen target. Following final construction of the target and verification of appropriate safety measures for its operation, it will be installed and commissioned in summer 2005. This will allow the experiment to begin taking production data.

Theory Background

The flavor-conserving weak interaction between hadrons is the most poorly tested aspect of electroweak theory.⁴ While much is known about quark-quark

weak interactions at high energies, the low-energy weak interactions of hadrons (particles made of quarks, such as the nucleons—the proton and the neutron) are not well measured. At low energies, the effects of the weak interaction are typically obscured by other processes, making their experimental study challenging. The weak nucleon-nucleon interaction has been expressed in various forms and models.^{3,4,5} Regardless of the formalism, pion exchange is particularly interesting because it is the longest-range component of the interaction, and is therefore presumably the most reliably calculable. The hadronic exchange of neutral currents, which is expected to dominate the weak pion exchange between nucleons, has not been isolated experimentally in an unambiguous way. For both of these reasons, the coupling constant H_π^1 for pion exchange in the weak nucleon-nucleon interaction is of special interest.

An accurate measurement of H_π^1 in a simple nucleon-nucleon system is needed to resolve previous experimental inconsistencies. A two-nucleon system such as in the $\bar{n} + p \rightarrow d + \gamma$ process is sufficiently simple that the measured asymmetry of the emitted gamma rays can be related to the weak

meson-nucleon-nucleon coupling with negligible uncertainty to nuclear structure. The relationship between the parity-violating asymmetry A_γ and H_π^1 , where A_γ is the correlation between the direction of emission of the gamma ray and the neutron polarization, is calculated to be $A_\gamma \approx -0.045 H_\pi^1$. The goal of NPDGamma is to measure A_γ to a precision of $\pm 5 \times 10^{-9}$, which will determine H_π^1 to $\pm 1 \times 10^{-7}$. Such a result will clearly distinguish between the values for H_π^1 extracted from experiments in nuclear systems as well as between predictions by various theories of the weak interaction of hadrons in the nonperturbative quantum chromodynamics regime.

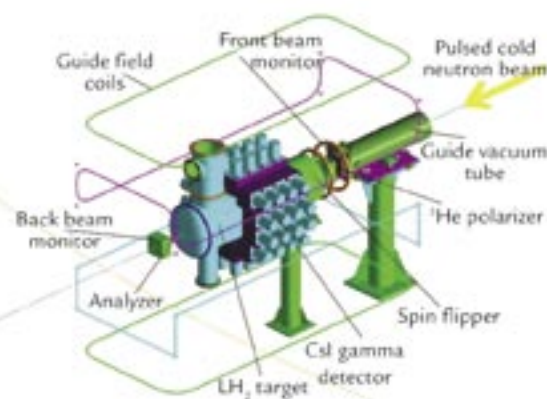


Figure 1. A drawing of the NPDGamma apparatus.

RESEARCH HIGHLIGHT
PHYSICS DIVISION

Nuclear Physics and Astrophysics Research Highlights



Figure 2. Photo of the FP12 chopper, before it is covered with concrete shielding. The horizontal yellow structure contains the neutron guide, and the aluminum housing in the center contains the spinning chopper element. A gap in the chopper allows neutrons of the desired energy range to pass, while the lower-energy neutrons are absorbed in the chopper coating of gadolinium oxide.

Experiment

To determine H_{π}^1 with an uncertainty of 1×10^{-7} , we must achieve a statistical uncertainty of 0.5×10^{-8} on A_{γ} . This means that the experiment must detect a few $\times 10^{17}$ of the 2.2 MeV gamma rays from the $\bar{n} + p \rightarrow d + \gamma$ reaction. In addition, possible systematic errors in the experiment require careful attention. The tiny parity-violating signal in the reaction will be isolated by flipping the neutron spin. The real asymmetry will change sign under spin reversal, while spin-independent false asymmetries will not. The weak interaction is the only fundamental particle interaction that can

produce a parity-violating signal; parity violation is simply described as a difference between a physical process and its mirror image. For example, in the $\bar{n} + p \rightarrow d + \gamma$ reaction, if more gamma rays are emitted in the same direction as the neutron spin, rather than in the opposite direction, then that is a parity-violating signal and must be caused by the weak interaction. The experiment then consists of observing the direction of emission of the gamma rays from many $\bar{n} + p \rightarrow d + \gamma$ captures, and if there is an asymmetry in their distribution with respect to the neutron polarization direction, the effect of H_{π}^1 has been observed.

The requirements for the experiment are the following: a large number of polarized, cold neutrons; a method of flipping the neutron polarization; a proton target; and a detector system for the 2.2 MeV gamma rays.

The experiment consists of a pulsed, cold neutron beam, transversely polarized by transmission through polarized helium-3, with polarization reversal achieved on a pulse-by-pulse basis by a radio frequency spin flipper (RFSF). The neutrons are incident on a liquid para-hydrogen target. The 2.2 MeV gamma rays from the capture reaction will be detected by an array of cesium iodide scintillators coupled to vacuum photodiodes and operated in current mode. A drawing of the setup for the experiment is shown in Figure 1.

Cold Neutron Beam and Polarizer

The experiment requires a high flux of cold neutrons, with energies below 15 meV. While such neutrons are available from cold moderators at both reactors and spallation neutron sources, the nature of the neutron flux from a pulsed spallation source provides a very powerful diagnostic tool for a number of possible systematic effects for this experiment. At LANSCE, the cold neutron source consists of a liquid-hydrogen moderator coupled to the 20 Hz pulsed neutron source. At cold-neutron energies, it is possible to use neutron guides to transport neutrons. The neutron guide possesses a reflectivity that is close to unity for neutrons incident at glancing angles below a (well-known) critical angle, and the reflectivity falls sharply above this angle. The function of the neutron guide is to conserve the high-cold-neutron flux available near the moderator.

For the experiment, a new beam line and neutron guide, Flight Path 12 (FP12), have been built at the Lujan Neutron Scattering Center.⁶ One element of this beam line is a frame overlap chopper, a large rotating disk coated with gadolinium oxide. A photo of the chopper before it was covered with shielding is shown in Figure 2. The purpose of the chopper is to keep each pulse's slowest neutrons from being passed by the faster neutrons from the following pulse. The chopper was commissioned in early 2004 and its effect is shown in Figure 3. The chopper is a key element of the flight path because it allows us to unambiguously associate a neutron's time of flight with its energy.

In order to observe parity violation (in the distribution of gamma rays with respect to the neutron polarization direction), the experiment requires polarized neutrons. Cold neutron beams can be polarized in several ways, but the best technology for NPDGamma is a helium-3 spin filter. Helium-3 spin filters are compact, possess a large phase-space acceptance, and produce a negligible fraction of gamma-ray background. In addition, they

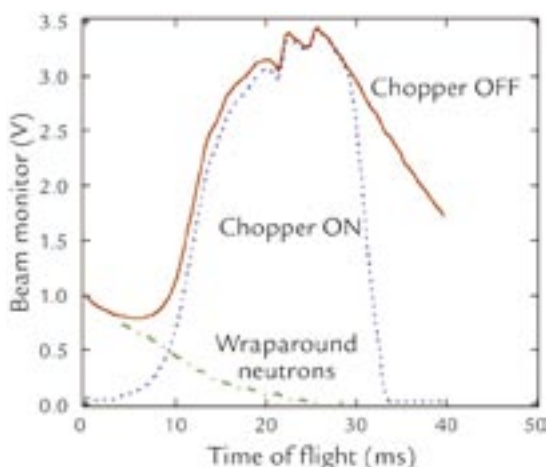


Figure 3. A plot showing beam-monitor response versus neutron time of flight. The beam-monitor voltage is proportional to the number of neutrons passing through it, and the time of flight is a measure of the neutron energy. The general shape of the red and blue curves (peaked in the middle) is characteristic of the neutron-energy spectrum. The chopper function is evident in the difference between the red and blue waveforms (shown as the green curve at low time of flight, or high energy) where the chopper eliminates low-energy neutrons from lingering until the succeeding beam pulse.

do not require strong magnetic fields or produce field gradients. This is important for the control of systematic errors in the experiment. The thickness of the spin filter can be optimized for polarization versus transmission.

Neutron Spin Flipper

For NPDGamma the neutron spins are flipped on a 20 Hz pulse-by-pulse basis with a RFSF. The RFSF is a shielded solenoid that operates according to the well-known principles of nuclear magnetic resonance. In the presence of a homogeneous constant magnetic field and an oscillating magnetic field in a perpendicular direction, the neutron spin will precess, and the amplitude of the oscillating field can be selected to precess the spin by 180° as the neutron travels through the spin-flipper volume. The spin flip is introduced on a pulse-by-pulse basis by simply turning the radio frequency field on and off. The solenoid produces only negligible external magnetic fields and field gradients, an important property given the possible sensitivity of the detector apparatus to magnetic-field-induced gain shifts. The spin-flipper efficiency was measured in commissioning data in early 2004 and determined to be $95\% \pm 5\%$ over the extent of the neutron beam.

Proton Target

In the liquid-hydrogen (proton) target, it is essential that the polarized neutrons retain their polarization until they capture. Many of the neutrons will scatter in the target before they are captured, and the spin dependence of the scattering is therefore important. The ground state of the hydrogen molecule (known as para-hydrogen) has spin of zero ($J=L=S=0$), and the first excited state, the lowest ortho-hydrogen state, is at 15 meV above the para- state. A large fraction of the cold neutrons possess energies lower than 15 meV. Because these neutrons cannot excite the para-hydrogen molecule into its first excited state, only elastic scattering and capture are allowed, and

spin-flip scattering is forbidden. The neutron polarization therefore survives the scattering events that occur before the capture. Higher-energy neutrons will undergo spin-flip scattering and therefore lose their polarization. The liquid-hydrogen target must be in the para- state. For liquid hydrogen held at 20 K and atmospheric pressure, the equilibrium concentration of para-hydrogen is 99.8%, low enough to ensure a negligible population of ortho-hydrogen. The target is under final construction and will be installed in the FP12 cave in the summer of 2005. Production data-taking will begin following this experiment.

Cesium-Iodide Gamma-Ray Detector Array

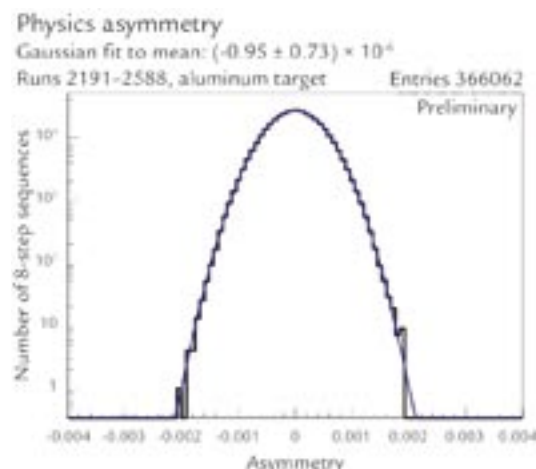
Finally, the experiment must detect the 2.2 MeV gamma rays from the neutron capture. Given the small size of the expected asymmetry and the goal precision of the experiment, the number of events required to achieve sufficient statistical accuracy in a reasonable time immediately leads to the conclusion that the 2.2 MeV gamma rays must be counted in current mode. This means that instead of observing individual events in the detector, many are seen at once, and the sum of their presence is detected (as a total voltage or current from the detector electronics, rather than as individual pulses). It is important to demonstrate in a current-mode measurement that the electronic noise is negligible compared to the shot noise due to the discrete nature of the energy deposited by each gamma ray and the number of photoelectrons produced by each event. In addition, the detector must cover a large solid angle with a large and time-independent efficiency that is unaffected by neutron spin reversal and radiation damage. Segmentation of the detector is required to resolve

Figure 5. A histogram of asymmetry values obtained with an aluminum target. The expected asymmetry is zero. The curve is a fit to a Gaussian distribution, and the data are Gaussian to four orders of magnitude.



Figure 4. A photo of the NPDGamma apparatus in the FP12 cave. The neutron beam enters from the left side of the photo. The four horizontal magnetic-field coils are visible surrounding the apparatus. The hydrogen target is not installed.

the angular dependence of the expected parity-violating signal and discriminate false effects. The fully constructed detector array of 48 cesium-iodide scintillator crystals is shown installed in the FP12 cave in Figure 4.⁷ The noise performance of the detectors and their preamplifier electronics has been measured in the laboratory, and it corresponds well to predictions based on the fundamental limit of Johnson noise. This allows the detectors to



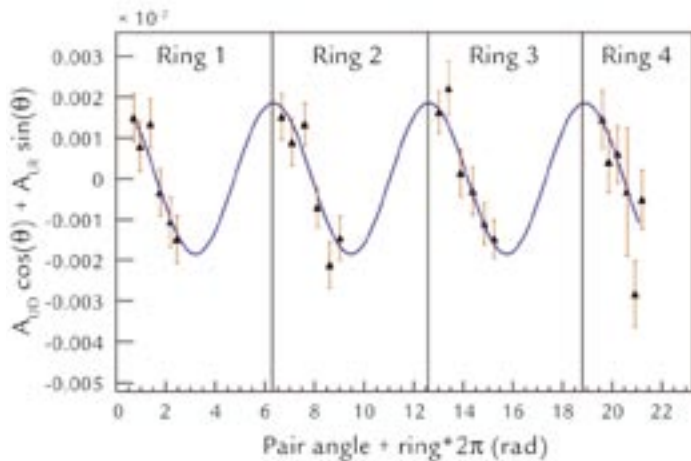


Figure 6. A plot showing asymmetry results by a detector pair for a chlorine target. Chlorine produces a known gamma-ray asymmetry of ~ 20 parts per million, a result reproduced by this data, shown by the amplitude of the blue fit curve shown on the plot. The data follow a sine and cosine dependence due to the geometry of the detector array. The result of the fit is that $A_{UD} = 19 \pm 2 \times 10^{-6}$, and $A_{LR} = 0.6 \pm 2 \times 10^{-6}$. The notation UD refers to up-down, or the parity-violating direction, while LR is left-right, or parity-conserving direction. No parity-conserving asymmetry is expected.

accumulate data at the counting statistics limit and to quickly demonstrate that no false experimental effects exist in the electronics. As evidence of this, Figure 5 shows a histogram of asymmetry values accumulated with gamma rays produced in an aluminum target. Aluminum is present in much of the experimental apparatus, and if it were to produce a gamma-ray asymmetry, it could obscure the effect we are looking for from our proton target. We have placed a sufficient limit on possible asymmetry arising from neutron capture in aluminum. Figure 6 shows results of gamma-ray asymmetry by a detector pair for a chlorine (CCl_4) target. The sine and cosine dependence of the asymmetry arises due to the physical locations of the detector pairs. Chlorine produces a known asymmetry of ~ 20 parts per million⁸, and this shows that our apparatus functions sufficiently to make a precision measurement of a very small asymmetry.

Summary

A sensitive measurement of the parity-violating gamma-ray asymmetry in the reaction $\bar{n} + p \rightarrow d + \gamma$ can give definitive information on one of the most important and interesting components of the weak nucleon-nucleon interaction. Commissioning results have demonstrated the performance of the essential components of the experiment; this includes published results for the FP12 moderator

performance and measurements of parity-violating asymmetries in neutron capture on nuclear targets (chlorine, aluminum, and others) to a precision of 2×10^{-6} , limited only by counting statistics. The experimental design incorporates a number of powerful diagnostics to isolate systematic effects. Commissioning of the final assembly of the experiment, including the hydrogen target, will begin in 2005. The NPDGamma experiment to search for the parity-violating gamma-ray asymmetry in the reaction $\bar{n} + p \rightarrow d + \gamma$ will achieve a sensitivity which is likely to obtain a nonzero result, providing an experimental and unambiguous measure of the hadronic weak interaction in a simple and calculable system.

References

1. W.M. Snow *et al.*, "Measurement of the parity violating asymmetry A_γ in $\bar{n} + p \rightarrow d + \gamma$," *Nuclear Instruments and Methods A* **440**, 729–735 (2000).

2. G.E. Mitchell *et al.*, "Parity violation in compound nuclei: Experimental methods and recent results," *Physics Reports* **354**, 157–241 (2001).
3. B. Desplanques, J.F. Donoghue, and B.R. Holstein, "Unified treatment of the parity-violating nuclear force," *Annals of Physics* **124**, 449–495 (1980).
4. E.G. Adelberger and W.C. Haxton, "Parity violation in the nucleon-nucleon interaction," *Annual Review of Nuclear and Particle Science* **35**, 501–558 (1985).
5. S.-L. Zhu *et al.*, "Nuclear parity-violation in effective field theory," ePrint Archives preprint nucl-th/0407087 (29 Dec 04).
6. P.-N. Seo *et al.*, "A measurement of the flight path 12 cold H_2 moderator brightness at LANSCE," *Nuclear Instruments and Methods A* **517**, 285–294 (2004).
7. M. Gericke *et al.*, "A current mode detector array for gamma asymmetry measurements," accepted for publication in *Nuclear Instruments and Methods A* (2005).
8. G.S. Mitchell *et al.*, "A measurement of parity-violating gamma-ray asymmetries in polarized cold neutron capture on ^{35}Cl , ^{113}Cd , and ^{139}La ," *Nuclear Instruments and Methods A* **521**, 468–479 (2004).

Acknowledgment

This work was supported in part by the U.S. DOE Office of Energy Research, under Contract W-7405-ENG-36, the National Science Foundation (Grant No. PHY-0100348), and the Natural Sciences and Engineering Research Council of Canada. Assistance in the construction and design of this experiment has been provided by the Manuel Lujan, Jr. Neutron Scattering Center (LANSCE-12) and Neutron and Nuclear Science (LANSCE-3).

For further information, contact Gregory Mitchell at 505-665-8484, gmitche1@lanl.gov.

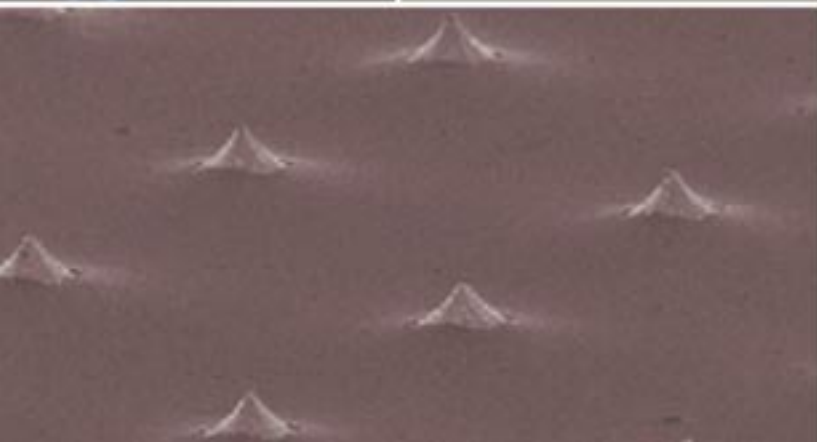
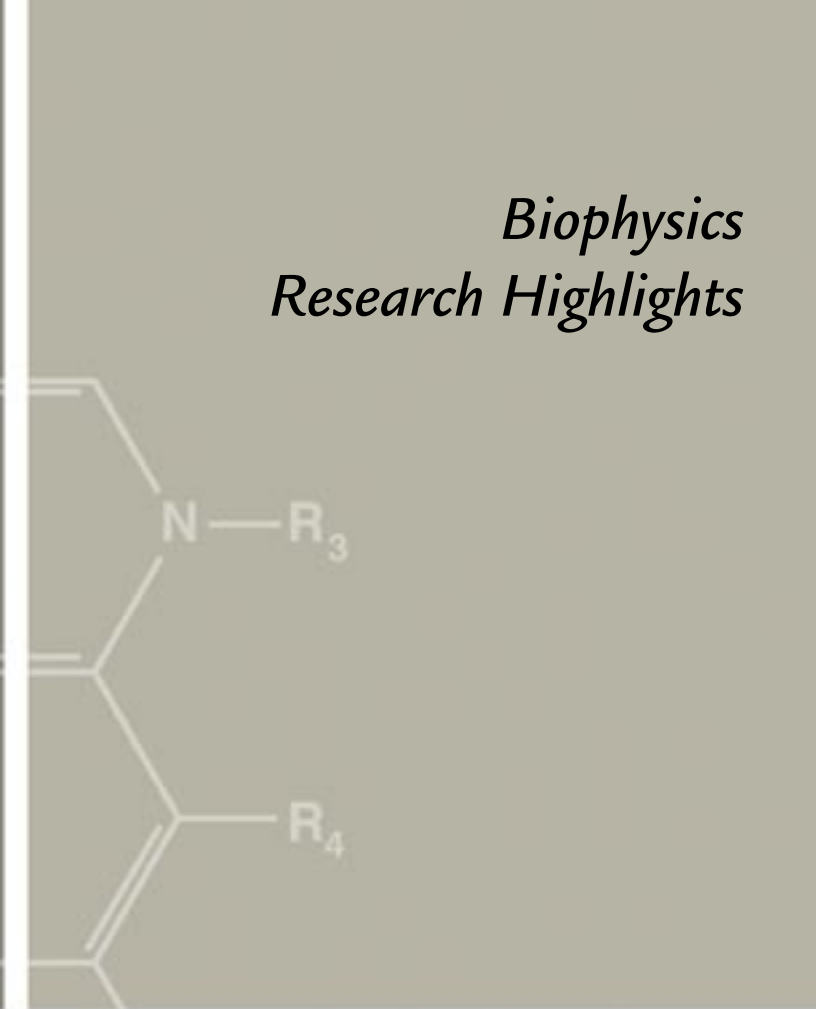
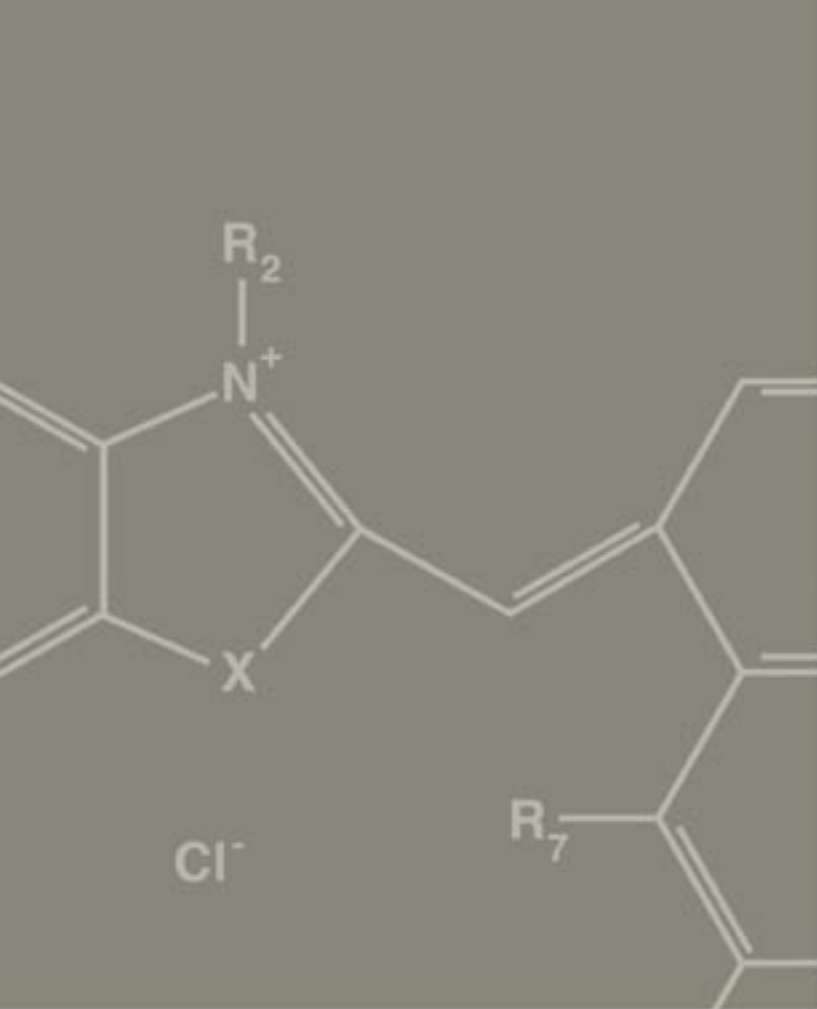


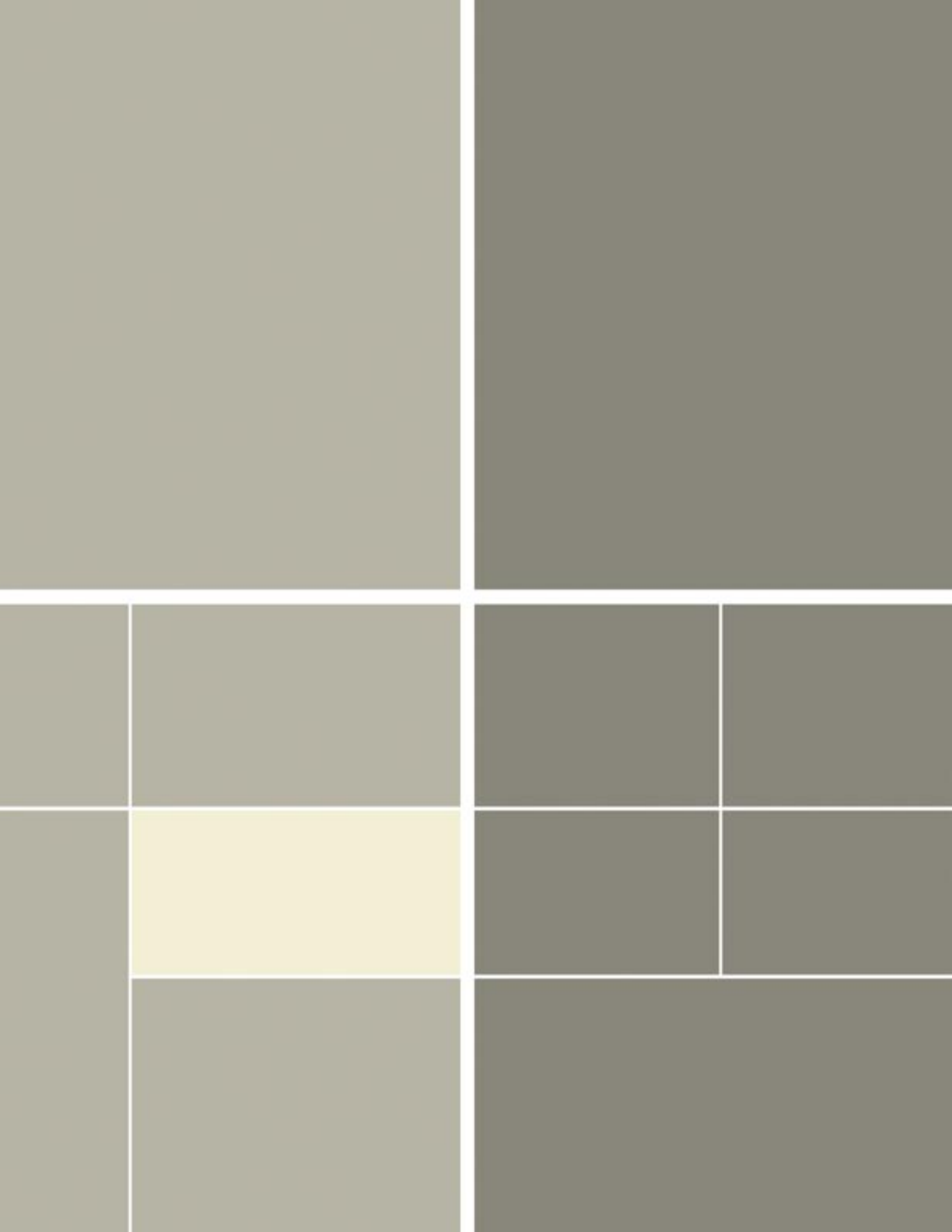
The World's Greatest Science Protecting America

Los Alamos National Laboratory, an affirmative action/equal opportunity employer, is operated by the University of California for the U.S. Department of Energy under contract W-7405-ENG-36.



*Biophysics
Research Highlights*





Experimental Studies and Computer Models of the Retina for Visual Prostheses

J. George, G.T. Kenyon, A. Yamauchi, B. Perry, X.-C. Yao, B. Barrows (P-21)
B. Travis (EES-6)

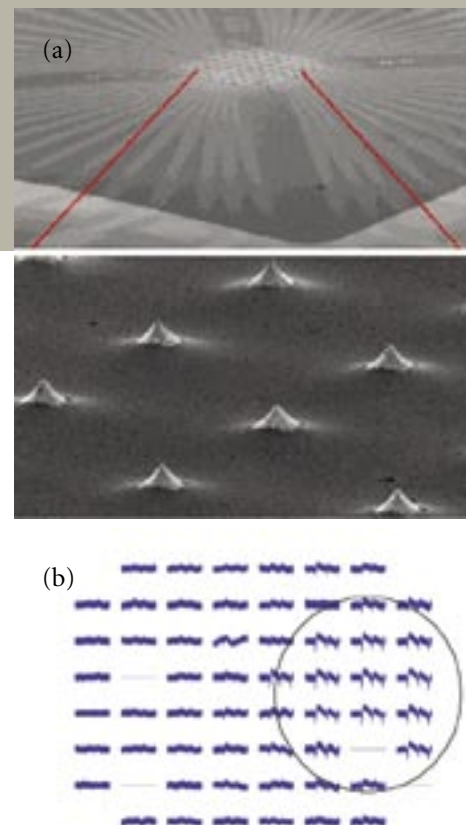


Figure 1. Retinal recordings with a MEA. (a) Scanning electron micrograph of a three-dimensional MEA used for single-unit and local field-potential recordings in an isolated amphibian retina. (b) Spatial pattern of electrophysiological response of an isolated retina to an illumination spot. The retina was placed ganglion cell surface down on a planar MEA. Location of an illumination spot produced by a light-emitting diode is illustrated.

Several common forms of adult-onset blindness are characterized by a massive loss of photoreceptors but a relative sparing of fibers in the optic nerve. In principle, patients suffering from such visual impairments could benefit from a prosthetic system capable of acquiring images, processing and properly encoding the information, and electrically (or magnetically) stimulating remaining retinal neurons. Preliminary studies using a crude prototype of such a device have yielded encouraging results¹, but a number of biomedical, electronic, and neuroscience issues must be addressed before the potential of this technology can be fully realized.

A consortium of DOE laboratories is working on the difficult technical problems that must be solved to achieve a satisfactory “artificial retina.” Los Alamos researchers are developing techniques for imaging patterns of activation within the retina, based on fast optical signals as well as microelectrode arrays (MEAs). These methods will be used to characterize the efficacy of electrical stimulation of the retina and evaluate alternative strategies for stimulation. In order to optimize the processing and encoding of visual information to drive a retinal prosthetic implant, we hope to discover and characterize important aspects of information processing performed by the visual system by coupling dynamic functional imaging techniques with detailed computational simulations of networks. Understanding how the retina encodes visual information is critical for achieving maximum benefit from a prosthetic device and may suggest new image-processing strategies for computer vision systems.

Retina Physiology

Electrophysiological measurements are the gold standard for characterization of neural function, allowing resolution of individual action potentials (spikes) from identified neurons. Multielectrode techniques increasingly allow studies of encoding strategies employed by entire populations of cells², but the measurements are limited by coarse sampling and crosstalk due to tissue conductivity and are disrupted (at least transiently) by electrical stimulation. We have developed functional optical imaging techniques based on measurements of intrinsic optical responses of neural tissue that are closely coupled to electrophysiological activity. However, the signals are tiny; a great deal of work has gone into enhancing size and quality of the responses.

We have undertaken studies of responses to both light and electrical stimulation in isolated amphibian retina (frog or tiger salamander). Electrophysiological recordings have been obtained with single microelectrodes and, more routinely, with MEAs fabricated on a glass substrate that serves as the bottom of the recording chamber. These MEAs consist of 60 metal electrodes in a rectangular array covering several square millimeters of area. The electrodes are connected via

insulated conductors to a multichannel amplifier and data-acquisition system. In some arrays, the electrodes are flat pads. In other commercially available arrays, the electrodes are 40 mm cones rising 70 mm off the array substrate [Figure 1(a)]. We have obtained patterns

RESEARCH HIGHLIGHT PHYSICS DIVISION

Biophysics Research Highlights

of electrophysiological responses reflecting the spatial distribution of the stimulating light using planar MEAs [Figure 1(b)]. With improved experimental technique and using the three-dimensional electrode array, we have been able to regularly record the electroretinogram (the integrated electrophysiological response of the entire retina) as well as local field potential responses with embedded multiunit spike activity (Figure 2). Spikes are extracted from other signal components using digital signal-processing techniques. In the local field potentials (and in single-unit data), we observed a strong oscillatory response (about 30 Hz in frog retina) that was often apparent in single-pass data. These responses are most strongly associated with off responses, i.e., responses to a decrement in illumination, and are most prominent with wide-field stimuli. Responses appear somewhat phase locked to the stimulus, i.e., peaks in the oscillating response waveform appear at about the same point in time relative to the onset or offset of the light stimulus. Signal averaging produced small reductions in the amplitude of the oscillations but did not eliminate them. The reductions were most prominent in the first few cycles of the oscillation, suggesting that the stimulus might reset some ongoing oscillatory driver.

In experiments with a photodiode and video detectors, we have demonstrated

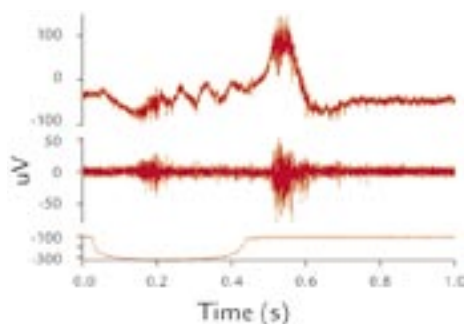


Figure 2. Electrophysiological response of isolated retina to light offset and onset. Upper trace: Single-pass record from one electrode of the MEA. Note the oscillatory off response and embedded spikes. Middle trace: High-pass filtered version of the upper trace showing spiking responses to light onset and offset. Lower trace: Photodiode record of stimulus

that fast intrinsic optical responses can be measured in response to physiological activation of neural circuits including retina (Figure 3), but the signals are very small.³ Unlike other experimental techniques that employ dyes to indicate changes in cellular ion concentration or membrane potential, our methods do not require delivery of chemical to the tissue, so that in principle such measurements can be made noninvasively in the intact human eye. Unlike intrinsic signal imaging based on changes in blood flow or tissue oxygen, we detect changes in tissue light scattering or birefringence that are tightly coupled to the electrical response dynamics of the neurons. With improvements in optical configuration, we have achieved 20-fold increases in signal-to-noise ratio, and recent work has identified other possible improvements. We recently obtained the first dynamic images of the spatial patterns of physiological activation in the retina using these fast intrinsic optical responses. However, because of the small size of the scattering response, we continue to work on improving the image quality. To demonstrate the feasibility of using optical responses to monitor the efficacy of electrical stimulation, we have recently begun a series of experiments to stimulate and record from the retina using a three-dimensional MEA, while simultaneously recording the functional scattered light

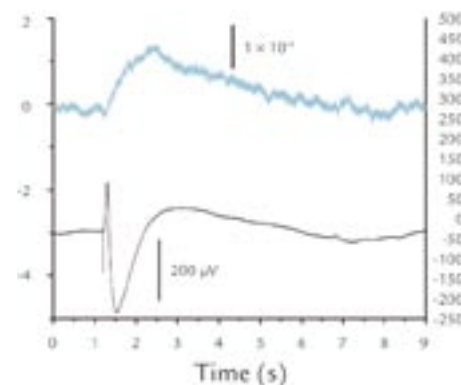


Figure 3. Intrinsic optical response of retina to light stimulation. The retina was placed on an MEA for electrophysiological recording and illuminated with near infrared light in a transmission configuration. Responses are an average of 100 trials. The optical response (upper trace) resembles an integral of the lower electrophysiological response.

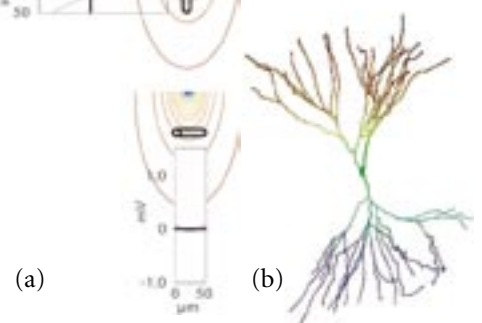
response elicited by stimulation. We have obtained convincing responses in several experiments, with close agreement between the duration of the plateau phase of the response in the optical signal and the corresponding electrophysiological responses recorded across a number of electrodes in the MEA. Optical measures may prove a particularly useful tool for clinical assessment of the retina. We have recently demonstrated that functional responses from retina can be recorded with optical coherence tomography⁴, a technique used routinely to assess retinal anatomy.

The availability of high-density neurophysiological data from this project provides new impetus for linking computational models of neural networks with experimental responses. If we can validate computational methods at the level of retinal neuronal networks, we increase confidence in the feasibility of modeling the dynamics of extended networks within the brain accessible by noninvasive methods.

Modeling Stimulation by a Retinal Prosthesis

An initial objective of computer modeling is to capture the biophysics of

Figure 4. Effects of geometry on electrical stimulation. (a) Change in “membrane potential” along a 50 mm passive cable in response to a 1 mA current. A vertically oriented segment experiences a maximum depolarization of nearly 1 mV at the proximal tip, while a horizontally oriented segment is virtually unaffected by the stimulus. Cable centers were 75 mm from the electrode. (b) Geometrical model of a neuron derived by tracing a labeled cell in the retina.



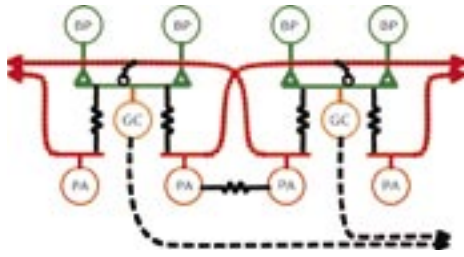


Figure 5. Computational model of retinal circuitry. The full model contained five cell types: bipolar (BP) cells; small, large, and polyaxonal amacrine (PA) cells; and alpha ganglion cells (GC) arranged as a 32×32 square mosaic. Light stimuli were implemented by injecting currents directly into BP cells. Only those elements directly responsible for synchronous oscillations are depicted. A combination of local excitation via gap junctions and long-range inhibition via axon-bearing amacrine cells produced physiologically realistic oscillations. Explanation of symbols: Excitation (triangles), inhibition (circles), and gap junctions (resistors).

electromagnetic stimulation of neural tissue. Neural processes are activated by “gradients” in the extracellular potential and are largely insensitive to the average magnitude, or “direct current offset.” The efficacy of stimulation depends on the design of the electrode array, the properties of the tissue, and the location and orientation of neural processes within the potential field. We have developed a simplified model of the gross anatomy of the retina, and associated structures including the vitreous, retina, and peripheral tissues, as well as the MEA itself. Prosthetic stimulation is modeled by first calculating the extracellular potentials produced by the applied currents and then computing how the resulting gradients act upon dendritic and axonal processes within the retina.

Currents passed through a single isolated electrode produce a dipole-like potential field that is nearly mirror symmetric. The addition of a large insulator (corresponding to a prosthetic device affixed to the vitreous surface) forces more of the current into the retina, enhancing the potential gradient within the tissue and thus the effects of prosthetic stimulation. Our results illustrate that the size of electrodes and the overall design

of the prosthetic device itself, can have a large impact on the spatial distribution of applied currents. After computing the potential distribution within the tissue, we introduce a passive cable segment to simulate the interaction between the tissue electric field and the dendritic structure of the neuron. This allows us to evaluate effects of applied currents on cellular membrane potential and thus for stimulation. Representative results are summarized in Figure 4(a).

This sort of study suggests that our ability to stimulate a particular retinal neuron will depend strongly on the details of the complicated microgeometry of the cell, as well as the spatial distribution of ionic channels within the cell. Our network-simulation software provides an adequate framework to model these functional details. We have recently added capabilities to import geometrical descriptions of real (or virtual) cells [Figure 4(b)], in order to assess the consequences of cellular geometry on the specificity of stimulation by a given configuration of stimulating electrodes. However, the sensitivity of cells to stimulation also depends on the interaction of cells within extended circuits and networks within the retina.

Computer Model of Retinal Coding and Oscillations

The retina consists of several layers of specialized neurons at the back of the eye that collectively perform the transduction and preprocessing of visual signals. The output neurons of the retina, ganglion cells whose axons make up the optic nerve, line the innermost surface of the retina (i.e., closest to the incoming light). In the absence of stimulation, most ganglion cells fire spikes in a random fashion at a background rate much lower than their maximum firing frequency. When stimulated, the firing rate increases markedly in proportion to the local contrast. This modulation of neuronal firing rate by stimulus properties and related observations are the basis for the “rate code hypothesis,” which posits that information is transmitted by the mean number of spikes per unit time irrespective

of their precise timing. Other evidence, however, that the rate code hypothesis is incomplete is that as the size of a visual feature (e.g., a light or dark spot) increases, the total number of spikes is reduced, but a distinct oscillation is often observed in the firing rate. The phase of the oscillation drifts randomly over time so that the responses evoked by separate spots will rapidly become uncorrelated. Remarkably, when a single large spot stimulates two groups of neurons, their oscillations become strongly phase locked, suggesting that the relative timing of spikes in the optic nerve may convey information about the connectedness of visual features.

To study the consequences of interconnections within the retinal circuitry and to explore mechanisms of processing and encoding, we constructed a computer model (Figure 5). The model accounts for responses of certain retinal neurons to temporally modulated stimuli. The temporal modulation transfer function (tMTF) measures how strongly the output of a system is modulated as a function of the frequency of a sinusoidal input. The model retina exhibited a sharp resonance peak in its tMTFs above 60 Hz at frequencies corresponding to experimentally observed oscillatory responses (Figure 6).^{5,6} The model accounts not only for the resonance frequency, but also for an associated kink in the phase response curve that plots how much the phase of the output modulation is shifted relative to the sinusoidal input. Using our computer model, we were able to show that the kink in the phase response curve obtained from retinal ganglion cells was due to entrainment. By exploiting such resonances, we may be able to selectively activate certain retinal neurons at their favored stimulation frequencies.

To assess stimulus-evoked oscillations in the retinal model, we analyzed the local field potentials directly and also considered correlations computed between spike trains from all pairs of ganglion cells activated by the stimulus. The results were combined into an averaged correlation measure. In both the cat retina and retinal model^{7,8}, the phases of the oscillations to

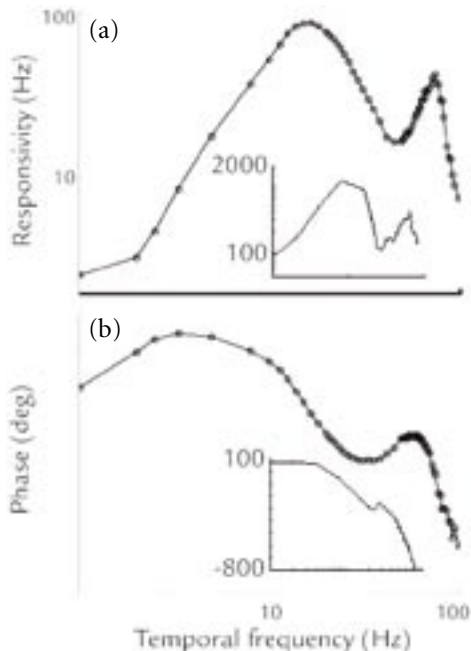


Figure 6. High-frequency resonance in a retinal model. (a) Multiunit tMTF recorded from model ganglion cells. Inset: Similar features were present in the tMTF recorded from a cat alpha ganglion cell in response to a diffuse grating. (b) The response phase plotted as a function of temporal modulation frequency. Inset: The phase-response curve of the cat alpha cell shows qualitatively similar behavior.

small stimuli drift randomly over time so that firing activity becomes uncorrelated over sufficiently long delays. This is a fundamentally nonlinear phenomenon arising from the threshold nature of spike generation; the phase of a linear harmonic oscillator, on average, always remains fixed relative to the stimulus onset. The retinal model was able to account for the experimentally observed size dependence of retinal oscillations (Figure 7). In both experimental data and retinal model results, small stimuli evoked little or no oscillatory response, whereas large stimuli evoked very large oscillations.

Conclusion

Evolving experimental techniques allow us to characterize the mechanism of activation of retinal neurons by electrical stimulation and to explore the processing and encoding of information by retinal neural networks. By coupling these neural population measures to computational models, we can build a useful tool for engineering the neural electronic interface, exploring advanced techniques for stimulation and optimizing the electronic systems employed to encode information for processing and interpretation by the brain.

Reference

1. M.S. Humayun *et al.*, "Visual perception in a blind subject with a chronic microelectronic retinal prosthesis," *Vision Research* **43**, 2573–2581 (2003).
2. B.P. Olveczky, S.A. Baccus, and M. Meister, "Segregation of object and background motion in the retina," *Nature* **423**, 401–408 (2003).
3. D.M. Rector *et al.*, "Scattered light imaging in vivo tracks fast and slow processes of neurophysiological activation," *Neuroimage* **14**, 977–994 (2001).
4. X.-C. Yao *et al.*, "Rapid optical coherence tomography and recording functional scattering changes from activated frog retina," *Applied Optics* (In press).
5. G.T. Kenyon *et al.*, "A model of high-frequency oscillatory potentials in retinal ganglion cells," *Visual Neuroscience* **20**, 465–480 (2003).
6. L.J. Frishman *et al.*, "Spatiotemporal frequency responses of cat retinal ganglion cells," *Journal of General Physiology* **89**, 599–628 (1987).

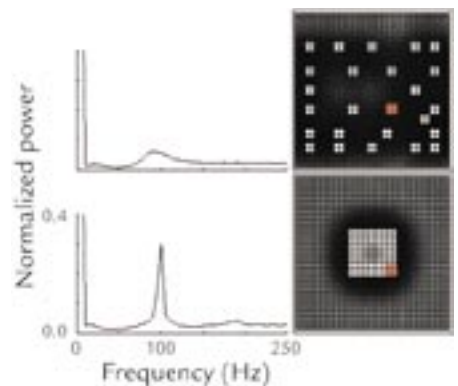


Figure 7. Size dependence of retinal oscillations. Correlation functions computed between model spike trains exhibit a strong increase in oscillatory activity as a function of increasing stimulus size, even when the total area of illumination remains constant. A similar size-dependence was apparent in retinal responses measured experimentally.

7. S. Neuenschwander and W. Singer, "Long-range synchronization of oscillatory light responses in the cat retina and lateral geniculate nucleus," *Nature* **379**, 728–732 (1996).
8. G.T. Kenyon *et al.*, "Stimulus-specific oscillations in a retinal model," *IEEE Transactions on Neural Networks: Special Issue on Temporal Coding for Neural Information Processing* **15**, 1083–1091 (2004).

Acknowledgments

This work has received previous support from LANL Laboratory-Directed Research and Development, National Institutes of Health, and is presently supported by the U.S. DOE as part of the Artificial Retina Consortium.

For further information, contact John George, 505-665-2550, jsg@lanl.gov or Garrett Kenyon, 505-667-1900, gkenyon@lanl.gov.

Ultra-Low-Field Nuclear Magnetic Resonance and Magnetic Resonance Imaging

A.N. Matlachov, P.L. Volegov, M.A. Espy, J.C. Mosher, J.S. George, R.H. Kraus, Jr. (P-21)

A primary thrust in clinical nuclear magnetic resonance (NMR) spectroscopy and magnetic resonance imaging (MRI) has been towards ever-higher magnetic-field strengths. For example, clinical images increasingly are moving from 1.5 T to 3–4 T and research instruments for humans are operating at 7 T or higher. This is largely motivated by the enhanced sensitivity at high fields due to increased polarization and increasing detection efficiency at higher frequencies.

Nevertheless, very low field (VLF, in the mT range) and ultra-low-field (ULF, in the μ T range) NMR and MRI are areas of active interest. Cost and size of systems could be significantly reduced. VLF and ULF systems could be easily portable and the sample need not be restricted to the interior of a magnet bore (*ex situ* or “inside out” imaging). Other interests are driven by the complications of using high-field MRI with samples containing metal (i.e., subjects with metal pins or implants), which are minimized at low fields. Furthermore, we recently demonstrated that samples contained entirely inside metallic shells may also be imaged at ULF.¹

Measurement fields do not have to be highly homogeneous to achieve narrow NMR line widths at ULF. Moreover, for a fixed relative homogeneity, the NMR line width scales linearly with the strength of the measurement field, allowing the possibility of very narrow NMR lines with high signal-to-noise at ULF.² Susceptibility artifacts caused by coupling between the applied magnetic field and different sample materials broaden resonance lines

at high fields but are significantly reduced at ULF. The absence of such artifacts may provide opportunities for novel forms of functional imaging at ULF. For example, it may be possible to manipulate T_1 (longitudinal relaxation time of the spin polarization) contrast at low field strength to provide significant contrast not realizable at high fields.

SQUIDS and Magnetic Scanning

NMR spectroscopy detects the magnetic signature of nuclear spins precessing in the measurement magnetic field. At low field strength, signals become increasingly difficult to measure with conventional detectors. Superconducting quantum interference devices (SQUIDS) are magnetic-flux-to-voltage converters of exquisite sensitivity with a response that is independent of frequency. For this reason, a number of low-field NMR systems have employed SQUID sensors at measurement fields below 10 mT, using both high- T_c (liquid-nitrogen cooled) and low- T_c (liquid-helium cooled) SQUIDS. Low- T_c SQUIDS provide higher sensitivity (due primarily to lower thermal noise) and greater reliability and robustness than presently available in high- T_c devices.

The frequency-independent response of SQUID detectors also enables one to simultaneously detect the signature from

multiple different nuclei, even though their NMR frequencies can differ by factors of 2 or more.³ We have recently demonstrated this in our own system as well.⁴ Various investigators, including ourselves, have already demonstrated that ULF MRI is possible (see for example, References 1, 3, and 5). In addition, we recently completed the first-ever demonstration of the feasibility of magnetic resonance (MR) measurements with simultaneous recordings of biomagnetic signals from the brain (magnetoencephalography, MEG), heart (magnetocardiography, MCG) and muscle (magnetomyography, MMG), using the same detectors.^{1,4,6,7}

SQUID-based biomagnetic measurements are noninvasive techniques that measure magnetic fields outside the body, for example at the surface of the head in MEG. These fields arise as a direct consequence of electrical activity (neurons or nerves) in the living body. MEG requires the use of SQUID sensors to measure the extraordinarily low-level magnetic fields, usually in the range from 10^{-15} to 10^{-12} T, produced by neuronal activity in the brain. While other functional imaging modalities, such as functional MRI, depend on the relatively slow and indirect hemodynamic response of the brain, MEG (and electroencephalography, or EEG) can provide measurement of the electromagnetic fields arising

RESEARCH HIGHLIGHT

PHYSICS DIVISION



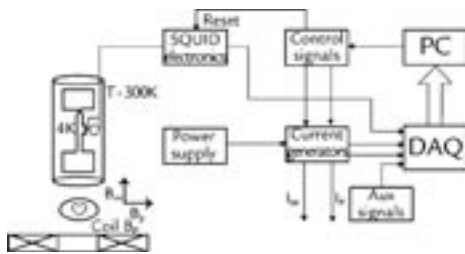


Figure 1. Schematic diagram of the system used to measure simultaneous NMR and biomagnetic signals. Current generators provide current to the magnetic field coils producing B_p and B_m . Control signals allow the computer (PC) to adjust SQUID settings and current levels. AUX signals are auxiliary signals acquired by the data acquisition (DAQ) such as trigger signals, ECG data, etc.

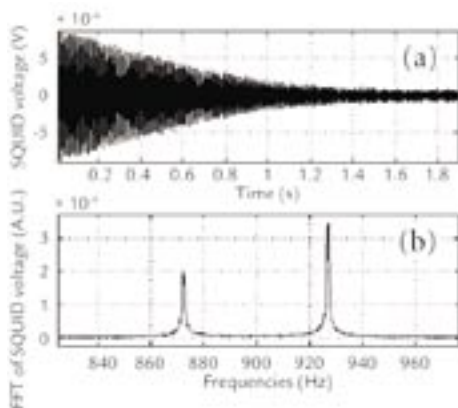


Figure 2. (a) FID for both H_2O and $C_{10}F_{18}$. (b) The FFT of the data in (a) showing the peaks from fluorine (~ 872 Hz) and protons (~ 927 Hz). Data for both solutions were taken simultaneously.

from the actual neuronal currents with submillisecond temporal resolution. Acquiring MR and biomagnetic data simultaneously will reduce most of the sources of error in colocalization of bioelectric sources with anatomy. This will be particularly valuable for MEG and EEG where data typically must be superimposed on conventionally acquired MRI images, introducing significant error.

Perhaps the most compelling application of NMR/MRI at ULF is to acquire direct evidence of biomagnetic signals with a tomographic imaging modality. Specifically, it is speculated that the

bioelectric currents that produce the signals we measure in MEG, MCG, or MMG may produce changes in the proton precession signal, in either frequency, phase, T_2^* (total relaxation time of the spin polarization), etc. If such a signature could be detected, it would allow one to tomographically localize the effect of those currents using MR techniques, thereby eliminating the complications of the inverse problem inherent in biomagnetic source localization. Our team has recently begun investigating this phenomenon.^{4,7}

Measurements of ULF NMR and MRI

Figure 1 shows a schematic diagram of the ULF NMR system designed in Biological and Quantum Physics (P-21). This configuration uses a tangential gradiometer and is optimized for the measurement of simultaneous measurements of MCG and NMR.⁴ Figure 2 shows the free induction decay (FID, the actual signal of spin precession) from a sample of H_2O and $C_{10}F_{18}$ taken simultaneously, and a fast Fourier transform (FFT) of the signal.⁴ As noted previously, this would not be possible with a conventional MR system, as the receiver coils would not be able to detect two frequencies so far apart. An example of the utility of such measurements is to food science, where conventional high-field NMR has already become a powerful tool for the detection of moisture content, sugar content, adulteration, bacterial spoilage, etc.⁸ Our methods suggest a strategy for inspecting food inside metallic cans. We measured the hydrogen-1 NMR signal from tomato juice and cola inside unopened aluminum cans and observed very different T_2^* times: cola ~ 1500 ms, tomato juice ~ 300 ms.

We have also been able to acquire simple images with our system. Figure 3(a) is a photograph of a 60 mm diam by 52 mm high cylindrical plastic phantom with seven 10 mm diam by 48 mm deep wells. Four of the wells were filled with water (shown filled with colored water for visibility). Figure 3(b) illustrates a two-dimensional (2-D) image of the

phantom constructed from a series of gradient-encoded FID spectra acquired at various angles by rotating the sample within a fixed measurement field. The measurement field was $7.8 \mu T$ and the gradient was $\sim 7 \mu T/m$.

Simultaneous Measurements of Biomagnetic Signals and NMR

Figure 4 shows data recorded for our measurement of simultaneous MEG and NMR. The blue trace is the proton FID curve and the red trace is the evoked somatosensory response from a region of human cortex. The stimulus was delivered to the median nerve (thumb) at time $t = 0.1$ s, producing the artifact seen at that time, and the expected N20 response at 20 ms poststimulus and subsequent somatosensory components⁹ are clearly visible. These measurements, combined with the imaging demonstrated in Figure 3, demonstrate that it is possible to combine the advantages of low-field NMR/MRI with high-temporal-resolution MEG measurements. The possibility of imaging simultaneously with biomagnetic recordings could be useful for cardiac diagnostic testing and may alleviate some of the issues surrounding localization of MEG sources relative to anatomy.

The Quest for a Signature or Direct Neuronal Measurements with ULF MR

One very compelling application of NMR/MRI at ULF is to acquire direct evidence of biomagnetic responses producing changes in the proton precession signal, in either frequency, phase, T_2^* , etc. If such a signature could be detected, it would allow one to tomographically localize the effect of those currents using MR techniques, thereby eliminating the complications of the inverse problem inherent in biomagnetic source localization. This would open up a whole new imaging modality.

To study these effects we looked at T_2^* values for NMR signals that were simultaneously acquired in the presence of biomagnetic signals such as those

from heart (MCG) and muscle (MMG). Our hypothesis was that the value of T_2^* in the presence of bioelectric currents would be shorter than that measured when such currents were absent, because inhomogeneity in the local fields should produce a dephasing of spin signals.

Figure 5 shows the simultaneously acquired NMR and MCG data. NMR signals were recorded at various times during the heartbeat, as indicated in the figure. Data for approximately 100 heartbeats were averaged after removing specific noise components (power-line harmonics, cryostat demagnetization signal, and eddy current signal), and filtering.

We focused on the values of T_2^* for NMR during the “T” peak (200–250 ms after the “R” peak) and for NMR during the resting phase of the heartbeat (400–700 ms after the “R” peak). These values were calculated by the direct exponential curve resolution algorithm (DECRA)¹⁰ and the estimated T_2^* was extracted from the damped exponential found at the Larmor (precession) frequency.

T_2^* values varied among subjects with the shortest being 76 ms and the longest being 123 ms. We hypothesize that physiological differences among subjects such as fat content in the chest wall contribute to the spread in values. We observed that the values of T_2^* for the resting phase appeared longer than those for the “T” peak by 2–9 ms for four of the five subjects (as we would expect), however was shorter by 5–7 ms for one subject. Our uncertainty in T_2^* for water phantoms with varying concentrations of copper sulfate was found to be ± 1 ms. However, it is very difficult to estimate the uncertainty in T_2^* for measurements where the sample geometry is so much more complicated and variable.

Because of the complexity of the muscle responses in the cardiac system, we chose to use MMG to investigate the effect of the bioelectric currents on the NMR signal T_2^* . The bioelectric currents during MMG are much larger than neuronal currents, and unlike MCG, effects such as motion,

blood flow, and blood volume of the sample being measured are significantly reduced.

The experiments provide data with interleaved epochs of NMR recorded while the muscles of the forearm were either stressed or relaxed. This protocol was chosen to try and reduce any hemodynamic or metabolic effects. The probability density functions (PDFs) of T_2^* were then inferred from the data for both stressed and relaxed conditions using a “bootstrap” method.⁴ The results are shown in Figure 6. The same analysis approach was then applied to random permutations of the stressed and relaxed sets. The inferred PDF for the randomly mixed data is shown in Figure 7.

The permutation test (Figure 7) shows no inherent preference in our processing between the two sets, while the bootstrap tests (Figure 6) suggest that the two conditions may be distinct, but with statistically low power. Our observed difference in T_2^* for the two conditions is not statistically significant; however, it is encouraging that the trend of a shorter T_2^* for the stressed condition is what one would expect if this effect were due to bioelectric currents dephasing the NMR signal. We caution that even if this effect were statistically significant, we are not yet able to rule out that the measured effect was due to a systematic error due to the slight differences in the experimental configuration between the two cases (i.e., slightly different arm position), some other systematic error in our hardware, or a biological effect that is not electrical in nature.

Discussion and Conclusions

We have demonstrated that biomagnetic signals can be acquired simultaneously with NMR data using SQUID sensors at ultralow magnetic fields. We have demonstrated MRI at these low fields for water phantoms. These results provide the basis of performing MR anatomical imaging simultaneously with bioelectric source localization. Such capability will greatly enhance the efficacy and

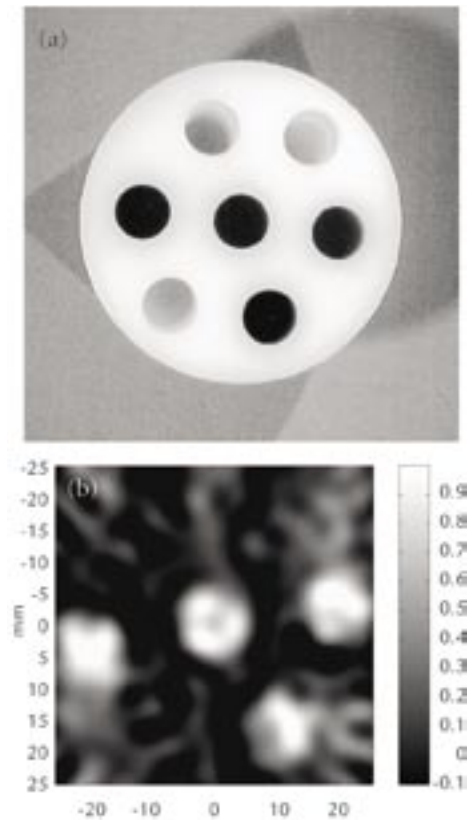


Figure 3. (a) Photograph of a 60 mm diam cylindrical plastic phantom with seven 10 mm diam wells. Four of the wells were filled with water (colored water for visibility). (b) Image of the phantom (2-D) constructed from a series of gradient encoded FID spectra acquired by rotating the sample within a fixed measurement field. The gradient was produced by slightly unbalancing the current in the Helmholtz coils. The average over ~ 100 epochs is shown.

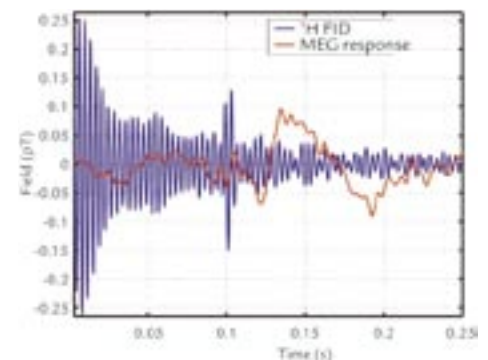


Figure 4. Simultaneous hydrogen-1 NMR FID (blue trace) and MEG somatosensory response (red trace) acquired from a region of the human head including the somatosensory cortex.

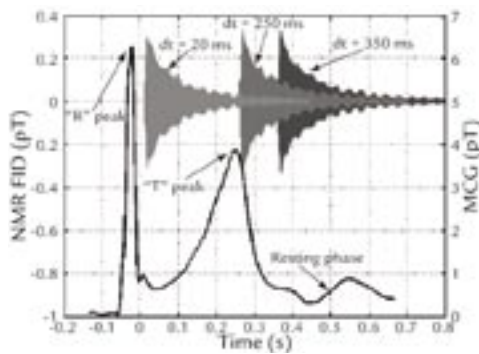


Figure 5. Simultaneously acquired NMR and MCG data. NMR was acquired at the various times indicated during the MCG.

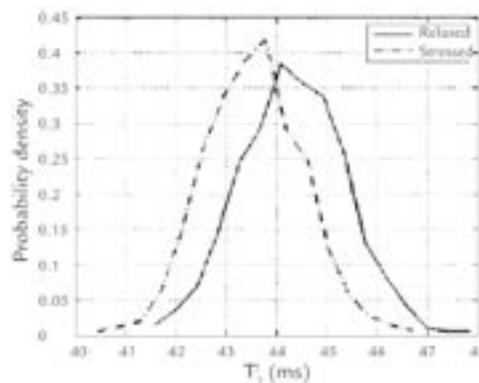


Figure 6. Probability density of T_2^* inferred from 1000 bootstraps for stressed and relaxed epochs.

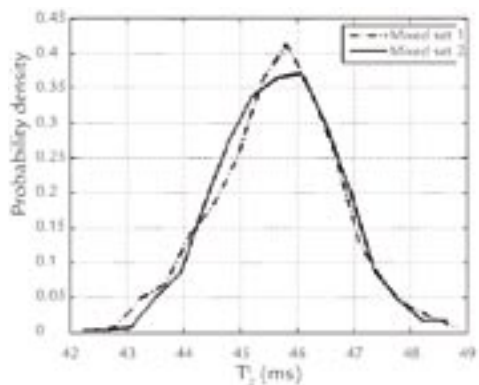


Figure 7. Probability density of T_2^* inferred from the randomly permuted data set.

reduce errors over current functional neuroimaging techniques. In addition, we have investigated the possibility of using MR techniques to tomographically image the direct consequence of bioelectric activity in living tissue. Although there is significant work to be done, we are encouraged that the modality of ULF NMR with SQUIDS is going to be able to see these direct effects and open up a whole new way to gain knowledge regarding bioelectric function.

If nothing else, we have demonstrated that simultaneous anatomical and bioelectric images are possible, and that the field of ULF NMR/MRI with SQUIDS has an exciting future.

References

1. A.N. Matlachov *et al.*, "SQUID detected NMR in microtesla magnetic fields," *Journal of Magnetic Resonance* **170**, 1–7 (2004).
2. R. McDermott *et al.*, "Liquid-state NMR and scalar couplings in microtesla magnetic fields," *Science* **295**, 2247–2249 (2002).
3. R. McDermott *et al.*, "SQUID-detected magnetic resonance imaging in microtesla magnetic fields," *Journal of Low Temperature Physics* **135**, 793–821 (2004).
4. M.A. Espy *et al.*, "SQUID-based simultaneous detection of NMR and biomagnetic signals at ultra-low magnetic fields," *Applied Superconductivity Conference: Harnessing the Magic (ASC'04)*, Jacksonville, Florida, USA, October 3–8, 2004, Los Alamos National Laboratory document LA-UR-04-1544 (accepted for publication in *IEEE Transactions on Applied Superconductivity*).
5. S. Kumar, W.F. Avrin, and B.R. Whitecotton, "NMR of room temperature samples with a flux-locked dc SQUID," *IEEE Transactions on Magnetics* **32**, 5261–5264 (1996).
6. P.L. Volegov *et al.*, "Simultaneous magnetoencephalography and SQUID detected nuclear MR in microtesla magnetic fields," *Magnetic Resonance in Medicine* **52**, 467–470 (2004).
7. M.A. Espy *et al.*, "Simultaneously detected biomagnetic signals and NMR," 14th International Conference on Biomagnetism (BIOMAG 2004), Boston, Massachusetts, USA, August 8–12, 2004, Los Alamos National Laboratory document LA-UR-04-6823.
8. I.L. Pykett, "NMR—a powerful tool for industrial process control and quality assurance," *IEEE Transactions on Applied Superconductivity* **10**, 721–723 (2000).
9. C.C. Wood *et al.*, "Electrical sources in human somatosensory cortex: Identification by combined magnetic and potential recordings," *Science* **227**, 1051–1053 (1985).
10. A. Nordon *et al.*, "Quantitative analysis of low-field NMR signals in the time domain," *Analytical Chemistry* **73**, 4286–4294 (2001).

Acknowledgment

The authors wish to thank Dr. C.C. Wood for his thoughtful discussions of the topics presented. Technical development of the instrumentation used for this work was supported by LANL and the Defense Advanced Research Projects Agency. Experimental studies received support from the U.S. DOE Office of Biological and Environmental Research.

For further information, contact Robert Kraus, Jr., 505-665-1938, rkraus@lanl.gov.

Stochastic Closure for Multiscale Simulations

D.M. Schmidt, S.C. Jun (P-21), B. Nadiga, D. Livescu (CCS-2), D. Higdon (D-1), D. Ranken (CCN-12)

In nonlinear systems, small-scale phenomena affect large-scale behavior. Computer simulations of large, nonlinear systems, therefore, require very large grids in order to both cover the domain of the problem and to resolve the finest relevant small-scale phenomenon. Existing computing capabilities are often inadequate to compute on grids that fully resolve the small-scale phenomena resulting in the use of coarser grids. In such cases, the equations governing the dynamics of the system to be simulated must be modified to try to replicate the effects of the now missing, subgrid-scale phenomena. This problem of how to modify the equations to replicate the subgrid phenomena is known as the problem of closure, and any particular modified set of partial differential equations (PDEs) is called a particular choice of closure relation. In practice, generating closure relations is a very problem-specific, time-consuming endeavor, often involving the generation and fine-tuning of models to incorporate phenomenological information and/or theoretical insights about the particular system to be simulated.^{1,2}

Yet another ubiquitous problem associated with simulating complex systems is uncertainty quantification. Input parameters, boundary conditions, and physics-model parameters are often unknown and affect the outcome of the simulation. In order to quantify the uncertainty of the output of the simulation, given that of the input parameters, the simulation must be run many times with different values of the parameters.^{3,4}

The problems of closure and of uncertainty quantification are correlated for a number of reasons. First, closure must be accomplished on a sufficiently coarse grid to allow for multiple runs of the simulation. Second, the act of up-scaling a system of equations to a coarse grid and choosing a closure relation is a source of uncertainty; different closure relations can be used, producing different results.

Our Approach to Closure

We are working to develop, validate, and apply a new probabilistic approach to the problems of closure and uncertainty quantification in multiscale simulations through stochastic closure (SC). Our SC approach uses a probability distribution of closure relations as the solution of the closure problem. This probability distribution represents information about the unresolved phenomena that may be obtained from the output of a simulation on a fine grid that resolves the small-scale phenomena over a smaller domain, as well as from relevant experimental results. Statistical methods for density estimation can be used to generate a distribution that encodes this information. Once the probability distribution is obtained, individual closure relations are drawn at random and used throughout the

evolution of the simulation. Uncertainties in the choice of closure relations are clearly defined and better sampled in this approach. Moreover, the effects of unresolved phenomena tend to be better represented with this SC approach than with the use of a single closure relation. Finally, by addressing the closure issue with generalized probabilistic methods, the tools and technologies that we are developing will be applicable to a range of multiscale systems.

Rationale

The rationale for SC derives from the following considerations. Any coarsely sampled or gridded field could have resulted from one of a large number of different nonsampled, or continuous fields. The different continuous fields generate different dynamics in the nonlinear terms of the dynamical equations, resulting in a large number of different closure relations that could be used. Constructing a probability distribution of closure relations allows one to incorporate information about the likelihood of any particular closure relation based on prior information about the subgrid-scale phenomenon for that dynamical system. This information is contained within the original dynamical equations and may be found by simulating the system over a

RESEARCH HIGHLIGHT
PHYSICS DIVISION

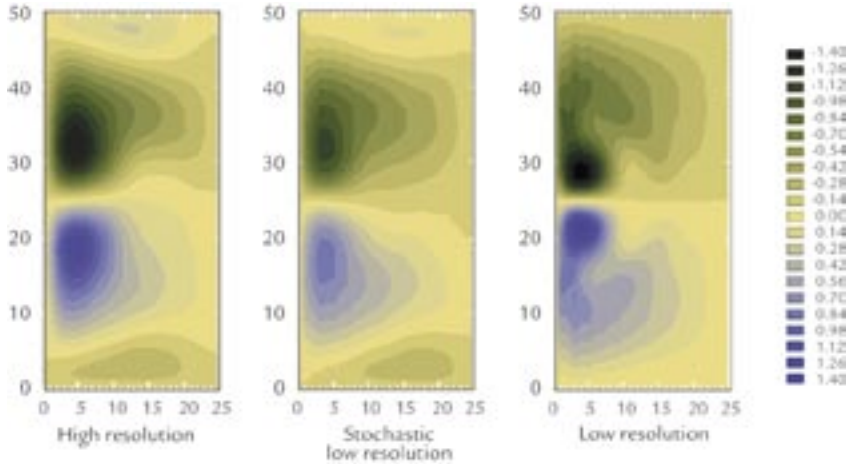


Figure 1. Time-averaged stream function plotted over the two-dimensional domain of the sample problem, resulting from three different simulations. Left panel is from a high-resolution simulation that fully resolves the nonlinear phenomena and represents the “true” results. Right panel resulted from an uncorrected simulation of the same PDEs but on a low-resolution coarse grid. Middle panel resulted from the average of 10 simulations with SC correction on the coarse grid.

small domain with a fine enough grid to resolve the small-scale phenomenon.

If successfully utilized, a number of potential benefits may result from these ideas. By treating closure as a probabilistic problem where a probability distribution is generated based on the output of a fine-scale simulation, the statistical techniques developed to generate such a distribution can be applied to a wide range of problems and in a nearly automated fashion. This diminishes the historical problem of generating closure relations as being a problem-specific, time-consuming endeavor. By drawing from a distribution of closure relations throughout multiple simulations, the uncertainty associated with up-scaling to a coarse grid are inherently included and in a manner that allows for other uncertainties to be included as well. This significantly aids the uncertainty quantification goal. Moreover, because multiple closure relations are being used, the time average of multiple moments of fields is well reconstructed, not just one or a few moments. Though others have used SC terms⁵, they have been problem specific and have not been formulated in the generalized statistical terms we propose here, nor did they address the important problem of uncertainty quantification.

Example

We have used a simple barotropic model of the subtropical/subpolar gyre (rotating flow) circulation in the ocean as a prototypical multiscale problem to illustrate the SC approach. The time-averaged stream function from a high-

resolution, 200×100 grid simulation shows a pair of inner wind-driven, counter-rotating gyres and a pair of outer gyres (left panel of Figure 1) that are driven by turbulent eddy fluxes.⁶ In a low-resolution 50×25 grid simulation, using the same dynamical equations and identical setting, the time-averaged stream function does not contain the outer pair of eddy-driven gyres and the magnitude of circulation is lower in the inner pair of wind-driven gyres (right panel of Figure 1).

To construct a distribution of closure relations for the low-resolution simulation, we used the results of the high-resolution simulation. The dynamical system involved a single nonlinear term in the PDEs that was a Jacobian of two fields, $J(p, q)$. To construct the SC distribution, we examined the local spatial average (to represent the act of down-sampling to a coarser grid) of the Jacobian versus the Jacobian of the spatially averaged fields. Specifically, we looked at $\langle J(p, q) \rangle$ versus $J(\langle p, q \rangle)$, where $\langle \rangle$ denotes local spatial average. A scatter plot of these quantities from the output of the fine-scale simulation for a local region in the

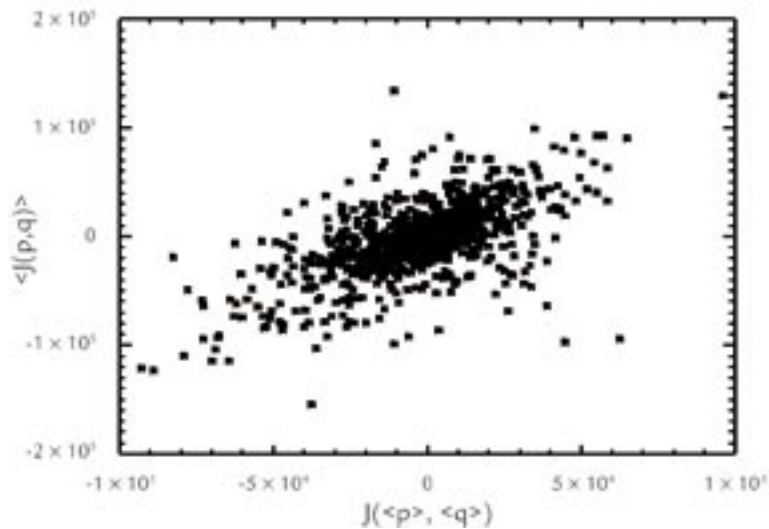


Figure 2. Scatter plot demonstrating the nonlinear Jacobian of the coarsely sampled fields (horizontal axis) versus the coarsely sampled Jacobian of the finely sampled fields (vertical axis). We are given the values on the horizontal axis during the evolution of the PDEs on a coarse field, but the true values of the Jacobian are on the vertical axis. This error is due to the coarse sampling of the fields, and a closure relation is the algorithm used to calculate the correction. Our SC approach samples closure relations from a probability distribution constructed to represent the nondeterministic nature of the closure problem.

two-dimensional spatial domain is shown in Figure 2. When integrating the PDEs on a coarse grid we are given $J(\langle p, q \rangle)$ but would like to know $\langle J(p, q) \rangle$. Clearly, no single choice exists for this but rather a range of choices that we approximate by constructing a distribution (Figure 2).

The low-resolution simulation was rerun, but modified to include a SC term to model the subgrid turbulence that was randomly sampled from the previously found distribution, assuming a temporally homogeneous model for the subgrid phenomena temporal correlation. Adding this sampling step did not significantly add to the run time of the code so that we could run multiple stochastic simulations in much less time than it took for one run of the high-resolution simulation. The middle panel of Figure 1 shows the average over multiple stochastic simulations of the time-averaged stream function. The outer pair of gyres now re-emerges and the magnitude of circulation in the wind-driven pair is improved as well.

We also calculated and compared the temporal variability (standard deviation over time) of the stream function for each type of simulation (Figure 3). The low-resolution run completely failed to reproduce the temporal variability found in the high-resolution run, but the low-resolution stochastic run did a good job in reproducing this variability. These results indicate that multiple moments of the fields are reproduced well with this SC approach. Moreover, the variance or uncertainty of any

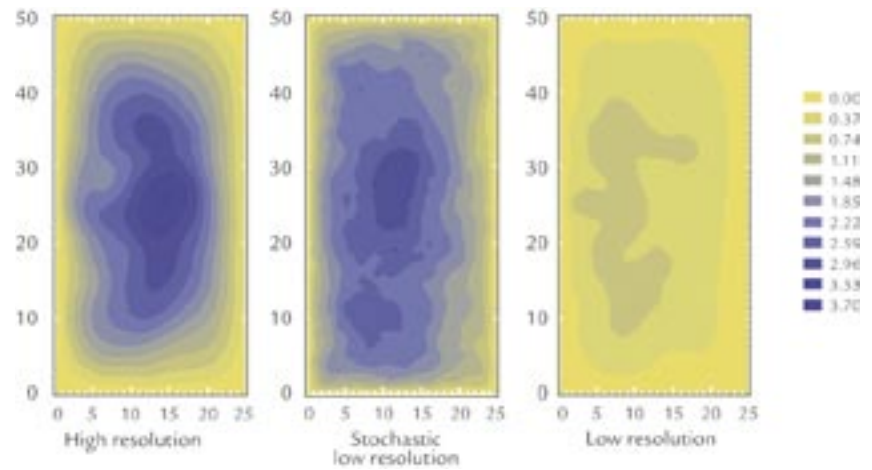


Figure 3. Similar to Figure 1, however, the standard deviation of the stream function over time is shown, rather than the average over time. This shows that multiple moments of the stream function are reproduced well in the SC approach.

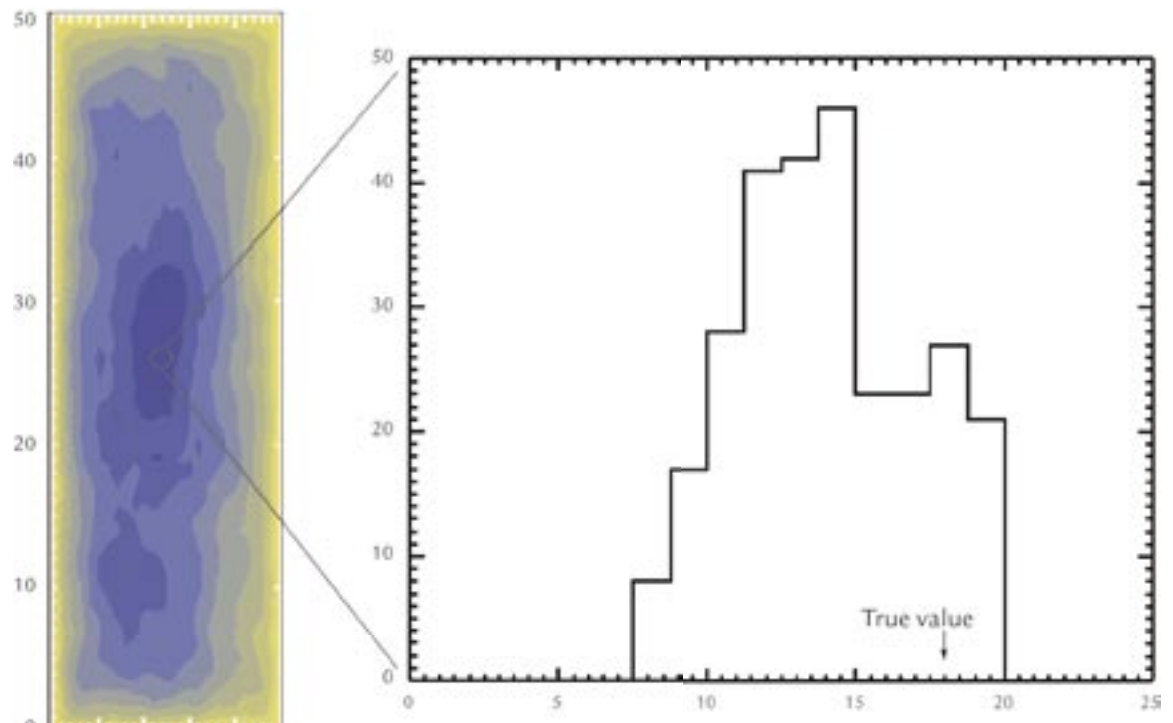


Figure 4. Illustrating how uncertainty is estimated in the SC approach. The left panel is a duplicate of the middle panel of Figure 3, showing the standard deviation over time of the stream function (SDSF) and averaged over multiple SC simulations. The panel on the right shows the histogram of this quantity over the multiple SC simulations for the region shown in the circle on the left panel figure. This histogram represents the relative probability of the SDFS values, which quantifies the uncertainty of this quantity. The true value is shown in the figure and is consistent with this distribution.

Biophysics Research Highlights

quantity may be estimated by simply calculating the variance of that quantity across the multiple stochastic closure runs, as shown in Figure 4.

Conclusion

We are developing a novel method to model the effects of unresolved subgrid phenomena and to quantify uncertainty in simulations of nonlinear PDEs. Our method is based on a probability distribution of closure relations that is sampled and added to each time evolution step of the simulation of the unmodified PDEs. We have demonstrated this approach with a simple two-dimensional ocean model and are working to develop this method so that it can generally be applied to a wide range of problems.

References

1. B.T. Nadiga and L.G. Margolin, "Dispersive eddy parameterization in a barotropic model," *Journal of Physical Oceanography* **31**, 2525–2531 (2001).
2. D.D. Holm, J.E. Marsden, and T.S. Ratiu, "Euler-Poincare models of ideal fluids with nonlinear dispersion," *Physical Review Letters* **80**, 4173–4177 (1998).
3. M.D. McKay, R.J. Beckman, and W.J. Conover, "A comparison of three methods for selecting values of input variables in the analysis of output from a computer code," *Technometrics* **21**, 239–245 (1979).
4. W.J. Welch *et al.*, "Screening, predicting, and computer experiments," *Technometrics* **34**, 15–25 (1992).
5. C.E. Leith, "Stochastic backscatter in a subgrid-scale model: plane shear mixing layer," *Physics of Fluids A* **2**, 297–299 (1990).
6. R.J. Greatbatch and B.T. Nadiga, "Four-gyre circulation in a barotropic model with double-gyre wind forcing," *Journal of Physical Oceanography* **30**, 1461–1471 (2000).

Acknowledgment

This work is supported by the LANL Laboratory-Directed Research and Development program.

For further information, contact David Schmidt, 505-665-3584, dschmidt@lanl.gov.

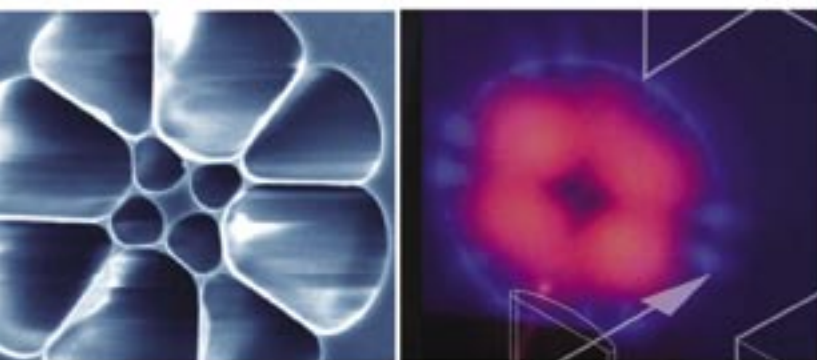


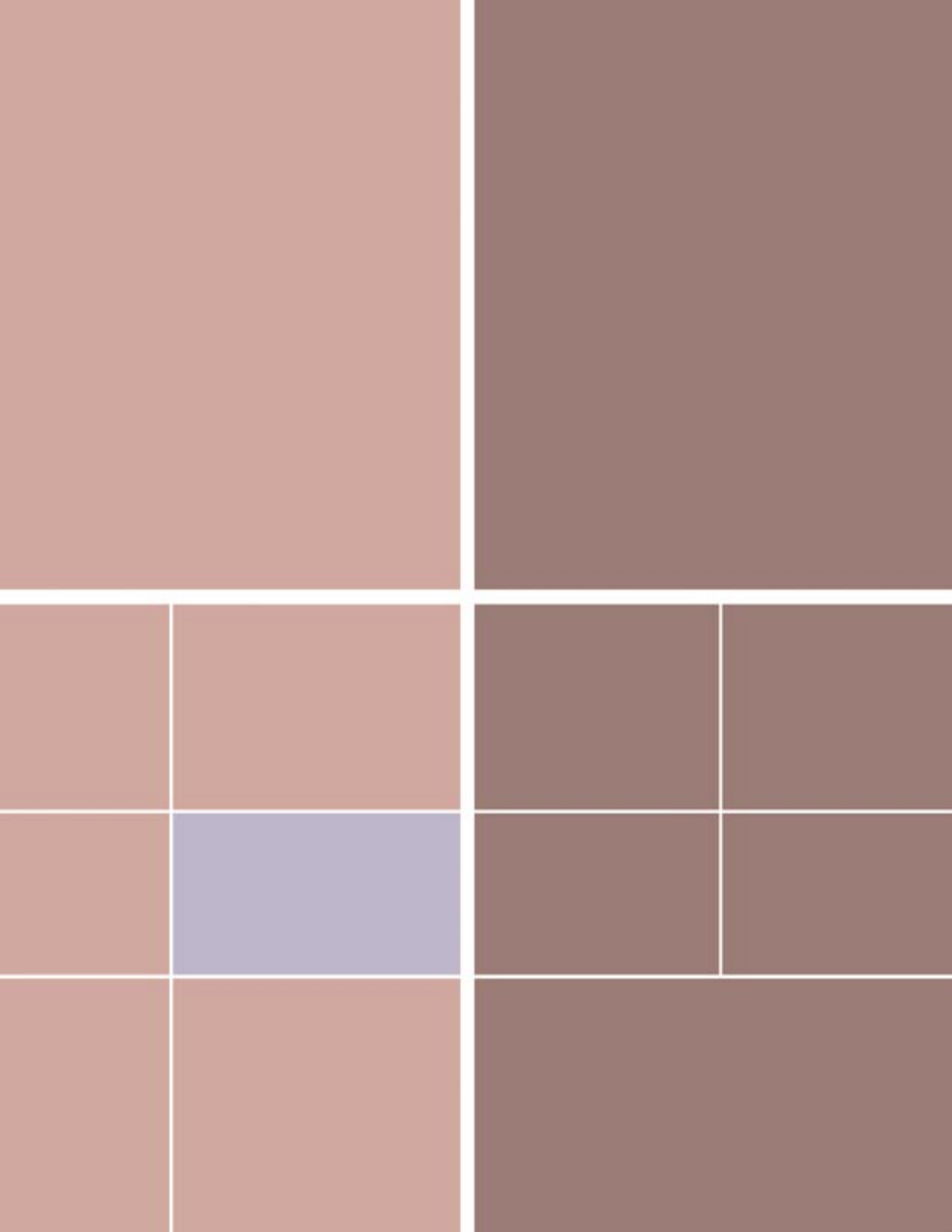
The World's Greatest Science Protecting America

Los Alamos National Laboratory, an affirmative action/equal opportunity employer, is operated by the University of California for the U.S. Department of Energy under contract W-7405-ENG-36.



Atomic Physics Research Highlights





Quantum Simulations of Condensed Matter Systems using Trapped Ions

D.J. Berkeland, G.H. Ogin, W.R. Scarlett (P-21), M.G. Blain, C.P. Tigges (SNL)

When Richard Feynman famously proposed a quantum computer, his intended application was actually to simulate quantum dynamical systems. This problem is difficult because as the number of elements of a quantum system increases *linearly*, the complexity of the equations modeling it grows *exponentially*. For example, to completely describe the dynamics of just 40 spin-1/2 particles requires $2^{40} \times 2^{40} = 10^{24}$ matrix elements, orders of magnitude greater than what can be stored on any classical supercomputer. This complexity is why we cannot even determine the correct theoretical behavior of some important systems. Our understanding of quantum phenomena such as superconductivity, antiferromagnetism, behavior of *f*-electrons in solids, and so on, is seriously limited.

Feynman's proposed solution to this problem was to simulate one quantum-mechanical system with another. The states of the simulator would follow the same equations of motion as the real system, yet would be directly accessible so the state evolution could be monitored. A decade later, Seth Lloyd showed that Feynman's conjectured solution was correct. He pointed out that "a mere 30 or 40 quantum bits would suffice to perform quantum simulations of multidimensional fermionic systems such as the Hubbard model," which is believed to explain phenomena such as high-temperature superconductivity, "that have proved resistant to conventional computational techniques."¹

A first-principles understanding of the behavior of materials would profoundly affect academia, defense, and industry. In spite of this, little experimental effort has been extended towards quantum simulations of condensed-matter systems. This is because theoretical proposals for quantum simulations have been cast in general terms. Only recently, quantum information theorists have begun to map these problems onto experimentally accessible atomic systems, urged on by correspondingly recent advances in coherent manipulations of those systems. For example, E. Jané proposed that several paradigms of condensed-matter physics can be modeled in trapped-ion systems and neutral atoms in optical lattices.² Subsequently, more detailed simulations were proposed for trapped ions in Porras' and Barjaktarevic's studies.^{3,4}

These proposals rely on several key concepts. A single atom can simulate a spin system (for example, an electron) which is the fundamental building block of real material. Laser light interacts with the atoms to simulate site-specific potentials (such as magnetic fields). State-dependent optical forces manipulate atomic positions to simulate interactions between the spin systems. Put together, these components map atomic systems onto equivalent arrays of quantum spins found in some condensed-matter systems. Yet, our atomic

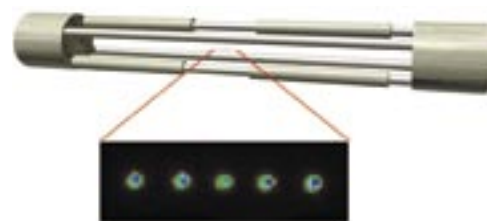


Figure 1. Our current ion trap and a depiction of five ions confined along its axis. The picture below the trap shows five ions imaged in our laboratory.

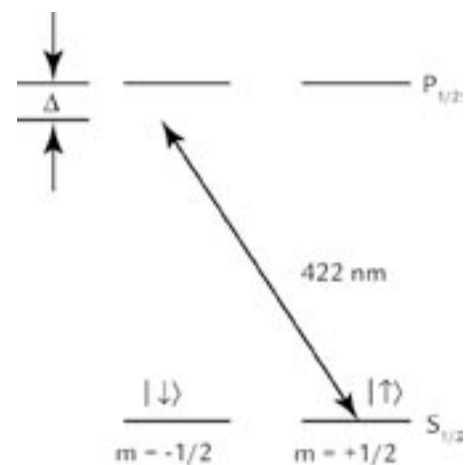


Figure 2. Relevant energy levels and optical transition in strontium-88(+). The $S_{1/2}$ states simulate a spin-1/2 system, and the near-resonant 422 nm light creates the state-dependent force described below.

RESEARCH HIGHLIGHT PHYSICS DIVISION

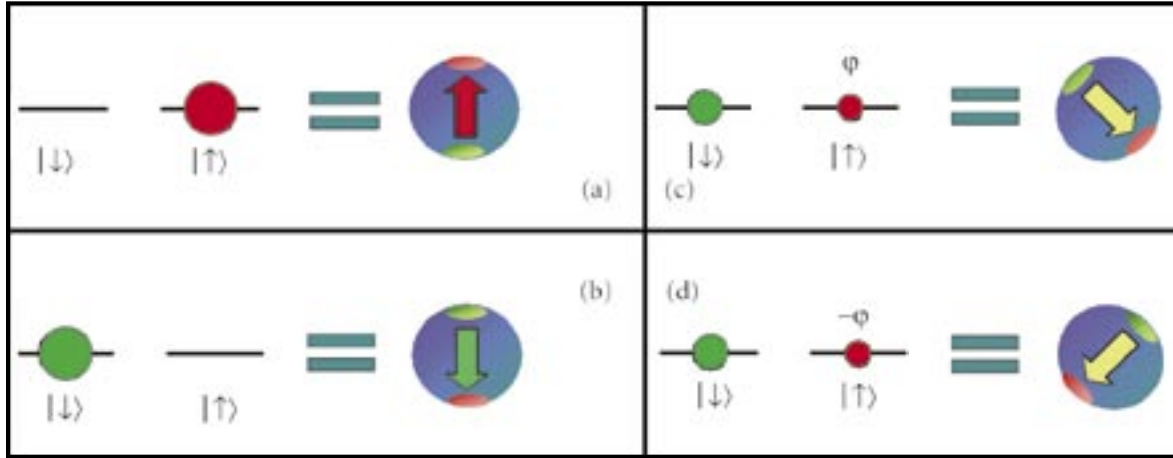


Figure 3. Simulated spin and its direction. In (a) the ion is in the $|\uparrow\rangle$ state and the spin points “up”; in (b) the ion is in the $|\downarrow\rangle$ state and the spin points “down”; in (c) the ion is in a superposition of states and its dipole points in a corresponding direction; in (d) the phase of the $|\uparrow\rangle$ component is reversed and the spin is rotated relative to (c).

spin systems can be free of complicating impurities and defects, we can precisely control the interatomic interactions, and the system evolution can be characterized and measured more easily than in real materials.

We will describe experiments we are just beginning, using arrays strontium-88(+) ions confined in our linear radio-frequency trap.⁵ This work is part of a larger LANL project on quantum simulations in Theoretical Division and Chemistry Division.

Basic Interactions

We confine ions in the trap shown in Figure 1. Figure 2 shows the relevant optical transition and quantum-mechanical states of strontium-88(+). The Zeeman levels of the ion’s ground state simulate the spin-up and spin-down states of a spin-1/2 particle: $|\downarrow\rangle = |S_{1/2}, m_J = -1/2\rangle$ and $|\uparrow\rangle = |S_{1/2}, m_J = +1/2\rangle$. The ion’s wavefunction is described by the equation $\psi = c_\uparrow |\uparrow\rangle + c_\downarrow |\downarrow\rangle$, where c_\uparrow and c_\downarrow are complex numbers with a relative phase ϕ between them. We can determine ψ using a series of laser and magnetic-field pulses not described here. As Figure 3 illustrates, this spin system of $|\downarrow\rangle$ and $|\uparrow\rangle$ states can be visualized as a vector. The vector’s direction depends on the relative probability of the ion being in one state

or the other and on the phase difference between c_\uparrow and c_\downarrow .

Figure 4 illustrates how we induce ion-ion interactions that simulate the spin-spin interactions in condensed-matter problems. A force on each ion pushes it in the α direction only if it is in the $|\uparrow\rangle_\alpha$ state ($|\uparrow\rangle$ in the basis in which α is the quantization axis). We derive this force from beams of 422 nm laser light that are tightly focused on points a few microns from each ion in the z -direction. This light is detuned $\Delta = 1$ to 10 GHz below resonance with the $S_{1/2} \leftrightarrow P_{1/2}$ transitions as shown in Figure 1. This detuning Δ is enough that spontaneously scattered light does not ruin the coherence between the spin states, but not so much that the laser no longer affects the ion. The atom-laser interaction creates an optical dipole force so that the ion moves towards the most intense part of the laser beam. Furthermore, the light is circularly polarized so that the $|\uparrow\rangle$ takes part in the atom-light interaction, but not the $|\downarrow\rangle$ state. If the ion is in a superposition of the $|\downarrow\rangle$ and $|\uparrow\rangle$ states, only its $|\uparrow\rangle$ component moves along the z -axis. This part of its wavefunction accumulates a phase ϕ because it moves through the combined potential of the trap and the other ions.⁶ Changing the relative phase between the $|\downarrow\rangle$ and $|\uparrow\rangle$ wave-function components is equivalent to rotating the simulated spin

about the z -axis. Because this rotation depends on the relative positions of the other ions in the trap, and because the state-dependent force of 422 nm laser beams also affects those positions, the rotation angle of one spin-1/2 system depends on the quantum states of the other ions.

It is not surprising, then, that these interactions result in a spin-spin interaction term in the equations describing this system. More rigorous calculations show that the interactions due to the 422 nm pushing laser can map onto the Ising model (in which just the vertical components of the particles’ spins interact), and the XYZ model (in which all three components of spins interact) if three sets of 422 nm beams propagate along the three orthogonal trap axes.³ These two models describe some of the most fundamental interactions in quantum many-body systems, from which many more complicated systems can be derived.

Quantum Simulations

All of our simulations will follow a similar basic procedure. The system will be initialized so that all ions are in the $|\downarrow\rangle$ state. The lasers will then be turned on for up to $\sim 100 \mu\text{s}$. After this process, we will measure the state of each ion. As an

example, we could search for a quantum phase transition in a one-dimensional array of trapped ions as the simulated spin-spin interaction grows relative to an applied magnetic field. At a particular value, we expect that the final state of the ion array changes from a disordered one to either one in which the spins are aligned with each other, or one in which the direction of the spins alternate along the ion array.

We can compare our experimental results to exact calculations when we use small numbers of ions and two sophisticated computer simulations using somewhat larger systems. This comparison of moderately large physical systems with computational results will let us check the precision of our experimental system and that of our theoretical techniques as they progress together. However, even the most sophisticated computer approximations cannot simulate the dynamics of one-dimensional systems with more than roughly 30 spins, and we expect to be able to perform such experiments in the next few years.

Two-dimensional arrays of trapped ions will allow more sophisticated and complex simulations. A good first choice for a two-dimensional spin array is a two-legged ladder such as that shown in Figure 5. Inducing XYZ and Ising interactions on such a ladder will let us investigate systems that display unusual phase transitions and systems that have possible connections to high- T_c superconductivity.⁷ In fact, we can make the interactions between opposite spins of a spin ladder XY-like, while coupling nearest neighbor spins with an Ising-like interaction. The resulting quantum-spin model is equivalent to a one-dimensional fermionic Hubbard model.⁸ This is the most widely used model of a strongly interacting system in condensed-matter physics, and the ability to simulate it vastly increases our ability to use our simulator to understand materials-science problems.

Through collaboration between LANL and Sandia National Laboratories, we are designing the new ion traps that are

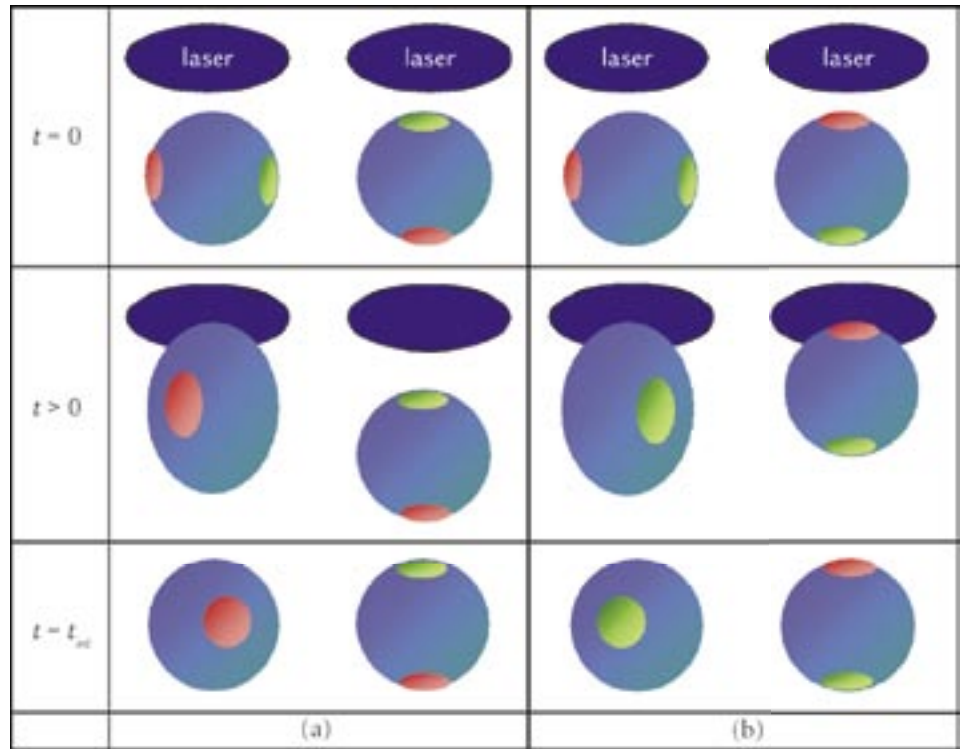


Figure 4. Effect of the 422 nm laser beam on the direction of the atomic spin depends on the state of the ion and that of the ions next to it. At $t = 0$, the 422 nm laser beams are turned on. In (a), the ion on the right is in the $|\downarrow\rangle$ state and not affected by the laser beam, but it is pushed downward due to the Coulomb repulsion from the ion on the left. In (b), the ion on the right is in the $|\uparrow\rangle$ state and is pulled toward the beam center. In both (a) and (b), the ion on the left sees its $|\uparrow\rangle$ component pulled into the laser beam. But in (a), its $|\uparrow\rangle$ component sees a phase shift ϕ as it moves through the Coulomb field of the other ion, while in (b), its $|\downarrow\rangle$ component feels almost the same shift ϕ as the other ion moves relative to it. So, when the 422 nm light is turned off at $t = t_{int}$, the ion in (a) has rotated by nearly the opposite amount as the ion in (b). This quantum gate operation, in which the final state of one ion depends on the quantum state of its neighbor, simulates interaction terms found in quantum condensed-matter systems.

required for simulations with tens of ions in one and two dimensions. Such traps will be microfabricated in a unique tungsten deposition process that has already made arrays of millions of micron-sized ion traps for mass-spectroscopy applications.⁹ We will push this process to build the first two-dimensional traps, to confine two parallel, interacting ion chains (a spin ladder), and to confine ions in configurations

such as a hexagonal close-packed array. These microfabrication techniques can build traps that are compatible with the trap-mounted photonics, electronics, and data-acquisition systems that will be necessary for our quantum simulations with larger ion arrays.

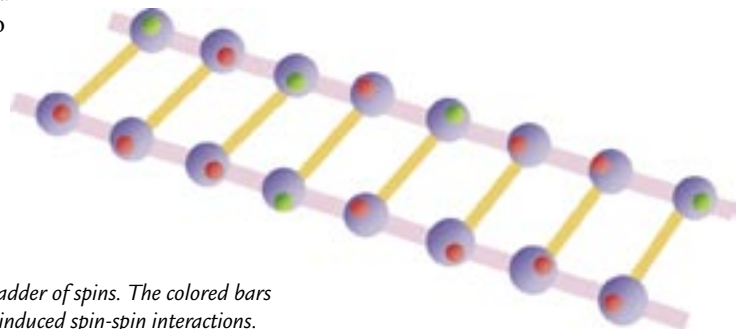


Figure 5: A two-legged ladder of spins. The colored bars represent different laser-induced spin-spin interactions.

Impact on Other Fields

What will we gain from these experiments? We have already described the sorts of first-principle understandings into materials science resulting from these physical simulations. These insights should lead to practical advances in real materials science. Historically, the ability to design and manufacture better materials has been crucial to military and industrial superiority. Developing such materials in fabrication labs with macroscopic samples is extremely expensive and time consuming, and investigating them in scientific labs is difficult because of imperfections and complications in real materials. Because of this, massive computational resources are applied to these problems, but these techniques falter when quantum-mechanical effects become important. A quantum simulator could ultimately be used to design advanced materials with new types of quantum-mechanical order. Even without using thousands of simulated spins, a quantum simulator could test the models that are used in the design of advanced materials before designers fully invest their funding and time.

Another significant benefit from these experiments is that they will represent the largest quantum computer test-bed to date. This special class of quantum computers is experimentally feasible because the stringent requirements of universal quantum computation are drastically reduced, largely because the interactions are simple and fast. The quantum simulator requires less laser stability than a universal quantum computer and less immunity from the external field noise that destroys quantum mechanical entanglement. The ions do not have to be prepared in their ground state of motion.^{3,6} Indeed, the extreme demands of error correction on

quantum computing are vastly reduced and probably unnecessary for simulations involving 30–50 ions.¹⁰ Consequently, we can leap from studying one and two ions for universal quantum computation to working with an order of magnitude more ions in more than one dimension. We therefore expect to gain crucial insight into the engineering and algorithmic demands of large-scale quantum computation.

Finally, even though a quantum simulator requires much less control over a physical system than a quantum computer does, it still uses the same technical resources. Both applications require traps that can hold large, two-dimensional arrays of ions. Both will ultimately require complex optical systems and compact data-acquisition systems that can function with thousands of ions, or more, simultaneously. Because the two systems share common needs, the technology developed while building a quantum simulator would lead to practical quantum computation.

In short, the work described here has the fortunate attributes of both basic, fundamental science and practical, applied technologies. We expect to contribute both to national-security interests and to the intellectual pursuits of condensed-matter and quantum-information scientists.

References

1. S. Lloyd, "Universal quantum simulators," *Science* **273**, 1073–1078 (1996).
2. E. Jané *et al.*, "Simulation of quantum dynamics with quantum optical systems," *Quantum Information and Computation* **3**, 15–37 (2003).
3. D. Porras and J.I. Cirac, "Effective quantum spin systems with trapped ions," *Physical Review Letters* **92**, 207901 (2004).
4. J.P. Barjaktarevic, G.J. Milburn, and R.H. McKenzie, "Fast simulation of a quantum phase transition in an ion-trap realisable unitary map," e-Print Archive preprint quant-ph/0401137 (22-Jan-04).
5. D.J. Berkeland, "Linear Paul trap for strontium ions," *Review of Scientific Instruments* **73**, 2856–2860 (2002).
6. T. Calarco, J.I. Cirac, and P. Zoller, "Entangling ions in arrays of microscopic traps," *Physical Review A* **63**, 062304-01–062304-20 (2001).
7. E. Dagotto and T.M. Rice, "Surprises on the way from one- to two-dimensional quantum magnets: The ladder materials," *Science* **271**, 618–623 (1996).
8. C.D. Batista and G. Ortiz, "Algebraic approach to interacting quantum systems," *Advances in Physics* **53**, 1–82 (2004).
9. M.G. Blain *et al.*, "Towards the hand-held mass spectrometer: design considerations, simulations, and fabrication of micrometer-scaled cylindrical ion traps," *International Journal of Mass Spectrometry* **236**, 91–104 (2004).
10. J.I. Cirac and P. Zoller, "New Frontiers in Quantum Information with Atoms and Ions," *Physics Today* **57**, 38–44 (March 2004).

Acknowledgments

This work is funded through the Laboratory-Directed Research and Development program as part of 20050076DR, "Cold Atom Quantum Simulators."

For further information, contact Dana Berkeland at 505-665-9148, djb@lanl.gov.



The World's Greatest Science Protecting America

Los Alamos National Laboratory, an affirmative action/equal opportunity employer, is operated by the University of California for the U.S. Department of Energy under contract W-7405-ENG-36.



Novel Broadband Light Sources— Guiding Light through Glass and Holes

F.G. Omenetto, M.R. Wehner, M.R. Ross, E.H. Gershgoren (P-23), A.V. Efimov (MST-10), A.J. Taylor (CINT)

Over the last seven years, photonic crystal fibers (PCFs) have become one of the success stories of modern photonics.¹ Starting as a highly speculative idea in 1991, it is now possible to obtain PCFs in different varieties with specifically tailored features.² A typical PCF consists of an array of microscopic holes (hollow capillaries with diameters precisely controllable in the range ~ 25 nm to ~ 50 nm) running along the fiber length (Figure 1). These holes act as optical barriers or scatterers which, suitably arranged, can trap light within a central core (either hollow or made of solid glass). The very large air-glass refractive-index difference opens up many new possibilities not available in standard fibers. For example, light can be guided in a hollow core by a photonic-bandgap effect. The revolutionary nature of the waveguides and their very high performance measured in terms of loss, nonlinearity, and dispersion control means that applications are emerging in many diverse areas of science and technology.

A Rainbow of Light

One of the immediate consequences of these new waveguides is the spawning of renewed interest in the study of nonlinear processes in optical fibers, specifically in regards to supercontinuum formation and various mixing and nonlinear frequency-conversion processes. A supercontinuum is formed when a short pulse of light (typically of subpicosecond duration) undergoes a nonlinear interaction with the material in which it propagates. Such interaction, in the appropriate conditions, leads to a dramatic broadening

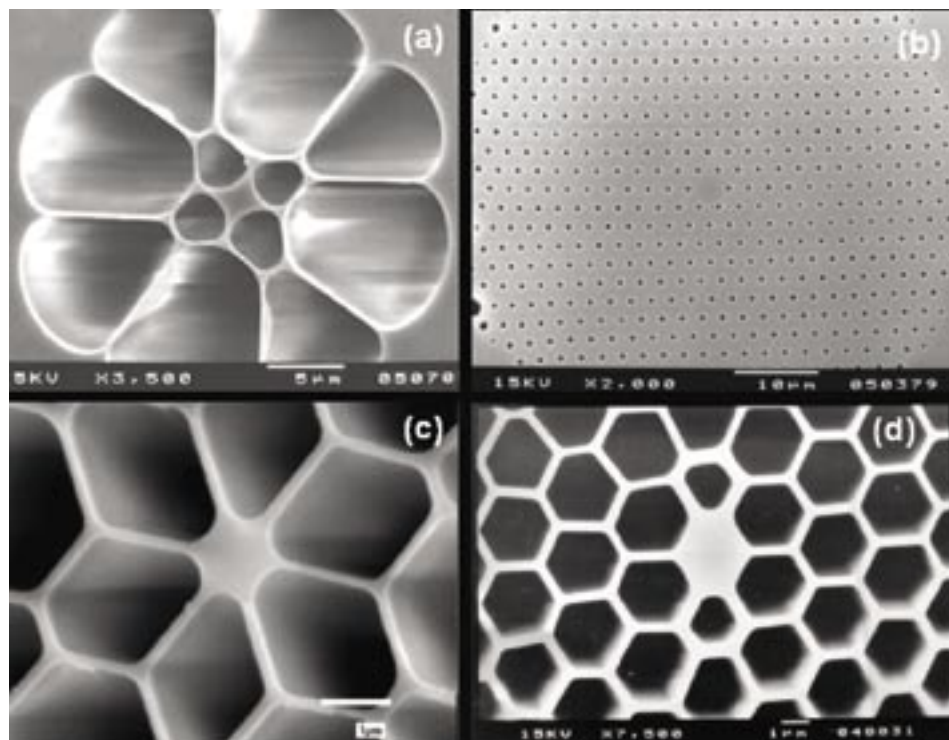


Figure 1. Scanning-electron-microscope images of the cross section of various PCF samples. Fiber (a) is the extruded soft-glass PCF used for ultrabroadband supercontinuum generation.^{10,11} Fiber (b) is the dispersion-flattened silica PCF that allows us to obtain flat and controlled dispersion curves (close to zero dispersion over ~ 300 nm).² Fibers (c) and (d) are both high air fill cladding PCF. Fiber (c) is used to generate supercontinuum with $\lambda \sim 800$ nm short-pulse pumping and phase-matched modes in the visible and ultraviolet.^{3,4,7,8} Fiber (d) is highly birefringent fiber for enhanced polarization dependent nonlinear effects (photo courtesy of the University of Bath).

RESEARCH HIGHLIGHT
PHYSICS DIVISION

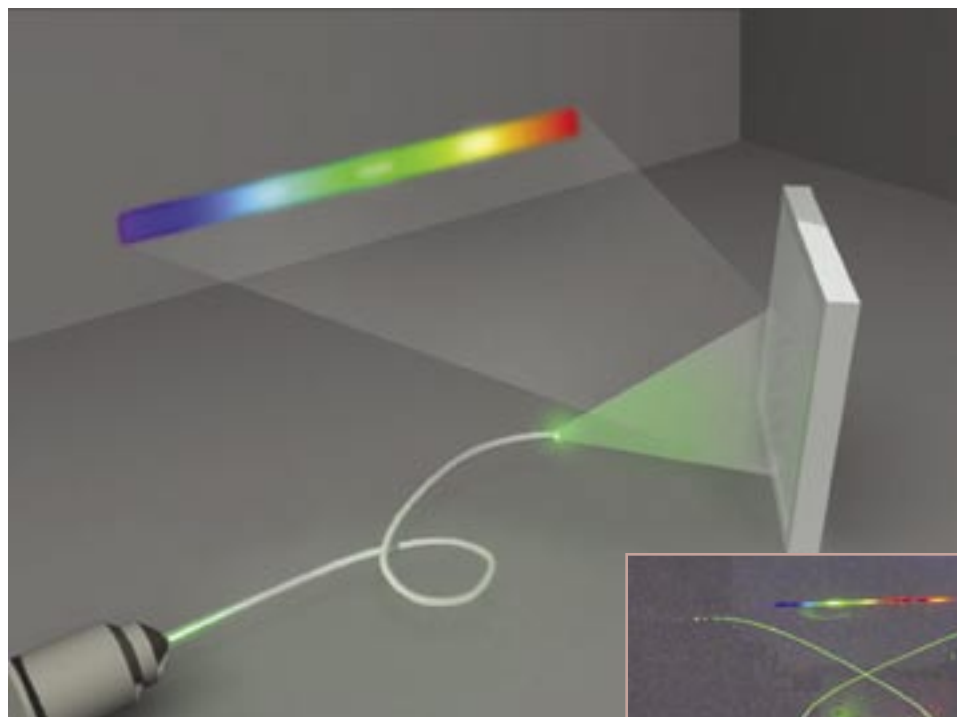


Figure 2. Supercontinuum generation in a 75 cm piece of SF₆ PCF. The background of the image shows the output of the fiber dispersed by a grating and focused on a white piece of paper. The visible components are generated by the nonlinear interactions that spectrally broaden the 1550 nm, 100 fs pulse coupled in the fiber.

of the pulse's bandwidth, and provides a "rainbow of colors" at the output. These conditions were traditionally obtained in the early 1980s by propagating high-intensity laser pulses through materials such as sapphire. PCFs provide the very desirable feature of confining and guiding the optical field in a glass core whose diameter does not exceed a few microns. Having a moderately high-intensity femtosecond laser pulse combined with the spatial confinement of the guided mode is enough to make the nonlinear interaction between light and glass the overwhelmingly dominant process governing pulse propagation in PCF.

Spectacular frequency-conversion phenomena occur in these conditions. We have described power-dependent generation of visible radiation by coupling femtosecond pulses at a wavelength of 1550 nm in a 95 cm segment of a "high- Δ " microstructured fiber (i.e., high-air

filling in the cladding). Two bands of visible radiation were generated by a combination of temporal pulse splitting of the fundamental pulse followed by Raman self-frequency shifting of one of the split pulses and a subsequent third harmonic generation of both frequencies.³ The visible generated radiation is dependent on the polarization state of the input pulse coupled into the PCF.

One of the most dramatic manifestations of the nonlinear effects in PCFs is supercontinuum generation.⁴ When 100 fs pulses from titanium-sapphire lasers ($\lambda \sim 800$ nm) were coupled in a few meters of these fibers, the combination of nonlinear effects gave rise to a significant spectral broadening spanning nearly 1000 nm. This result provided a practical means to achieve an efficient pulsed white light source encompassing an "optical octave" (400–800 nm). This latter feature is of great value in realizing

precision measurement techniques based on supercontinuum frequency combs (Figure 2).

The appeal of controlling supercontinuum as a practical source of light remains very high. The availability of such a broad-bandwidth source is extremely important for a variety of applications such as spectroscopic detection and interrogation, new laser source generation, broad-bandwidth communication sources, and arbitrary signal generation. Typically made of silica, the PCFs used to generate supercontinuum radiation provide slightly in excess of one optical octave usually limited by the physical properties of the fiber itself (such as modes supported, wavelength-dependent absorption, dispersion etc.).

Summary of Some Experimental Results

We experimentally observed that the propagation of a pulse of fixed energy, though linearly polarized along different directions, yields very distinct visible components at the output.⁵ These results suggest a polarization-dependent selectivity for phase-matching (i.e., frequency conversion) according to the input polarization state. Such polarization-dependent selectivity provides a means to generate specific harmonics and, therefore, a means to control the output's visible frequency through the input pulse polarization state. These approaches are promising for the research and development of all-fiber signal control and in-fiber ultrafast optical switching.⁶ Furthermore, through intramodal phase matching processes in PCFs, one can generate guided modes well into the ultraviolet region ($\lambda < 250$ nm)^{7–9} (Figure 3).

In collaboration with the University of Bath, we have experimented with soft Schott glass (SF6) PCFs and studied supercontinuum formation in these new structures. This glass exhibits greater transparency in the infrared than silica

and also has a higher nonlinear index of refraction, thereby enhancing the nonlinear interaction between the optical pulse and the glass. Initial results indicated a broader supercontinuum than what was conventionally achievable with silica-based PCFs, extending the spectral span to ~ 1400 nm after propagating pulses in a 75 cm piece of fiber.¹⁰

We have recently demonstrated the broadest supercontinuum formation ever recorded¹¹ by propagation $\lambda = 1550$ nm, ~ 100 fs pulses of 1 nJ energy in a short ($Z = 4.7$ mm) piece of the SF6 PCF. The measurement illustrated in Figure 4 compares a typical supercontinuum trace obtained with silica PCF. The present measurement is limited by the finite spectral sensitivity of the cooled mercury-cadmium-titanium detector, which does not go beyond $3 \mu\text{m}$. The extensive span of this supercontinuum offers opportunities across multiple wavelength areas, covering seven optical octaves of 400 nm, for instance, and extending the wavelength ranges well into the infrared region. In addition to the spectral extent of this source, this result has given us further insight into the physical mechanism of supercontinuum.⁴

Conclusion

The study of these fibers and the nonlinear effects that take place in them is an area rich in opportunities in the basic and applied sciences. A glimpse of the breadth of the field is offered by the future possibilities that include new approaches to optical fiber sensors, high-power fiber lasers, sources for medical imaging, and hollow-core photonic crystal fibers

(which open exciting avenues to realize enhanced, specialized Raman cells for high-sensitivity spectroscopy, or for the sensing of atmospheric contaminants such as molecules or viruses).

The future looks bright for guided light.

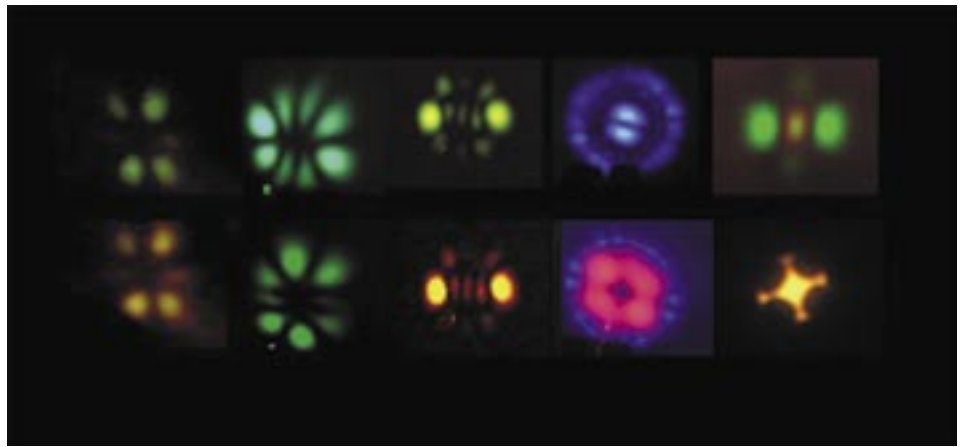
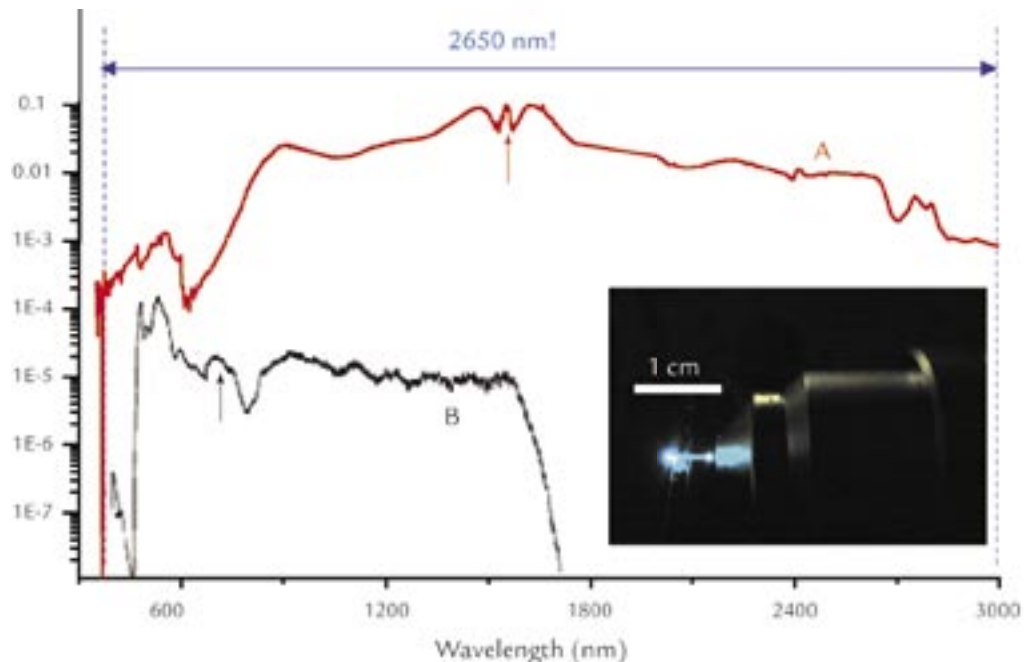


Figure 3. Far-field images of the generated, visible-guided modes resulting from frequency-conversion processes in PCFs. All of these modes are obtained by phase-matched generation of third harmonic in silica PCF with the exception of the last pair, which is generated in the SF6 fiber (for a detailed description and analysis refer to References 5–10).

Figure 4. Ultrabroad supercontinuum (curve A) generated in a $Z = 4.7$ mm piece of SF6 PCF. Pulses used in the experiment have temporal duration of 110 fs at $\lambda = 1550$ nm, and the energy per pulse is ~ 1 nJ ($P_{\text{avg}} = 80$ mW at an 80 MHz repetition rate). The supercontinuum average power at the output of the fiber is 20 mW. And the radiation generated spans a range from at least 350 nm to 3000 nm (the detectors used were sensitive only in this wavelength range). Curve B represents the typical supercontinuum obtained by coupling 800 nm pulses in silica PCFs (after Reference 10). The axes have been adjusted to match the scales for both cases. The arrows indicate the pumping wavelength in the two cases. The inset shows a picture of the SF6 fiber when supercontinuum is being generated. The microscope objective used for coupling the pulses is also visible.



Atomic Physics Research Highlights

References

1. P. Russell, "Photonic crystal fibers," *Science* **299**, 358–362 (2003).
2. W.H. Reeves *et al.*, "Supercontinuum generation in dispersion flattened photonic crystal fiber," *Nature* **424**, 511–515 (2003).
3. F.G. Omenetto *et al.*, "Polarization dependent third harmonic generation in photonic crystal fibers," *Optics Express* **11**, 61–67 (2003).
4. J.K. Ranka, R.S. Windeler, and A.J. Stentz, "Visible continuum generation in air-silica microstructure optical fibers with anomalous dispersion at 800 nm," *Optics Letters* **25**, 25–27 (2000).
5. F.G. Omenetto *et al.*, "Simultaneous generation of spectrally distinct third harmonic in photonic crystal fibers," *Optics Letters* **26**, 1558–1560 (2001).
6. F.G. Omenetto *et al.*, "Polarization dependent third harmonic generation in photonic crystal fibers," *Optics and Photonics News* **14**, 36 (2003).
7. F.G. Omenetto, "Femtosecond pulses in optical fibers," in *Progress in Optics*, E. Wolf (Ed.), (Elsevier, Amsterdam, 2002), **44**, pp. 85–141.
8. A. Efimov *et al.*, "Phase-matched third harmonic generation in microstructured fibers," *Optics Express* **11**, 2567–2576 (2003).
9. A. Efimov *et al.*, "Nonlinear generation of very high order UV modes in microstructured fibers," *Optics Express* **11**, 910–918 (2003).
10. V.V. Ravi Kanth Kumar *et al.*, "An extruded soft glass photonic crystal fiber for supercontinuum generation," *Optics Express* **10**, 1520–1525 (2002).
11. F.G. Omenetto *et al.*, "An ultrabroad supercontinuum laser source," (in preparation).

Acknowledgment

We gratefully acknowledge our collaborators at the University of Bath (Philip Russell and Jonathan Knight) for the continuous collaboration and for the endless supply of new PCF samples, and specifically Will Reeves and V.V.R.K. Kumar for the early work on SF6 fibers. This work was funded by the Laboratory-Directed Research and Development program.

For further information, contact
Fio Omenetto, 505-665-5847,
omenetto@lanl.gov.



The World's Greatest Science Protecting America

Los Alamos National Laboratory, an affirmative action/equal opportunity employer, is operated by the University of California for the U.S. Department of Energy under contract W-7405-ENG-36.



Time Variation of Alpha

J.R. Torgerson, S.K. Lamoreaux, T. Fortier, E. Gershgoren, F.G. Omenetto, M.M. Schauer (P-23), D. Budker, T. Nguyen (University of California, Berkeley), S.A. Diddams (National Institute of Standards and Technology), V.V. Flambaum (University of New South Wales)

If we accept the idea that our universe formed from nothing with the “big bang,” it must also seem reasonable that, at some point in the past, fundamental constants of physics were varying with time. Moreover, events that likely occurred immediately following the big bang, such as inflation and later acceleration, suggest a modification of the values of fundamental constants. A smooth evolution of the values of such parameters would thus lead to the conclusion that they are still changing and that this change may be measurable even today. Because our most widely accepted theories of nature do not allow for such variation, such evidence would be proof of physics beyond our current understanding. It is important to point out that there is little basis to assert that many of the parameters in our theories of nature are constants independent of space and time.

The question of whether the fundamental constants are still varying has been of interest at least since Dirac put forward his “large number hypothesis.”¹ Dirac noticed that certain dimensionless combinations of physical constants fell into three groups of order: unity, 10^{40} , and 10^{80} . The 10^{40} group, in particular, was thought to depend on the size of the universe. Although this hypothesis was based on coincidental observations, the formalism of modern string theory allows for the possibility of a dependence of the fundamental constants on the gravitational potential, or possibly on the dark energy responsible for the nonzero cosmological constant.

Of particular interest for variation of fundamental constants are the

dimensionless gauge coupling constants, such as the fine-structure constant ($\alpha = 1/137 = e^2/\hbar c$) whose value determines the strength of electromagnetic interactions. Table 1 summarizes the results of some of the recent searches for time variation of α . Recent astronomical observations have indicated that over the last 10 billion or so years the value of α has changed and that the average rate of fractional variation is $\dot{\alpha}/\alpha \approx 10^{-16}/\text{yr}$,² although this result remains controversial³. Analysis of the ancient nuclear fission reactor in Gabon, West Africa, can also be used to search for ancient variation of α , and the two most recent results are listed in Table 1 and discussed below.

Recent precision laboratory clock-comparison experiments, where different atomic transitions that depend differently on α are used as frequency references and are measured over a period of years, have limited the rate of variation to $\dot{\alpha}/\alpha < 10^{-15}/\text{yr}$.⁴⁻⁶ The purpose of our studies is to further improve the limit on (or observe!) time variations at the level of $10^{-18}/\text{yr}$. For this purpose, we have started efforts which include two laboratory measurements with atomic references and a study of the Oklo natural-reactor phenomena.

Reanalysis of the Oklo Natural Reactor

Two billion years ago, the relative isotopic fraction of uranium-235 in natural

Table 1. Status of searches for α variation

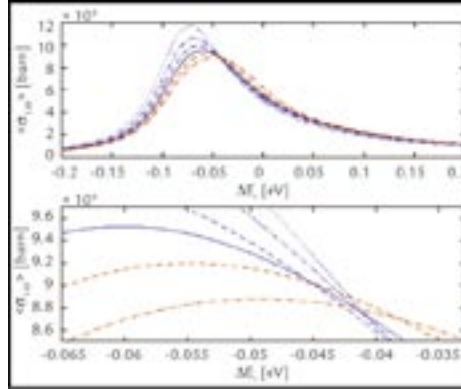
	$\dot{\alpha}/\alpha \text{ (yr}^{-1}\text{)}$	Method	Quantity	Reference
Distant	$\leq 5 \times 10^{-15}$	Re ₁₁₇ decay	$\alpha(m_f/\Lambda_{\text{QCD}})^{1/2}$	14
	$(6.4 \pm 1.4) \times 10^{-16}$	QSO spectra	α	2
	$(0.6 \pm 0.6) \times 10^{-16}$	QSO spectra	α	3
	$\leq 0.8 \times 10^{-17}$	Oklo reactor	$\alpha(m_f/\Lambda_{\text{QCD}})^{1/2}$	8
	$-(2.3 \pm 0.7/-0.3) \times 10^{-17}$	Oklo reactor	$\alpha(m_f/\Lambda_{\text{QCD}})^{1/2}$	10
Local	$\leq 3.7 \times 10^{-14}$	H \leftrightarrow Hg ⁺	$g_{\text{Hg}}/g_{\text{H}} \cdot \alpha^{2.2}$	15
	$\leq 1.2 \times 10^{-15}$	opt-Hg ⁺ \leftrightarrow Cs	$g_{\text{Cs}} \cdot m_f/m_p \cdot \alpha^{6.0}$	4
	$(-0.04 \pm 1.6) \times 10^{-15}$	Rb \leftrightarrow Cs	$g_{\text{Cs}}/g_{\text{Rb}} \cdot \alpha^{0.44}$	5
	$(-0.3 \pm 2.0) \times 10^{-15}$	Opt-Yb ⁺ \leftrightarrow Cs	$g_{\text{Cs}} \cdot m_f/m_p \cdot \alpha^{2.0}$	6

RESEARCH HIGHLIGHT
PHYSICS DIVISION



Atomic Physics Research Highlights

Figure 1. Calculation of the neutron-absorption cross section for ^{149}Sm $\hat{\sigma}_{149} \equiv \langle \sigma_{149} \rangle$ as a function of change in resonance energy E_r and as a function of temperature for $\Sigma_a/\Sigma_s = \sqrt{300/T}$, where Σ_a and Σ_s are total neutron-absorption and -scattering cross sections, respectively. Blue dots: 300 K; blue dot-dash: 400 K; blue dashes: 500 K; solid blue: 600 K; red dashes: 700 K; and red dot-dash: 800 K. The measured value for $\hat{\sigma}_{149} \approx 90$ kb, which suggests that E_r has shifted towards larger values since Oklo was an active reactor.



uranium was 3.7% compared to the present value of 0.7%. It is not possible to have a self-sustained nuclear chain reaction with a homogeneous mixture of water and uranium with isotopic composition at the 0.7% level. However, with 3.7% enrichment, it is possible to attain a neutron multiplication factor of about 1.38 with 2.4 water molecules per uranium atom. As suggested by P. Kuroda in 1956, if an ancient uranium ore deposit was sufficiently concentrated, saturated with water, and had a low concentration of neutron absorbers, an ore deposit could become a natural nuclear reactor.

The remnants of such a natural reactor were discovered in Gabon, Africa, in 1972 during routine analysis of uranium samples. (With the exception of lead and helium, the isotopic composition of the chemical elements in the Earth's crust is so constant that deviations are used to identify, for example, rocks from Mars that have ended up on Earth.) This natural reactor ran for about 100,000 years, two billion years ago, and the ore deposit and reactor products were preserved in an extremely stable geological formation. Subsequent isotopic analysis, after correcting for influx of natural isotopic-abundance chemical elements, matches the isotopic composition of spent fuel from modern nuclear reactors.

Shlyachter⁷ pointed out that it is possible to test for a variation in α (or other parameters that determine nuclear energy levels) by determining fission fragment concentrations for isotopes that have a low-energy neutron absorption resonance

due to the strong energy dependence of the low-energy neutron population.

Two analyses of samples from the Oklo deposit indicated no variation of the resonance energy and yielded an upper limit for the fractional variation of α at the $10^{-17}/\text{yr}$ level.^{8,9} However, in addition to the total neutron flux and the location of the resonance, the specific spectrum of the neutron flux is important. The previous analyses assumed a Maxwell-Boltzmann spectrum, known to be incorrect in the presence of absorbers (which include uranium and water, which formed the basis of the reactor). We repeated the analysis with a more realistic neutron spectrum and found $\dot{\alpha}/\alpha \geq 2.3 \times 10^{-17}/\text{yr}$ with 8σ confidence.¹⁰ A result of our analysis is shown in Figure 1. This result is about ten times smaller than the astrophysical result² and of opposite sign; both the magnitude and sign of the variation can be accommodated in modern theories of the universe.¹¹ Our result was covered as a feature article in *New Scientist*.¹²

Comparison of Optical Frequency References

Although laboratory measurements do not have the advantage of integrating over 10^9 – 10^{10} years, they provide significant conveniences—they can be made in a carefully prepared environment and are reproducible. Furthermore, the resolution on parameters of interest can be increased by a large factor which can allow a measurement with higher precision but on a laboratory time scale. Laboratory

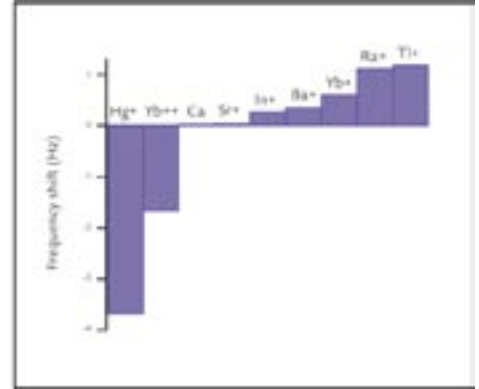


Figure 2. Frequency shift of proposed optical references for a fractional shift $\Delta\alpha/\alpha = 10^{-15}$.

measurements are also sensitive to short-time variations and to possible spatial and gravitational dependencies.

Because α determines the strength of electromagnetic interactions, the energies of atomic states depend upon α . Moreover, different states have different dependencies on α primarily due to relativistic corrections to the energies. That these corrections can be calculated accurately is the basis for nearly all ideas regarding laboratory measurements of α variation.

Twenty-five years ago, Hans Dehmelt recognized that group-III A ions, in particular, indium and thallium (In^+ and Tl^+), would be excellent choices on which to base atomic clocks of unprecedented stability. By the same fundamental considerations, we recently identified a ytterbium ion (Yb^{2+}) as another promising candidate. These atomic ions possess metastable energy states that decay back to the ground state. This transition is insensitive to fluctuating ambient fields and the transition frequency is $\sim 10^{15}$ Hz (in the optical regime), which improves the short-term stability of a reference based upon it. In addition, atomic ions can be trapped and cooled until they are nearly motionless unlike clouds of neutral atoms that suffer from systematic collisional effects and are not trapped. These ions were chosen as candidates for this effort because these “clock” transitions are some of the most α sensitive (Figure 2). We are

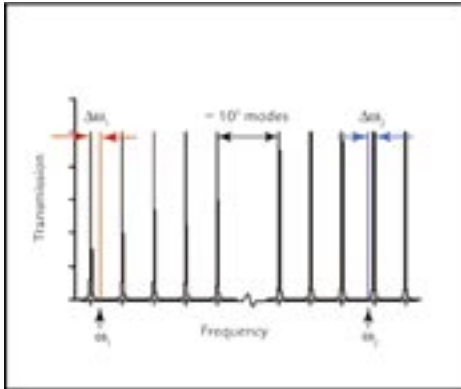


Figure 3. Mode population for the OCR or OFC as a function of frequency. Light from optical references is shown in red (ω_1) and blue (ω_2).

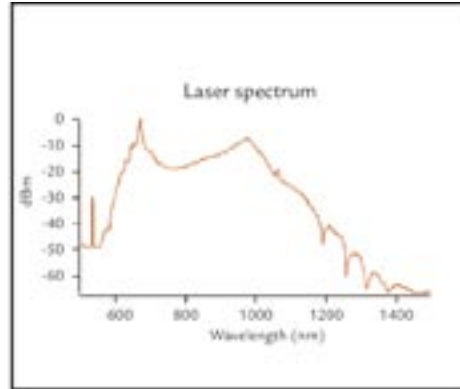


Figure 4. Light output from the “GHz” optical comb generator. The spectrum consists of extremely well defined spectral components separated by 500 MHz (not resolved on this plot).

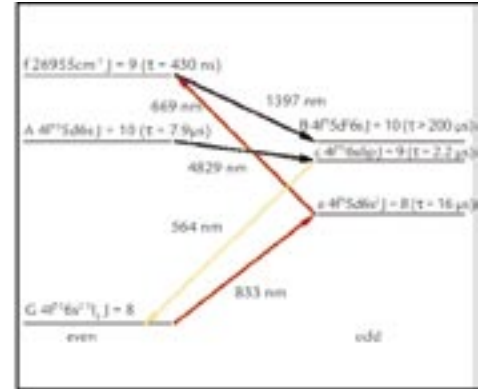


Figure 5. Partial Grotrian diagram for dysprosium. The levels of interest for a search for variation in α are labeled A and B.

currently constructing an ion-trapping/-imaging apparatus for spectroscopy of both indium(+) and ytterbium(2+) as the first step towards our goal of comparing all three. A measurement with these three ions has the potential to achieve a sensitivity of $\delta(\dot{\alpha}/\alpha) \approx 10^{-18}/\text{yr}$ with a measurement time of one year. This is over 1000 times more sensitive than current laboratory measurements.

We are constructing narrow-band laser sources to probe the metastable transitions, thereby creating accurate ion-stabilized optical frequency references. Other transitions from the ground state are strong enough to be used to optically cool the ions and serve as “readout” transitions to determine the electronic states of the ions.

One of the main obstacles in performing an experiment to compare frequency references in which at least one of the references is optical is that the appropriate high-speed electronics do not exist to directly measure the 10^{14} – 10^{15} Hz frequency. However, our experiment does not require accurate knowledge of the frequencies of the references, or even the difference frequency. It is sufficient to measure changes in the difference of frequencies of relatively stable atomic references to measure changes in α . It is this fact that makes this experiment feasible with existing experimental methods.

We will use two existing technologies—the optical comparison resonator (OCR) and the femtosecond optical frequency comb (OFC)—to make redundant measurements to verify our results. The underlying concept is illustrated in Figure 3 and is similar for both the OCR and OFC although its implementation differs. For the OCR, the ion-stabilized frequency references are shifted into resonance with passive optical resonator modes, and the frequency shift is measured. For the OFC, the stable references beat with populated modes emitted from the OFC laser source and the beat frequency is measured.

The OFC relies on a broadband, mode-locked laser. When operated in the mode-locked regime, the output of the laser consists of well-defined pulses whose repetition frequency is the free spectral range (FSR) of the laser resonator. The spectral components of the output are then separated by the FSR and span the fraction of the gain bandwidth of the laser over which dispersion is compensated. With our collaborators at the National Institute of Standards and Technology

(NIST), we have constructed a titanium-doped sapphire laser with an FSR of 500 MHz and a spectrum covering more than an octave centered at about 800 nm (Figure 4). This spectral region easily includes wavelengths of interest for indium(+), thallium(+), and ytterbium(2+) optical frequency references and is sufficient to allow accurate stabilization without additional noisy measurements. We are currently working to stabilize the spectrum of this laser and understand its subtleties.

Atomic Dysprosium

We are also conducting an experiment at the University of California (UC), Berkeley, which takes advantage of a

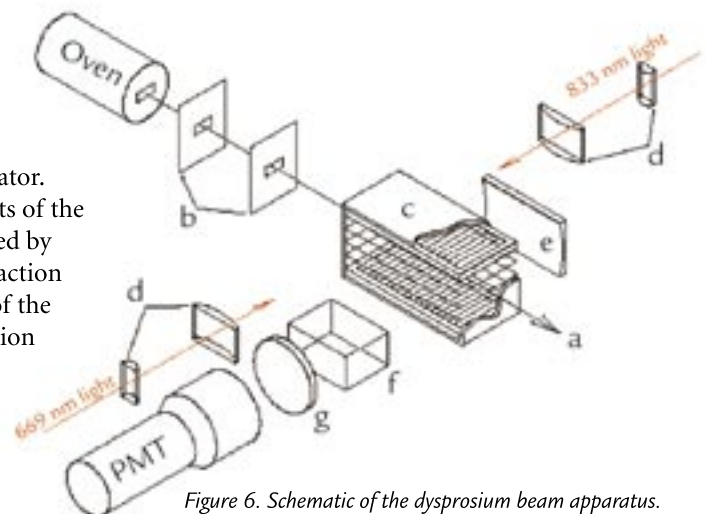


Figure 6. Schematic of the dysprosium beam apparatus.

fortunate near degeneracy of two energy levels in atomic dysprosium.¹³ As shown in Figure 5, two states of opposite parity are separated by as little as 300 MHz for a particular isotope (and by as much as 1 GHz for other isotopes). Careful mathematical modeling of these levels has been conducted due to interest in these states for measurements of parity nonconservation, and the states have been determined to be nearly as sensitive to variations of α as ytterbium(2+). Although optical transitions offer advantages for frequency references, a measurement of α variation does not require the use of two separated references.

The advantage of this system over others is that the frequency measurements have been reduced from optical frequencies to radio frequencies, which can be monitored with well-developed techniques. A determination of a fractional shift of $\dot{\alpha}/\alpha \approx 10^{-18}$ requires an uncertainty $\delta\nu \approx 1$ mHz. This is a fractional uncertainty of only $\delta\nu/\nu \approx 10^{-12}$, which can be achieved with a commercially available radio-frequency reference, such as that derived from a cesium beam standard.

A schematic of the apparatus currently in use at UC-Berkeley is shown in Figure 6. The apparatus is essentially a simple radio-frequency atomic “clock” based upon a dysprosium beam and possessing a single interaction region. The transition between states A and B can be addressed with an applied electric field at the appropriate frequency. Spectroscopy on this transition is performed by monitoring the fluorescence of the atoms at 564 nm. We are currently studying several systematics that can affect the sensitivity of our measurements for tests of α variation.

References

1. P.A.M. Dirac, *Nature* **139**, 323 (1937).
2. M.T. Murphy *et al.*, “Possible evidence for a variable fine-structure constant from QSO absorption lines: motivations, analysis and results,” *Monthly Notices of the Royal Astronomical Society* **327**, 1208–1222 (2001); J.K. Webb *et al.*, “Further evidence for cosmological evolution of the fine-structure constant,” *Physical Review Letters* **87**, 091301-1–091301-4 (2001).
3. R. Srianand *et al.*, “Limits on the time variation of the electromagnetic fine structure constant in the low energy limit from absorption lines in the spectra of distant quasars,” *Physical Review Letters* **92**, 121302-1–121302-4 (2004).
4. S. Bize *et al.*, “Testing the stability of fundamental constants with the $^{199}\text{Hg}^+$ single-ion optical clock,” *Physical Review Letters* **90**, 150802-1–150802-4 (2003).
5. H. Marion *et al.*, “Search for variations of fundamental constants using atomic fountain clocks,” *Physical Review Letters* **90**, 150801-1–150801-4 (2003).
6. E. Peik *et al.*, “New limit on the present temporal variation of the fine structure constant,” *Physical Review Letters* **93**, 170801-1–170801-4 (2004).
7. A.I. Schlyakter, *Nature* **264**, 340 (1976).
8. Y. Fujii *et al.*, “The nuclear interaction at Oklo 2 billion years ago,” *Nuclear Physics B* **573**, 377–401 (2000).
9. T. Damour and F. Dyson, “The Oklo bound on the time variation of the fine-structure constant revisited,” *Nuclear Physics B* **480**, 37–54 (1996).
10. S.K. Lamoreaux and J.R. Torgerson, “Neutron moderation in the Oklo natural reactor and the time variation of alpha,” *Physical Review D* **69**, 121701-1–121701-5 (2004).
11. D.F. Mota and J.D. Barrow, “Local and global variations of the fine-structure constant,” *Monthly Notices of the Royal Astronomical Society* **349**, 291–302 (2004).
12. E.S. Reich, “Speed of light may have changed recently,” *New Scientist*, 3 July 2004 (No. 2454), pp. 6–7.
13. A.T. Nguyen *et al.*, “Towards a sensitive search for variation of the fine-structure constant using radio-frequency E1 transitions in atomic dysprosium,” *Physical Review A* **69**, 022105-1–022105-8 (2004).
14. F.J. Dyson, “The fundamental constants and their time variation” in *Aspects of Quantum Theory*, A. Salam and E.P. Wigner, Eds. (Cambridge University Press, Cambridge, 1972), pp. 213–236.
15. J.D. Prestage, R.L. Tjoelker, and L. Maleki, “Atomic clocks and variations of the fine structure constant,” *Physical Review Letters* **74**, 3511–3514 (1995).

Acknowledgment

We would like to thank our LANL management for their ongoing support of our efforts. This work is currently funded through the LANL Laboratory Directed Research and Development program, the UC/LANL Campus-Laboratory Collaborations Program and by a NIST Precision Measurements Grant.

For further information, contact Justin Torgerson, 505-665-3365, torgerson@lanl.gov.

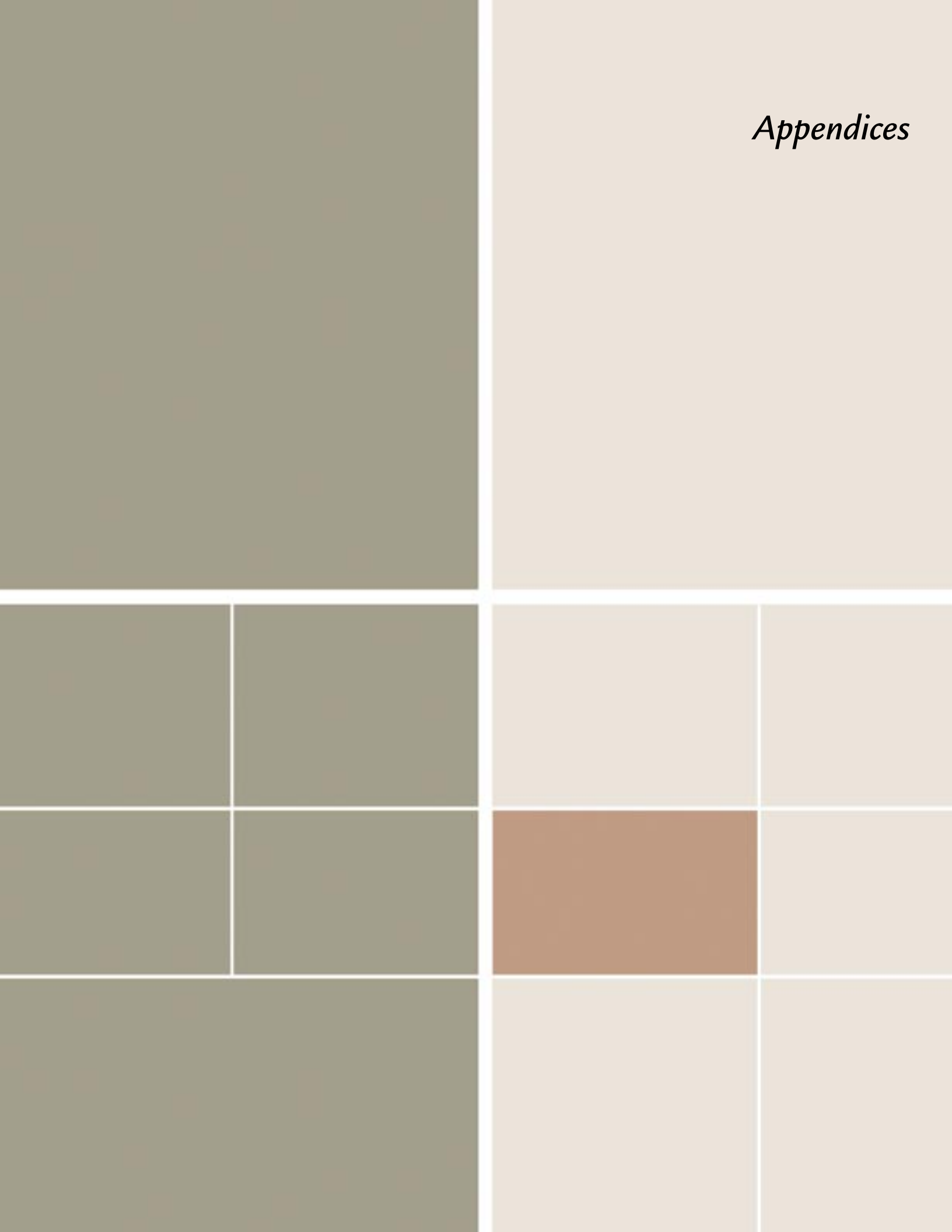


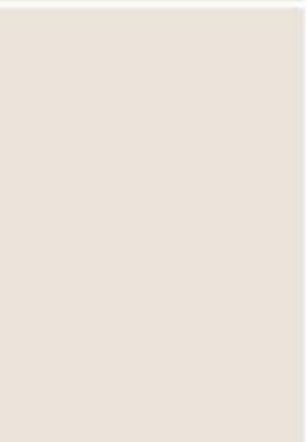
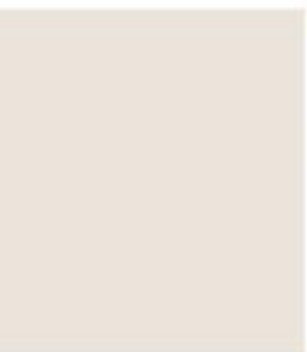
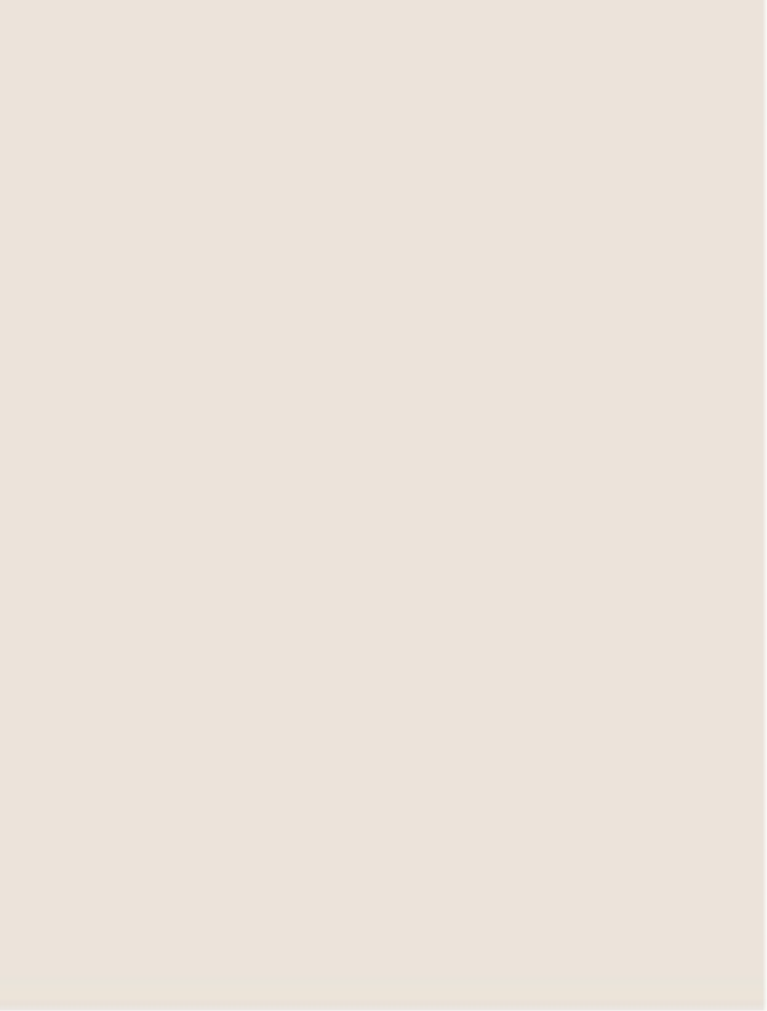
The World's Greatest Science Protecting America

Los Alamos National Laboratory, an affirmative action/equal opportunity employer, is operated by the University of California for the U.S. Department of Energy under contract W-7405-ENG-36.



Appendices





Appendix A: Acronyms

A

ac	alternating current
AD	Associate Director
AGS	Alternating Gradient Synchrotron
AHF	Advanced Hydrotest Facility
ASRT	advanced, single-rotor turbine

B

BATSE	Burst and Transient Source Experiment
BILBO	backside ion LaGrangian blow-off
BN	Bechtel Nevada
BNL	Brookhaven National Laboratory
BooNE	Booster Neutrino Experiment

C

CCD	charge-coupled device
CERN	European Organization for Nuclear Research (in French)
CGC	color glass condensate
CLEAN	Cryogenic Low-Energy Astrophysics with Neon
COMPTEL	Imaging Compton Telescope
CORRTEX	continuous reflectometry for radius versus time experiments
cw	continuous wave

D

DARHT	Dual-Axis Radiographic Hydrodynamic Test (facility)
DBD	dielectric barrier discharge
dc	direct current
DD	deuterium-deuterium
DIS	deep inelastic scattering (lepton-nucleus)
DOE	U.S. Department of Energy
DT	deuterium-tritium

E

EAS	extensive air shower
EDM	electric dipole moment
EEG	electroencephalography
EGRET	Energetic Gamma-Ray Experiment Telescope
EOS	equation of state
ESA	Engineering Sciences and Applications (Division)

F

FFT	fast Fourier transform
FID	free induction decay
FMP	flowing magnetized plasma
FNAL	Fermi National Accelerator Laboratory
FP	flight path
FSR	free spectral range
FWHM	full-width at half maximum

G

H

HE	high explosive
HiRes	High Resolution Fly's Eye (experiment)

I

ICF	inertial-confinement fusion
IEC	inertial-electrostatic-confinement (fusion)
IST	Information Society Technologies
IVA	inductive-voltage adder

J

K

L

LAMPF	Los Alamos Meson Physics Facility
LANL	Los Alamos National Laboratory
LANSCCE	Los Alamos Neutron Science Center
LDRD	Laboratory-Directed Research and Development
LDRD-DR	Laboratory-Directed Research and Development-Directed Research
LDRD-DR	Laboratory-Directed Research and Development-Director's Reserve
LEH	laser entrance hole
LLNL	Lawrence Livermore National Laboratory
LSND	Liquid Scintillator Neutrino Detector
LSO	lutetium oxyorthosilicate

Appendix A: Acronyms

M

MCG	magnetocardiography
MCNP	Monte Carlo neutron and photon
MEA	microelectrode array
MEG	magnetoencephalography
ML	magnetically limited
MMG	magnetomyography
MR	magnetic resonance
MRC	Mission Research Corporation
MRI	magnetic resonance imaging
MRI	magnetorotational instability
MSA	management self-assessment
MST	Materials Science and Technology (Division)
MTS	mechanical threshold stress
MuID	muon identification

N

nEDM	neutron electric dipole moment
NIF	National Ignition Facility
NMR	nuclear magnetic resonance
NMT	Nuclear Materials Technology (Division)
NRL	Naval Research Laboratory
NRS	neutron resonance spectroscopy
NTP	nonthermal plasma
NTS	Nevada Test Site
NUEX	neutron experiments

O

OCR	optical comparison resonator
OFC	optical frequency comb
OSSE	Oriented Scintillator Spectrometer Experiment

P

P	Physics (Division)
PCF	photonic crystal fibers
PDE	partial differential equations
PDF	parton density function
PDF	probability density function
P-DO	Physics Division Office
PDRC	Physics Division Review Committee
PFL	pulse-forming lines
PHENIX	Pioneering High-Energy Nuclear Interaction Experiment
PINEX	pinhole neutron experiments
PMT	photomultiplier tube

POPS

POPS	periodically oscillating plasma sphere
PPH	pulsed-power hydrodynamics
pRad	proton radiography
PSD	Pulse Sciences Division (Titan)
PTW	Preston, Tonks, and Wallace

Q

QCD	quantum chromodynamics
QGP	quark-gluon plasma
QKD	quantum key distribution

R

R&D	research and development
rf	radio frequency
RFSF	radio-frequency spin flipper
RGa	residual-gas analyzer
RHIC	Relativistic Heavy-Ion Collider
RT	Rayleigh-Taylor

S

SC	stochastic closure
SCE	subcritical experiment
SCL	space-charge limited
SF6	Schott glass
SG	Steinberg-Guinan
SNL	Sandia National Laboratories
SNO	Sudbury Neutrino Observatory
SPS	super proton synchrotron
SQUID	superconducting quantum interference device
STAR	Solenoidal Tracker at RHIC

T

THREX	threshold experiments
tMTF	temporal modulation transfer function
TPC	total project cost

U

UC	University of California
UCN	ultracold neutrons
UHECR	ultra-high-energy cosmic rays
ULF	ultra-low-field (NMR)

V

VISAR	velocity interferometer system for any reflector
-------	--

VLF	very low field
VNIIEF	All-Russian Scientific Research Institute of Experimental Physics

W	
WACT	Wide-Angle Cerenkov Telescope
WIMP	weakly interacting massive particle

X, Y, Z	
X	Applied Physics (Division)
XRFC	x-ray framing camera
Z	impedance

Appendix B: Publications

2004 Journal Articles

C.E. Aalseth *et al.* (Majorana Collaboration) [including Los Alamos authors: T. Ball, S.R. Elliott, A. Hime, G.B. Mills, R.G. van de Water, J.M. Wouters, and V.I. Yumatov], “The Majorana neutrinoless double-beta decay experiment,” *Physics of Atomic Nuclei* **67**, 2002–2010 (2004).

R.U. Abbasi *et al.* (High Resolution Fly’s Eye Collaboration) [including Los Alamos authors: J.F. Amann, C.M. Hoffman, M.H. Holzschneider, L.J. Marek, C.A. Painter, G. Sinnis, and D. Tupa], “Study of small-scale anisotropy of ultra-high-energy cosmic rays observed in stereo by the High Resolution Fly’s Eye detector,” *Astrophysical Journal Letters* **610**, L73–L76 (2004).

R.U. Abbasi *et al.* (High Resolution Fly’s Eye Collaboration) [including Los Alamos authors: J.F. Amann, C.M. Hoffman, M.H. Holzschneider, L.J. Marek, C.A. Painter, G. Sinnis, and D. Tupa], “Measurement of the flux of ultrahigh energy cosmic rays from monocular observations by the High Resolution Fly’s Eye Experiment,” *Physical Review Letters* **92**, 151101-1–151101-4 (2004).

R.U. Abbasi *et al.* (High Resolution Fly’s Eye Collaboration) [including Los Alamos authors: J.F. Amann, C.M. Hoffman, M.H. Holzschneider, L.J. Marek, C.A. Painter, G. Sinnis, and D. Tupa], “Search for global dipole enhancements in the HiRes I monocular data above $10^{18.5}$ eV,” *Astroparticle Physics* **21**, 111–123 (2004).

R.U. Abbasi *et al.* (High Resolution Fly’s Eye Collaboration) [including Los Alamos authors: J.F. Amann, C.M. Hoffman, M.H. Holzschneider, L.J. Marek, C.A. Painter, G. Sinnis, and D. Tupa], “A search for arrival direction clustering in the HiRes I monocular data above $10^{19.5}$ eV,” *Astroparticle Physics* **22**, 139–149 (2004).

D. Acosta *et al.* (CDF Collaboration) [including Los Alamos author: G.P. Grim], “Measurement of the average time-integrated mixing probability of I-flavored hadrons produced at the Fermilab Tevatron,” *Physical Review D* **69**, 012002-1–012002-16 (2004).

D. Acosta *et al.* (CDF Collaboration) [including Los Alamos author: G.P. Grim], “Search for pair production of scalar top quarks in R -parity violating decay modes in $p\bar{p}$ collisions at square $\sqrt{s} = 1.8$ TeV,” *Physical Review Letters* **92**, 051803-1–051803-7 (2004).

D. Acosta *et al.* (CDF Collaboration) [including Los Alamos author: G.P. Grim], “Search for Kaluza-Klein graviton emission in $p\bar{p}$ collisions at square $\sqrt{s} = 1.8$ TeV using the missing energy signature,” *Physical Review Letters* **92**, 121802-1–121802-7 (2004).

P.D. Adams, K. Gopal, R.W. Grosse-Kunstleve, L.W. Hung, T.R. Ioerger, A.J. McCoy, N.W. Moriarty, R.K. Pai, R.J. Read, T.D. Romo, J.C. Sacchetti, N.K. Sauter, L.C. Stononi, and T.C. Terwilliger, “Recent developments in the PHENIX software

for automated crystallographic structure determination,” *Journal of Synchrotron Radiation* **11**, 53–55 (2004).

K. Adcox *et al.* (PHENIX Collaboration) [including Los Alamos authors: P.D. Barnes, M.J. Bennett, M.L. Brooks, T.A. Carey, M.S. Chung, A.G. Hansen, W.W. Kinnison, D.M. Lee, M.J. Leitch, M.X. Liu, P.L. McGaughey, R.E. Mischke, J.M. Moss, A.P.T. Palounek, B.R. Schlei, T. Shiina, J. Simon-Gillo, J.P. Sullivan, R.S. Towell, and H.W. van Hecke], “Single identified hadron spectra from $\sqrt{s_{NN}} = 130$ GeV Au + Au collisions,” *Physical Review C* **69**, 024904-1–024904-28 (2004).

S.S. Adler *et al.* (PHENIX Collaboration) [including Los Alamos authors: P.D. Barnes, J.G. Boissvain, M.L. Brooks, A.G. Hansen, C.H. Kuberg, D.M. Lee, M.J. Leitch, M.X. Liu, P.L. McGaughey, R.E. Mischke, J.M. Moss, A.P.T. Palounek, J.-C. Peng, M.R. Shaw, T. Shiina, D. Silvermyr, W.E. Sondheim, J.P. Sullivan, J.D. Tepe, and H.W. van Hecke], “Bose-Einstein correlations of charged pion pairs in Au + Au collisions at $\sqrt{s_{NN}} = 200$ GeV,” *Physical Review Letters* **93**, 152302-1–152302-6 (2004).

S.S. Adler *et al.* (PHENIX Collaboration) [including Los Alamos authors: P.D. Barnes, J.G. Boissvain, M.L. Brooks, A.G. Hansen, C.H. Kuberg, D.M. Lee, M.J. Leitch, M.X. Liu, P.L. McGaughey, R.E. Mischke, J.M. Moss, A.P.T. Palounek, J.-C. Peng, M.R. Shaw, T. Shiina, D. Silvermyr, W.E. Sondheim, J.P. Sullivan, J.D. Tepe, and H.W. van Hecke], “Measurement of nonrandom event-by-event fluctuations of average transverse momentum in $\sqrt{s_{NN}} = 200$ GeV Au + Au and $p + p$ collisions,” *Physical Review Letters* **93**, 092301-1–092301-6 (2004).

S.S. Adler *et al.* (PHENIX Collaboration) [including Los Alamos authors: P.D. Barnes, J.G. Boissvain, M.L. Brooks, A.G. Hansen, C.H. Kuberg, D.M. Lee, M.J. Leitch, M.X. Liu, P.L. McGaughey, R.E. Mischke, J.M. Moss, A.P.T. Palounek, J.-C. Peng, M.R. Shaw, T. Shiina, D. Silvermyr, W.E. Sondheim, J.P. Sullivan, J.D. Tepe, and H.W. van Hecke], “ J/ψ production from proton-proton collisions at $\sqrt{s} = 200$ GeV,” *Physical Review Letters* **92**, 051802-1–051802-6 (2004).

S.S. Adler *et al.* (PHENIX Collaboration) [including Los Alamos authors: P.D. Barnes, J.G. Boissvain, M.L. Brooks, A.G. Hansen, C.H. Kuberg, D.M. Lee, M.J. Leitch, M.X. Liu, P.L. McGaughey, R.E. Mischke, J.M. Moss, A.P.T. Palounek, J.-C. Peng, M.R. Shaw, T. Shiina, D. Silvermyr, W.E. Sondheim, J.P. Sullivan, J.D. Tepe, and H.W. van Hecke], “Double helicity asymmetry in inclusive midrapidity π^0 production for polarized $p + p$ collisions at $\sqrt{s} = 200$ GeV,” *Physical Review Letters* **93**, 202002-1–202002-6 (2004).

S.S. Adler *et al.* (PHENIX Collaboration) [including Los Alamos authors: P.D. Barnes, J.G. Boissvain, M.L. Brooks, A.G. Hansen, C.H. Kuberg, D.M. Lee, M.J. Leitch, M.X. Liu, P.L. McGaughey, R.E. Mischke, J.M. Moss, A.P.T. Palounek, J.-C. Peng, M.R. Shaw, T. Shiina, D. Silvermyr, W.E. Sondheim, J.P. Sullivan, J.D. Tepe, and H.W. van Hecke], “High- p_T charged hadron suppression in Au + Au collisions at $\sqrt{s_{NN}} = 200$ GeV,” *Physical Review C* **69**, 034910-1–034910-20 (2004).

S.S. Adler *et al.* (PHENIX Collaboration) [including Los Alamos
PHYSICS DIVISION

authors: P.D. Barnes, J.G. Boissevain, M.L. Brooks, A.G. Hansen, C.H. Kuberg, D.M. Lee, M.J. Leitch, M.X. Liu, P.L. McGaughey, R.E. Mischke, J.M. Moss, A.P.T. Palounek, J.-C. Peng, M.R. Shaw, T. Shiina, D. Silvermyr, W.E. Sondheim, J.P. Sullivan, J.D. Tepe, and H.W. van Hecke], “Identified charged particle spectra and yields in Au + Au collisions at $\sqrt{s_{NN}} = 200$ GeV,” *Physical Review C* **69**, 034909-1–034909-32 (2004).

S.S. Adler *et al.* (PHENIX Collaboration) [including Los Alamos authors: P.D. Barnes, J.G. Boissevain, M.L. Brooks, A.G. Hansen, C.H. Kuberg, D.M. Lee, M.J. Leitch, M.X. Liu, P.L. McGaughey, R.E. Mischke, J.M. Moss, A.P.T. Palounek, J.-C. Peng, M.R. Shaw, T. Shiina, D. Silvermyr, W.E. Sondheim, J.P. Sullivan, J.D. Tepe, and H.W. van Hecke], “ J/ψ production in Au-Au collisions at $\sqrt{s_{NN}} = 200$ GeV,” *Physical Review C* **69**, 014901-1–014901-10 (2004).

B. Aharmim *et al.* (SNO Collaboration) [including Los Alamos authors: M.G. Boulay, T.J. Bowles, S.J. Brice, M.R. Dragowsky, S.R. Elliott, M.M. Fowler, K. Frame, Gagnon, A.S. Hamer, J. Heise, A. Hime, M.S. Kos, G.G. Miller, R.G. Van de Water, J.B. Wilhelmy, and J.M. Wouters], “Electron antineutrino search at the Sudbury Neutrino Observatory,” *Physical Review D* **70**, 093014-1–093014-8 (2004).

S.N. Ahmed *et al.* (SNO Collaboration) [including Los Alamos authors: M.G. Boulay, T.J. Bowles, S.J. Brice, M.R. Dragowsky, S.R. Elliott, M.M. Fowler, N. Gagnon, A.S. Hamer, J. Heise, A. Hime, G.G. Miller, R.G. Van de Water, J.B. Wilhelmy, and J.M. Wouters], “Measurement of the total active ^8B solar neutrino flux at the Sudbury Neutrino Observatory with enhanced neutral current sensitivity,” *Physical Review Letters* **92**, 181301-1–181301-6 (2004).

S.N. Ahmed *et al.* (SNO Collaboration) [including Los Alamos authors: M.G. Boulay, T.J. Bowles, S.J. Brice, M.R. Dragowsky, S.R. Elliott, M.M. Fowler, N. Gagnon, A.S. Hamer, J. Heise, A. Hime, G.G. Miller, R.G. Van de Water, J.B. Wilhelmy, and J.M. Wouters], “Constraints on nucleon decay via invisible modes from the Sudbury Neutrino Observatory,” *Physical Review Letters* **92**, 102004-1–102004-4 (2004).

J.A. Akins, S.N. Luo, P.D. Asimow, and T.J. Ahrens, “Shock-induced melting of MgSiO_3 perovskite and implications for melts at Earth’s lowermost mantle,” *Geophysical Research Letters* **31**, L14612-1–L14612-4 (2004).

P. Ambrozewicz, J. Mitchell, J. Dunne, P. Markowitz, C.J. Martoff, J. Reinhold, B. Zeidman, D.J. Abbott, A. Ahmidouch, C.S. Armstrong, J. Arrington, K.A. Assamagan, K. Bailey, O.K. Baker, S. Beedoe, H. Breuer, R. Carlini, J. Cha, G. Collins, C. Cothran, W.J. Cummings, S. Danagoulouian, D. Day, F. Duncan, D. Dutta, T. Eden, R. Ent, L. Ewell, H.T. Fortune, H. Gao, D.F. Geesaman, P. Gueye, K.K. Gustafsson, J.O. Hansen, W. Hinton, C.E. Keppel, A. Klein, D. Koltenuk, D.J. Mack, R. Madey, D.G. Meekins, H. Mkrtchyan, R.M. Mohring, S.K. Mtingwa, G. Niculescu, I. Niculescu, T.G. O’Neill, D. Potterveld, J.W. Price, B.A. Raue, P. Roos, G. Savage, R. Sawafta, R.E. Segel, S. Stepanyan, V. Tadevosyan, L. Tang, B.P. Terburg, S. Wood, C. Yan, and B. Zihlmann, “Near threshold electroproduction of the ω meson at $Q^2 \approx 0.5$ GeV 2 ,” *Physical*

Review C **70**, 035203-1–035203-9 (2004).

Y. Ashie *et al.* (The Super-Kamiokande Collaboration) [including Los Alamos author: T.J. Haines], “Evidence for an oscillatory signature in atmospheric neutrino oscillations,” *Physical Review Letters* **93**, 101801-1–101801-6 (2004).

R. Atkins, W. Benbow, D. Berley, E. Blaufuss, J. Bussons, D.G. Coyne, T. DeYoung, B.L. Dingus, D.E. Dorfan, R.W. Ellsworth, L. Fleyscher, R. Fleyscher, G. Gisler, M.M. Gonzalez, J.A. Goodman, T.J. Haines, E. Hays, C.M. Hoffman, L.A. Kelley, C.P. Lansdell, J.T. Linnemann, J.E. McEnery, R.S. Miller, A.I. Mincer, M.F. Morales, P. Nemethy, D. Noyes, J.M. Ryan, F.W. Samuelson, A. Shoup, G. Sinnis, A.J. Smith, G.W. Sullivan, D.A. Williams, S. Westerhoff, M.E. Wilson, X.W. Xu, and G.B. Yodh, “Search for very high energy gamma rays from WIMP annihilations near the Sun with the Milagro detector,” *Physical Review D* **70**, 083516-1–083516-8 (2004).

R. Atkins, W. Benbow, D. Berley, E. Blaufuss, J. Bussons, D.G. Coyne, T. DeYoung, B.L. Dingus, D.E. Dorfan, R.W. Ellsworth, L. Fleyscher, R. Fleyscher, G. Gisler, M.M. Gonzalez, J.A. Goodman, T.J. Haines, E. Hays, C.M. Hoffman, L.A. Kelley, J.E. McEnery, R.S. Miller, A.I. Mincer, M.F. Morales, P. Nemethy, D. Noyes, J.M. Ryan, F.W. Samuelson, A. Shoup, G. Sinnis, A.J. Smith, G.W. Sullivan, D.A. Williams, S. Westerhoff, M.E. Wilson, X. Xu, and G.B. Yodh, “Limits on very high energy emission from gamma-ray bursts with the Milagro observatory,” *Astrophysical Journal* **604**, L25–L28 (2004).

R. Atkins, W. Benbow, D. Berley, E. Blaufuss, J. Bussons, D.G. Coyne, T. DeYoung, B.L. Dingus, D.E. Dorfan, R.W. Ellsworth, L. Fleyscher, R. Fleyscher, G. Gisler, M.M. Gonzalez, J.A. Goodman, T.J. Haines, E. Hays, C.M. Hoffman, L.A. Kelley, C.P. Lansdell, J.T. Linnemann, J.E. McEnery, R.S. Miller, A.I. Mincer, M.F. Morales, P. Nemethy, D. Noyes, J.M. Ryan, F.W. Samuelson, A. Shoup, G. Sinnis, A.J. Smith, G.W. Sullivan, D.A. Williams, S. Westerhoff, M.E. Wilson, X.W. Xu, and G.B. Yodh, “TeV gamma-ray survey of the northern hemisphere sky using the Milagro observatory,” *Astrophysical Journal* **608**, 680–685 (2004).

L.B. Auerbach, R.L. Burman, D.O. Caldwell, E.D. Church, A.K. Cochran, J.B. Donahue, A.R. Fazely, G.T. Garvey, R.M. Gunasingha, R.L. Imlay, G. Kahrmanis, W.C. Louis, R. Majkic, A. Malik, K.L. McIlhany, W.J. Metcalf, G.B. Mills, D. Rupnik, V.D. Sandberg, D. Smith, R.F. Somodi, I. Stancu, W.D. Strossman, M. Sung, R. Tayloe, G.J. VanDalen, W. Vernon, N. Wadia, D.H. White, S. Yellin, and H. Yi (LSND Collaboration), “Search for $\pi^0 \rightarrow \nu \bar{\nu}$ decays in the LSND detector,” *Physical Review Letters* **92**, 091801-1–091801-4 (2004).

H. Avakian *et al.* [Continuous Electron Beam Accelerator Facility (CEBAF) Large Acceptance Spectrometer (CLAS) Collaboration] [including Los Alamos author: A. Klein], “Measurement of beam-spin asymmetries for π^+ electroproduction above the baryon resonance region,” *Physical Review D* **69**, 112004-1–112004-7 (2004).

Appendix B: Publications

- M.S. Bakeman, S.C. Evans, J.A. Oertel, P.J. Walsh, and C.W. Barnes, "Characterization of x-ray framing cameras for use in inertial confinement fusion and radiation hydrodynamics experiments," *Proceedings of SPIE* **5194**, 205–213 (2004).
- M.M. Balkey, R.D. Day, S.H. Batha, N.E. Elliot, T. Pierce, and D.L. Sandoval, "Production and metrology of cylindrical inertial confinement fusion targets with sinusoidal perturbations," *Fusion Science and Technology* **45**, 107–112 (2004).
- S.H. Batha and J.R. Fincke, "Quantified reduction of wall material influx during hohlraum experiments," *Review of Scientific Instruments* **75**, 3934–3936 (2004).
- A.B. Belonoshko, S.I. Simak, A.E. Kochetov, B. Johansson, L. Burakovsky, and D.L. Preston, "High-pressure melting of molybdenum," *Physical Review Letters* **92**, 195701-1–195701-4 (2004).
- D.J. Berkeland, D.A. Raymondson, and V.M. Tassin, "Tests for nonrandomness in quantum jumps," *Physical Review A* **69**, 052103-1–052103-4 (2004).
- K. Boboridis, A. Seifter, A.W. Obst, and D. Basak, "Radiance temperatures and normal spectral emittance (in the wavelength range of 1500–5000 nm) of tin, zinc, aluminum, and silver at their melting points by a pulse-heating technique," *International Journal of Thermophysics* **25**, 1187–1202 (2004).
- D.S. Bracken, K. Kwiatkowski, E.R. Foxford, K.B. Morley, V.E. Viola, N.R. Yoder, J. Brzychczyk, E.C. Pollacco, R. Legrain, C. Volant, R.G. Korteling, and H. Breuer, "Moving-source and caloric-curve analyses of reactions induced by 1.8–4.8 GeV ^3He beams on $^{\text{nat}}\text{Ag}$ and ^{197}Au nuclei," *Physical Review C* **69**, 034612-1–034612-11 (2004).
- M. Brooks, "J/ψ and open charm production," *Journal of Physics G – Nuclear and Particle Physics* **30**, S861–S870 (2004).
- A.C. Bruno and M.A. Espy, "Design of a SQUID array as a discrete spatial filter," *Superconductor Science and Technology* **17**, 908–915 (2004).
- L. Burakovsky and D.L. Preston, "Analytic model of the Grüneisen parameter at all densities," *Journal of the Physics and Chemistry of Solids* **65**, 1581–1587 (2004).
- L. Burakovsky, D.L. Preston, and Y. Wang, "Cold shear modulus and Grüneisen parameter at all densities," *Solid State Communications* **132**, 151–156 (2004).
- C. Carey, I. Furno, and H. Weisen, "The application of the singular value decomposition method for the inversion of interferometer measurements in TCV plasmas," *Review of Scientific Instruments* **75**, 3411–3413 (2004).
- K.M. Carter, J.S. George, and D.M. Rector, "Simultaneous birefringence and scattered light measurements reveal anatomical features in isolated crustacean nerve," *Journal of Neuroscience Methods* **135**, 9–16 (2004).
- A. Castro, D.A.R. Dalvit, and L. Paz-Matos, "Ultrasensitive detection of DNA sequences in solution by specific enzymatic labeling," *Analytical Chemistry* **76**, 4169–4174 (2004).
- C.R. Christensen, D.C. Wilson, C.W. Barnes, G.P. Grim, G.L. Morgan, M.D. Wilke, F.J. Marshall, V.Y. Glebov, and C. Stoeckl, "The influence of asymmetry on mix in direct-drive inertial confinement fusion experiments," *Physics of Plasmas* **11**, 2771–2777 (2004).
- F. Cooper, M.X. Liu, and G.C. Nayak, "J/ψ production in pp collisions at $\sqrt{s} = 200$ GeV at the BNL relativistic heavy ion collider," *Physical Review Letters* **93**, 171801-1–171801-4 (2004).
- G.R. Court, M.A. Houlden, S. Bultmann, D.G. Crabb, D.B. Day, Y.A. Prok, S.I. Penttila, and C.D. Keith, "High precision measurement of the polarization in solid state polarized targets using NMR," *Nuclear Instruments and Methods in Physics Research, Section A – Accelerators, Spectrometers, Detectors and Associated Equipment* **527**, 253–263 (2004).
- C.D. Dermer and B.L. Dingus, "Blazar flaring rates measured with GLAST," *New Astronomy Reviews* **48**, 537–541 (2004).
- S. Desai *et al.* (The Super-Kamiokande Collaboration) [including Los Alamos author: T.J. Haines], "Search for dark matter WIMPs using upward through-going muons in Super-Kamiokande," *Physical Review D* **70**, 083523-1–083523-11 (2004).
- A. Efimov, A.J. Taylor, F.G. Omenetto, A.V. Yulin, N.Y. Joly, F. Biancalana, D.V. Skryabin, J.C. Knight, and P.S.J. Russell, "Time-spectrally-resolved ultrafast nonlinear dynamics in small-core photonic crystal fibers: Experiment and modelling," *Optics Express* **12**, 6498–6507 (2004).
- A. Efimov, A.J. Taylor, F.G. Omenetto, and E. Vanin, "Adaptive control of femtosecond soliton self-frequency shift in fibers," *Optics Letters* **29**, 271–273 (2004).
- A. Efimov, A.J. Taylor, F.G. Omenetto, J.C. Knight, W.J. Wadsworth, and P.S. Russell, "Simple optical profiling of complex guiding structures," *Applied Optics* **43**, 29–32 (2004).
- H. Ejiri, P. Doe, S.R. Elliott, J. Engel, M. Finger, J.A. Formaggio, K. Fushimi, V. Gehman, A. Gorin, M. Greenfield, R. Hazama, K. Ichihara, Y. Ikegami, H. Ishii, T. Itahashi, P. Kavitov, V. Kekelidze, K. Kuroda, V. Kutsalo, I. Manouilov, K. Matsuoka, F. Nakamura, M. Nomachi, T. Ogama, A. Para, A. Rjazanysev, R.G.H. Robertson, Y. Shichijo, T. Shima, Y. Shimada, G. Shirkov, A. Sissakian, L.C. Stonehill, Y. Sugaya, A. Titov, V. Vaturin, O.E. Vilches, V. Voronov, J.F. Wilkerson, D.I. Will, and S. Yoshida, "Double beta decays and solar neutrinos with ^{100}Mo ," *Czechoslovak Journal of Physics* **54**, B317–B325 (2004).
- S.R. Elliott and J. Engel, "Double-beta decay," *Journal of Physics G – Nuclear and Particle Physics* **30**, R183–R215 (2004).
- R.J. Faehl, B.G. Anderson, D.A. Clark, C.A. Ekdahl, J.H. Goforth, I.R. Lindemuth, R.E. Reinovsky, P.T. Sheehy, T. Peterson, L.J. Tabaka, V.K. Chernyshev, V.N. Mokhov, V.N. Buzin, O.M. Burenkov, A.M. Buyko, V.V. Vakhrushev, S.F. Garanin,

- B.E. Grinevich, G.G. Ivanova, V.A. Demidov, V.I. Dudoladov, V.V. Zmushko, A.I. Kuzyaev, A.I. Kuchero, B.M. Lovyagin, P.N. Nizovtsev, A.A. Petrukhin, A.I. Pishurov, V.N. Sofronov, S.S. Sokolov, V.P. Solov'yev, A.I. Startsev, V.B. Yakubov, and E.V. Gubkov, "Results of a 100-megaampere liner implosion experiment," *IEEE Transactions on Plasma Science* **32**, 1972–1985 (2004).
- J.R. Fincke, J.B. Workman, G.A. Kyrala, P.J. Walsh, S.C. Evans, D. Tafoya, and D.J. Landers, "Close-in nosecone configuration and blast damage in point backlight x-ray radiography," *Review of Scientific Instruments* **75**, 3966–3968 (2004).
- J.R. Fincke, N.E. Lanier, S.H. Batha, R.M. Hueckstaedt, G.R. Magelssen, S.D. Rothman, K.W. Parker, and C.J. Horsfield, "Postponement of saturation of the Richtmyer-Meshkov instability in a convergent geometry," *Physical Review Letters* **93**, 115003-1–115003-4 (2004).
- R. Fleysher, L. Fleysher, P. Nemethy, A.I. Mincer, and T.J. Haines, "Tests of statistical significance and background estimation in gamma-ray air shower experiments," *Astrophysical Journal* **603**, 355–362 (2004).
- N. Fotiades, G.D. Johns, R.O. Nelson, M.B. Chadwick, M. Devlin, W.S. Wilburn, P.G. Young, J.A. Becker, D.E. Archer, L.A. Bernstein, P.E. Garrett, C.A. McGrath, D.P. McNabb, and W. Younes, "Measurements and calculations of $^{238}\text{U}(n, xn')$ partial γ -ray cross sections," *Physical Review C* **69**, 024601-1–024601-14 (2004).
- I. Furno and G.A. Wurden, "Near infrared spectroscopy of the divertor region in the Alcator C Mod tokamak," *Review of Scientific Instruments* **75**, 4112–4114 (2004).
- P.E. Garrett, D.E. Archer, J.A. Becker, L.A. Bernstein, K. Hauschild, E.A. Henry, D.P. McNabb, M.A. Stoyer, W. Younes, G.D. Johns, R.O. Nelson, and W.S. Wilburn, "Rotational bands and isomeric states in ^{175}Lu ," *Physical Review C* **69**, 017302-1–017302-4 (2004).
- D. Graham, P. Maas, G.B. Donaldson, and C. Carr, "Impact damage detection in carbon fibre composites using HTS SQUIDS and neural networks," *NDT&E International* **37**, 565–570 (2004).
- G.P. Grim, G.L. Morgan, M.D. Wilke, P.L. Gobby, C.R. Christensen, and D.C. Wilson, "Progress on neutron pinhole imaging for inertial confinement fusion experiments," *Review of Scientific Instruments* **75**, 3572–3574 (2004).
- M. Hausmann, D.J. Vieira, J. Wu, X. Zhao, M.G. Boulay, and A. Hime, "Beta-asymmetry studies on polarized ^{82}Rb atoms in a TOP trap," *Nuclear Physics A* **746**, 669–672 (2004).
- M.E. Hayden, G. Archibald, P.D. Barnes, W.T. Buttler, D.J. Clark, M.D. Cooper, M.A. Espy, R. Golub, G.L. Greene, S.K. Lamoreaux, C. Lei, L.J. Marek, J.C. Peng, and S.I. Penttila, "Neutron-detected tomography of impurity-seeded superfluid helium," *Physical Review Letters* **93**, 105302-1–105302-4 (2004).
- L. Heller, D. Ranken, and E. Best, "The magnetic field inside special conducting geometries due to internal current," *IEEE Transactions on Biomedical Engineering* **51**, 1310–1318 (2004).
- E. Hemsing, I. Furno, and T. Intrator, "Analysis of visible light images from a fast-gated intensified CCD camera during flux rope interaction and magnetic reconnection," *Review of Scientific Instruments* **75**, 4106–4108 (2004).
- D.J. Hoarty, C.C. Smith, E.L. Clark, J.M. Foster, S.G. Gales, G. Magelssen, J. Workman, W.M. Wood, S. Caldwell, R. Chrien, J. Sandoval, T. Sedillo, P. Walsh, B. Carpenter, S. Compton, and T. Perry, "Fluorescence spectroscopy as a diagnostic of the radiation environment in high energy density experiments (invited)," *Review of Scientific Instruments* **75**, 3655–3659 (2004).
- C.J. Horsfield, K.W. Parker, S.D. Rothman, J. Fincke, and N.E. Lanier, "Correcting for gain effects in an x-ray framing camera in a cylindrical implosion experiment," *Review of Scientific Instruments* **75**, 3947–3949 (2004).
- T.P. Intrator, J.Y. Park, J.H. Degnan, I. Furno, C. Grabowski, S.C. Hsu, E.L. Ruden, P.G. Sanchez, J.M.T. Taccetti, A. Tuszewski, W.J. Waganaar, G.A. Wurden, S.Y. Zhang, and Z.H. Wang, "A high-density field reversed configuration plasma for magnetized target fusion," *IEEE Transactions on Plasma Science* **32**, 152–160 (2004).
- T.P. Intrator, S.Y. Zhang, J.H. Degnan, I. Furno, C. Grabowski, S.C. Hsu, E.L. Ruden, P.G. Sanchez, J.M. Taccetti, M. Tuszewski, W.J. Waganaar, and G.A. Wurden, "A high density field reversed configuration (FRC) target for magnetized target fusion: First internal profile measurements of a high density FRC," *Physics of Plasmas* **11**, 2580–2585 (2004).
- T.P. Intrator, J.Y. Park, J.H. Degnan, I. Furno, C. Grabowski, S.C. Hsu, E.L. Ruden, P.G. Sanchez, J.M. Taccetti, M. Tuszewski, W.J. Waganaar, G.A. Wurden, S.Y. Zhang, and Z. Wang, "A high-density field reversed configuration plasma for magnetized target fusion," *IEEE Transactions on Plasma Science* **32**, 152–160 (2004).
- K. Jerbi, S. Baillet, J.C. Mosher, G. Nolte, L. Garnerio, and R.M. Leahy, "Localization of realistic cortical activity in MEG using current multipoles," *NeuroImage* **22**, 779–793 (2004).
- H.T. Ji, M. Brown, S.C. Hsu, H. Li, and R.P. Drake, "Mini-conference and related sessions on laboratory plasma astrophysics," *Physics of Plasmas* **11**, 2976–2983 (2004).
- M.B. Johnson, "Propagation of fast partons in the nuclear medium," *European Physical Journal A* **19**, 105–110 (2004).
- M.B. Johnson, L.S. Kisslinger, E.M. Henley, W.Y.P. Hwang, and T. Stevens, "Non-Abelian dynamics in first-order cosmological phase transitions," *Modern Physics Letters A* **19**, 1187–1194 (2004).
- K. Joo *et al.* [Continuous Electron Beam Accelerator Facility (CEBAF) Large Acceptance Spectrometer (CLAS) Collaboration] [including Los Alamos author: A. Klein], "Measurement of the polarized structure function σ_{LT} for $p(\vec{e}, e'\pi^+)n$ in the $\Delta(1232)$ resonance region," *Physical Review C* **70**, 042201-1–042201-6 (2004).

Appendix B: Publications

- K. Kazkaz, C.E. Aalseth, T.W. Hossbach, V.M. Gehman, J.D. Kephart, and H.S. Miley, "MEGA: A low-background radiation detector," *IEEE Transactions on Nuclear Science* **51**, 1029–1033 (2004).
- P.A. Keiter and G.A. Kyrila, "Static characterization of aerogel targets for high energy density physics using x-ray radiography," *Review of Scientific Instruments* **75**, 4057–4059 (2004).
- C.D. Keith, Z. Chowdhuri, D.R. Rich, W.M. Snow, J.D. Bowman, S.L. Penttila, D.A. Smith, M.B. Leuschner, V.R. Pomeroy, G.L. Jones, and E.I. Sharapov, "Neutron cross sections for ^3He at epithermal energies," *Physical Review C* **69**, 034005-1–034005-6 (2004).
- G.T. Kenyon, B.J. Travis, J. Theiler, J.S. George, G.J. Stephens, and D.W. Marshak, "Stimulus-specific oscillations in a retinal model," *IEEE Transactions on Neural Networks* **15**, 1083–1091 (2004).
- G.T. Kenyon, D. Hill, J. Theiler, J.S. George, and D.W. Marshak, "A theory of the Benham Top based on center-surround interactions in the parvocellular pathway," *Neural Networks* **17**, 773–786 (2004).
- G.T. Kenyon, J. Theiler, J.S. George, B.J. Travis, and D.W. Marshak, "Correlated firing improves stimulus discrimination in a retinal model," *Neural Computation* **16**, 2261–2291 (2004).
- Y.H. Kim, W.S. Kang, J.M. Park, S.H. Hong, Y.H. Song, and S.J. Kim, "Experimental and numerical analysis of streamers in pulsed corona and dielectric barrier discharges," *IEEE Transactions on Plasma Science* **32**, 18–24 (2004).
- R.K. Kirkwood, T. McCarville, D.H. Froula, B. Young, D. Bower, N. Sewall, C. Niemann, M. Schneider, J. Moody, G. Gregori, F. Holdener, M. Chrisp, B.J. MacGowan, S.H. Glenzer, and D.S. Montgomery, "Calibration of initial measurements from the full aperture backscatter system on the National Ignition Facility," *Review of Scientific Instruments* **75**, 4174–4176 (2004).
- A. Klein, P. Protopapas, S.G. Rohozinski, and K. Starosta, "Kerman-Klein-Donau-Fraundorf model for odd-odd nuclei: Formal theory," *Physical Review C* **69**, 034338-1–034338-18 (2004).
- G.A. Kyrila, M.M. Balkey, C.W. Barnes, S.H. Batha, C.R. Christensen, J.A. Cobble, J. Fincke, P. Keiter, N. Lanier, D. Paisley, M. Sorem, D. Swift, and J. Workman, "Target fabrication: A view from the users," *Fusion Science and Technology* **45**, 286–295 (2004).
- S.K. Lamoreaux and J.R. Torgerson, "Neutron moderation in the Oklo natural reactor and the time variation of alpha," *Physical Review D* **69**, 121701-1–121701-5 (2004).
- M.J. Leitch, "J/ ψ and heavy-quark production in E866/FNAL and PHENIX," *European Physical Journal A* **19**, 129–132 (2004).
- V.I. Levitas, A.V. Idesman, and D.L. Preston, "Microscale simulation of Martensitic microstructure evolution," *Physical Review Letters* **93**, 105701-1–105701-4 (2004).
- C.-Y. Liu and S.K. Lamoreaux, "A new search for a permanent dipole moment of the electron in a solid state system," *Modern Physics Letters A* **19**, 1235–1238 (2004).
- D. Liu *et al.* (The Super-Kamiokande Collaboration) [including Los Alamos author: T.J. Haines], "Limits on the neutrino magnetic moment using 1496 days of Super-Kamiokande I solar neutrino data," *Physical Review Letters* **93**, 021802-1–021802-5 (2004).
- M.X. Liu *et al.* (PHENIX Collaboration) [including Los Alamos authors: P.D. Barnes, J.G. Boissevain, M.L. Brooks, A.G. Hansen, C.H. Kuberg, D.M. Lee, M.J. Leitch, M.X. Liu, P.L. McGaughey, R.E. Mischke, J.M. Moss, A.P.T. Palounek, J.-C. Peng, M.R. Shaw, T. Shiina, D. Silvermyr, W.E. Sondheim, J.P. Sullivan, J.D. Tepe, and H.W. van Hecke], "Hadron production in the forward and backward rapidities in *d*-Au collisions at RHIC," *Journal of Physics G – Nuclear and Particle Physics* **30**, S1193–S1196 (2004).
- S.-N. Luo and T.J. Ahrens, "Shock-induced superheating and melting curves of geophysically important minerals," *Physics of the Earth and Planetary Interiors* **143/44**, 369–386 (2004).
- S.-N. Luo, A. Strachan, and D.C. Swift, "Nonequilibrium melting and crystallization of a model Lennard-Jones system," *Journal of Chemical Physics* **120**, 11640–11649 (2004).
- S.-N. Luo and D.C. Swift, "Comment on 'Extreme superheating and supercooling of encapsulated metals in Fullerene-like shells,'" *Physical Review Letters* **92**, 139601-1 (2004).
- S.-N. Luo and D.C. Swift, "On asymmetry between superheating and supercooling in solid-liquid transitions: Landau models," *Journal of Chemical Physics* **121**, 7387–7389 (2004).
- S.-N. Luo, D.C. Swift, R.N. Mulford, N.D. Drummond, and G.J. Ackland, "Performance of an *ab initio* equation of state for magnesium oxide," *Journal of Physics: Condensed Matter* **16**, 5435–5442 (2004).
- S.-N. Luo, J.A. Akins, T.J. Ahrens, and P.D. Asimow, "Shock compressed MgSiO_3 glass, enstatite, olivine and quartz: Optical emission, temperatures and melting," *Journal of Geophysical Research – Solid Earth* **109**, B05205-1–B05205-14 (2004).
- S.-N. Luo, O. Tschauner, P.D. Asimow, and T.J. Ahrens, "A new dense silica phase: A possible link between tetrahedrally and octahedrally coordinated silica," *American Mineralogist* **89**, 455–461 (2004).
- K. Maharajh, P.L. Volegov, and R.H. Kraus, "Forward model theoretical basis for a superconducting imaging surface magnetoencephalography system," *Physics in Medicine and Biology* **49**, 523–532 (2004).
- O. Marina and A. Castro, "Applications of single-molecule detection to the analysis of pathogenic DNA," *Current Pharmaceutical Biotechnology* **5**, 279–284 (2004).

- F.J. Marshall, J.A. Oertel, and P.J. Walsh, “Framed, 16-image, Kirkpatrick-Baez microscope for laser-plasma x-ray emission,” *Review of Scientific Instruments* **75**, 4045–4047 (2004).
- J.C. Martin, M.A. Espy, A.C. Bergstrom, S.W. Graves, C. Carr, T.J. Matsson, A.N. Matlachov, R.H. Kraus, and J.P. Nolan, “A magnetic field sensing flow cytometer,” *Cytometry* **59A**, 147 (2004).
- A.N. Matlachov, P.L. Volegov, M.A. Espy, J.S. George, and R.H. Kraus, “SQUID detected NMR in microtesla magnetic fields,” *Journal of Magnetic Resonance* **170**, 1–7 (2004).
- K. McCormick *et al.* [Continuous Electron Beam Accelerator Facility (CEBAF) Large Acceptance Spectrometer (CLAS) Collaboration] [including Los Alamos author: A. Klein], “Tensor polarization of the ϕ meson photoproduced at high t ,” *Physical Review C* **69**, 032203-1–032203-5 (2004).
- J. McNabb *et al.* [Continuous Electron Beam Accelerator Facility (CEBAF) Large Acceptance Spectrometer (CLAS) Collaboration] [including Los Alamos author: A. Klein], “Hyperon photoproduction in the nucleon resonance region,” *Physical Review C* **69**, 042201-1–042201-5 (2004).
- P.W. Milonni, J.H. Carter, C.G. Peterson, and R.J. Hughes, “Effects of propagation through atmospheric turbulence on photon statistics,” *Journal of Optics B: Quantum and Semiclassical Optics* **6**, S742–S745 (2004).
- M. Mirazita *et al.* [Continuous Electron Beam Accelerator Facility (CEBAF) Large Acceptance Spectrometer (CLAS) Collaboration] [including Los Alamos author: A. Klein], “Complete angular distribution measurements of two-body deuteron photodisintegration between 0.5 and 3 GeV,” *Physical Review C* **70**, 014005-1–014005-12 (2004).
- G.S. Mitchell, C.S. Blessinger, J.D. Bowman, T.E. Chupp, K.P. Coulter, M. Gericke, G.L. Jones, M.B. Leuschner, H. Nann, S.A. Page, S.I. Penttila, T.B. Smith, W.M. Snow, and W.S. Wilburn, “A measurement of parity-violating gamma-ray asymmetries in polarized cold neutron capture on ^{35}Cl , ^{113}Cd , and ^{139}La ,” *Nuclear Instruments and Methods in Physics Research, Section A – Accelerators, Spectrometers, Detectors and Associated Equipment* **521**, 468–479 (2004).
- D.S. Montgomery, A. Nobile, and P.J. Walsh, “Characterization of National Ignition Facility cryogenic beryllium capsules using x-ray phase contrast imaging,” *Review of Scientific Instruments* **75**, 3986–3988 (2004).
- D.S. Montgomery, J.L. Kline, and T.E. Tierney IV, “Detailed characterization of plasma wave behavior using collective Thomson scattering (invited),” *Review of Scientific Instruments* **75**, 3793–3799 (2004).
- A.T. Nguyen, D. Budker, S.K. Lamoreaux, and J.R. Torgerson, “Towards a sensitive search for variation of the fine-structure constant using radio-frequency $E1$ transitions in atomic dysprosium,” *Physical Review A* **69**, 022105-1–022105-8 (2004).
- S. Niccolai *et al.* [Continuous Electron Beam Accelerator Facility (CEBAF) Large Acceptance Spectrometer (CLAS) Collaboration] [including Los Alamos author: A. Klein], “Complete measurement of three-body photodisintegration of ^3He for photon energies between 0.35 and 1.55 GeV,” *Physical Review C* **70**, 064003-1–064003-18 (2004).
- C. Niemann, S.H. Glenzer, J. Knight, L. Divol, E.A. Williams, G. Gregori, B.I. Cohen, C. Constantin, D.H. Froula, D.S. Montgomery, and R.P. Johnson, “Observation of the parametric two-ion decay instability with Thomson scattering,” *Physical Review Letters* **93**, 045004-1–045004-4 (2004).
- R.A. Niyazov *et al.* [Continuous Electron Beam Accelerator Facility (CEBAF) Large Acceptance Spectrometer (CLAS) Collaboration] [including Los Alamos author: A. Klein], “Two-nucleon momentum distributions measured in $^3\text{He}(e,e'pp)n$,” *Physical Review Letters* **92**, 052303-1–052303-5 (2004).
- R.A. Niyazov *et al.* [Continuous Electron Beam Accelerator Facility (CEBAF) Large Acceptance Spectrometer (CLAS) Collaboration] [including Los Alamos author: A. Klein], “Publisher’s note: Two-nucleon momentum distributions measured in $^3\text{He}(e,e'pp)n$,” *Physical Review Letters* **92**, 099902-1 (2004).
- R.A. Niyazov *et al.* [Continuous Electron Beam Accelerator Facility (CEBAF) Large Acceptance Spectrometer (CLAS) Collaboration] [including Los Alamos author: A. Klein], “Two-nucleon momentum distributions measured in $^3\text{He}(e,e'pp)n$,” *Physical Review Letters* **92**, 052303-1–052303-5 (2004).
- A. Nobile, M.M. Balkey, J.J. Bartos, S.H. Batha, R.D. Day, J.E. Elliott, N.E. Elliott, V.M. Gomez, D.J. Hatch, N.E. Lanier, J.R. Fincke, R. Manzanares, T.H. Pierce, D.L. Sandoval, D.W. Schmidt, and W.P. Steckle, “Recent developments in fabrication of direct drive cylinder targets for hydrodynamics experiments at the Omega laser,” *Fusion Science and Technology* **45**, 95–105 (2004).
- J.A. Oertel, T. Archuleta, M.S. Bakeman, P. Sanchez, G. Sandoval, L. Schrank, P.J. Walsh, and N. Pederson, “A large-format gated x-ray framing camera,” *Proceedings of SPIE* **5194**, 214–222 (2004).
- R. Oldenborg, J. Tiee, T. Shimada, C. Wilson, D. Remelius, J. Fox, and C. Swim, “Heterodyne LIDAR for chemical sensing,” *Proceedings of SPIE* **5416**, 186–193 (2004).
- R.E. Olson, R.J. Leeper, A. Nobile, J.A. Oertel, G.A. Chandler, K. Cochrane, S.C. Dropinski, S. Evans, S.W. Haan, J.L. Kaae, J.P. Knauer, K. Lash, L.P. Mix, A. Nikroo, G.A. Rochau, G. Rivera, C. Russell, D. Schroen, R.J. Sebring, D.L. Tanner, R.E. Turner, and R.J. Wallace, “Shock propagation, preheat, and x-ray burnthrough in indirect-drive inertial confinement fusion ablator materials,” *Physics of Plasmas* **11**, 2778–2789 (2004).
- A. Ossadtchi, S. Baillet, J.C. Mosher, D. Thyerlei, W. Sutherling, and R.M. Leahy, “Automated interictal spike detection and source localization in magnetoencephalography using independent components analysis and spatio-temporal clustering,” *Clinical Neurophysiology* **115**, 508–522 (2004).

Appendix B: Publications

- K. Parker, C.J. Horsfield, S.D. Rothman, S.H. Batha, M.M. Balkey, N.D. Delamater, J.R. Fincke, R.M. Hueckstaedt, N.E. Lanier, and G.R. Magelssen, "Observation and simulation of plasma mix after reshock in a convergent geometry," *Physics of Plasmas* **11**, 2696–2701 (2004).
- D.E. Post and R.P. Kendall, "Software project management and quality engineering practices for complex, coupled multiphysics, massively parallel computational simulations: Lessons learned from ASCI," *International Journal of High Performance Computing Applications* **18**, 399–416 (2004).
- E.S. Rangarajan, Y.G. Li, P. Iannuzzi, A. Tocili, L.W. Hung, A. Matte, and M. Cygler, "Crystal structure of a dodecameric FMN-dependent UbiX-like decarboxylase (Pad1) from *Escherichia coli* O157: H7," *Protein Science* **13**, 3006–3016 (2004).
- R.E. Reinovsky, J.H. Goforth, and J. Graham, "Surface-discharge switches for high-performance closing applications," *IEEE Transactions on Plasma Science* **32**, 1765–1777 (2004).
- L.A. Rosocha, D.M. Coates, D. Platts, and S. Stange, "Plasma-enhanced combustion of propane using a silent discharge," *Physics of Plasmas* **11**, 2950–2956 (2004).
- A. Saunders, J.M. Anaya, T.J. Bowles, B.W. Filippone, P. Geltenbort, R.E. Hill, M. Hino, S. Hoedl, G.E. Hogan, T.M. Ito, K.W. Jones, T. Kawai, K. Kirch, S.K. Lamoreaux, C.Y. Liu, M. Makela, L.J. Marek, J.W. Martin, C.L. Morris, R.N. Mortensen, A. Pichlmaier, S.J. Seestrom, A. Serebrov, D. Smith, W. Teasdale, B. Tipton, R.B. Vogelaar, A.R. Young, and J. Yuan, "Demonstration of a solid deuterium source of ultra-cold neutrons," *Physics Letters B* **593**, 55–60 (2004).
- M.M. Schauer, D.C. Barnes, and K.R. Umstadter, "Physics of non-thermal Penning-trap electron plasma and application to ion trapping," *Physics of Plasmas* **11**, 9–15 (2004).
- J. Schreiber, M. Kaluza, F. Gruner, U. Schramm, B.M. Hegelich, J. Cobble, M. Geissler, E. Brambrink, J. Fuchs, P. Audebert, D. Habs, and K. Witte, "Source-size measurements and charge distributions of ions accelerated from thin foils irradiated by high-intensity laser pulses," *Applied Physics B – Lasers and Optics* **79**, 1041–1045 (2004).
- L.J. Schultz, K.N. Borozdin, J.J. Gomez, G.E. Hogan, J.A. McGill, C.L. Morris, W.C. Friedhorsky, A. Saunders, and M.E. Teasdale, "Image reconstruction and material Z discrimination via cosmic ray muon radiography," *Nuclear Instruments and Methods in Physics Research, Section A – Accelerators, Spectrometers, Detectors and Associated Equipment* **519**, 687–694 (2004).
- A. Seifter, K. Boboridis, and A.W. Obst, "Emissivity measurements on metallic surfaces with various degrees of roughness: A comparison of laser polarimetry and integrating sphere reflectometry," *International Journal of Thermophysics* **25**, 547–560 (2004).
- P.-N. Seo, J.D. Bowman, M. Gericke, G. Greene, J. Long, G.S. Mitchell, S.I. Penttila, and W.S. Wilburn, "A measurement of the Flight Path 12 cold H₂ moderator brightness at LANSCE," *Nuclear Instruments and Methods in Physics Research, Section A – Accelerators, Spectrometers, Detectors and Associated Equipment* **517**, 285–294 (2004).
- P.-N. Seo, J.D. Bowman, M. Gericke, G. Greene, J. Long, G.S. Mitchell, S.I. Penttila, and W.S. Wilburn, "A measurement of the Flight Path 12 cold H₂ moderator brightness at LANSCE," *Nuclear Instruments and Methods in Physics Research, Section A – Accelerators, Spectrometers, Detectors and Associated Equipment* **517**, 285–294 (2004).
- E.C. Sittler, R.E. Johnson, S. Jurac, J.D. Richardson, M. McGrath, F. Crary, D.T. Young, and J.E. Nordholt, "Pickup ions at Dione and Enceladus: Cassini Plasma Spectrometer simulations," *Journal of Geophysical Research – Space Physics* **109**, A01214-1–A01214-22 (2004).
- M.B. Smy *et al.* (The Super-Kamiokande Collaboration) [including Los Alamos author: T.J. Haines], "Precise measurement of the solar neutrino day-night and seasonal variation in Super-Kamiokande I," *Physical Review D* **69**, 011104-1–011104-5 (2004).
- A.V. Stavinsky *et al.* [Continuous Electron Beam Accelerator Facility (CEBAF) Large Acceptance Spectrometer (CLAS) Collaboration] [including Los Alamos author: A. Klein], "Proton source size measurements in the $eA \rightarrow e'ppX$ reaction," *Physical Review Letters* **93**, 192301-1–192301-6 (2004).
- A.O. Sushkov, E. Williams, V.V. Yashchuk, D. Budker, and S.K. Lamoreaux, "Kerr effect in liquid helium at temperatures below the superfluid transition," *Physical Review Letters* **93**, 153003-1–153003-4 (2004).
- D.C. Swift, J.T. Gammel, and S.M. Clegg, "Treatment of compounds and alloys in radiation hydrodynamics simulations of ablative laser loading," *Physical Review E* **69**, 056401-1–056401-9 (2004).
- D.C. Swift, T.E. Tierney IV, R.A. Kopp, and J.T. Gammel, "Shock pressures induced in condensed matter by laser ablation," *Physical Review E* **69**, 036406-1–036406-9 (2004).
- J.R. Torgerson and S.K. Lamoreaux, "Low-frequency character of the Casimir force between metallic films," *Physical Review E* **70**, 047102-1–047102-4 (2004).
- S. Turbide, L. Beaulieu, P. Danielewicz, V.E. Viola, R. Roy, K. Kwiatkowski, W.C. Hsi, G. Wang, T. Lefort, D.S. Bracken, H. Breuer, E. Cornell, F. Gimeno-Nogues, D.S. Ginger, S. Gushue, R. Huang, R. Korteling, W.G. Lynch, K.B. Morley, E. Ramakrishnan, L.P. Remsberg, D. Rowland, M.B. Tsang, H. Xi, and S.J. Yennello, "Effects of in-medium cross sections and optical potential on thermal-source formation in $p + {}^{197}\text{Au}$ reactions at 6.2–14.6 GeV/c," *Physical Review C* **70**, 014608-1–014608-11 (2004).

P. Volegov, A. Matlachov, J. Mosher, M.A. Espy, and R.H. Kraus, "Noise-free magnetoencephalography recordings of brain function," *Physics in Medicine and Biology* **49**, 2117–2128 (2004).

P. Volegov, A.N. Matlachov, M.A. Espy, J.S. George, and R.H. Kraus, "Simultaneous magnetoencephalography and SQUID detected nuclear MR in microtesla magnetic fields," *Magnetic Resonance in Medicine* **52**, 467–470 (2004).

Z. Wang and G.A. Wurden, "Hypervelocity dust beam injection for national spherical torus experiment," *Review of Scientific Instruments* **75**, 3436–3438 (2004).

Z.H. Wang and X.Z. Tang, "Compact toroids with Alfvénic flows," *Physics of Plasmas* **11**, 3502–3509 (2004).

G. Warren *et al.* (Jefferson Lab E93 026 Collaboration) [including Los Alamos author: A. Klein], "Measurement of the electric form factor of the neutron at $Q^2 = 0.5$ and $1.0 \text{ GeV}^2/c^2$," *Physical Review Letters* **92**, 042301-1–042301-5 (2004).

J. Workman, J.R. Fincke, P. Keiter, G.A. Kyralla, T. Pierce, S. Sublett, J.P. Knauer, H. Robey, B. Blue, S.G. Glendinning, and O.L. Landen, "Development of intense point x-ray sources for backlighting high energy density experiments (invited)," *Review of Scientific Instruments* **75**, 3915–3920 (2004).

D.T. Young, F.J. Crary, J.E. Nordholt, F. Bagenal, D. Boice, J.L. Burch, A. Eviatar, R. Goldstein, J.J. Hanley, D.J. Lawrence, D.J. McComas, R. Meier, D. Reisenfeld, K. Sauer, and R.C. Wiens, "Solar wind interactions with Comet 19P/Borrelly," *Icarus* **167**, 80–88 (2004).

S.W. Yu, N. Muller, U. Heinzmann, C. Pettenkofer, A. Klein, and P. Blaha, "Band symmetries of GaSe(0001) studied by spin-resolved electron spectroscopy using circularly polarized radiation," *Physical Review B* **69**, 045320-1–045320-7 (2004).

S.Y. Zhang, E.M. Tejero, J.M. Taccetti, G.A. Wurden, T.P. Intrator, W.J. Waganaar, and R. Perkins, "Separatrix radius measurement of field-reversed configuration plasma in FRX-L," *Review of Scientific Instruments* **75**, 4289–4292 (2004).

2004 Conference Papers and Presentations

T.J. Asaki, R. Chartrand, K.N. Borozdin, N. Hengartner, L.L. Schultz, M. Sottile, K. Vixie, and B. Wohlberg, "Scattering muon radiography for border inspections," Montana State University Physics Colloquium, Bozeman, Montana, USA, September 24, 2004, Los Alamos National Laboratory document LA-UR-04-5767.

S.H. Batha and J.R. Fincke, "Quantified reduction of wall material influx during hohlraum experiments," 15th Topical Conference on High-Temperature Plasma Diagnostics, San Diego, California, USA, April 19–22, 2004, Los Alamos National Laboratory document LA-UR-04-2605.

S.H. Batha, J.R. Fincke, J.M. Taccetti, J.R. Lanier, N.D. Delamater, G.R. Magelssen, R.M. Hueckstaedt, S.D. Rothman, K.W. Parker,

and C.J. Horsfield, "Convergent reshock experiments," Meeting of the Joint Working Group (U.S.-UK) (JOWOG-32Mix), Aldermaston, Berkshire, UK, May 17–21, 2004, Los Alamos National Laboratory document LA-UR-04-2026.

S.H. Batha, J.R. Fincke, J.M. Taccetti, J.R. Lanier, N.D. Delamater, G.R. Magelssen, R.M. Hueckstaedt, S.D. Rothman, K.W. Parker, and C.J. Horsfield, "Reshock of a convergent, unstable system," 46th Annual Meeting of the American Physical Society Division of Plasma Physics, Savannah, Georgia, USA, November 15–19, 2004, Los Alamos National Laboratory document LA-UR-04-4150.

D.J. Berkeland, "Tests for non-randomness in quantum jumps," Nonlinear Optics: Materials, Fundamentals and Applications, Waikoloa, Hawaii, USA, August 2–6, 2004, Los Alamos National Laboratory document LA-UR-04-3272.

D.J. Berkeland, V.M. Tassin, A.M. Chamberlin, G. Ortiz, and J.P. Paz, "Quantum mechanics and condensed matter simulations with trapped ions," Workshop on Trapped Ion Quantum Computation, Ann Arbor, Michigan, USA, May 13–15, 2004, Los Alamos National Laboratory document LA-UR-04-3566.

K.N. Borozdin, T. Asaki, R. Chartrand, N. Hengartner, and C.L. Morris, "Information extraction from muon radiography data," Cybernetics and Information Technologies, Systems, and Applications (CITSA2004), Orlando, Florida, USA, July 21–25, 2004, Los Alamos National Laboratory document LA-UR-04-3985.

M.G. Boulay, "Design constraints for a liquid neon detector for dark matter and pp solar neutrinos," 2004 Annual Spring Meeting of the American Physical Society, Denver, Colorado, USA, May 1–4, 2004, Los Alamos National Laboratory document LA-UR-04-2237.

J.D. Bowman and S.I. Penttila, "On the measurement the neutron lifetime using ultra-cold neutrons in a vacuum quadrupole trap," International Conference on Precision Measurements with Slow Neutrons, Gaithersburg, Maryland, USA, April 5–7, 2004, Los Alamos National Laboratory document LA-UR-04-3785.

J.D. Bowman, "On the measurement of the electron-neutrino correlation in neutron beta decay," International Conference on Precision Measurements with Slow Neutrons, Gaithersburg, Maryland, USA, April 5–7, 2004, Los Alamos National Laboratory document LA-UR-04-3784.

J.M. Burward-Hoy, " $J/\psi \rightarrow \mu^+ \mu^-$ in high energy $d+Au$ collisions," 20th Winter Workshop on Nuclear Dynamics, Montego Bay, Jamaica, March 15–20, 2004, Los Alamos National Laboratory document LA-UR-04-1755.

J.M. Burward-Hoy, M.S. Krick, W.H. Geist, and D.R. Mayo, "Achieving accurate neutron-multiplicity analysis of metals and oxides with weighted point model equations," 45th Annual Institute of Nuclear Materials Management (INMM) Meeting, Orlando, Florida, USA, July 18–22, 2004, Los Alamos National Laboratory document LA-UR-04-0762.

Appendix B: Publications

W.T. Buttler, "Piezo probe and optical pin measurement diagnostics," Meeting of the Joint Working Group (U.S.-UK) (JOWOG), Aldermaston, Berkshire, UK, January 2004, Los Alamos National Laboratory document LA-UR-04-0124.

G.H. Canavan, "Assesment of missile defense agency modeling & simulation," Defense Science Board, Washington, DC, USA, January 2004.

G.H. Canavan, "Assessment of contributions of space based radar to missile defense," Defense Science Board Task Force, U.S. DOD Office of U.S. Defense, June 2004.

G.H. Canavan, "Boost-phase missile defense for the 21st century," Marshall Foundation Seminar, Washington, DC, USA, May 4, 2004, Los Alamos National Laboratory document LA-UR-04-0376.

G.H. Canavan, "Boost-phase missile defense for the 21st century," Boost-Phase Missile Defenses for the 21st Century, Washington, DC, USA, January 10–11, 2004, Los Alamos National Laboratory document LA-UR-04-0376.

G.H. Canavan, "Directed energy applications to the modern battlefield," Army Science Board Summer Study, Newport Beach, Virginia, USA, July 11–24 2004.

G.H. Canavan, "Energy and environment: Some passing observations," Workshop on Global Issues, Central Intelligence Agency, Washington DC, USA, April 26, 2004, Los Alamos National Laboratory document LA-UR-04-2829.

G.H. Canavan, "ISAG CONOPS in horizontal integration format," Air Force Space Command Independent Strategic Assessment Group Plenary, Colorado Springs, Colorado, USA, February 29, 2004, LA-UR-04-0934.

G.H. Canavan, "Missile defense for the 21st century: An update," Marshall Institute Colloquium, Washington DC, USA, April, 2004, Los Alamos National Laboratory document LA-UR-04-0697.

G.H. Canavan, "Missile defense phase III modeling and simulation," Defense Science Board Task Force, U.S. DOD Office of U.S. Defense, March 2004.

G.H. Canavan, "Missile defense: The good, the bad, and the ugly," Sandia National Laboratory Senior Management Seminar, Washington DC, USA, May 29, 2004, Los Alamos National Laboratory document LA-UR-04-3060.

G.H. Canavan, "Technical issues in space based radars," Air Force Space Command Independent Strategic Assessment Group Plenary, Colorado Springs, Colorado, USA, February 20, 2004, Los Alamos National Laboratory document LA-UR-04-0474.

G.H. Canavan, "Technical issues in space-based radars," Defense Science Board, Washington, DC, USA, April 19, 2004, Los Alamos National Laboratory document LA-UR-04-0474.

G.H. Canavan, "Weapons testing and SDI: Reflections of an accidental advisor," Bridging the Gap Between Science and Society

(Rice University), Houston, Texas, USA, November 2, 2003, Los Alamos National Laboratory document LA-UR-04-0696.

T.M. Cannon, F.E. Merrill, K.P. Prestridge, and Q.K. Zuo, "A fragmentation study of uranium-6% niobium using proton radiography," 2004 Nuclear Explosives Code Developers Conference (NECDC 2004), Livermore, California, USA, October 4–8, 2004, Los Alamos National Laboratory controlled publication LA-CP-04-0527.

C.S. Carey, I.S. Furno, H. Weisen, R. Behn, and E. Fable, "The application of the singular value decomposition method for the inversion of interferometer measurements in TCV plasmas," 15th Topical Conference on High-Temperature Plasma Diagnostics, San Diego, California, USA, April 19–22, 2004, Los Alamos National Laboratory document LA-UR-04-2261.

C. Carr, M.A. Espy, T.G. Abeln, and R.H. Kraus, Jr., "The determination of inertia weld quality by eddy current-based SQUID NDE," Applied Superconductivity Conference: Harnessing the Magic (ASC'04), Jacksonville, Florida, USA, October 3–8, 2004, Los Alamos National Laboratory document LA-UR-04-1545 (to be published in IEEE Transactions on Applied Superconductivity).

C.R. Christensen, G.P. Grim, G.L. Morgan, M.D. Wilke, and D.C. Wilson, "Neutron imaging for the NIF," 15th Topical Conference on High-Temperature Plasma Diagnostics, San Diego, California, USA, April 19–22, 2004, Los Alamos National Laboratory document LA-UR-04-0391.

C.R. Christensen, S.E. Caldwell, S.C. Evans, R. Griffith, R.S. King, R.A. Lerche, J.M. Mack, and C.S. Young, "Improvements in gas Cherenkov detection of ICF burn history," 46th Annual Meeting of the American Physical Society Division of Plasma Physics, Savannah, Georgia, USA, November 15–19, 2004, Los Alamos National Laboratory document LA-UR-04-5026.

J.A. Cobble, B.M. Hegelich, K.A. Flippo, J.C. Fernández, and S.A. Letzring, "Neutral particles in Thomson parabola spectra," 46th Annual Meeting of the American Physical Society Division of Plasma Physics, Savannah, Georgia, USA, November 15–19, 2004, Los Alamos National Laboratory document LA-UR-04-5021.

J.A. Cobble, D.L. Tubbs, N.M. Hoffman, D.C. Swift, and T.E. Tierney, "Radiation drive with a composite laser pulse Sharpe," 34th Anomalous Absorption Meeting, Gleneden Beach, Oregon, USA, May 2–7, 2004, Los Alamos National Laboratory document LA-UR-04-2913.

T.E. Cowan, J. Fuchs, H. Ruhl, Y. Sentoku, A. Kemp, P. Audebert, M. Roth, R. Stephens, I. Barton, A. Blazevic, E. Brambrink, J.A. Cobble, J.C. Fernández, J.-C. Gauthier, M. Geissel, M. Hegelich, J. Kaae, S. Karsch, G.P. Le Sage, S.A. Letzring, M. Manclossi, S. Meyroneinc, A. Newkirk, H. Pépin, and N. Renard-LeGalloudec, "Ultra-low emittance, high current proton beams produced with a laser-virtual cathode sheath accelerator," 15th International Symposium on Heavy Ion Inertial Fusion, Princeton, New Jersey, USA, June 7–11, 2004.

- K.L. Creek, "The search for a portable method for rapid airborne beryllium measurement: The current state of the science," American Industrial Hygiene Conference and Exposition, Atlanta, Georgia, USA, May 8–13, 2004, Los Alamos National Laboratory document LA-UR-04-3156.
- N.D. Delamater, S.H. Batha, J.R. Fincke, J.M. Taccetti, and G.R. Magelssen, "Calculations of double cylinder implosions at Omega," 46th Annual Meeting of the American Physical Society Division of Plasma Physics, Savannah, Georgia, USA, November 15–19, 2004, Los Alamos National Laboratory document LA-UR-04-4938.
- N.D. Delamater, S.H. Batha, J.R. Fincke, J.M. Taccetti, and N.E. Lanier, "Calculations of double cylinder implosions at Omega," 34th Anomalous Absorption Meeting, Gleneden Beach, Oregon, USA, May 2–7, 2004, Los Alamos National Laboratory document LA-UR-04-1765.
- B.L. Dings, "The most sensitive survey of the TeV sky," 8th Meeting of the High-Energy Astrophysics Division of the American Astronomical Society (HEAD 2004), New Orleans, Louisiana, USA, September 8–11, 2004, Los Alamos National Laboratory document LA-UR-04-6027.
- V. Douence, Y. Bai, H. Durmus, A. Joshi, P.-O. Pettersson, D. Sahood, K. Kwiatkowski, N.S.P. King, C.L. Morris, and M.D. Wilke, "Hybrid image sensor with multiple on-chip frame storage for ultra high-speed imaging," 26th International Congress on High-Speed Photography and Photonics, Alexandria, Virginia, USA, September 19–24, 2004.
- L.M. Earley, H.C. Kirbie, F.E. Sigler, R. Carlson, R.M. Wheat, R.W. Brown, W.B. Haynes, S.J. Russell, E.I. Smirnova, and P. Ferguson, "A 120 kV IGBT modulator for driving a Pierce electron gun," 2004 IEEE Power Modulator Conference, San Francisco, California, USA, May 23–26, 2004, Los Alamos National Laboratory document LA-UR-04-0438.
- L.M. Earley, R.W. Brown, R. Carlson, and P. Ferguson, "A 120 kV IGBT modulator for driving a Pierce electron gun," 2004 Spring Meeting of the Materials Research Society, San Francisco, California, USA, March 28–April 1, 2004, Los Alamos National Laboratory document LA-UR-04-0457.
- C.A. Ekdadl, E.O. Abeyta, L.D. Caudill, D.E. Dalmás, S.A. Eversole, R.A. Gallegos, J.F. Harrison, M.H. Holzscheiter, J.B. Johnson, E.B. Jacquez, B.T. McCuistian, N.A. Montoya, S. Nath, K.E. Neilsen, D.M. Oro, L.R. Rodriguez, P. Rodriguez, M. Sanchez, R. Scarpetti, M.M. Schauer, D.F. Simmons, H.V. Smith, J.K. Studebaker, G.W. Sullivan, and C.A. Swinney, "First commissioning experiments at DARHT-II," 9th Biennial European Particle Accelerator Conference (EPAC'04), Lucerne, Switzerland, July 5–9, 2004, Los Alamos National Laboratory document LA-UR-04-0421.
- S.R. Elliott, "Experimental double-beta decay," 32nd SLAC Summer Institute on Particle Physics: Nature's Greatest Puzzles (SSI 2004), Menlo Park, California, USA, August 2–13, 2004, Los Alamos National Laboratory document LA-UR-04-6073.
- M.A. Espy and P.L. Volegov, "Simultaneously detected biomagnetic signals and NMR," 14th International Conference on Biomagnetism (BIOMAG 2004), Boston, Massachusetts, USA, August 8–12, 2004, Los Alamos National Laboratory document LA-UR-04-6823.
- M.A. Espy, C. Carr, A.N. Matlachov, J.C. Martin, J.P. Nolan, S.W. Graves, D. Leslie-Pelecky, and R.H. Kraus, Jr., "SQUID-based bioassay with magnetic particles in flow," Applied Superconductivity Conference: Harnessing the Magic (ASC'04), Jacksonville, Florida, USA, October 3–8, 2004, Los Alamos National Laboratory document LA-UR-04-1544.
- J.C. Fernández, B.M. Hegelich, J.A. Cobble, and S.A. Letzring, "Laser-ablation treatment of short-pulse laser targets: Towards an experimental program on energetic-ion interactions with dense plasmas," International Workshop on Fast Ignition and High Field Physics, Kyoto, Japan, April 25–29, 2004, Los Alamos National Laboratory document LA-UR-04-0666.
- J.C. Fernández, B.M. Hegelich, J.A. Cobble, K.A. Flippo, S.A. Letzring, R.P. Johnson, C. Gautier, T. Shimada, G.A. Kyrala, Y. Wang, C.J. Wetteland, and J. Schreiber, "Laser-ablation treatment of short-pulse laser targets: Towards an experimental program on energetic-ion interactions with dense plasmas," 28th European Conference on Laser Interaction with Matter, Rome, Italy, September 6–10, 2004, Los Alamos National Laboratory document LA-UR-04-6168.
- J.C. Fernández, B.M. Hegelich, J.A. Cobble, S.A. Letzring, R.P. Johnson, C. Gautier, T. Shimada, and J. Schreiber, "Laser-ablation treatment of short-pulse targets: Towards an experimental program on energetic-ion interactions with dense plasma," 34th Anomalous Absorption Meeting, Gleneden Beach, Oregon, USA, May 2–7, 2004, Los Alamos National Laboratory document LA-UR-04-2962.
- J.C. Fernández, D.C. Gautier, S.R. Goldman, and G.P. Grim, "Gas-filled hohlraum experiments at the National Ignition Facility," 46th Annual Meeting of the American Physical Society Division of Plasma Physics, Savannah, Georgia, USA, November 15–19, 2004, Los Alamos National Laboratory document LA-UR-04-5037.
- J.R. Fincke, J.B. Workman, G.A. Kyrala, P.J. Walsh, S.C. Evans, D. Tafoya, and D.J. Landers, "Close-in nosecone configurations and blast damage in point projection x-ray radiography," 15th Topical Conference on High-Temperature Plasma Diagnostics, San Diego, California, USA, April 19–22, 2004, Los Alamos National Laboratory document LA-UR-04-2116.
- J.R. Fincke, J.R. Lanier, S.H. Batha, G.R. Magelssen, C.J. Horsfield, K.W. Parker, and S.D. Rothman, "Postponment of saturation of the Richmyer-Meshkov instability by convergence," 9th International Workshop on the Physics of Compressible Turbulent Mixing (IWPCTM 2004), Cambridge, UK, July 19–23, 2004, Los Alamos National Laboratory document LA-UR-04-3899.

Appendix B: Publications

J.R. Fincke, J.R. Lanier, S.H. Batha, R.L. Holmes, G.R. Magelssen, C.J. Horsfield, K.W. Parker, and S.D. Rothman, "The effects of convergence on the growth of the Richmyer-Meshkov and Rayleigh-Taylor instabilities," 28th European Conference on Laser Interaction with Matter, Rome, Italy, September 6–10, 2004, Los Alamos National Laboratory document LA-UR-04-3896.

J.R. Fincke, N.E. Lanier, S.H. Batha, R.L. Holmes, G.R. Magelssen, R.M. Huechstaedt, N.D. Delamater, J.M. Scott, M.M. Balkey, and C.J. Horsfield, "Apparent postponement of saturation of the Richtmyer-Meshkov instability convergence," 9th International Workshop on the Physics of Compressible Turbulent Mixing, Cambridge, UK, July 19–23, 2004, Los Alamos National Laboratory document LA-UR-04-0113.

K.A. Flippo, T. Lin, A. Maksimchuk, R. Matthew, V. Wong, K. Nash, and D. Umstadter, "Proton beam dynamics from the front and surface of dielectric and conductive targets," 46th Annual Meeting of the American Physical Society Division of Plasma Physics, Savannah, Georgia, USA, November 15–19, 2004, Los Alamos National Laboratory document LA-UR-04-5071.

C.M. Frankle, J.A. Becker, K.B. Butterfield, L.A. Chavez, J.W. Collins, C.P. Cork, L. Fabris, S.E. Garner, N.W. Madden, W.S. Murray, C.D. Romero, S.A. Salazar, and B.A. Sapp, "GN-5 handheld isotope identification instrument," DHS Innovative Technologies in Homeland Security, San Diego, California, USA, July 13–15, 2004, Los Alamos National Laboratory controlled publication LA-CP-04-0668.

R.D. Fulton, "The Stallion subcritical experiment (SCE) series supports certification of the W 88," Atomic Weapons Establishment – HRF, Los Angeles, California, USA, January 2004, Los Alamos National Laboratory document LA-UR-04-0256.

I.G. Furno, T.P. Intrator, E.W. Hemsing, S.C. Hsu, and S.A. Abbate, "Relaxation of flux ropes and magnetic reconnection in the reconnection scaling experiment," U.S.-Japan Compact Torroids Workshop 2004, Santa Fe, New Mexico, USA, September 14–17, 2004, Los Alamos National Laboratory document LA-UR-04-6698.

I.G. Furno, G.A. Wurden, and J. Terry, "Infrared spectroscopy of the divertor region in the Alcator C-Mod tokamak," 15th Topical Conference on High-Temperature Plasma Diagnostics, San Diego, California, USA, April 19–22, 2004, Los Alamos National Laboratory document LA-UR-04-2596.

I.G. Furno, T.P. Intrator, and E.W. Hemsing, "Experimental investigation of the interaction of multiple magnetized current carrying plasma channels," Innovative Confinement Concepts workshop (ICC-2004), Madison, Wisconsin, USA, May 25–28, 2004, Los Alamos National Laboratory document LA-UR-04-3650.

V.M. Gehman, "Status of underground construction at the Waste Isolation Pilot Plant in support of the Majorana project," Annual APS Spring Meeting 2004, Denver, Colorado, USA, May 1–4, 2004, Los Alamos National Laboratory document LA-UR-04-2777.

J.S. George, D. Barnes, and K.T. Ng, "Parallel adaptive neural electromagnetic modeling," 2004 Annual Meeting of the Biomedical Engineering Society (BMES'04), Philadelphia, Pennsylvania, USA, October 13–16, 2004, Los Alamos National Laboratory document LA-UR-04-3461.

M.T. Gericke, J.D. Bowman, G.S. Mitchell, S.I. Penttila, and W.S. Wilburn, "Commissioning of the NPDGamma detector array," International Conference on Precision Measurements with Slow Neutrons, Gaithersburg, Maryland, USA, April 5–7, 2004, Los Alamos National Laboratory document LA-UR-04-3727.

M.T. Gericke, "Weak pion-nucleon coupling and parity violation in the radiative capture of polarized cold neutrons on hydrogen," Nuclear Physics Seminar: TRIUMF, Vancouver, British Columbia, Canada, February, 2004, Los Alamos National Laboratory document LA-UR-03-9048.

M.T. Gericke, "Weak pion-nucleon coupling and parity violation in the radiative capture of polarized cold neutrons on hydrogen," Nuclear Physics Seminar: Virginia Polytechnical Institute, Blacksburg, Virginia, USA, February, 2004, Los Alamos National Laboratory document LA-UR-03-9048.

S.R. Goldman, J.C. Fernández, N.M. Hoffman, D.W. Schmidt, and D.C. Swift, "Calculations for LANL hohlraum IET experiments on the first quad at NIF," 46th Annual Meeting of the American Physical Society Division of Plasma Physics, Savannah, Georgia, USA, November 14–19, 2004, Los Alamos National Laboratory document LA-UR-04-7757.

S.R. Goldman, J.C. Fernández, N.M. Hoffman, J.M. Kindel, and B.A. Langdon, "Calculations for NIF first quad gas-filled hohlraum experiments testing beryllium microstructure growth and laser plasma interaction physics," 34th Anomalous Absorption Meeting, Gleneden Beach, Oregon, USA, May 2–7, 2004, Los Alamos National Laboratory document LA-UR-04-1926.

S.R. Greenfield, D.C. Swift, D.L. Paisley, and A.C. Koskelo, "Transient interferometric microscopy: Applications to shock physics and laser ablation," 26th International Congress on High-Speed Photography and Photonics 2004, Alexandria, Virginia, USA, September 19–24, 2004, Los Alamos National Laboratory document LA-UR-04-6611.

G.P. Grim, G.L. Morgan, M.D. Wilke, P.L. Gobby, and C.R. Christensen, "Progress in neutron imaging as a diagnostic for ICF experiments," 15th Topical Conference on High-Temperature Plasma Diagnostics, San Diego, California, USA, April 19–22, 2004, Los Alamos National Laboratory document LA-UR-04-0258.

J.E. Hammerberg, D.L. Preston, and T.C. Germann, "A source model for ejecta," Meeting of the Joint Working Group (U.S.-UK) (JOWOG-32), Aldermaston, Berkshire, UK, May 17–21, 2004, Los Alamos National Laboratory document LA-UR-04-3371.

- A. Hauer, "Reviewing of 10.2 activities at Los Alamos," DOE/ NNSA Semi-Annual Campaign Meeting, Las Vegas, Nevada, USA, August 24–25, 2004, Los Alamos National Laboratory document LA-UR-04-5848.
- B.M. Hegelich, J.A. Cobble, and J.C. Fernández, "Acceleration physics of laser-driven MeV-ion beams," HIRSCHEGG 2004: Probing Nuclei and Nucleons with Electrons and Photons – 32nd International Workshop on Gross Properties of Nuclei and Nuclear Excitations, Hirschegg, Austria, January 11–17, 2004, Los Alamos National Laboratory document LA-UR-04-0600.
- B.M. Hegelich, J.C. Fernández, J.A. Cobble, and S.A. Letzring, "Physics and production techniques of laser-accelerated MeV heavy-ions," 31st European Physical Society Conference on Plasma Physics, London, UK, June 28–July 2, 2004, Los Alamos National Laboratory document LA-UR-04-4392.
- B.M. Hegelich, J.C. Fernández, J.A. Cobble, S.A. Letzring, J. Schreiber, P. Audebert, E. Brambrink, J.C. Cooley, R.D. Field, J. Fuchs, S. Gaillard, P. Papin, U. Schramm, E. Veuillot, and K. Wittle, "Acceleration physics of laser-driven MeV-ion beams," International Workshop on Fast Ignition and High Field Physics, Kyoto, Japan, April 25–29, 2004, Los Alamos National Laboratory document LA-UR-04-0765.
- B.M. Hegelich, J.C. Fernández, J.A. Cobble, S.A. Letzring, J. Schreiber, P. Audebert, J.C. Cooley, T. Cowan, R.D. Field, J. Fuchs, S. Gaillard, P. Papin, U. Schramm, E. Veuillot, and K. Wittle, "Acceleration physics of laser-driven MeV-ion beams," 34th Anomalous Absorption Meeting, Gleneden Beach, Oregon, USA, May 2–7, 2004, Los Alamos National Laboratory document LA-UR-04-2048.
- B.M. Hegelich, J.C. Fernández, J.A. Cobble, S.A. Letzring, J. Schreiber, P. Audebert, E. Brambrink, J.C. Cooley, R.D. Field, J. Fuchs, S. Gaillard, P. Papin, U. Schramm, and E. Veuillot, "Physics and production techniques of laser-accelerated MeV heavy-ions," 31st European Physical Society Conference on Plasma Physics, London, UK, June 28–July 2, 2004, Los Alamos National Laboratory document LA-UR-04-1316.
- B.M. Hegelich, J.C. Fernández, J.A. Cobble, S.A. Letzring, J. Schreiber, and T. Shimada, "Physics and production techniques of laser-accelerated MeV heavy-ions," 28th European Conference on Laser Interaction with Matter, Rome, Italy, September 6–10, 2004, Los Alamos National Laboratory document LA-UR-04-3898.
- J.C. Heise, "Installation and operation of the SNO neutral current detector array," 21st International Conference on Neutrino Physics and Astrophysics (NEUTRINO 2004), Paris, France, June 14–19, 2004, Los Alamos National Laboratory document LA-UR-04-3160.
- J.C. Heise, "Installation and operation of the SNO neutral current detector array," 2004 Fall Meeting of the APS Division of Nuclear Physics, Chicago, Illinois, USA, October 27–30, 2004, Los Alamos National Laboratory document LA-UR-04-6377.
- E.W. Hemsing, I.G. Furno, T.P. Intrator, and D. Wei, "Analysis of visible light images from a fast-gated, intensified CCD camera during flux rope interaction and magnetic reconnection," 15th Topical Conference on High-Temperature Plasma Diagnostics, San Diego, California, USA, April 19–22, 2004, Los Alamos National Laboratory document LA-UR-04-0337.
- S.J. Higginson and G.A. Wurden, "Radiation measurements on plasmas," 46th Annual Meeting of the American Physical Society Division of Plasma Physics, Savannah, Georgia, USA, November 15–19, 2004, Los Alamos National Laboratory document LA-UR-04-5019.
- G.E. Hogan, "Detecting special nuclear materials by muon radiography," 2004 Annual Spring Meeting of the American Physical Society, Denver, Colorado, USA, May 1–4, 2004, Los Alamos National Laboratory document LA-UR-04-3057.
- A.S. Hoover, W. Baird, R.M. Kippen, M.W. Rawool-Sullivan, and J.P. Sullivan, "A Compton imaging device for homeland security," SPIE 49th Annual Meeting, Denver, Colorado, USA, August 2–6, 2004, Los Alamos National Laboratory document LA-UR-04-0619.
- S.C. Hsu, Z. Wang, P.D. Beinke, C.W. Barnes, and G.A. Wurden, "Flowing magnetized plasma experiment & plans," Innovative Confinement Concepts Workshop (ICC 2004), Madison, Wisconsin, USA, May 25–28, 2004, Los Alamos National Laboratory document LA-UR-04-2580.
- S.C. Hsu, Z. Wang, P.D. Beinke, C.W. Barnes, and G.A. Wurden, "Flowing magnetized plasma experiment: Progress and plans," Innovative Confinement Concepts Workshop (ICC 2004), Madison, Wisconsin, USA, May 25–28, 2004, Los Alamos National Laboratory document LA-UR-04-3585.
- R.M. Hueckstaedt, S.H. Batha, M.M. Balkey, J.R. Fincke, R.L. Holmes, N.E. Lanier, G.R. Magelssen, J.M. Scott, J.M. Taccetti, C.J. Horsfield, K.W. Parker, and S.D. Rothman, "Richtmyer-Meshkov experiments on the Omega laser," 5th International Conference on High Energy Density Laboratory Astrophysics, Tucson, Arizona, USA, March 10–13, 2004, Los Alamos National Laboratory document LA-UR-04-2857.
- R.M. Hueckstaedt, S.H. Batha, N.D. Delamater, J.R. Fincke, R.L. Holmes, J.R. Lanier, G.R. Magelssen, J.M. Scott, J.M. Taccetti, C.J. Horsfield, K.W. Parker, and S.D. Rothman, "Three-dimensional simulations of Richtmyer-Meshkov experiments," 9th International Workshop on the Physics of Compressible Turbulent Mixing (IWPCTM 2004), Cambridge, United Kingdom, July 19–23, 2004, Los Alamos National Laboratory document LA-UR-04-6487.
- R.J. Hughes and J.E. Nordholt, "A quantum information science and technology roadmap - Part 2: quantum cryptography," 2004 Quantum Cryptography Program Review, McLean, Virginia, USA, August 31–September 1, 2004, Los Alamos National Laboratory document LA-UR-04-4805.

Appendix B: Publications

R.J. Hughes, "A quantum information science & technology roadmap - Part 1: quantum computation," 2004 Quantum Computing Program Review, Orlando, Florida, USA, August 16–20, 2004, Los Alamos National Laboratory document LA-UR-04-1778.

T.P. Intrator, "Magnetic reconnection driven by coalescence instability: An example of merging flux tubes in RSX," Invited Seminar at University of Wisconsin-Madison, Madison, Wisconsin, USA, January 2004, Los Alamos National Laboratory document LA-UR-04-0491.

T.P. Intrator, G.A. Wurden, W.J. Waganaar, and S.Y. Zhang, "Magnetized target fusion collaboration and recent progress," 2004 U.S.-Japan Compact Torus Workshop, Santa Fe, New Mexico, USA, September 13–16, 2004, Los Alamos National Laboratory document LA-UR-04-6699.

T.P. Intrator, I.G. Furno, S. Hsu, G. Lapenta, and E.W. Hemsing, "Magnetic reconnection, merging flux ropes, 3D effects in RSX," 2nd Workshop on Thin Current Sheets, College Park, Maryland, USA, April 19–21, 2004, Los Alamos National Laboratory document LA-UR-04-2712.

T.P. Intrator, S.Y. Zhang, L. Dorf, I.G. Furno, J. Degnan, J. C. Grabowski, S.C. Hsu, E.L. Ruden, W.J. Waganaar, and G.A. Wurden, "Magnetized target fusion collaboration and recent progress," 46th Annual Meeting of the American Physical Society Division of Plasma Physics, Savannah, Georgia, USA, November 15–19, 2004, Los Alamos National Laboratory document LA-UR-04-7900.

S.C. Jun, J.S. George, J. Pare-Blagoev, S.M. Plis, D.M. Ranken, D.M. Schmidt, and C.C. Wood, "Spatial-temporal Bayesian inference dipole analysis for MEG," 14th International Conference on Biomagnetism (BIOMAG 2004), Boston, Massachusetts, USA, August 8–12, 2004, Los Alamos National Laboratory document LA-UR-03-8575.

S.C. Jun, J.S. George, J. Pare-Blagoev, S.M. Plis, D.M. Ranken, D.M. Schmidt, and C.C. Wood, "Dipole analysis on spatiotemporal MEG signals using Bayesian inference," 10th Annual Meeting of the Organization for Human Brain Mapping, Budapest, Hungary, June 13–17, 2004, Los Alamos National Laboratory document LA-UR-03-8575.

P.A. Keiter, G.A. Kyralla, R.G. Watt, G.C. Idzorek, R.R. Peterson, and R.E. Chrien, "March 12–17 2003 WPS 1 campaign post shot document," 5th International High Energy Density Laboratory Astrophysics, Tucson, Arizona, USA, March 10–13, 2004, Los Alamos National Laboratory document LA-UR-04-0389.

P.A. Keiter, G.A. Kyralla, R.G. Watt, G.C. Idzorek, R.R. Peterson, and B.P. Wood, "Results from a radiation transfer experiment," 46th Annual Meeting of the American Physical Society Division of Plasma Physics, Savannah, Georgia, USA, November 15–19, 2004, Los Alamos National Laboratory document LA-UR-04-5024.

P.A. Keiter, G.A. Kyralla, R.G. Watt, G.C. Idzorek, R.R. Peterson, R.E. Chrien, M.M. Wood-Schultz, B.P. Wood, L. Peterson, and P.J. Adams, "Preliminary results from an astrophysically relevant radiation transfer experiment," 5th International High Energy Density Laboratory Astrophysics, Tucson, Arizona, USA, March 10–13, 2004, Los Alamos National Laboratory document LA-UR-04-2025.

G.T. Kenyon, N.R. Harvey, G.J. Stephens, and J.P. Theiler, "Dynamic segmentation of gray-scale images in a computer model of the mammalian retina," SPIE Annual Meeting on Optical Science and Technology, Denver, Colorado, USA, August 2–6, 2004, Los Alamos National Laboratory document LA-UR-04-0004.

Y. Kim, J. Park, L.A. Rosocha, H.L. Teslow, and J.L. Lyman, "Measurements of chemically active species in an atmospheric pressure plasma jet used for surface decontamination," 4th International Symposium on Non Thermal Plasma Technology for Pollution Control and Sustainable Energy Development (ISNTPT 4), Panama City Beach, Florida, USA, May 10–14, 2004, Los Alamos National Laboratory document LA-UR-04-1910.

Y. Kim, S.M. Stange, and L.A. Rosocha, "Combustion enhancement of propane by dielectric barrier discharges," 4th International Symposium on Non Thermal Plasma Technology for Pollution Control and Sustainable Energy Development (ISNTPT 4), Panama City Beach, Florida, USA, May 10–14, 2004, Los Alamos National Laboratory document LA-UR-04-1942.

R.M. Kippen, M.W. Rawool-Sullivan, J.P. Sullivan, A.S. Hoover, and W. Baird, "Construction and evaluation of the LANL prototype Compton gamma-ray imager," IEEE Foundations of Computer Science (FOCS 2004), Rome, Italy, October 17–19, 2004, Los Alamos National Laboratory document LA-UR-04-3478.

R.M. Kippen, M.W. Rawool-Sullivan, J.P. Sullivan, A.S. Hoover, W. Baird, and E. Sorensen, "The LANL prototype Compton gamma-ray imager: Design and image reconstruction techniques," IEEE Nuclear Science Symposium, Rome, Italy, October 16–22, 2004, Los Alamos National Laboratory document LA-UR-04-7208.

S. Kleinfelder K. Kwiatkowski, and A. Shah, "A solid state streak camera," 26th International Congress on High-Speed Photography and Photonics, Alexandria, Virginia, USA, September 19–24, 2004.

J.L. Kline and D.S. Montgomery, "Fluid and kinetic nonlinearities for Langmuir waves driven by stimulated Raman scattering in a single laser hot spot," 28th European Conference on Laser Interaction with Matter, Rome, Italy, September 6–10, 2004, Los Alamos National Laboratory document LA-UR-04-4256.

J.L. Kline, B. Afeyan, N.A. Kurnit, D.S. Montgomery, K. Won, W.A. Bertsche, and V. Savchenko, "Experimental confirmation of the persistence of ponderomotively driven kinetic electrostatic electron nonlinear (KEEN) waves in laser produced plasmas,"

46th Annual Meeting of the American Physical Society Division of Plasma Physics, Savannah, Georgia, USA, November 15–19, 2004, Los Alamos National Laboratory document LA-UR-04-5070.

J.L. Kline, B. Afeyan, N.A. Kurnit, D.S. Montgomery, K. Won, W.A. Bertsche, and V. Savchenko, “Development of an experimental design to detect kinetic electron nonlinear waves,” 46th Annual Meeting of the American Physical Society Division of Plasma Physics, Savannah, Georgia, USA, November 15–19, 2004, Los Alamos National Laboratory document LA-UR-04-5023.

J.L. Kline, D.S. Montgomery, B. Bezzerides, J.A. Cobble, D.F. Dubois, R.P. Johnson, H.A. Rose, and H. Vu, “Observation of a transition from fluid to kinetic nonlinearities for Langmuir waves driven by stimulated Raman scattering,” 2004 Annual Spring Meeting of the American Physical Society, Denver, Colorado, USA, May 1–4, 2004, Los Alamos National Laboratory document LA-UR-04-0334.

K. Kwiatkowski, “Ultra-fast multi-frame mega-pixel imager for proton radiography,” Large Synoptic Survey Telescope (LSST) Focal Plane Array Workshop, Brookhaven National Laboratory, New York, USA, February 4–5, 2004, Los Alamos National Laboratory document LA-UR-04-0874.

K. Kwiatkowski, R. Fillon, J. Lyke, J.R.J. Wojnarowski, C. Kapusta, V. Douance, and P.O. Pettersson, “3-D interconnect for fast mega-pixel imager for proton radiography,” 5th International Symposium on Development and Application of Semiconductor Tracking Detectors, Hiroshima, Japan, June 14–17, 2004, Los Alamos National Laboratory document LA-UR-04-3929.

G.A. Kyrala, K.A. Klare, N.D. Delamater, D.C. Wilson, J.A. Guzik, D. Haynes, M. Gunderson, K. Klare, R.W. Watt, W.M. Wood, and W. Varnum, “Direct drive double shell target implosion hydrodynamics on Omega,” 28th European Conference on Laser Interaction with Matter, Rome, Italy, September 6–10, 2004, Los Alamos National Laboratory document LA-UR-04-3788.

G.A. Kyrala, S.H. Batha, J.B. Workman, J.R. Fincke, P.A. Keiter, C.R. Christensen, N.E. Lanier, J.A. Cobble, and T.E. Tierney, “High speed x-ray imaging in high power laser experiments,” 26th International Congress on High Speed Photography & Photonics, Alexandria, Virginia, USA, September 19–24, 2004, Los Alamos National Laboratory document LA-UR-04-4391.

S.K. Lamoreaux, “Neutron electric dipole moment,” An invited talk given at the Fermilab Precision Weak Interaction Workshop, May 2004, Los Alamos National Laboratory document LA-UR-04-3295.

S.K. Lamoreaux, “The Casimir force,” Colloquium at the University of Nebraska, April 2004, Los Alamos National Laboratory document LA-UR-04-4458

S.K. Lamoreaux, “The neutron and electron electric dipole moments,” Colloquium at the University of Kentucky, April 2004, Los Alamos National Laboratory document LA-UR-04-3295.

S.K. Lamoreaux, “Washing up with hot and cold running neutrons: Tests of fundamental physical laws,” International Conference on Nuclear Data for Science, Santa Fe, New Mexico, USA, September 26–October 1, 2004, Los Alamos National Laboratory document LA-UR-04-6467.

D.M. Lee, “A proposed silicon vertex tracker for the PHENIX detector at forward rapidity,” IEEE Nuclear Science Symposium, Rome, Italy, October 16–22, 2004, Los Alamos National Laboratory document LA-UR-04-3410.

M.J. Leitch, “ J/ψ production and nuclear effects for d +Au and p + p collisions in PHENIX at RHIC,” Lake Louise Winter Institute 2004, Lake Louise, Alberta, Canada, February 15–21, 2004, Los Alamos National Laboratory document LA-UR-04-2856.

M.J. Leitch, “Overview of charm production: J/ψ ’s and open charm,” Quark Confinement and the Hadron Spectrum VI, Villasimius, Italy, September 21–25, 2004, Los Alamos National Laboratory document LA-UR-04-8521.

M.J. Leitch, “Quarkonia production in p -A collisions,” International Conference on Hard and Electromagnetic Probes of High Energy Nuclear Collisions (Hard Probes 2004), Ericeira, Portugal, November 4–10, 2004, Los Alamos National Laboratory document LA-UR-04-7686.

J.J. Lidgard, “R&D efforts in support of the clean detector for dark matter and solar neutrino interactions,” 2004 Fall Meeting of the APS Division of Nuclear Physics, Chicago, Illinois, USA, October 27–30, 2004, Los Alamos National Laboratory document LA-UR-04-5249.

M.X. Liu, “Charm production at PHENIX,” Meeting of the Division of Particle and Fields of the American Physical Society, Riverside, California, USA, August 27–31, 2004, Los Alamos National Laboratory document LA-UR-04-5931.

M.X. Liu, “Charm production at RHIC,” 39th Rencontres De Moriond on Electroweak Interactions and Unified Theories, La Thuile, Aosta Valley, Italy, March 21–28, 2004, Los Alamos National Laboratory document LA-UR-04-4287.

M.X. Liu, “Muon production in the forward and backward rapidities in d -Au collisions at RHIC,” 17th International Conference on Ultra-Relativistic Nucleus-Nucleus Collisions (Quark Matter 2004), Oakland, California, USA, January 11–17, 2004, Los Alamos National Laboratory document LA-UR-04-1935.

M.X. Liu, “Open charm production in p - p and d -Au collisions measured by the PHENIX experiment,” 2004 Fall Meeting of the APS Division of Nuclear Physics, Chicago, Illinois, USA, October, 27–30, 2004, Los Alamos National Laboratory document LA-UR-04-7534.

W.C. Louis, “FINeSSE: An experiment to make precision measurements of neutrino-nucleon cross sections,” 21st International Conference on Neutrino Physics and Astrophysics (Neutrino 2004), Collège de France, Paris, June 14–19, 2004, Los Alamos National Laboratory document LA-UR-04-3702.

Appendix B: Publications

S.-N. Luo, T.E. Tierney, D.C. Swift, D.L. Paisley, G.A. Kyrala, R.P. Johnson, A. Hauer, O. Tschauner, and P.D. Asimow, "Laser-induced shock waves in condensed matter: Some techniques and applications," International Union of Crystallography – High Pressure Commission Workshop: Crystallography at High Pressure, Saskatoon, Canada, August 18–21, 2004, Los Alamos National Laboratory document LA-UR-04-5642.

S.-N. Luo, and D.C. Swift, "Equilibrium and dynamic melting: Implications for shock melting of beryllium," 46th Annual Meeting of the American Physical Society Division of Plasma Physics, Savannah, Georgia, USA, November 15–19, 2004, Los Alamos National Laboratory document LA-UR-04-7814.

S.-N. Luo, D.C. Swift, R. Mulford, A. Strachan, H. Huang, N.D. Drummond, G.J. Ackland, and W. Goddard, "MGO: *Ab initio* equation of state and its dislocation properties from molecular dynamics simulations," 2004 American Geophysical Union Fall Meeting, San Francisco, California, USA, December 13–17, 2004, Los Alamos National Laboratory document LA-UR-04-6363.

S.-N. Luo, T.E. Tierney, D.C. Swift, D.L. Paisley, G.A. Kyrala, R.P. Johnson, A. Hauer, O. Tschauner, and P.D. Asimow, "Laser-induced shock waves in condensed matter and their geophysical applications," 2004 American Geophysical Union Fall Meeting, San Francisco, California, USA, December 13–17, 2004, Los Alamos National Laboratory document LA-UR-04-6544.

S.-N. Luo, T.E. Tierney, D.C. Swift, O. Tschauner, and P.D. Asimow, "Possible novel carbon structures synthesized by laser-induced shock waves," 46th Annual Meeting of the American Physical Society Division of Plasma Physics, Savannah, Georgia, USA, November 15–19, 2004, Los Alamos National Laboratory document LA-UR-04-7852

J.M. Mack, R.R. Berggren, S.E. Caldwell, C.E. Christensen, S.C. Evans, J.R. Faulkner Jr., R. Griffith, G.M. Hale, R.S. King, D.K. Lash, R.A. Lerche, J. Oertel, D.M. Pacheco, and C.S. Young, "Observation of high-energy deuterium-tritium fusion gamma rays using gas Cherenkov detectors," International Conference P.A. Cherenkov and Modern Physics, Moscow, Russia, June 22–25, 2004, Los Alamos National Laboratory document LA-UR-04-4064.

G.R. Magelssen, J.B. Workman, W.M. Wood, S.E. Caldwell, R.E. Chrien, D.J. Hoarty, C.C. Smith, E.L. Clark, J.M. Foster, S.G. Gales, J. Sandoval, T.J. Sedillo, P. Walsh, B. Carpenter, S. Compton, and T. Perry, "Fluorescence spectroscopy as a diagnostic of the radiation environment in HED experiments," 15th High-Temperature Plasma Diagnostics Conference, San Diego, California, USA, April 19–22, 2004, Los Alamos National Laboratory document LA-UR-04-2562.

G.R. Magelssen, J.R. Fincke, J.R. Lanier, S.H. Batha, N.D. Delamater, R.M. Hueckstaedt, J.M. Taccetti, K.W. Parker, C.J. Horsfield, and S.D. Rothman, "Double shell and single shell defect experiments on Omega," Meeting of the Joint Working Group (U.S.-UK) (JOWOG-32Mix), Aldermaston, Berkshire, UK, May 17–21, 2004, Los Alamos National Laboratory document LA-UR-04-3107.

G.R. Magelssen, J.R. Fincke, N.E. Lanier, S.H. Batha, N.D. Delamater, R.M. Hueckstaedt, J.M. Taccetti, K.W. Parker, C.J. Horsfield, and S.D. Rothman, "Double-shell defect experiments on Omega," 46th Annual Meeting of the American Physical Society Division of Plasma Physics, Savannah, Georgia, USA, November 15–19, 2004, Los Alamos National Laboratory document LA-UR-04-4858.

G.R. Magelssen, J.R. Fincke, N.E. Lanier, S.H. Batha, N.D. Delamater, R.M. Hueckstaedt, J.M. Taccetti, K.W. Parker, C.J. Horsfield, and S.D. Rothman, "Rayleigh-Taylor instability experiments in cylindrical geometry at Omega," 57th Annual Meeting of the Division of Fluid Dynamics, American Physical Society (APS DFD '04), Seattle, Washington, USA, November 21–23, 2004, Los Alamos National Laboratory document LA-UR-04-4859.

H.E. Makaruk, R.M. Owczarek, and N.A. Sakhanenko, "Vector space of path and completeness of white-box software testing," American Mathematical Society Western Sectional Meeting #1000, Albuquerque, New Mexico, USA, October 16–17, 2004, Los Alamos National Laboratory document LA-UR-04-5732.

C.W. McCluskey, M.D. Wilke, W.D. Turley, G.D. Stevens, L.R. Veaser, M. Grover, and A. Adams, "Infrared images of shock-heated tin," 26th International Congress on High Speed Photography and Photonics, Alexandria, Virginia, USA, September 20–24, 2004, Los Alamos National Laboratory document LA-UR-04-6635.

G.A. McGregor, "Status and data/MC comparisons from the MiniBooNE experiment," 2004 Annual Spring Meeting of the American Physical Society, Denver, Colorado, USA, May 1–4, 2004, Los Alamos National Laboratory document LA-UR-04-2611.

D.-M. Mei, "Muon-induced background studies for underground laboratories," 2004 American Physical Society Spring Meeting, Denver, Colorado, USA, May 1–4, 2004, Los Alamos National Laboratory document LA-UR-04-2182.

D.-M. Mei, "Neutron background evaluation at the WIPP site for dark matter experiments," 2004 Fall Meeting of the APS Division of Nuclear Physics, Chicago, Illinois, USA, October 27–30, 2004, Los Alamos National Laboratory document LA-UR-04-6580.

G.S. Mitchell, "A new flight path at LANSCE for the NPDGamma experiment," 2004 American Physical Society Spring Meeting, Denver, Colorado, USA, May 1–4, 2004, Los Alamos National Laboratory document LA-UR-04-2891.

D.S. Montgomery, "Detailed characterization of plasma wave behavior using collective Thomson scattering," 15th Topical Conference on High-Temperature Plasma Diagnostics, San Diego, California, USA, April 19–22, 2004, Los Alamos National Laboratory document LA-UR-04-0230.

D.S. Montgomery, "Utilization of x-ray phase contrast imaging in ICF and HEDP experiments," 46th Annual Meeting of the American Physical Society Division of Plasma Physics, Savannah,

Georgia, USA, November 15–19, 2004, Los Alamos National Laboratory document LA-UR-04-5038.

D.S. Montgomery, A. Nobile, and P.J. Walsh, “Characterization of NIF cryogenic beryllium capsules using x-ray phase contrast imaging,” 15th Topical Conference on High-Temperature Plasma Diagnostics, San Diego, California, USA, April 19–22, 2004, Los Alamos National Laboratory document LA-UR-0392.

D.S. Montgomery and J.L. Kline, “Observation of fluid and kinetic nonlinearities for Langmuir waves driven by stimulated Raman scattering,” 31st European Physical Society Conference on Plasma Physics, London, UK, June 28–July 2, 2004, Los Alamos National Laboratory document LA-UR-04-4310.

J.C. Mosher, “A review on the importance of volume currents,” BIOMAG 2004 Conference, Boston, Massachusetts, USA, August 8–12, 2004, Los Alamos National Laboratory document LA-UR-04-5246.

M.M. Nieto, A.C. Hayes, W.B. Wilson, C.M. Teeter, and W.D. Stanbro, “Antineutrino detection for non-proliferation,” 2004 Fall Meeting of the Division of Nuclear Physics of the American Physical Society, Chicago, Illinois, USA, October 27–30, 2004, Los Alamos National Laboratory document LA-UR-04-4469.

A. Nobile, M.M. Balkey, J.J. Bartos, S.H. Batha, P.M. Brooks, B.J. Cameron, J.A. Cobble, R.D. Day, J.M. Edwards, J. Elliott, N.E. Elliott, J.R. Fincke, V.M. Gomez, D.J. Hatch, P.A. Keiter, G.J. Kyrila, N.E. Lanier, R. Manzanarez, R. Perea, T.H. Pierce, R.B. Randolph, D.L. Sandoval, R.J. Sebring, G. Rivera, and D.W. Schmidt, “Recent developments in high energy density physics targets for experiments at NIF, Omega and the Sandia Z-pinch facility,” 46th Annual Meeting of the American Physical Society Division of Plasma Physics, Savannah, Georgia, USA, November 15–19, 2004, Los Alamos National Laboratory document LA-UR-04-5257.

B.E. Norman, “Reaction plane determination at intermediate rapidity in $\sqrt{s_{NN}} = 200$ GeV Au - Au collisions in PHENIX at RHIC-BNL,” 2004 Fall Meeting of the APS Division of Nuclear Physics, Chicago, Illinois, USA, October, 27–30, 2004, Los Alamos National Laboratory document LA-UR-04-7547.

A.W. Obst, “Surface finish dependence of temperature measurements on shocked tin,” Meeting of the Joint Working Group (U.S.-UK) (JOWOG-32Mix), Aldermaston, England, May 17–21, 2004, Los Alamos National Laboratory document LA-UR-04-3282.

F.G. Omenetto, “Nonlinear optics and photonic crystals for ultrafast optical processing,” 17th Annual Meeting of the IEEE Lasers and Electro-Optics Society (LEOS), Rio Mar Beach, Puerto Rico, November 7–11, 2004, Los Alamos National Laboratory document LA-UR-04-5215.

F.G. Omenetto, A. Effimov, and A.J. Taylor, “Ultrafast pulse shape driven dynamics in optical waveguides,” Photonics West 2004, San Jose, California, USA, January 24–29, 2004, Los Alamos National Laboratory document LA-UR-04-0060.

H. Oona, J.H. Goforth, G.C. Idzorek, D.H. Herrera, J.C. King, E.A. Lopez, D.G. Tasker, and D.T. Torres, “Explosive pulsed power for new radiation sources,” 10th International Conference on Megagauss Magnetic Field Generation and Related Topics (MG X), Berlin, Germany, July 18–23, 2004, Los Alamos National Laboratory document LA-UR-04-4816.

D.L. Paisley, D.C. Swift, T.E. Tierney, and C.P. Munson, “Diagnostics for confined plasma ablation for plate launch and shock generation,” 26th International Congress on High Speed Photography and Photonics, Alexandria, Virginia, USA, September 20–24, 2004, Los Alamos National Laboratory document LA-UR-04-6845.

D.L. Paisley, D.C. Swift, T.E. Tierney, S.-N. Luo, C. Munson, and R.P. Johnson, “Confined plasma, tamped ablation for acceleration of thin (2 μm –2 mm) solid, 1D metal plates for dynamic material response experiments,” 46th Annual Meeting of the American Physical Society Division of Plasma Physics, Savannah, Georgia, USA, November 14–19, 2004, Los Alamos National Laboratory document LA-UR-04-5014.

S.I. Penttila and J.D. Bowman, “Precision neutron polarimetry for neutron beta decay,” International Conference on Precision Measurements with Slow Neutrons, Gaithersburg, Maryland, USA, April 5–7, 2004, Los Alamos National Laboratory document LA-UR-04-4201.

R.R. Peterson, R.E. Chrien, D.L. Peterson, and R.G. Watt, “Trans-sonic radiation transport in foams as a radiation power diagnostic on Z,” 46th Annual Meeting of the American Physical Society Division of Plasma Physics, Savannah, Georgia, USA, November 15–19, 2004, Los Alamos National Laboratory document LA-UR-4943.

S.M. Plis, J.S. George, S.C. Jun, J. Pare-Blagoev, D.M. Schmidt, C.C. Wood, and D.M. Ranken, “Spatiotemporal noise covariance model for MEG/EEG data source analysis,” BIOMAG 2004 Conference, Boston, Massachusetts, USA, August 8–12, 2004, Los Alamos National Laboratory document LA-UR-04-3643.

R. Porter, A. Nugent, and G. Kenyon, “Unsupervised adaptation to improve fault tolerance of neural classifiers,” 2004 NAS/DOD Conference on Evolvable Hardware, Seattle, Washington, USA, June 24–26, 2004, Los Alamos National Laboratory document LA-UR-04-1028.

D.E. Post, “Lessons learned from ASCI: The challenges of large software projects,” DOE SC-NE International Workshop on Advanced Computational Materials Science: Application to Fusion and Generation-IV Fission Reactors, Washington, DC, March 30–April 2, 2004, revision of Los Alamos National Laboratory documents LA-UR-04-0388 and LA-UR-03-1274.

D.E. Post, “Perspectives on validation and simulation,” DOE SC-NE International Workshop on Advanced Computational Materials Science: Application to Fusion and Generation-IV Fission Reactors, Washington, DC, March 30–April 2, 2004, revision of Los Alamos National Laboratory documents LA-UR-04-0388 and LA-UR-03-1274.

Appendix B: Publications

D.E. Post, "Software engineering lessons learned," 9th Annual Community Climate System Model (CCSM) Workshop, Software Engineering Group, Santa Fe, New Mexico, July 7–9, 2004, Los Alamos National Laboratory document LA-UR-04-4151

D.E. Post, "Software engineering lessons learned," Fall Creek Falls Conference, Fall Creek Falls, Tennessee, USA, October 17–19, 2004, revision of Los Alamos National Laboratory document LA-UR-04-5015 and LA-UR-04-8184.

D.E. Post, "The challenges facing computational science," IEEE/ACM/BCS International Conference on Software Engineering, Edinburgh, UK, May 24–28, 2004, Los Alamos National Laboratory document LA-UR-04-2270.

D.E. Post, "The coming crisis in computational science," IEEE/ACM International Conference on High Performance Computing Architectures, Madrid, Spain, February 14–18, 2004, Los Alamos National Laboratory document LA-UR-04-0388

D.E. Post, D.B. Henderson, R.P. Kendall, and E.M. Whitney, "Software engineering for scientific computer simulations," 46th Annual Meeting of the American Physical Society Division of Plasma Physics, Savannah, Georgia, USA, November 15–19, 2004, Los Alamos National Laboratory document LA-UR-04-8184.

D.E. Post, J. Carver., S. Chulani., K. Ebcioğlu, S. Faulk, A. Fun, H. Gordon, D. Henderson, R. Kendall, J. Kepner, R. Lucas, W. Mann, A. Mark, T. Meuse, D. Mizell, D. Shaffer, D. Shires, S. Squires, T. Trucano, M. van de Vanter, J. Vetter, L. Votta, T. White, E.M. Whitney, and C. Williams, "Case studies of existing scientific simulations," IEEE Conference on Super Computing 2004, Pittsburgh, Pennsylvania, November 8–12, 2004, Los Alamos National Laboratory document LA-UR-04-8183.

H. Ray, "Current MiniBooNE status," Meeting of the Division of Particle and Fields of the American Physical Society, Riverside, California, USA, August 27–31, 2004, Los Alamos National Laboratory document LA-UR-04-4984.

H. Ray, "Implications of confirmation of the LSND muon antineutrino to electron antineutrino oscillation signal," 6th International Workshop on Neutrino Factories and Superbeams (NUFACT 04), Osaka, Japan, July 26–August 1, 2004, Los Alamos National Laboratory document LA-UR-04-4980.

H. Ray, "MiniBooNE status: Neutral current pion analysis," 2004 Fall Meeting of the APS Division of Nuclear Physics, Chicago, Illinois, USA, October, 27–30, 2004, Los Alamos National Laboratory document LA-UR-04-7407.

R.E. Reinovsky and W.L. Atchison, "Combining VNIIEF and LANL technology to explore new and challenging physics," Briefing to RF Subpanel WSSIC Committee, Washington, DC, USA, July 9, 2004, Los Alamos National Laboratory document LA-UR-04-5044.

R.E. Reinovsky, "Pulsed power hydrodynamics: Applying pulsed power and high magnetic fields to produce extreme conditions," 2004 Power Modulator Conference, San Francisco, California, USA, May 23–26, 2004, Los Alamos National Laboratory document LA-UR-04-2595.

R.E. Reinovsky, "VNIIEF/LANL collaboration in pulsed power hydrodynamics (overview and prospective)," LANL/VNIIEF Program Review, Sarov, Russia, November 1–4, 2004, Los Alamos National Laboratory document LA-UR-04-7622.

L.A. Rosocha, "Atmospheric-pressure, non-thermal plasma processing: Basic theory and applications," New Mexico State University Chemical Engineering Department Seminar, Las Cruces, New Mexico, USA, October 2004, Los Alamos National Laboratory document LA-UR-04-6891.

L.A. Rosocha, Y. Kim, and S.M. Stange, "Application of a non-thermal plasma to combustion enhancement," 6th Joint IEJ-ESA Electrostatics Symposium: International Symposium on Electrostatics and Atmospheric Pressure Plasma Applications, Tokyo, Japan, November 7–10, 2004, Los Alamos National Laboratory document LA-UR-04-6890.

S.J. Russell, B.E. Carlsten, L.M. Earley, R.W. Brown, R. Carlson, M. Fazio, M.G. Garcia, C.E. Heath, H.C. Kirbie, F.L. Krawczyk, F.E. Sigler, E.I. Smirnova, R.M. Wheat, J.G. Wohlbiel, and P. Ferguson, "Development of sheet beam electron source for traveling wave tube experiment at Los Alamos National Laboratory," 22nd International Linear Accelerator Conference, Lubeck, Germany, August 16–20, 2004, Los Alamos National Laboratory document LA-UR-04-2245.

N. Sakhanenko, H. Makaruk, and R. Owczarek, "Grapha applied in theory of white-box software testing," American Mathematical Society Sectional Meeting #1000, Albuquerque, New Mexico, USA, October 16–17, 2004, Los Alamos National Laboratory document LA-UR-04-5237.

R.C. Schirato, "Development of cosmic ray muon radiography for the detection of high-Z objects," 9th Topical Seminar on Innovative Particle and Radiation Detectors (IPRD04), Siena, Italy, May 23–26, 2004, Los Alamos National Laboratory document LA-UR-04-3508.

D.M. Schmidt, "Bayesian approaches to the MEG/EEG inverse problem," BIOMAG 2004 Conference, Boston, Massachusetts, USA, August 8–12, 2004, Los Alamos National Laboratory document LA-UR-04-5245.

J. Schreiber, M. Kaluza, F. Gruner, U. Schramm, B.M. Hegelich, J.A. Cobble, M. Geissler, E. Brambrink, J. Fuchs, P. Audebert, D. Habs, and K. Witte, "Source-size measurements and charge distributions of ions accelerated from thin foils irradiated by high-intensity laser pulses," Spring Meeting of the Quantum Optics and Photonics Section of the German Physical Society, Munich, Germany, March 22–26, 2004.

L.J. Schultz and N.W. Hengartner, "Tomographic reconstruction for cosmic ray muon radiography," IEEE Nuclear Science Symposium, Rome, Italy, October 16–22, 2004, Los Alamos National Laboratory document LA-UR-04-7219.

L.J. Schultz, C.L. Morris, G.E. Hogan, N.W. Hengartner, K.N. Borozdin, T.J. Asaki, R. Chartrand, W. Friedhorshy, R. Schirato, M. Sottile, K. Vixie, B. Wohlberg, and G. Blanpied,

- "Cosmic ray muon radiography for the detection of contraband SNM," Workshop on Active Interrogation for the Detection of Weapons of Mass Destruction, Idaho Falls, Idaho, USA, June 29–30, 2004, Los Alamos National Laboratory document LA-UR-04-4335.
- C. Schwartz, "Proton radiography of (U6Nb) uranium-6 coupon fragmentation," Meeting of the Joint Working Group (U.S.-UK) (JOWOG 32P VISAM 2115), Aldermaston, Berkshire, UK, July 2004, Los Alamos National Laboratory document LA-UR-04-4917.
- A. Seifter, "High speed temperature measurements of shock-loaded molybdenum," Invited talk at the Institute of Experimental Physics at the University of Technology, Graz, Austria, July 2, 2004, Los Alamos National Laboratory document LA-UR-04-2561.
- A. Seifter, D.B. Holtkamp, J. Payton, P. Rodriguez, A.W. Obst, "Low-temperature measurements on shock-loaded tin," SPIE 26th International Congress on High Speed Photography and Photonics, Alexandria, Virginia, USA, September 19–24, 2004, Los Alamos National Laboratory document LA-UR-04-6515.
- A. Seifter, K. Boboridis, D.A. Clark, R.B. Corrow, D.B. Holtkamp, C.W. McCluskey, G.L. Morgan, J. Payton, P. Quintana, C.E. Ragan, P. Rodriguez, H.L. Stacy, W.S. Vogan, V.W. Yuan, and A.W. Obst, "High speed temperature measurements of shock-loaded molybdenum," 9th International Symposium on Temp and Thermal Measurements in Industry and Science 2004, Dubrovnik, Croatia, June 22–25, 2004, Los Alamos National Laboratory document LA-UR-04-2561.
- A. Seifter, K. Boboridis, J.R. Payton, and A.W. Obst, "A high-speed, four-wavelength infrared pyrometer for low-temperature shock physics experiments," SPIE 26th International Congress on High Speed Photography and Photonics, Alexandria, Virginia, USA, September 19–24, 2004, Los Alamos National Laboratory document LA-UR-04-6087.
- P.-N. Seo, J.D. Bowman, G.S. Mitchell, S.I. Penttila, and W.S. Wilburn, "Detector development for the ABba experiment," International Conference on Precision Measurements with Slow Neutrons, Gaithersburg, Maryland, USA, April 5–7, 2004, Los Alamos National Laboratory document LA-UR-04-3782.
- P.-N. Seo, J.D. Bowman, M.T. Gericke, G.S. Mitchell, and S.I. Penttila, "A pulsed cold neutron beamline: Flight Path 12 at LANSCE for fundamental nuclear physics," International Conference on Precision Measurements with Slow Neutrons, Gaithersburg, Maryland, USA, April 5–7, 2004, Los Alamos National Laboratory document LA-UR-04-2189.
- P.-N. Seo, J.D. Bowman, M.T. Gericke, R.C. Gillis, G.S. Mitchell, G.L. Greene, M.B. Leuschner, J. Long, R. Mahurin, and S.I. Penttila, "New pulsed cold neutron beam line for fundamental nuclear physics at LANSCE," International Conference on Precision Measurements with Slow Neutrons, Gaithersburg, Maryland, USA, April 5–7, 2004, Los Alamos National Laboratory document LA-UR-04-3783.
- P.T. Sheehey, J. Binstock, G.J. Garduno, M. Haertling, D.M. Oro, J.M. Scott, M.D. Ulibarri, "Hydrotest 3598 (LANL Weapons Working Group #509)," Inter-Laboratory Technical Review Meeting 2004, Albuquerque, New Mexico, USA, April 2004, Los Alamos National Laboratory controlled publication LA-CP-04-0356.
- R.L. Sheffield, K.F. Schoenberg, D.E. Post, and B.R. Stults, "An initial fusion materials testing facility," 46th Annual Meeting of the American Physical Society Division of Plasma Physics, Savannah, Georgia, USA, November 15–19, 2004, Los Alamos National Laboratory document LA-UR-04-5039.
- C. Sinnis, "HAWC: A future TeV gamma-ray telescope," China Centre of Advanced Science and Technology (CCAST) Particle Astrophysics Conference, Beijing, China, April 2004, Los Alamos National Laboratory document LA-UR-04-1071.
- W.M. Snow, J.D. Bowman, T.V. Cianciolo, M. Cooper, J. Doyle, C.R. Gould, G.L. Greene, and P.R. Huffman, "Fundamental physics with slow neutrons," International Conference on Nuclear Data for Science & Technology (ND 2004), Santa Fe, New Mexico, USA, September 26–October 1, 2004.
- D.S. Sorenson, R.A. Gore, and M. Furnish, "Ejecta mass distributions from the Thoroughbred subcritical experiment," Meeting of the Joint Working Group (U.S.-UK) (JOWOG-32Mix), Aldermaston, Berkshire, UK, May 17–21, 2004, Los Alamos National Laboratory controlled publication LA-CP-04-0364.
- D.C. Swift, "Quasi-isentropic compression by ablative laser loading, and on beryllium at Z," Isentropic Compression Workshop, Livermore, California, USA, December 7–9, 2004, Los Alamos National Laboratory document LA-UR-04-8926.
- D.C. Swift, T.E. Tierney, D.L. Paisley, G.A. Kyrala, S. Luo, A. Hauer, S.R. Greenfield, A.C. Koskelo, K.J. McClellan, H.E. Lorenzana, M.D. Knudson, and P.P. Peralta, "Dynamic response of materials on sub-nanosecond time scales, and beryllium properties for ICF," 46th Annual Meeting of the American Physical Society Division of Plasma Physics, Savannah, Georgia, USA, November 15–19, 2004, Los Alamos National Laboratory document LA-UR-04-7760.
- J.M. Taccetti, S.H. Batha, J.R. Fincke, N.D. Delamater, N.E. Lanier, G.R. Magelssen, R.M. Hueckstaedt, S.D. Rothman, C.J. Horsfield, and K.W. Parker, "Richtmyer-Meshkov instability reshock experiments using laser-driven double-cylinder implosions," 34th Anomalous Absorption Meeting, Gleneden Beach, Oregon, USA, May 2–7, 2004, Los Alamos National Laboratory document LA-UR-04-3050.
- J.M. Taccetti, S.H. Batha, J.R. Fincke, N.D. Delamater, N.E. Lanier, G.R. Magelssen, R.M. Hueckstaedt, S.D. Rothman, C.J. Horsfield, and K.W. Parker, "Richtmyer-Meshkov instability reshock experiments using laser-driven double-cylinder implosions," 5th International Conference on High Energy Density Laboratory Astrophysics, Tucson, Arizona, USA, March 10–13, 2004, Los

Appendix B: Publications

Alamos National Laboratory document LA-UR-04-1509.

D.G. Tasker, H. Oona, J.H. Goforth, J.C. King, D.T. Torres, D.H. Herrera, P.A. Rigg, D. Dennis-Koller, F.C. Sena, F.G. Abeyta, and L.J. Tabaka, “HEPP-ICE review: Experiment, data analysis, and technique evaluation,” International Conference on Plasma Science (2004 ICOPS), Baltimore, Maryland, USA, June 27–July 1, 2004, Los Alamos National Laboratory document LA-UR-04-3779.

D.G. Tasker, J.H. Goforth, H. Oona, P.A. Rigg, D. Dennis-Koller, J.C. King, D.T. Torres, D.H. Herrera, F.C. Sena, F.G. Abeyta, and L.J. Tabaka, “Results of explosively-driven isentropic compression experiments (HEPP-ICE),” International Conference on Plasma Science (2004 ICOPS), Baltimore, Maryland, USA, June 27–July 1, 2004, Los Alamos National Laboratory document LA-UR-04-4281.

H.L. Teslow, L.A. Rosocha, and Y. Kim, “Modeling of an atmospheric-pressure He/Cf₄/O₂ plasma used for surface decontamination,” 4th International Symposium on Non Thermal Plasma Technology for Pollution Control and Sustainable Energy Development (ISNTPT 4), Panama City, Florida, USA, May 10–14, 2004, Los Alamos National Laboratory document LA-UR-04-1405.

J.P. Theiler, N.R. Harvey, M.C. Flynn, G.T. Kenyon, N.A. David, S.P. Brumby, S.J. Perkins, and J. Irvine, “New approaches to target detection and new methods for scoring performance,” ATR S&T Transition Symposium, Dayton, Ohio, USA, June 2004, Los Alamos National Laboratory document LA-UR-04-4237.

J.C. Thome, J.D. Keener, Z. Wang, and G.A. Wurden, “Ion flow temperature study for the FMP experiment,” 46th Annual Meeting of the American Physical Society Division of Plasma Physics, Savannah, Georgia, USA, November 15–19, 2004, Los Alamos National Laboratory document LA-UR-04-5016.

R. Trainham, R.R. Bartsch, A.P. Tipton, and H.A. Bender, “A negative ion source for spectrometer calibration,” International Conference on Plasma Science (2004 ICOPS), Baltimore, Maryland, USA, June 27–July 1, 2004, Los Alamos National Laboratory document LA-UR-04-0647.

I. Vitev and J. Qiu, “Coherent multiple scattering and dihadron correlations in heavy ion collisions,” 32nd International Conference on High Energy Physics (ICHEP 2004), Beijing, China, August 16–22, 2004, Los Alamos National Laboratory document LA-UR-04-7408.

I. Vitev, “Jets in nuclear collisions,” 34th International Symposium on Multiparticle Dynamics (ISMD 2004), Sonoma County, California, USA, July 26–August 1, 2004, Los Alamos National Laboratory document LA-UR-04-4945.

I. Vitev, “Probing the phases of QCD in ultra-relativistic nuclear collisions,” Meeting of the Division of Particle and Fields of the American Physical Society, Riverside, California, USA, August 27–31, 2004, Los Alamos National Laboratory document LA-UR-04-4983.

I. Vitev, “The perturbative QCD factorized approach in high energy nuclear collisions,” Workshop for Young Scientists on the Physics of Ultrarelativistic Nucleus-Nucleus Collisions (Hot Quarks 2004), Taos, New Mexico, USA, July 18–24, 2004, Los Alamos National Laboratory document LA-UR-04-4944.

P.L. Volegov, A.N. Matlachov, M.A. Espy, J.S. George, and R.H. Kraus, Jr., “Simultaneous magnetoencephalography and SQUID detected nuclear magnetic resonance in microtesla magnetic fields,” 45th Experimental Nuclear Magnetic Resonance Conference, Pacific Grove, California, USA, April 18–23, 2004, Los Alamos National Laboratory document LA-UR-04-2624.

Z. Wang and G.A. Wurden, “Hypervelocity dust beam injection for NSTX,” 15th Topical Conference on High-Temperature Plasma Diagnostics, San Diego, California, USA, April 19–22, 2004, Los Alamos National Laboratory document LA-UR-04-0335.

Z. Wang, S.C. Hsu, C.W. Barnes, D.C. Barnes, and G.A. Wurden, “Diamagnetism and paramagnetism in the flowing magnetized plasma (FMP) experiment,” 46th Annual Meeting of the American Physical Society Division of Plasma Physics, Savannah, Georgia, USA, November 15–19, 2004, Los Alamos National Laboratory document LA-UR-04-5017.

Z. Wang, S.C. Hsu, C.W. Barnes, G.A. Wurden, and D.C. Barnes, “Study of diamagnetism in the Los Alamos flowing magnetized plasma experiment,” Innovative Confinement Concepts Workshop (ICC 2004), Madison, Wisconsin, USA, May 25–28, 2004, Los Alamos National Laboratory document LA-UR-04-2579.

W.S. Wilburn, J.D. Bowman, G.S. Mitchell, J.M. O’Donnell, and P.-N. Seo, “Measurement of neutron decay parameters: The ABba experiment,” International Conference on Precision Measurements with Slow Neutrons, Gaithersburg, Maryland, USA, April 5–7, 2004, Los Alamos National Laboratory document LA-UR-04-3900.

W.S. Wilburn, J.D. Bowman, G.S. Mitchell, J.M. O’Donnell, and P.-N. Seo, “Measurement of neutron decay parameters: The ABba experiment,” Nuclear Physics Seminar: Indiana University Cyclotron Facility, Bloomington, Indiana, USA, April 2, 2004, Los Alamos National Laboratory document LA-UR-04-3900.

W.S. Wilburn, J.D. Bowman, G.S. Mitchell, J.M. O’Donnell, and P.-N. Seo, “Measurement of neutron decay parameters: The ABba experiment,” Medium Energy Seminar: University of Illinois, Urbana-Champaign, Illinois, USA, February 18, 2004, Los Alamos National Laboratory document LA-UR-04-3900.

D.C. Wilson, A. Hauer, A. Nobile, J.C. Cooley, P.S. Ebey, N.M. Hoffman, D.L. Tubbs, C.R. Christensen, and G.P. Grim, “Los Alamos progress towards NIF ignition,” DOE/CEA Technical Exchange, Livermore, California, USA, May 2004, Los Alamos National Laboratory document LA-UR-04-3220.

D.C. Wilson, A. Hauer, A. Nobile, J.C. Fernández, J.C. Cooley, P.S. Ebey, N.M. Hoffman, D.L. Tubbs, C.R. Christensen, and G.P. Grim, “Los Alamos progress toward NIF ignition,” DOE/CEA Technical Cooperation Agreement Co-Chairmen’s Meeting,

Bordeaux, France, June, 2004, Los Alamos National Laboratory document LA-UR-04-3651.

J.B. Workman, J.R. Fincke, P.A. Keiter, G.A. Kyrala, T.H. Pierce, J.P. Knauer, S. Sublett, H. Robey, and S.G. Glendinning, “Development of intense point x-ray sources for backlighting HED experiments,” 15th Topical Conference on High-Temperature Plasma Diagnostics, San Diego, California, USA, April 19–22, 2004, Los Alamos National Laboratory document LA-UR-04-0263.

G.A. Wurden, “Overview of magneto-inertial fusion,” 16th American Nuclear Society Topical Conference on the Technology of Fusion Energy, Madison, Wisconsin, USA, September 14–16, 2004, Los Alamos National Laboratory document LA-UR-04-6547.

G.A. Wurden, T.P. Intrator, I.G. Furno, and S.C. Hsu, “Progress and plans for plasma studies on the FRX-L field reversed configuration experiment,” Innovative Confinement Concepts Workshop (ICC 2004), Madison, Wisconsin, USA, May 25–28, 2004, Los Alamos National Laboratory document LA-UR-04-2711.

G.A. Wurden, T.P. Intrator, S.Y. Zhang, I.G. Furno, S.C. Hsu, J.Y. Park, R. Kirkpatrick, R.M. Renneke, K.F. Schoenberg, M.J. Taccetti, M.G. Tuszewski, W.J. Waganaar, Z. Wang, R.E. Siemon, J.H. Degnan, D.G. Gale, C. Grabowski, E.L. Ruden, W. Sommars, M.H. Frese, S. Coffey, G. Craddock, S.D. Frese, and N.F. Roderick, “FRC plasma studies on the FRX-L plasma injector for magnetized target fusion,” 20th IAEA Fusion Energy Conference, Vilamoura, Portugal, November 1–6, 2004, Los Alamos National Laboratory document LA-UR-04-7967.

A.M. Yamauchi, X.-C. Yao, D.M. Rector, and J.S. George, “Rapid OCT recording of intrinsic optical evoked responses in amphibian retina,” 34th Annual Meeting of the Society for Neuroscience (Neuroscience2004), San Diego, California, USA, October 23–27, 2004, Los Alamos National Laboratory document LA-UR-04-3630.

X.-C. Yao and J.S. George, “Rapid phase modulation for optical coherence tomography using electro-optic phase modulator,” OSA Biomedical Topic Meeting, Miami Beach, Florida, USA, April 14–17, 2004, Los Alamos National Laboratory document LA-UR-03-8762.

S.Y. Zhang, E.M. Tejero, M.J. Taccetti, G.A. Wurden, T.P. Intrator, and W.J. Waganaar, “The separatrix radius measurement of field-reversed configuration plasma in FRX-L,” 15th Topical Conference on High-Temperature Plasma Diagnostics, San Diego, California, USA, April 19–22, 2004, Los Alamos National Laboratory document LA-UR-04-2566.

S.Y. Zhang, G.A. Wurden, T.P. Intrator, W.J. Waganaar, R.M. Renneke, M.J. Taccetti, I.G. Furno, S.C. Hsu, E.M. Tejero, C. Grabowski, and E.L. Ruden, “Formation of target field-reversed configuration plasma for magnetized target in FRX-L,” Innovative Confinement Concepts workshop (ICC-2004), Madison, Wisconsin, USA, May 25–28, 2004, Los Alamos National Laboratory document LA-UR-04-2577.

